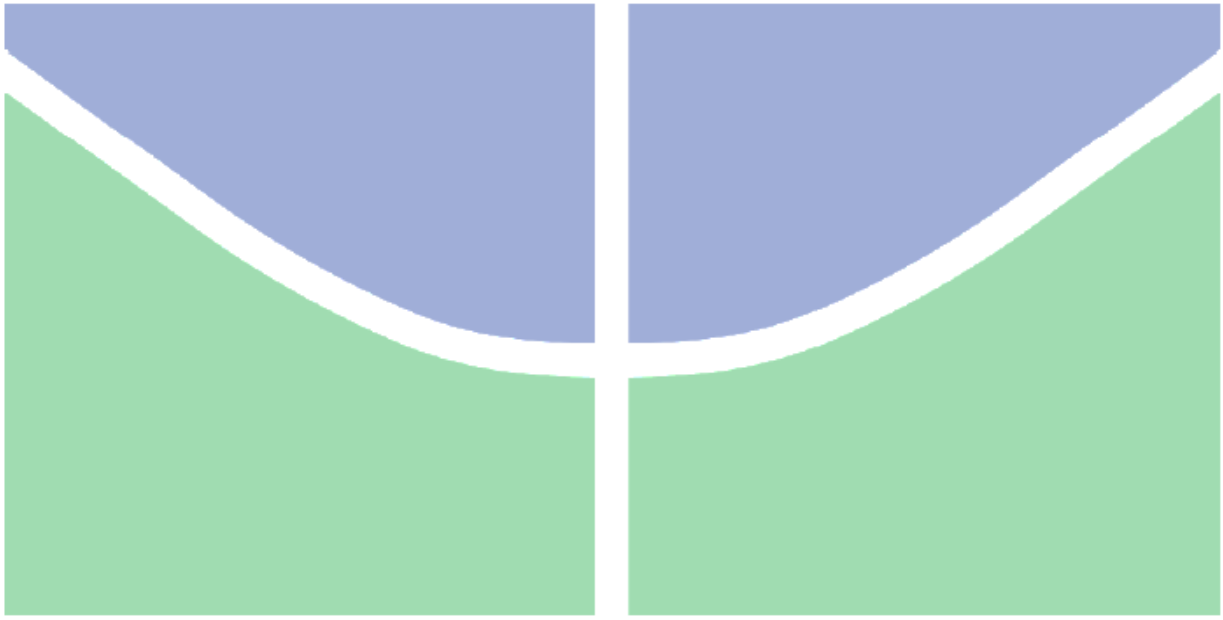


DEVELOPMENT OF CHARACTERIZATION TEST FOR FIBER REINFORCED SELF-COMPACTING CONCRETE OF SMALL THICKNESS ELEMENTS

PEDRO PAULO MARTINS DE CARVALHO

TESE DE DOUTORADO EM ESTRUTURAS E CONSTRUÇÃO CIVIL

DEPARTAMENTO DE ENGENHARIA CIVIL E AMBIENTAL

FACULDADE DE TECNOLOGIA

UNIVERSIDADE DE BRASÍLIA

UNIVERSIDADE DE BRASÍLIA

FACULDADE DE TECNOLOGIA

DEPARTAMENTO DE ENGENHARIA CIVIL E AMBIENTAL

DEVELOPMENT OF CHARACTERIZATION TEST FOR FIBER REINFORCED SELF-COMPACTING CONCRETE OF SMALL THICKNESS ELEMENTS

PEDRO PAULO MARTINS DE CARVALHO

ORIENTADOR: RODRIGO DE MELO LAMEIRAS

COORIENTADOR: RAÚL DARÍO DURAND FARFÁN

TESE DE DOUTORADO EM ESTRUTURAS E CONSTRUÇÃO CIVIL

BRASÍLIA/DF, 26 DE MARÇO DE 2025

PEDRO PAULO MARTINS DE CARVALHO

DEVELOPMENT OF CHARACTERIZATION TEST FOR FIBER REINFORCED SELF-COMPACTING CONCRETE OF SMALL THICKNESS ELEMENTS

TESE SUBMETIDA AO DEPARTAMENTO DE ENGENHARIA CIVIL E AMBIENTAL DA FACULDADE DE TECNOLOGIA DA UNIVERSIDADE DE BRASÍLIA COMO PARTE DOS REQUISITOS NECESSÁRIOS PARA A OBTENÇÃO DO GRAU DE DOUTOR EM ESTRUTURAS E CONSTRUÇÃO CIVIL.

APROVADO POR:

_____

Prof. Dr. Rodrigo de Melo Lameiras (UnB)

(Orientador)

_____

Prof. Dr. Francisco Evangelista Junior (UnB)

(Examinador interno)

_____

Prof. Dr. Vitor Manuel do Couto Fernandes da Cunha (UMinho)

(Examinador externo)

_____

Prof. Dr. Leandro Mouta Trautwein (UNICAMP)

(Examinador externo)

BRASÍLIA/DF, 26 DE MARÇO DE 2025

DEDICATION

I dedicate this thesis to my parents, who taught me the value of knowledge and have always been my foundation.

To my sister, for her friendship and unconditional support.

To my family, who, in many ways, contributed to my journey to this point.

To my wife, for her patience, encouragement, and unwavering love throughout this journey.

DEDICATÓRIA

Dedico esta tese aos meus pais, que me ensinaram
o valor do conhecimento e sempre foram meu alicerce.
À minha irmã, pela sua amizade e apoio incondicional.
A minha família, que, de diversas formas, contribuiu para minha jornada até aqui.
À minha esposa, pela sua paciência, incentivo e amor inabalável ao longo dessa jornada.

ACKNOWLEDGMENTS

The journey to the completion of this thesis has been marked by challenges, learning, and the support of many individuals to whom I express my deep gratitude.

I would first like to thank my advisor, Prof. Dr. Rodrigo de Melo Lameiras, for his competent guidance, patience, and dedication throughout this research. His expertise and encouragement were essential for the completion of this work. I also thank my co-advisor, Prof. Dr. Raúl Darío Durand Farfán, for his valuable contributions that enriched this investigation.

I am grateful to the other professors who shared their knowledge and contributed academically to my formation. I also thank the laboratory technicians who provided essential support in carrying out the experiments and analyses.

I extend my gratitude to the members of my Ph.D. qualifying exam and PhD dissertation defense: Prof. Dr. Vitor Manuel do Couto Fernandes da Cunha, Prof. Dr. Francisco Evangelista Junior, Prof. Dr. Leandro Mouta Trautwein, and Prof. Dr. Raúl Darío Durand Farfán, as well as my advisor Prof. Dr. Rodrigo de Melo Lameiras, for the time dedicated to evaluating this work, for the valuable suggestions, and for the contributions that significantly helped to improve this research.

I am deeply grateful to my friends and colleagues from the Graduate Program in Structures and Civil Construction and from the Scientific Initiation Program at the University of Brasília (UnB) for the encouraging conversations during difficult times, the support with concrete casting, testing, transportation of equipment and research materials, the exchange of knowledge that made this journey more enriching, and the many other forms of contribution. I would like to especially thank John Kennedy, Matheus Galvão, Wallas, Luana, Mara, Késsio, Geovanna, Renan, Nathaniel, Paulo, Gianlucca, Fernanda, Tiago, Carol, Amir, Éder, Luciano, Izabel, Luísa, Karine, Jonas, Iana, Larissa, Jerfson, Guilherme, Augusto, Pedro, Iago, Iarly, Maurício, Bernardo, Layane, Rodolfo, Matheus Silva, Brenda, and Júlia. I also extend my gratitude to many others who, although not mentioned by name here, were equally important throughout this journey.

I would also like to thank the Universidade Federal do Oeste da Bahia (UFOB) for granting me leave for qualification, as well as for the financial support in the form of a salary, which enabled my dedication to this study

I am thankful to the Graduate Support Program (PROAP) for the student aid that contributed to the success of this research.

I thank the University of Brasília for providing me with the opportunity to pursue this doctorate and for its institutional support. The university, with its resources, infrastructure, and learning environment, was fundamental to the development of this research and my growth as a researcher.

To my parents, for their unconditional love, the values they instilled in me, the support they have given me throughout my life, and for always believing in my potential. To my sister and other family members, for their affection and continuous support.

To my wife, for her patience, encouragement, and for being by my side at every moment of this journey, making the challenges lighter and the achievements even more meaningful.

My deepest gratitude goes to all those who, in one way or another, contributed to the success of this research, even if I am unable to name them all individually at this moment.

To all of you, my sincere thanks.

AGRADECIMENTOS

A jornada até a conclusão desta tese foi marcada por desafios, aprendizado e pelo apoio de muitas pessoas às quais expresso minha profunda gratidão.

Gostaria, primeiramente, de agradecer ao meu orientador, Prof. Dr. Rodrigo de Melo Lameiras, por sua orientação competente, paciência e dedicação ao longo desta pesquisa. Sua experiência e incentivo foram essenciais para a conclusão deste trabalho. Também agradeço ao meu coorientador, Prof. Dr. Raúl Darío Durand Farfán, pelas valiosas contribuições que enriqueceram esta investigação.

Sou grato aos outros professores da UnB que compartilharam seu conhecimento e contribuíram academicamente para a minha formação. Agradeço também aos técnicos de laboratório da UnB que forneceram suporte essencial na execução dos experimentos e análises.

Expresso minha gratidão aos membros do meu exame de qualificação e da defesa de tese doutorado: Prof. Dr. Vitor Manuel do Couto Fernandes da Cunha, Prof. Dr. Francisco Evangelista Junior, Prof. Dr. Leandro Mouta Trautwein e Prof. Dr. Raúl Darío Durand Farfán, além do presidente das bancas, meu orientador, Prof. Dr. Rodrigo de Melo Lameiras, pelo tempo dedicado à avaliação deste trabalho, pelas valiosas sugestões e pelas contribuições que ajudaram a aprimorar significativamente esta pesquisa.

Aos meus amigos e colegas do Programa de Pós-Graduação em Estruturas e Construção Civil e da Iniciação Científica da UnB, sou profundamente grato pelas conversas encorajadoras durante os momentos difíceis, pelo apoio nas concretagens, ensaios, transporte de equipamentos e materiais da pesquisa, pela troca de conhecimentos que tornaram essa jornada mais enriquecedora e pelas diversas outras formas de contribuição. Agradeço, em especial, a John Kennedy, Matheus Galvão, Wallas, Luana, Mara, Késsio, Geovanna, Renan, Nathaniel, Paulo, Gianlucca, Fernanda, Tiago, Carol, Amir, Éder, Luciano, Izabel, Luísa, Karine, Jonas, Iana, Larissa, Jerfson, Guilherme, Augusto, Pedro, Iago, Iarly, Maurício, Bernardo, Layane, Rodolfo, Matheus Silva, Brenda e Júlia. Estendo também meu agradecimento a tantos outros que, mesmo não sendo aqui nomeados, foram igualmente importantes ao longo dessa trajetória.

Gostaria também de agradecer à Universidade Federal do Oeste da Bahia (UFOB) pela concessão de afastamento para qualificação, assim como pelo suporte financeiro na forma de salário, que possibilitou minha dedicação a este estudo.

Sou grato ao Programa de Apoio à Pós-Graduação (PROAP) pelo auxílio estudantil, que contribuiu para a realização desta pesquisa.

Agradeço à Universidade de Brasília pela oportunidade de realizar este doutorado e pelo apoio institucional. Os recursos, a infraestrutura e o ambiente de aprendizado da universidade foram fundamentais para o desenvolvimento desta pesquisa e para o meu crescimento como pesquisador.

Aos meus pais, pelo amor incondicional, pelos valores que me transmitiram, pelo apoio que me deram durante toda a minha vida e por sempre acreditarem no meu potencial. À minha irmã e demais familiares, pelo carinho e apoio contínuo.

À minha esposa, pela paciência, incentivo e por estar ao meu lado em cada momento dessa jornada, tornando os desafios mais leves e as conquistas ainda mais significativas.

Minha mais profunda gratidão a todos aqueles que, de alguma forma, contribuíram para o sucesso desta pesquisa, mesmo que eu não consiga nomeá-los individualmente neste momento.

A todos vocês, meu sincero agradecimento.

ABSTRACT

DEVELOPMENT OF CHARACTERIZATION TEST FOR FIBER REINFORCED SELF-COMPACTING CONCRETE OF SMALL THICKNESS ELEMENTS

Author: Pedro Paulo Martins de Carvalho

Supervisor: Rodrigo de Melo Lameiras

Co-Supervisor: Raúl Darío Durand Farfán

Programa de Pós-graduação em Estruturas e Construção Civil

Universidade de Brasília

Brasília, 26 de março de 2025

The test methods for determining the post-cracking behavior parameters of Steel Fiber Reinforced Self-Compacting Concrete (SFRSCC) have been constantly improved. The Semi-Circular Bending Test (SCBT) for this composite is a new proposal that is promising and shown important advantages such as the possibility of carrying out the test on cores extracted directly from the structural element and the low cost and simplicity of carrying out. However, the literature on this topic is still scarce. This work aims to propose a new test, hereinafter called Modified Semi-Circular Bending Test (MSCBT), which is a modified version of the SCBT, through an experimental program involving innovations such as: the monitoring of the Crack Mouth Opening Displacement (CMOD), the study of sample dimensions, the influence of different types and contents of steel fibers, as well as the type of concrete and the comparison with other tests already well covered in the literature for the same purpose. A computational algorithm for carrying out the inverse analysis progressive procedure is developed and its results compared with those of different literatures. The tensile parameters of SFRSCC were employed for simulation using Finite Element Method (FEM) software for MSCBT.

Keywords: Modified Semi-Circular Bending Test (MSCBT), Post-Cracking Behavior, Steel Fiber Reinforced Self-Compacting Concrete (SFRSCC).

RESUMO

DESENVOLVIMENTO DE ENSAIO DE CARACTERIZAÇÃO DE CONCRETO AUTO-ADENSÁVEL REFORÇADO COM FIBRAS DE ELEMENTOS DE PEQUENA ESPESSURA

Autor: Pedro Paulo Martins de Carvalho
Orientador: Rodrigo de Melo Lameiras
Coorientador: Raúl Darío Durand Farfán
Programa de Pós-graduação em Estruturas e Construção Civil
Universidade de Brasília
Brasília, 26 de março de 2025

Os métodos de ensaio para determinação dos parâmetros do comportamento pós-fissuração do Concreto Auto-Adensável Reforçado com Fibras de Aço (SFRSCC) têm sido constantemente aprimorados. O Ensaio de Flexão Semi-Circular (SCBT) para este compósito é uma nova proposta que se mostra promissora e apresenta importantes vantagens, como a possibilidade de realizar o teste em amostras extraídas diretamente do elemento estrutural, o baixo custo e simplicidade na execução. No entanto, a literatura sobre este tema ainda é escassa. Este trabalho tem como objetivo propor um novo ensaio, doravante denominado Ensaio de Flexão Semi-Circular Modificado (MSCBT), que é uma versão modificada do SCBT, por meio de um programa experimental envolvendo inovações, como: o monitoramento da Deslocamento da Abertura da Boca da Fissura (CMOD), o estudo das dimensões das amostras, a influência de diferentes tipos e teores de fibras de aço, bem como o tipo de concreto e a comparação com outros testes já bem abordados na literatura para o mesmo propósito. Um algoritmo computacional para a realização do procedimento de análise inversa progressiva é desenvolvido e seus resultados comparados com os de diferentes literaturas. Os parâmetros de tensão do SFRSCC foram empregados para simulação utilizando software de Método dos Elementos Finitos (MEF) para o MSCBT.

Palavras-chave: Teste de Flexão Semi-Circular Modificado (MSCBT), Comportamento Pós-Fissuração, Concreto Auto-Adensável Reforçado com Fibras de Aço (SFRSCC).

TABLE OF CONTENTS

1. INTRODUCTION 32

2. OBJECTIVES 34

3. LITERATURE REVIEW 35

3.1. Fiber Reinforced Concrete (FRC) 35

3.2. Steel Fibers on the Mechanical Behavior of Steel Fiber-Reinforced Concrete (SFRC) 36

3.3. Post-Cracking Residual Strength Parameters, according to the *fib* Model Code 2010 (2012) 38

3.3.1. FRC simplified stress-crack opening constitutive laws for bending 40

3.4. FRC properties 41

3.5. Tests for Characterization of the FRC and Disk-Shaped Compact Tension (DCT) 42

3.5.1. Uniaxial Tensile Test (UTT) 42

3.5.2. Bending tests 48

3.5.3. Wedge Splitting Test (WST) 51

3.5.4. Double Punch Test (DPT) and Barcelona Test (BT) 53

3.5.5. Splitting Test (ST) 55

3.5.6. Round Panel Test (RPT) 58

3.5.7. DEWST (Double Edge Wedge Splitting Test) 61

3.5.8. Montevideo (MVD) and Modified Wedge Splitting Test (MWST) 63

3.5.9. Disk-Shaped Compact Tension (DCT) 64

3.5.10. Semi-Circular Bending Test (SCBT) 66

3.6. Inverse Analysis 69

3.7. Analytical Model for Determination of (F–CMOD) Diagrams 73

3.8. Simulation of Fiber Reinforced Concrete (FRC) with Finite Element Method (FEM) 78

3.9. Julia programming language 81

3.10. The Amaru.jl Library for Finite Element Analysis in Solid Mechanics 82

3.11. Inverse method for determining the stress-crack width (σ-w) 84

3.12. Influence of fiber orientation on Fiber Reinforced Concrete (FRC) 86

3.13. Wall effect 88

3.14. Influence of dimensions on SFRC behavior and structural specimen 89

4. METHODOLOGY 92

4.1. Flowchart of work activities 92

4.2. Characteristics of parameter monitoring equipment during tests 94

4.3. Molding characteristics of test samples 95

4.4. Compressive tests and flow spread 97

4.5. Sample Preparation for the 3PBT 97

4.6. Sample Preparation for the MSCBT 98

4.6.1. Details of sample extraction 99

4.6.2. Sample marking 100

4.6.3. Cutting of samples by means of a core drilling machine 101

4.6.4. Cutting samples by means of a concrete block cutter 102

4.6.5. Notches 105

4.6.6. Preparation of plates for fixing transducers 107

4.6.7. Preparation of support for the test 109

4.6.8. Monitoring throughout the test 111

4.7. Sample preparation for UTT 111

4.7.1. Choice of sample extraction position 111

4.7.2. Sample marking 113

4.7.3. Cutting of samples by means of a core extraction 114

4.7.4. Cutting samples by means of a block saw 114

4.7.5. Making of notches 117

4.7.6. Preparation of plates for fixing transducers 118

4.7.7. Characteristics of the apparatus for carrying out the test 119

4.7.8. Monitoring throughout the test 123

4.8. Preparation of samples for the ST 123

4.8.1. Extraction of sample 123

4.8.2. Sample cutting 123

4.8.3. Preparation of plates for fixing transducers and support system 128

4.8.4. Monitoring throughout the test 129

4.9. IA algorithm for 3PBT (progressive method) 130

4.9.1. The Conception of Inverse Analysis 131

4.9.2. Initial Parameters Determination 134

4.9.3. f_{ct} determination 136

4.9.4. σ_1 / f_{ct} determination 138

4.9.5. σ_2 / f_{ct} determination 139

4.9.6. σ_3 / f_{ct} determination 139

4.9.7. Choice of the Best Fit Curve 139

4.9.8. Validation of the Inverse Analysis Procedure 141

4.10. IA algorithm for MSCBT (preliminary results) 143

4.11. General Information on the Numerical Simulation Tools Used in this work 143

4.12. Diana numerical model for MSCBT (simulation) 144

4.13. Numerical model for MSCBT using the Amaru library 148

4.13.1. Cohesive Elements 149

4.13.2. Cohesive Zone Model 151

4.13.3. Power Yield Crack 153

4.13.4. Asinh Yield Crack 155

4.13.5. Willam-Warnke model 155

4.13.6. Comparing simulations with experimental results 156

4.13.7. Parametric study 160

4.14. MSCBT (conception) 164

4.15. MSCBT (sample thickness) 165

4.16. ST (conception) 165

4.17. Fiber counting procedure for 3PBT, MSCBT and ST 166

5. RESULTS 168

5.1. IA algorithm for 3PBT (progressive method) 168

5.1.1. Determination of f_{ct} 168

5.1.2. Determination of σ_1 170

5.1.3. Determination of σ_2 172

5.1.4. Determination of σ_3 173

5.1.5. $F-CMOD$ Full Diagram 176

5.1.6. Inverse Analysis 178

5.1.7. Discussions 183

5.2. Compressive tests 183

5.3. 3PBT 184

5.4. MSCBT (conception) 189

5.4.1. Concrete Mixture 189

5.4.2. Compressive tests 189

5.4.3. F-CMOD results (MSCBT) 189

5.4.4. F_i equations 198

5.4.5. Discussions 201

5.4.6. Comparing MSCBT with 3PBT 202

5.5. Uniaxial Tensile Tests (UTT) 202

5.5.1. Concrete Mixture 203

5.5.2. Compressive tests 204

5.5.3. Tensile vs. *COD* results (UTT) 204

5.6. ST (conception) 208

5.6.1. Concrete Mixture 209

5.6.2. Compressive tests 209

5.6.3. F-COD results (ST) 209

5.6.4. Discussions 216

5.7. MSCBT (sample thickness) 217

5.7.1. MSCBT - F-CMOD results 217

5.7.2. Discussions 221

5.8. IA algorithm for MSCBT (preliminary results) 222

5.9. IA algorithm for MSCBT and 3PBT and numerical model (simulation) 225

5.9.1. Inverse Analysis 225

5.9.2. Numerical simulation with Diana FEA 229

5.9.3. Numerical simulation with Julia (comparing simulations with experimental results for 3PBT, UTT and MSCBT) 230

5.9.4. Numerical simulation with Julia (parametric study) 239

5.9.5. Discussion of results 247

6. CONCLUSIONS 249

6.1. General conclusions 249

6.1.1. Final Considerations on the Feasibility and Robustness of the MSCBT Methodology 250

6.1.2. MSCBT applied to specimens of varying thicknesses 252

6.1.3. Effectiveness of the used Splitting Tensile Test (ST) in Evaluating Fracture and Residual Behavior of SFRSCC 253

6.1.4. Computational Simulations 254

6.2. Limitations of the Study 254

6.3. Recommendations for future research 256

6.3.1. Proposed Modifications to MSCBT Specimen Geometry for Enhanced Test Reliability 256

6.3.2. Proposed Application of MSCBT to Core Samples Extracted from Real Structural Elements 257

6.3.3. Further Investigation on the Influence of Specimen Thickness in MSCBT . 258

6.3.4. Mitigating Lateral Restraint Effects in MSCBT through Improved Boundary Conditions..... 259

6.3.5. Parametric Calibration of Inverse Analysis Inputs Based on Fiber Content and Hook Geometry..... 259

6.3.6. initial estimate for w_u on inverse analysis procedure..... 260

6.3.7. Use of clip gauge for MSCBT..... 260

6.3.8. Test Simulations..... 261

REFERENCES 262

LIST OF TABLES

Table 3.1 – Classification method for FRC post-cracking strength according to *fib* Model Code 2010 (2012). 40

Table 3.2 – Works that address contributions on the UTT. 47

Table 3.3 – References that address contributions on the 3PBT. 51

Table 3.4 – Main contributions to WST. 52

Table 3.5 – Main contributions to DPT and BT. 55

Table 3.6 – Main contributions to ST. 57

Table 3.7 – Works that address contributions on the RPT and SRDP tests. 61

Table 3.8 – Works that address contributions on the DEWST. 63

Table 3.9 - Contributions and dimensions of samples tested for SCBT for fiber concretes 68

Table 3.10 – Different values of *Lh* adopted by the literature, adapted from Montaignac *et al*. (2012) and Salehian (2015). 72

Table 4.1 – Concrete components to be used in the work for strength of 20 MPa and 40 MPa. 95

Table 4.2 – Characteristics of the fibers of the samples tested according to the concrete. . 96

Table 4.3 – Characteristics of the hooked-end steel fibers of the samples used in this research. 96

Table 4.4 – Characteristics of the analyzed fibers and concretes. 142

Table 4.5 – Finite element models elements and nodes for UTT, 3PBT and MSCBT. 158

Table 4.6 – Material properties of simulations according to the concrete type. 160

Table 4.7 – Dimensions and notations of simulations performed varying notch size and sample length. 161

Table 4.8 – Finite element models elements and nodes for MSCBT simulations with varying notch depth and sample length. 163

Table 5.1 – Parameters from the inverse analysis for different FRC types. 179

Table 5.2 – average compressive strength results (f_{cm}) in MPa for each type of concrete. 184

Table 5.3 – Values obtained (Average and CoV.) from 3PBT for: Residual strengths (f_{r1}, f_{r2}, f_{r3} and f_{r4}), $f_{fct,L}$ and f_{ct}. Adapted from Cardoso (2021). 187

Table 5.4 – Average (Avg.), upper bound (U.B.) and lower bound (L.B.) values for the areas of the *F-CMOD* diagrams for each type of concrete. 194

Table 5.5 – Parameters $f_{fct,L,}$ $f_{ct,}$ $F_{1,}$ $F_{2,}$ F_3 and F_4 determined experimentally for MSCBT with thickness 75mm. 197

Table 5.6 – Predicted and experimental values of the parameters $F_{1,}$ $F_{2,}$ F_3 and F_4, as well as error (between predicted and experimental values) for MSCBT. 200

Table 5.7 – Residual flexural strength of the concretes determined for 3PBT as recommended by fib Model Code 2010 (fib, 2012). 202

Table 5.8 – Average (Avg.), upper bound (U.B.) and lower bound (L.B.) values for the areas of the Tensile Stress versus *COD* diagrams for UTT. 206

Table 5.9 – Average (Avg.), upper bound (U.B.) and lower bound (L.B.) values for the areas of the σ-*COD* diagrams in kN.mm for each type of concrete. 213

Table 5.10 – Average (Avg.), upper bound (U.B.) and lower bound (L.B.) values for the areas of the *F-CMOD* diagrams in kN.mm for each thickness and each type of concrete for MSCBT. 220

Table 5.11 – Area under Tensile Stress vs. Crack Opening diagrams for $L_{h1}=H/2$ and $L_{h2}=H$ and percentage difference between them. 224

Table 5.12 – Parameters of the $\sigma - w$ diagram after inverse analysis procedure. 225

Table 5.13 – Fracture parameters for the average behavior obtained by inverse analysis of MSCBT and 3PBT. 229

Table 5.14 – Material properties of simulations according to the concrete type. 231

Table 5.15 – Area under the Tensile vs. COD for the UTT numerical results, compared with the experimental average for concretes: (a) C-10, (b) C-11, and (c) C-12. 236

Table 5.16 - Area under the Force vs. CMOD for the 3PBT numerical results, compared with the experimental average for concretes: (a) C-10, (b) C-11, and (c) C-12. 238

Table 5.17 - Area under the Force vs. CMOD for the 3PBT numerical results, compared with the experimental average for concretes: (a) C-10, (b) C-11, and (c) C-12. 239

Table 5.18 – Material properties of simulations according to the concrete type. 240

Table 5.19 - Area under the Force vs. CMOD diagrams for simulations at each notch depth and each sample length. 245

Table 5.20 – Vertical coordinates (y) of points $a1$, $a2$, $a3$, $a4$ and $a5$ and the respective εxx, relative to the coordinate axes for simulations S-150-13 and S-150-28. 246

LIST OF FIGURES

Figure 3.1 – Schematic representation of FRC behavior: hardening (a) and softening (b). 36

Figure 3.2 – hsp position on 3PBT sample. 39

Figure 3.3 – Load-CMOD curve. Adapted from *fib* Model Code 2010 (2012). 39

Figure 3.4 – Post-cracking linear constitutive law of the FRC. Adapted from *fib* Model Code 2010 (2012). 41

Figure 3.5 – Schematic representation of the uniaxial tensile test (a) bone-shaped specimen. (b) free rotation configuration. (c) fixed end configuration (Salehian, 2015). 43

Figure 3.6 – Samples with notch for UTT in shapes: (a) prismatic and (b) cylindrical. 43

Figure 3.7 – Curves: Tensile Stress vs. Crack Oppening Displacement. 45

Figure 3.8 – Shapes of the usual samples for the UTT: (a) dog bone with straight parts shape, (b) dog bone with curve shape, (c) cylindrical-shaped, (d) dog bone with profile I shape and (e) prismatic shape. 47

Figure 3.9 – Bending Tests: (a) Four Point Bending Test (4PBT) or (b) Three Point Bending Test (3PBT) highlighting the notch in the middle of the span, (c) sample side view with LVDT and (d) view of LVDT with backing plates, (e) sample side view with clip gage and (f) view of clip gage. 49

Figure 3.10 – Sample test setup for Wedge Splitting Test. 52

Figure 3.11 – Barcelona Test sample illustration with crack lines. 54

Figure 3.12 – Sample shapes for the ST (front view and three-dimensional perspective): (a) Side view and (b) Perspective view of the traditional test without notch (Ozyurt, et al., 2007; Carmona & Aguado, 2012), (c) Side view and (d) Perspective view of the MSTT test (Abrishambaf, Barros and Cunha, 2013), (e) Side view and (f) Perspective view of the test proposed by Lameiras, Barros and Azenha (2015). 57

Figure 3.13 – Illustration of the samples of: (a) SPT, (b) RPT with Simple Support (RPT-WSS), (c) RPT with Three Pivots (RPT-WTP) and (d) bottom view of RPT-WTP with LVDTs. 59

Figure 3.14 – Sample illustration for performing the DEWST. 62

Figure 3.15 – Modifications: (a) MVD test, (b) MWST test setup, (c) Description of the elements of the MWST apparatus. 64

Figure 3.16 – DCT geometry. 65

Figure 3.17 – Illustration of semicircular specimen for bending test. 67

Figure 3.18 – Schematic representation of the diagrams of the inverse analysis procedure: (a) input (Force vs. Displacement or CMOD) and (b) output (Tensile Stress vs. Crack Opening Displacement. Adapted from Carvalho & Lameiras (2023). 70

Figure 3.19 – Representative scheme of the beam under the 3PBT test, highlighting: (a) overview of the test with dimensional parameters, (b) plastic hinge element with plastic hinge length (Lh), and (c) layering of the cross-section. Adapted from Carvalho & Lameiras (2023) and Salehian (2015). 74

Figure 3.20 - Schematic representation of the representative model employed to characterize the post-cracking behavior of FRC and determine the F-δ response with adaptations (Salehian, 2015). Within this context, L_f and d_f denote the length and diameter of the fibers, respectively, while $n_L=H-h$. Additionally, $\sigma_{cc}(\varepsilon_{cc})$ represents the compressive stress derived from the modified constitutive model (Barros & Figueiras, 1999a), and $\sigma_{ct}(\varepsilon_{ct})$ is the tensile stress derived from the bilinear stress-strain relationship of *fib* Model Code 2010 (fib, 2012). 77

Figure 3.21 – Parameters of Inverse Analysis procedure. 85

Figure 3.22 - Relationship between concrete flow orientation according to molding position and predominant fiber orientation. 86

Figure 3.23 – Scenarios in which the mold walls can influence the preferential orientation of the fibers: (a) No boundaries, (b) Two boundaries and (c) Four boundaries. 89

Figure 4.1 – General work flowchart. 93

Figure 4.2 – 3PBT setup illustration (dimensions in mm): (a) overview and dimensions, (b) notch dimensions and LVDT position, (c) detail of LVDT positioning scheme. 98

Figure 4.3 – Sample illustration: (a) after bending test and (b) after extraction of cylindrical core for MSCBT 100

Figure 4.4 – Samples with markings for extracting cylindrical cores. 101

Figure 4.5 – Core extraction using a drill. 102

Figure 4.6 – Sample cuts using a block cutter performed on the sample to obtain the semicircular shape. 103

Figure 4.7 – Sample extraction and cutting procedure for MSCBT (dimensions in mm) with x, y and z axis: (a) prismatic 3PBT sample parts 1 and 2, (b) cilynders extraction of 3PBT sample part, (c) extracted cylinder with cut 1 marking, (d) resulting sample after cut 1 with cut marking 2 (performed only for 75 mm wide specimens), (e) notch cut position, (f) enlarged view of notch with dimensions, (g) final dimensions of the sample and (h) Illustration of the fiber dimension in relation to the sample. 104

Figure 4.8 – Samples with markings for making notches in semicircular samples for MSCBT with emphasis on fixing with c-clamp metallic claw and marble saw for cutting. 106

Figure 4.9 – Samples after making the notches for MSCBT. 106

Figure 4.10 – Illustration of specimens for MSCBT after cutting (dimensions in mm): (a) specimen with a thickness of 150 mm and (b) specimen with a thickness of 75 mm 107

Figure 4.11 – Illustration of fixation plates: (a) aluminum plates glued to the sample passing through the lower end of the sample and plate with threading for screws of 5 mm in diameter; (b) sample ready for testing with steel plates with hexagonal screws of 10 mm in diameter; (c) initial placement of larger plates. 108

Figure 4.12 – Scheme for performing the MSCBT (dimensions in mm). 110

Figure 4.13 – Bottom view of sample for MSCBT highlighting teflon tape and grease placement. 111

Figure 4.14 – Cutting process to obtain sample for UTT (dimensions in mm): (a) 3PBT half samples scheme, (b) Final UTT sample with dimensions (z-axis represents the molding direction and y-axis represents the predominant orientation of the fibers), (c) Notch scheme with dimensions, (d) Final sample illustration for UTT. 112

Figure 4.15 – Samples with line markings for core extraction in prismatic shape to obtain samples for UTT. 114

Figure 4.16 – Cuts in samples using a block saw. (a) first cut of the prismatic sample (discard fractured part of the sample), (b) second cut of the prismatic sample, (c) third cut of the prismatic sample. 115

Figure 4.17 – Schematic illustration of the cuts for obtaining a sample for the UTT test: (a) First cut, (b) second cut and (c) third cut. 116

Figure 4.18 – Sample for UTT with markings for making notches. 117

Figure 4.19 – Prismatic sample with notch for UTT test execution. 118

Figure 4.20 – Detail illustration of plates for fixing transducers for monitoring CMOD during UTT test. 119

Figure 4.21 – Illustration of the UTT setup: (a) Perspective of the setup with emphasis on Demonstration without reinforcement of side plates, transducers and fitting in the test machine's claws; (b) Highlight for sudden rupture in the glue region; (c) View of the reinforcement of the side plates 120

Figure 4.22 – Illustration of experimental apparatus for performing the UTT: (a) overview, (b) scheme of the assembled system and (c) scheme detailing the parts of the system. ... 122

Figure 4.23 – Illustration of the sample for the ST test with emphasis on the sample region between the support plates for the transducers (X region). 124

Figure 4.24 – Marking for orientation of cuts in sample for ST test. 124

Figure 4.25 – Fixing the sample to the block saw table. 125

Figure 4.26 – Sample for performing the ST after cuts with emphasis on straight notches. 126

Figure 4.27 – Samples for carrying out the ST test after performing cuts for notches and after division. 126

Figure 4.28 – Schemes with dimensions and steps of notch cuts for ST samples (dimensions in mm): (a) first step, (b) second step, (c) third step, (d) detail of the depth and thickness of the straight notch with dimensions and (e) top view of the sample with projection of the tips of the V-notches. 127

Figure 4.29 – Illustration of a sample for the ST, highlighting the teflon tape glued and grease on its surface. 128

Figure 4.30 – ST test setup. 129

Figure 4.31 - Flowchart detailing the procedure for determining the parameters σ_1, σ_2, σ_3, w_1, w_2, w_3, w_u to perform the inverse analysis procedure. 132

Figure 4.32 - Illustration of the point generalization process for the inverse analysis procedure. 135

Figure 4.33 – The branch for calculating the area of CMOD between 0 and lim_1. 137

Figure 4.34 – The branches for calculating the areas of CMOD between lim_{p-1} and lim_p are established. 138

Figure 4.35 – Answer $(F - CMOD)anal$ vs. $(F - CMOD)exp.$ 141

Figure 4.36 – Mesh used to the FEM-based model to simulate the MSCBT with the two notches marked with circles which was taken as a reference for determining the CMOD. 146

Figure 4.37 – Results of linear elastic model corresponding to a load equal to 44 N: (a) Color map of the strain (ε_{xx}) distribution in the specimen (dimensions in mm); (b) Strain distribution along the notched section (a_1 *to* a_5) section. 147

Figure 4.38 – Four-node 2D cohesive element with zero thickness ($a = 0$). 149

Figure 4.39 – Representation of the crack in quasi-brittle materials: (a) Fracture process zone and (b) Distribution of cohesive stress within the FPZ. Adapted from Silva (2021). 151

Figure 4.40 – Idealization of fracture in quasi-brittle materials: (a) cohesive crack with crack surfaces in contact ($wt < wc$), and (b) cohesive crack with partial separation of crack surfaces ($wt \geq wc$). Adapted from Bazant and Planas (1998) and Silva (2021)..... 152

Figure 4.41 – Yield and potential plasticity functions, together with the compressive and tensile Mohr's circles. Adapted from Durand et al. (2023). 154

Figure 4.42 – Illustration of the mesh models used for the simulations with the Julia programming language: (a) for the UTT, (b) for the MSCBT, and (c) for the 3PBT. 158

Figure 4.43 – Illustrations of the geometries used in the MSCBT simulations, including notch dimensions, span, and effective span. 162

Figure 4.44 – Mesh models for MSCBT simulations: (a) S-150-13, (b) S-150-19, (c) S-150-24, (d) S-150-28, (e) S-200-16, (f) S-200-24, (g) S-200-31 and S-200-37. 164

Figure 4.45 – Fiber count on section of the samples (the section corresponding to the notch area did not have fibers counted, therefore it is not illustrated) according to test load direction and molding direction for: (a) 3PBT, (b) MSCBT and (c) UTT. UTT (UP UE) and UTT (UP LE) correspond to Section C. UTT (LP UE) and UTT (LP LE) correspond to Section D. 167

Figure 5.1 – Inverse analysis - determination of fct for $\sigma 1/fct$=0.8 compared with experimental result (Lameiras, 2016). 170

Figure 5.2 – Inverse analysis—determination of fct for $\sigma 1/fct = 1.2$ compared with experimental result (Lameiras, 2016). 170

Figure 5.3 – Inverse analysis - determination of $\sigma 1$ for $\sigma 2/fct = 0.8$ compared with experimental result (Lameiras, 2016). 171

Figure 5.4 – Inverse analysis - determination of $\sigma 1$ for $\sigma 2/fct = 1.2$ compared with experimental result (Lameiras, 2016). 172

Figure 5.5 – Inverse analysis—determination of $\sigma 2$ for $\sigma 3/fct = 1.2$ compared with experimental result (Lameiras, 2016). 173

Figure 5.6 – Inverse analysis - determination of $\sigma 2$ for $\sigma 3/fct = 0.8$ compared with experimental result (Lameiras, 2016). 173

Figure 5.7 – Inverse analysis - determination of $\sigma 3$ for $wu = 4.375$ mm compared with experimental result (Lameiras, 2016). 174

Figure 5.8 – Inverse analysis - determination of $\sigma 3$ for $wu = 3.5$ mm compared with experimental result (Lameiras, 2016). 175

Figure 5.9 – Inverse analysis - determination of $\sigma 3$ for $wu = 8.75$ mm compared with experimental result (Lameiras, 2016). 175

Figure 5.10 – Force–CMOD diagram for SFRSCC B concrete compared with experimental resul (Lameiras, 2016). 177

Figure 5.11 – Force–CMOD diagram for FRC60-1 concrete compared with experimental result (Nour, et al., 2015). 177

Figure 5.12 – Force–CMOD diagram for C45-f90 concrete compared with experimental result (Salehian, 2015). 178

Figure 5.13 – Force–CMOD diagram for RSFRC1%_2 concrete compared with experimental result (Frazão, 2019). 178

Figure 5.14 – Stress–COD diagram obtained through inverse analysis for concrete SFRSCC B compared with experimental result (Lameiras, 2016). 181

Figure 5.15 – Stress–COD diagram obtained through inverse analysis for concrete C45-f90 compared with experimental result (Salehian, 2015). 181

Figure 5.16 – Stress–COD diagram obtained through inverse analysis for concrete RSFRC1%_2 compared with experimental result (Frazão, 2019). 182

Figure 5.17 – Stress–COD diagram obtained through inverse analysis for concrete FRC60-1 compared with experimental result (Nour, et al., 2015). 182

Figure 5.18 – *F-CMOD* results for 3PBT samples for concretes with 20 MPa: (a) C-1, (b) C-2, (c) C-3, (d) C-4, (e) C-5 and (f) C-6. Adapted from Cardoso (2021). 185

Figure 5.19 – *F-CMOD* results for 3PBT samples for concretes with 40 MPa: (a) C-7, (b) C-8, (c) C-9, (d) C-10, (e) C-11 and (f) C-12. Adapted from Cardoso (2021). 186

Figure 5.20 – Illustration of the types of cracks during the MSCBT: (a) Support crack, (b) Lateral crack, (c) Multiple cracks, and (d) Single crack. 190

Figure 5.21 – *F-CMOD* results for MSCBT samples with a thickness of 75 mm for concretes with 20 MPa: (a) C-1, (b) C-2, (c) C-3, (d) C-4, (e) C-5 and (f) C-6. 192

Figure 5.22 – *F-CMOD* results for MSCBT samples with a thickness of 75 mm for concretes with 40 MPa: (a) C-7, (b) C-8, (c) C-9, (d) C-10, (e) C-11 and (f) C-12. 193

Figure 5.23 – Relationships between the average number of effective fibers per square centimeter and the average area of F-CMOD diagram for each kind of concrete. 196

Figure 5.24 – Peculiar behaviors observed during the execution of the UTT: (a) Crack outside the notch position, and (b) Sample curvature. 204

Figure 5.25 – Average and envelope form experimental curves Tensiles Stress versus COD for UTT results molded with the concretes: (a) C-10, (b) C-11 and (c) C-12. 205

Figure 5.26 - Relationships between the average number of effective fibers and the toughness. 207

Figure 5.27 – Illustration of the types of cracks during the ST: (a) Single crack, (b) Peripheral crack, (c) Cracks in the bonding region and (d) Transversal crack. 210

Figure 5.28 – *σ-COD* results for ST for concretes with 20 MPa: (a) C-1, (b) C-2, (c) C-3, (d) C-4, (e) C-5 and (f) C-6. 211

Figure 5.29 – *σ-COD* results for ST for concretes with 40 MPa: (a) C-7, (b) C-8, (c) C-9, (d) C-10, (e) C-11 and (f) C-12. 212

Figure 5.30 - Relationships between the average number of effective fibers and the toughness. 215

Figure 5.31 – Illustration of the types of cracks during the MSCBT with a thickness of 150 mm: (a) Single crack, (b) Peripheral crack, (c) Transversal crack (bottom view of the sample). 218

Figure 5.32 – *F-CMOD* results for MSCBT samples with 150 mm of thickness: (a) for concrete C-7 and (b) for concrete C-9. 219

Figure 5.33 – *F-CMOD* results for MSCBT samples with 75 mm of thickness: (a) for concrete C-7 and (b) for concrete C-9. 219

Figure 5.34 - Relationships between the average number of effective fibers and the area under *F-CMOD* diagram. 221

Figure 5.35 – Experimental results for F–CMOD response for the SCB specimens: average, upper and lower bound: (a) CMOD: 0-6 mm and (b) CMOD: 0-0.2 mm. Adapted from (Carvalho & Lameiras, 2023b). 223

Figure 5.36 – $\sigma - w$ results for the analytical responses obtained through the inverse analysis procedure of this work. 224

Figure 5.37 – Load-CMOD for MSCBT: comparison between average experimental and inverse analysis. 226

Figure 5.38 – Load-CMOD for 3PBT: comparison between average experimental result and inverse analysis result. 227

Figure 5.39 – Tensile Stress versus COD, average UTT experimental and inverse analysis results for MSCBT and 3PBT for concretes: (a) C-10, (b) C-11 and (c) C-12. 228

Figure 5.40 – Load–CMOD for MSCBT: comparison between average experimental result and numerical result. 230

Figure 5.41 – Displacements (Ux) in the x direction for UTT for concretes: (a) C-10, (b) C-11, and (c) C-12. 232

Figure 5.42 – Displacements (Ux) in the x direction for 3PBT for concretes: (a) C-10, (b) C-11, and (c) C-12. 233

Figure 5.43 – Displacements (Ux) in the x direction for MSCBT for concretes: (a) C-10, (b) C-11, and (c) C-12. 234

Figure 5.44 – Tensile vs. COD for the UTT numerical results, compared with the experimental average and envelope for concretes: (a) C-10, (b) C-11, and (c) C-12. 235

Figure 5.45 – Force vs. CMOD diagrams for the 3PBT numerical results, compared with the experimental average and envelope for concretes: (a) C-10, (b) C-11, and (c) C-12.. 237

Figure 5.46 – Force vs. CMOD diagrams for the MSCBT numerical results, compared with the experimental average and envelope for concretes: (a) C-10, (b) C-11, and (c) C-12.. 238

Figure 5.47 – Displacements (Ux) [m] from the MSCBT simulations conducted for: (a) S-150-13, (b) S-150-19, (c) S-150-24, (d) S-150-28, (e) S-200-16, (f) S-200-24, (g) S-200-31, (h) S-200-37..... 241

Figure 5.48 – Force vs. CMOD response from experimental results of C-10 with samples with 100 mm of diameter and 40 mm of effective height (just for reference) and simulations of MSCBT varying the notch depth for: (a) S-150-13, (b) S-150-19, (c) S-150-24, (d) S-150-28, (e) S-200-16, (f) S-200-24, (g) S-200-31, (h) S-200-37. 244

Figure 5.49 – Illustration of the selected points εxx for the analysis under a small vertical displacement increment for S-150-13. 245

Figure 5.50 – Vertical coordinates y (depth) of points $a1$, $a2$, $a3$, $a4$ and $a5$ and the respective εxx, relative to the coordinate axes for S-150-13. 246

Figure 5.51 – Vertical coordinates y (depth) of points $a1$, $a2$, $a3$, $a4$ and $a5$ and the respective εxx, relative to the coordinate axes for S-150-28. 247

NOTATIONS AND SYMBOLS

F	Load
F_j	Load corresponding to $CMOD_j$
ST	Splitting Test
STT	Splitting Tensile Test
LVDT	Linear Variable Differential Transducer
3PBT	Three-point bending test
4PBT	Four-point bending test
DPT	Double Punch Test
MDPT	Multidirectional Double Punch Test
MSTT	Modified Splitting Tensile Test
MVD	Montevideo
MWST	Modified Wedge Splitting Test
BT	Barcelona Test
TCOD	Total Circumferential Opening Displacement
F-CMOD	Diagram composed by Force (y-axis) and CMOD (x-axis)
$(F\text{-}CMOD)_{exp}$	Diagram with experimental results of *F-CMOD*
$(F\text{-}CMOD)_{anal}$	Diagram with analytical results of *F-CMOD*
FRC	Fiber Reinforced Concrete
FRSCC	Fiber Reinforced Self-Compacting Concrete
SFRC	Steel Fiber Reinforced Concrete
SFRSCC	Steel Fiber Reinforced Self-Compacting Concrete
WST	Wedge Splitting Test
COD	Crack Opening Displacement

CMOD	Crack Mouth Opening Displacement
DEWST	Double Edge Wedge Splitting Test
MSCBT	Modified Semi-Circular Bending Test
NSCBT	Notched Semi-Circular Bend Test
RPT	Round Panel Test
RPT-WSS	Round Panel Test with simple support
RPT-WTP	Round Panel Test with three pivots
SCBT	Semi-Circular Bending Test
SPT	Square Panel Test
UTT	Uniaxial Tensile Test
FRHSC	Fiber-Reinforced High-Strength Concrete
SFRHSC	Steel Fiber-Reinforced High-Strength Concrete
FEM	Finite Element Method
$A_{lim1,n,i}$	Area of the *i*-th segment of the *n*-th analytical curve
$A_{lim1,exp,i}$	Area of the *i*-th segment of the *n*-th experimental curve
$A_{dif,n,lim1}$	Differences between each of the n areas of the analytical vs numerial responses
b	Specimen width
D_i^k	Extension due to a rotation θ_k
d_f	Fiber diameter
d_i	Layer on depth i
d_{na}	Neutral line depth
$E_{c,\sec}$	Secant modulus os elasticity of concrete ($E_{c,\sec} = f_{cc} / \varepsilon_{cc}$) (fib, 2012)
E_c	Elastic modulus determined according to *fib* Model Code 2010 (fib, 2012)
E_{c1}	Secant modulus os elasticity from origin to the peak compressive stress

E_{ci}	Tangent modulus of elasticity
E_s	Steel Young's modulus
$f_{R,j}$	Residual tensile strength of the FRC corresponding to the $CMOD_j$
f_L	Proportionality limit (according *fib* Model Code 2010)
F_L	Load at the limit of proportionality
$f_{fct,L}$	Proportionality limit (according EN 14651, 2005)
f_{Ftu}	Ultimate post-cracking residual strength of the FRC
f_{ctm}	Average Tensile Strength
f_{cr}	Cracking resistance
f_{ct}	Tensile strength of the concrete
$F_{cc,i}^{k}$	Compression force on interaction k and on layer i
$F_{ct,i}^{k}$	Tension force on interaction k and on layer i
f_{cc}	Compressive strenght of FRC
f_{ck}	Characteristic value of compressive strenght
f_{cr}	Concrete cracking strength
f_{ctm}	Mean axial tensile strength
f_{cm}	Mean value of compressive strenght
G_f	Specific fracture energy
h	Effective height element
H	Full-height ($n_e + h$)
h_{sp}	Distance between the tip of the notch and the upper face of the specimen
j	The parameter associated with the corresponding $CMOD_j$ (mm) value
k	Computational interaction
l	Specimen test span
L_f	Fiber length

L_h	Non-linear plastic hinge length
L_s	Length of the beam
M_k	Bending moment for interaction k
n_e	Height of the notch
n_L	Number of layers in cross section
q	Incremental interactions of tensile parameter variations
t	Thickness of individual layers
v_j	Values fixed for the relations σ_1/f_{ct}.
W_f	Percentage of fibers
w_1	Parameter corresponding to the first crack opening
w_2	Parameter corresponding to the second crack opening
w_3	Parameter corresponding to the third crack opening
w_i^k	Crack opening for each layer *i* during the incremental rotation interaction k
w_u	Crack opening beyond which cohesive stresses become null, or the critical cracking opening
$\Delta\theta$	Prestabilished constant rate
δ	Vertical deflection
$\delta_{\max}$	Maximum deflection
ε_c	Compressive strain
ε_{c1}	Strain at maximum compressive strain
$\varepsilon_{c,\lim}$	Ultimate compressive strain
$\varepsilon_{ef,i}^k$	Relationship between D_i^k and L_h
$\varepsilon_{ct,p}$	Strain corresponding to tensile strength
$\varepsilon_{cc,p}^{PC}$	strain corresponding to the plain concrete (fib, 2012)
η	Relationship between ε_c and ε_{c1}

θ	Overall rotation ($\theta_k = k\Delta\theta$)
σ_{ct}	Tensile Stress
$\sigma_{ct}(w_i^k)$	Tensile Stress determined interactively and corresponding to w_i^k
$\sigma_{cc}(\varepsilon_{ef,i}^k)$	Compressive Stress for $\varepsilon_{ef,i}^k$ according compression model (Barros & Figueiras, 1999a)
σ_1	Parameter corresponding to the first tensile stress
σ_2	Parameter corresponding to the second tensile stress
σ_3	Parameter corresponding to the third tensile stress

1. INTRODUCTION

Steel Fiber Reinforced Self-Compacting Concrete (SFRSCC) is a Fiber Reinforced Concrete (FRC) that has important advantages such as no need for external vibration and resistant capacity after the formation of cracks, which means that it can be used in some structures in which this characteristic is distinguishing, such as tunnels. Currently, some guidelines and standards contemplate different test methodologies to verify the post-cracking behaviour of FRC (RILEM TC 162-TDF, 2000; EN 14651, 2005; CNR-DT 204, 2006). There is already standardization for Ultra high performance fiber-reinforced concretes (AFGC, 2013). However, this behaviour is related to parameters whose exact determination through simplified tests is still difficult to perform. Therefore, a series of tests have been proposed for this investigation, such as: prismatic sample bending (RILEM TC 162-TDF, 2002; EN 14651, 2005 and CNR-DT 204, 2006), Round Panel Test (RPT) (Bernard, 2000), Uniaxial Tensile Test (UTT) (RILEM TC 162-TDF, 2002), DEWST (Double Edge Wedge Splitting Test) proposed by di Prisco *et al.* (2010) and the Splitting Test (ST) (Lameiras, et al., 2015; Abrishambaf, et al., 2015). However, most of these tests still cannot determine with great accuracy the post-cracking parameters of the SFRSCC. In addition, they have some limitations. The beam bending tests and the RPT involve samples of significant size, which makes them difficult to handle and a consumption of a lot of concrete for molding. DEWST requires intricate adjustments to ensure proper load application, posing a challenging implementation. The Barcelona test poses challenges in accurately measuring the circumferential perimeter (Simão, 2019). The test that yield the best results in this investigation is still the UTT, however its performance involves a major disadvantage, that is difficult to carry out. Therefore, this is a relevant field of research to be studied.

The dimensions of the samples to be tested are an important aspect for carrying out the tests (size effect) (Bazant, 1999; di Prisco, et al., 2004; Bazant & Jaime, 1998; Shoaib, et al., 2014). This is valid for the SFRSCC, because the orientation of the fibers can significantly influence the materials properties (Abrishambaf, et al., 2013). The need to develop a simplified test methodology that can be used as an alternative to the determination of parameters of the post-cracking behaviour of the SFRSCC involving an approach for the study of thin elements supported the proposal of this study. Another important factor to be considered in SFRSCC studies is the predominant direction of the fibers in relation the

principal tensile stress. It is a consensus that when both are parallel, the influence of fibers on post-cracking properties is greater, which is an important consideration in the development of new tests (Abrishambaf, et al., 2013; Lameiras, 2016).

The Semi-Circular Bending Test (SCBT) is known for its simplicity. Initially, it was used to evaluate the mechanical behavior of rocky materials and to study properties such as tensile strength, fatigue and rupture parameters of asphalt mixtures (Arabani & Ferdowsi, 2008). Carrying out this test is simple due to its dimensions and to load application process. These are important advantages when comparing SCBT to the tests already known to evaluate the post-cracking behavior of the SFRSCC. The test proved to be satisfactory for evaluating the effect of loading rate on high-strength fiber-reinforced concrete in different fiber types, including glass, polypropylene, and steel (Aziminezhad, et al., 2020).

This work aimed to propose and study a Modified Semi-Circular Bending Test (MSCBT) for the characterization of post-cracking behavior (mode I fracture) of SFRSCC. Innovations are proposed in this work: the monitoring of Crack Mouth Opening Displacement (CMOD) and the inverse analysis procedure are conducted for MSCBT. The ability of this test to represent well the properties of different types of SFRSCC is studied, as well as the influence of parameters: strength class of concrete, sample dimensions, influence of type and fiber content. A study is performed with the MSCBT, UTT and ST to study the post-cracking behavior of the SFRSCC.

2. OBJECTIVES

To propose a novel testing method for characterizing the post-cracking tensile behavior of Steel Fiber Reinforced Self-Compacting Concrete (SFRSCC) under Mode I fracture. It is proposed that the test be suitable for application to cores extracted from actual structural elements. Additionally, to develop a new analytical procedure for Inverse Analysis (IA) applicable to both the 3PBT and for proposed test, aimed at reducing the number of computational iterations required for the accurate determination of SFRSCC properties.

The specific objectives of the work are:

- To develop an Inverse Analysis (IA) tool for the Three-Point Bending Test (3PBT) and validate it using data from the literature.

- To develop an IA tool for the MSCBT and validate it using Finite Element Method (FEM) simulations and experimental results from MSCBT and Uniaxial Tensile Tests (UTT).

- To conduct an experimental study for the development of the MSCBT by varying the concrete type, fiber content, and fiber type.

- To conduct an experimental study for the development of the MSCBT by varying the specimen thickness.

- To conduct an experimental study for the development of the Splitting Test (ST) with V-notched specimens, varying the concrete type, fiber content, and fiber type.

- To conduct a numerical simulation study of the MSCBT, UTT, and 3PBT tests with SFRSCC, aiming to validate the experimental results of these tests.

- To carry out a parametric study using numerical simulations of the MSCBT with SFRSCC under increased notch depth in order to assess the sample's performance under different span-to-effective depth (L/h) ratios.

3. LITERATURE REVIEW

3.1. Fiber Reinforced Concrete (FRC)

The oldest records of the use of fibers as material reinforcement come from ancient times, in Egypt and around Baghdad (Bentur & Mindess, 2007). Currently, Fiber Reinforced Concrete (FRC), which has had significant application in civil construction, continuous and precast structures, and infrastructure works with great social demand, such as basic sanitation and transport, involving pavements and tunnels (Figueiredo, 2011). FRC is a composite material that presents as components: cement, binder, aggregates, possibility of additives and additions, and fibers.

Plain concrete has low tensile strength compared to its compressive strength, which results in the formation of cracks when its tensile strength limit is exceeded in some region where it is under tension. The most usual solution to this problem is the use of reinforced concrete, in which steel bars or steel wires contribute to a significant increase in its capacity to requests. An alternative to overcome this deficiency in concrete is the use of fibers. However, the fibers are not necessarily employed to promote the increase of the resistance capacity to the requests. Its main advantages are to promote ductility and an increase in the capacity of the concrete to resist the effect of large cracks.

Fibers have several manufacturing methods. In general, they are produced from low-carbon steel wires and are anchored in the folds of their ends, in the form of a hook (hooked-end), thus presenting greater mechanical resistance (Arcelor Mittal, 2016).

Although steel fibers contribute to controlling the cracking propagation in the SFRSCC, generally, the distribution of fibers in concrete is random around the aggregates, forming a web with the structural functioning similar to that of a spatial truss in which the concrete resists compression efforts and the fibers resist tensile efforts. This makes concrete with steel fibers dispersed in this way to present better deformation capacity and also, a significant residual tensile strengh (Singh, 2016).

Conventional SFRSCC is a material that generally presents reduction in resistance after cracking under uniaxial tension, but several reasons justify the interest in this material: reduction in the opening of cracks provided by the fibers, greater durability, thickness reduction, possibility of partial or total replacement of conventional reinforcement (Sorelli,

et al., 2005; Salehian, 2015), providing freedom to create structures with curved shapes or more robust aesthetics (Laranjeira, 2010). The reduction of conventional reinforcement is considered an important economic advantage, impacting on the reduction of the execution time of buildings (mainly in relation to constructive issues of reinforcement assembly), making the use of this material a competitive advantage, however, not yet fully exploited potentiality, in addition to not having its mechanical properties fully known (Cunha, 2010).

When a FRC element begins to be subjected to tension, it initially presents a linear elastic behavior until the formation of the first cracks (stress σ_f) and after this state, the behavior called post-cracking occurs (Figure 3.1), when progressive increase (hardening or strain-hardening) or decrease (softening or strain-softening) of resistance can occur (Singh, 2016). Following the formation of the first crack, strain-hardening behavior generally results in greater energy absorption in FRC than strain-softening behavior (Soranakom & Mobasher, 2008; Taheri & Barros, 2011; Barros, et al., 2012; Taheri, et al., 2012).

This behavior depends on FRC parameters such as the type of fiber used. Another parameter is the critical volume (V_f), which causes the FRC to hold resistance approximately constant when the matrix reaches its resistance limit (Figueiredo, 2011; Ding, et al., 2018). Another parameter is used in FRC, which is the aspect ratio. It corresponds to the length of the fiber (l) to diameter (d) ratio.

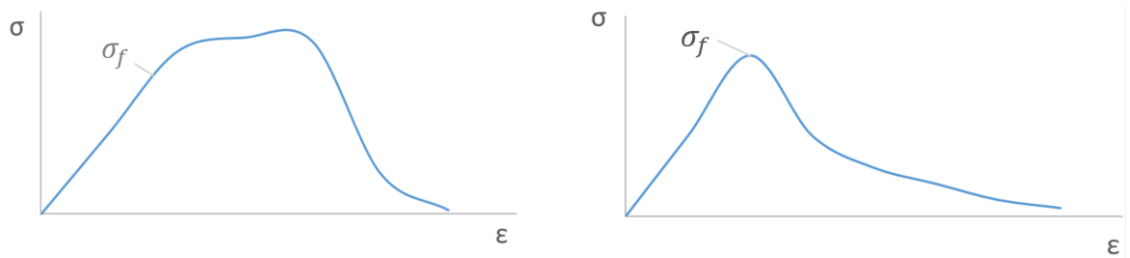


Figure 3.1 – Schematic representation of FRC behavior: hardening (a) and softening (b).

3.2. Steel Fibers on the Mechanical Behavior of Steel Fiber-Reinforced Concrete (SFRC)

Steel Fiber-Reinforced Concrete (SFRC) has emerged as a pivotal advancement in concrete technology, offering enhanced mechanical properties and durability. This composite

material incorporates short, randomly distributed steel fibers into the concrete matrix, which improve several mechanical properties of the concrete, minimizing its brittleness and low tensile strength (Mena-Alonso, et al., 2024). The inclusion of steel fibers has been shown to significantly improve both compressive and especially flexural and tensile strengths of concrete.

The performance of SFRC is influenced by various factors, including fiber content, geometry, distribution, and orientation. Higher fiber volumes generally lead to better mechanical properties, including increased strength and toughness. The shape of the fibers also plays a critical role; hooked-end and crimped fibers provide better anchorage within the concrete matrix, enhancing load transfer and crack bridging capabilities. Hooked-end fibers, due to their mechanical anchorage, offer superior capabilities and load transfer efficiency. The effects of different end hook configurations on the flexural strength and toughness of SFRC beams were investigated, finding that more complex hook geometries (e.g., 5D hooks) provided greater enhancements in flexural performance (Chu, et al., 2024). The pull-out behavior of hooked-end fibers is also significantly influenced by hook geometry, with more deformed shapes offering better anchorage and energy dissipation (Abdallah & Fan, 2017).

Steel fibers contribute to the post-cracking behavior of concrete by bridging cracks and providing resistance to crack propagation. This results in improved tensile strength, ductility and flexural strength compared to plain concrete with the degree of improvement dependent on fiber content and geometry (Yoo & Banthia, 2019). This makes FRC suitable for structures subjected to dynamic and fatigue loads (Germano, et al., 2016; Singh, et al., 2006; Parvez & Foster, 2015).

The impact resistance of concrete is significantly improved by the addition of steel fibers. Various types of impact test methods have been studied (Yoo & Banthia, 2019) and the superior performance of SFRC under dynamic loading conditions was highlighted. It has been shown that steel fiber reinforced concrete targets remained intact under high-velocity impacts, with only minor cracks, while conventional high-strength concrete targets were severely damaged (Luo, et al., 2001). Abid et al. (2021) It has already been investigated the impact resistance of steel fiber-reinforced self-compacting concrete, demonstrating significant improvements in energy absorption with increased fiber content (Abid, et al., 2021).

3.3. Post-Cracking Residual Strength Parameters, according to the *fib* Model Code 2010 (2012)

The *fib* Model Code 2010 (*fib*, 2012) contain recommendations for the design of fiber reinforced concrete structures, which will be addressed in this item. The post-cracking strength classification of FRC is presented, in which a linear normal stress distribution is considered along the cross section. The equation (3-1) is employed to derive post-cracking residual strength parameters ($f_{R,j}$).

$$f_{R,j} = \frac{3 \cdot F_j \cdot l}{2 \cdot b \cdot h_{sp}^2} \tag{3-1}$$

$f_{R,j}$ – residual flexural tensile strength of the FRC corresponding to the Crack Mouth Opening Displacement j ($CMOD_j$).

F_j – load corresponding to $CMOD_j$.

l – specimen test span.

b – specimen width.

h_{sp} – distance between the tip of the notch and the upper face of the specimen according to Figure 3.2.

j – parameter associated with the corresponding $CMOD_j$ (mm) value shown in Figure 3.3.

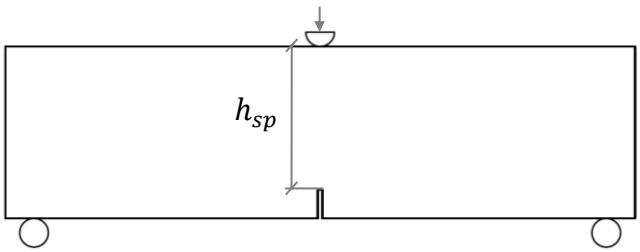


Figure 3.2 – h_{sp} position on 3PBT sample.

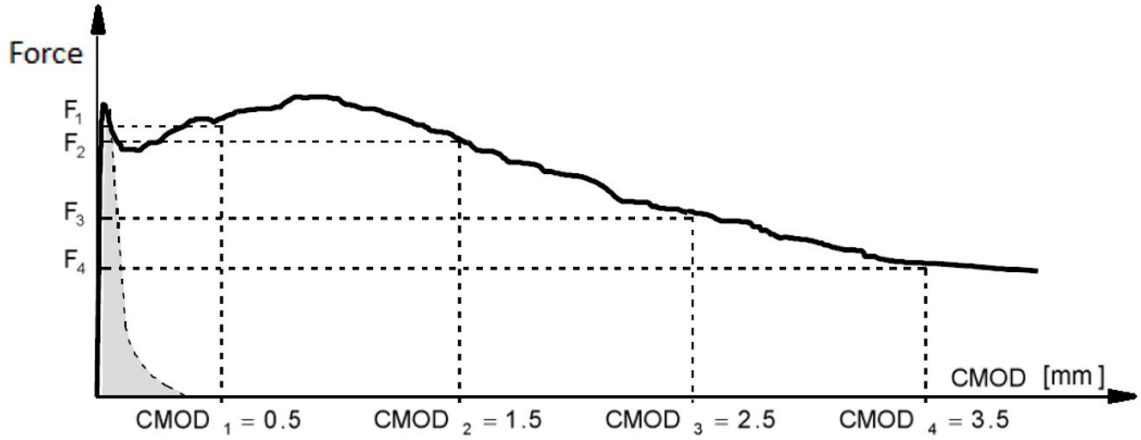


Figure 3.3 – Load-CMOD curve. Adapted from *fib* Model Code 2010 (2012).

With the parameters monitored during the Three-Point Bending Test (3PBT), it is possible to generate the Force-CMOD diagram (Figure 3.3) and thus calculate the residual tensile strengths. The *fib* Model Code 2010 (2012) recommends the expression (3-1) to determine the residual tensile strength of the FRC corresponding to the CMOD.

Table 3.1 illustrates the characteristic residual resistances $\frac{f_{R,3k}}{f_{R,1k}}$ where the letters *a*, *b*, *c*, or *d* represent the classification of the concrete.

Table 3.1 – Classification method for FRC post-cracking strength according to *fib* Model Code 2010 (2012).

Letter	Interval
a	$0.5 < \frac{f_{R,3k}}{f_{R,1k}} \leq 0.7$
b	$0.7 < \frac{f_{R,3k}}{f_{R,1k}} \leq 0.9$
c	$0.9 < \frac{f_{R,3k}}{f_{R,1k}} \leq 1.1$
d	$1.1 < \frac{f_{R,3k}}{f_{R,1k}} \leq 1.3$
e	$1.3 < \frac{f_{R,3k}}{f_{R,1k}}$

The proportionality limit (f_L) is defined according to the equation (3-2) (fib, 2012), where F_L is the load at the limit of proportionality. Both the residual tensile strength and the proportionality limit are determined similarly in European standard (EN 14651, 2005) but the mathematical notation of f_L is changed to $f_{fct,L}$.

$$f_L = \frac{3 \cdot F_L \cdot l}{2 \cdot b \cdot h_{sp}^2} \tag{3-2}$$

3.3.1. FRC simplified stress-crack opening constitutive laws for bending

For sections normally stressed in tension, it is possible to obtain a stress-crack opening diagram (Figure 3.4), which is defined through the post-cracking behavior of the FRC, in which Ultimate Limit State (ELU) considerations are applied. Two constitutive laws can then be applied: the rigid-plastic model and the linear model.

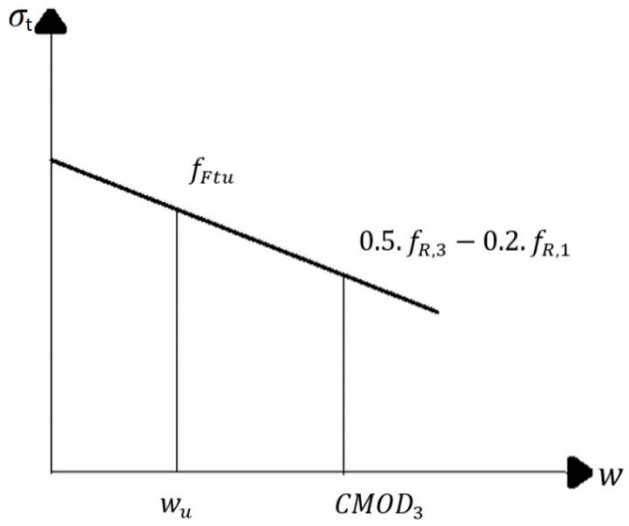


Figure 3.4 – Post-cracking linear constitutive law of the FRC. Adapted from *fib* Model Code 2010 (2012).

On the Figure 3.4, f_{Ftu} is the ultimate tensile strength of the FRC and w_u is the crack opening beyond which cohesive stresses become null, or critical cracking opening. This value is related to the necessary ductility.

Despite existing proposals in European standards and guidelines, there is still no widely accepted constitutive law for the structural design of elements in FRC, therefore, these regulations must be analyzed and discussed (Laranjeira, 2010).

3.4. FRC properties

For the quality control of plain concrete, FRC properties are evaluated according to technical standards. These properties are related to the composition with fiberless concrete (cement matrix and aggregates).

Fracture toughness is a measure considered to be an important property of any material, as it indicates the magnitude of fracture toughness or the ability of the material to resist crack propagation, and specifically for FRC, it can be considered that increasing the fibers leads to increased tenacity (Vasconcelos, 2012).

For FRC, it is necessary to evaluate properties that depend on the matrix and also others that depend on the presence of the fibers. The fiber-matrix interaction shown how much the addition of fibers leads to significant improvements in properties such as toughness, crack control, impact resistance and the important properties to be evaluated through FRC tests in the fresh state: workability, fiber content, and plastic shrinkage (Bentur & Mindess, 2007).

In the hardened state, an important property to be evaluated is the compressive strength: the fibers do not exhibit significant changes in the compressive strength of concrete. To evaluate this FRC property, the same tests as for conventional concrete are used. However, to evaluate the specific properties of FRC, especially its post-cracking performance, specific tests are used, the main ones being described in the next item.

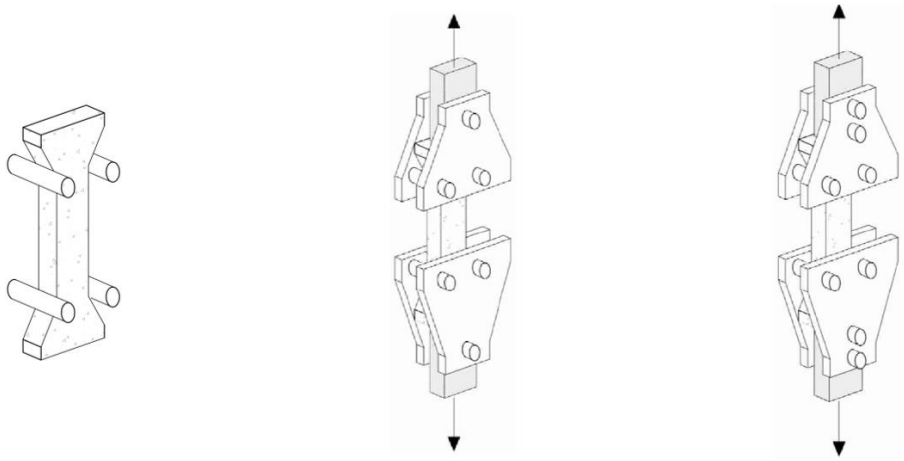
3.5. Tests for Characterization of the FRC and Disk-Shaped Compact Tension (DCT)

The most common test methods for characterizing the post-cracking behavior of the FRC will be presented below.

3.5.1. Uniaxial Tensile Test (UTT)

The Uniaxial Tensile Test (UTT) consists of subjecting the specimen to a uniaxial tensile load. For the evaluation of failure characteristics of plain concrete, this test is usually avoided due to the difficulty of performing it. In these cases, it is common to carry out an indirect test, as is the case with the Three- or Four-Point Bending test and the Splitting Test, as they are simpler to perform. Despite the difficulties of the UTT, it can be considered robust (Laranjeira, 2010). This is attributed to its tendency to yield more realistic results than the bending test, since in the first one, only the tensile is present in the tested cross section (Soranakom & Mobasher, 2008). It is considered that the most appropriate means to evaluate the post-cracking mechanical behavior of the structural FRC involves the use of the UTT (Borges, 2017).

The illustration of the test is presented in the Figure 3.5, where the sample has the shape of bone, free rotation and fixed end; in these illustrations, the body of the sample has a prismatic shape. None of the boundary conditions can be classified as ideal: the free-rotating configuration provides a lower tensile strength, a lower fracture energy, a smoother softening curve and, after crack formation, a non-uniform strain distribution; in fixed-end configuration tests, the strain distribution is uniform during most of the experiment (except during the steep part of the softening curve), the tensile strength is higher, and so is the fracture energy (Planas, et al., 2007; Amin, et al., 2018; Salehian, 2015; Zhou, 1988).

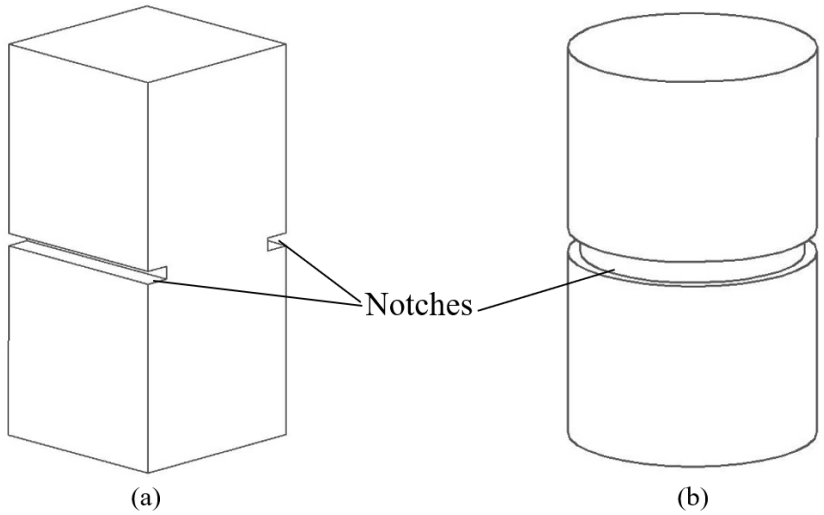


(a) (b) (c)

Figure 3.5 – Schematic representation of the uniaxial tensile test (a) bone-shaped specimen. (b) free rotation configuration. (c) fixed end configuration (Salehian, 2015).

When adopting a test methodology to characterize FRC, special care must be taken to ensure that the geometry of the cracked sections remains similar, otherwise the mechanical properties may differ due to the variation in the orientation of the fibers in relation to each other. (Laranjeira, 2010).

The UTT can also be performed with cylindrical-shaped samples. The Figure 3.6 presents illustration of prismatic and cylindrical samples.



(a) (b)

Figure 3.6 – Samples with notch for UTT in shapes: (a) prismatic and (b) cylindrical.

There is still no consensus in the literature about the best configuration for performing the uniaxial tensile test, because the main concern in considering the uniaxial tensile test as a pure mechanical test is the test settings that may interfere with the results (Salehian, 2015).

For the test to be performed satisfactorily, care must be taken to ensure that the specimen is perfectly aligned in relation to the loading direction. The concrete sample must have an appropriate geometric shape, and in addition, the appropriate use of the acquisition system must be carried out to avoid bending, which can change the test results (Hordijk, 1991). The boundary conditions of the specimens, in terms of attachment of the specimen to the loading machine, also have a crucial influence on the structural behavior (Salehian, 2015). These factors make the UTT test the most difficult to perform, when compared to the diametral compression and bending tests, and justifies the relatively low number of existing technical standards that deal with the same.

The RILEM TC162-TDF (2002) deals about the technical standardization of the UTT to determine the relationship between tensile stress and crack opening in the FRC. The standard may eventually also be used for concrete with other types of fibers beyond steel fibers.

Planas *et al.* (2007) presents a series of recommendations for carrying out the UTT, some of which are presented below:

- For prismatic specimens, cross-sectional dimensions of 50x50 mm² to 100x100 mm² are recommended, with aggregates of characteristic dimensions up to 8 mm and 16 mm, respectively. Recommended length is twice the width;
- Notches ≥ 5 mm are recommended, corresponding to 5% to 25% of the sample width;
- The samples must be rectified and cleaned, so that the dimensional deviation is limited to 1 mm to avoid load eccentricity;
- The strain control is preferably performed with LVDTs in conjunction with a data acquisition system. In addition, there must be a record of load and time.
- The Tensile Stress – Crack Opening Displacement (COD) curve (Figure 3.7) approximates the softening behavior, and the characteristic values for the post-cracking behavior are obtained and the area under the curve represents the fracture energy (Figure 3.7).

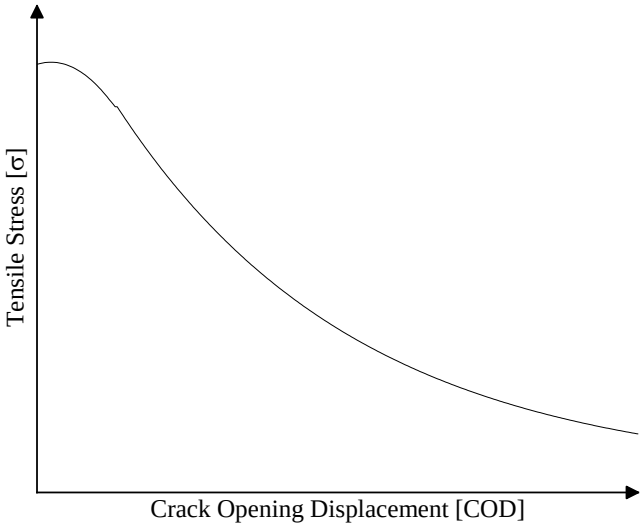


Figure 3.7 – Curves: Tensile Stress vs. Crack Oppening Displacement.

Fixation of the specimen of the UTT to the tensile equipment must be carried out with due care. The literature (Cunha, 2010; Salehian, 2015; Planas *et al.*, 2007) reports the importance of ensuring rotational rigidity in this connection, and on the proper care with cleaning the surfaces. During the execution of the UTT test, it is possible that the glue fails and not the sample itself, which invalidates the test. Therefore, the method of bonding the fasteners to the sample to be tested also significantly influences the results.

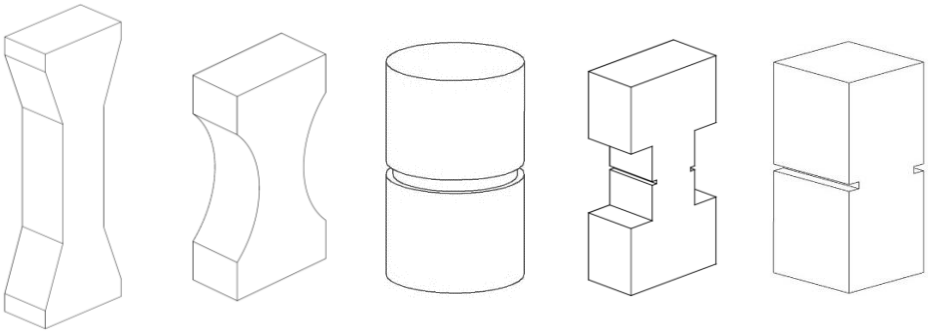
Cunha (2010) carried out an experimental investigation on a micro and macro scale of the SFRSCC with different types of fibers. The work involved carrying out the UTT test with cylinders and highlighted the importance of care to be taken when fixing using high-resistance epoxy glue (so that its cure does not harm the geometry of the sample) and the need for the crack to occurs from the notch.

Fiber orientation is also a factor with a relevant impact on the results of UTT. Qing *et al.* (2019) studied the performance of an SFRSCC using a UTT, whose fibers were oriented through a magnetic field, and a SFRC with randomly oriented fibers, with subsequent thermographic analysis. The authors found that the steel fiber content can be reduced with alignment to maintain similar tensile strengths. Furthermore, the cracking pattern of the samples with aligned fibers is lower.

Oliveira (2010) proposes a direct method for determining the tensile behavior of SFRC through the formulation of a constitutive model with the purpose of carrying out structural design. The main relevance of the work is the identification of the real curve stress–opening

of cracks involving high strength and self-compacting concrete with different types and fiber contents, presenting contributions in the orientation parameters and fiber pullout.

The following sample shapes for UTT are used: dog bone with straight parts shape (Kwon, et al., 2014; Zhu, et al., 2019; Zhao, et al., 2019; Blazy, et al., 2021), dog bone with curve shape (Van Vliet, 2000; Paegle & Fischer, 2013; Deluce & Vecchio, 2013; Amin, et al., 2018), cylindrical-shaped (RILEM TC 162-TDF, 2002; Cunha, 2010; De Smedt, et al., 2021; Mudadu, et al., 2018) and prismatic shapes (Salehian, 2015; Zhou, 1988; Qing, et al., 2019). Another specimen of the dog bone type without curvatures in the section (dog bone with profile I shape), with rectangular ends and smaller width in the central region was also used in which the tensile machine applies load through top and bottom flange of the sample (Islam, et al., 2014). One of the objectives of using the dog bone geometry is inducing the occurrence of cracks in the region of smallest width of the sample (Van Vliet, 2000), so that the results tend to be more homogeneous. The dog bone with straight parts shape (Figure 3.8a) it is a common geometry, and the sample has the same width in this region. In the case of the dog bone with curve shape (Figure 3.8b), the crack can occur in regions of different widths, which can make the behavior more complex (Van Vliet, 2000). The cylindrical-shaped (Figure 3.8c) is a standardized test by RILEM TC 162-TDF (RILEM TC 162-TDF, 2002). The dog bone with profile I shape is illustrated in Figure 3.8d. In the prismatic sample test (Figure 3.8e) and also in the case of a cylindrical sample, to ensure the transfer of load from the test equipment to the sample, the ends of the sample are glued to metallic supports, which are connected to adaptations for connection with the load equipment. In such cases, high-adhesion glue, like a high strength epoxy resin, should be used and the bonding surface should be sufficient to ensure that bonding fails. The sample surfaces must be carefully cleaned by applying solvent, in addition, after applying the glue, it is recommended to use a compression force before carrying out the tensile test (Salehian, 2015; Cunha, 2010).



(a) (b) (c) (d) (e)

Figure 3.8 – Shapes of the usual samples for the UTT: (a) dog bone with straight parts shape, (b) dog bone with curve shape, (c) cylindrical-shaped, (d) dog bone with profile I shape and (e) prismatic shape.

The Table 3.2 shows the main contributions in each type of UTT.

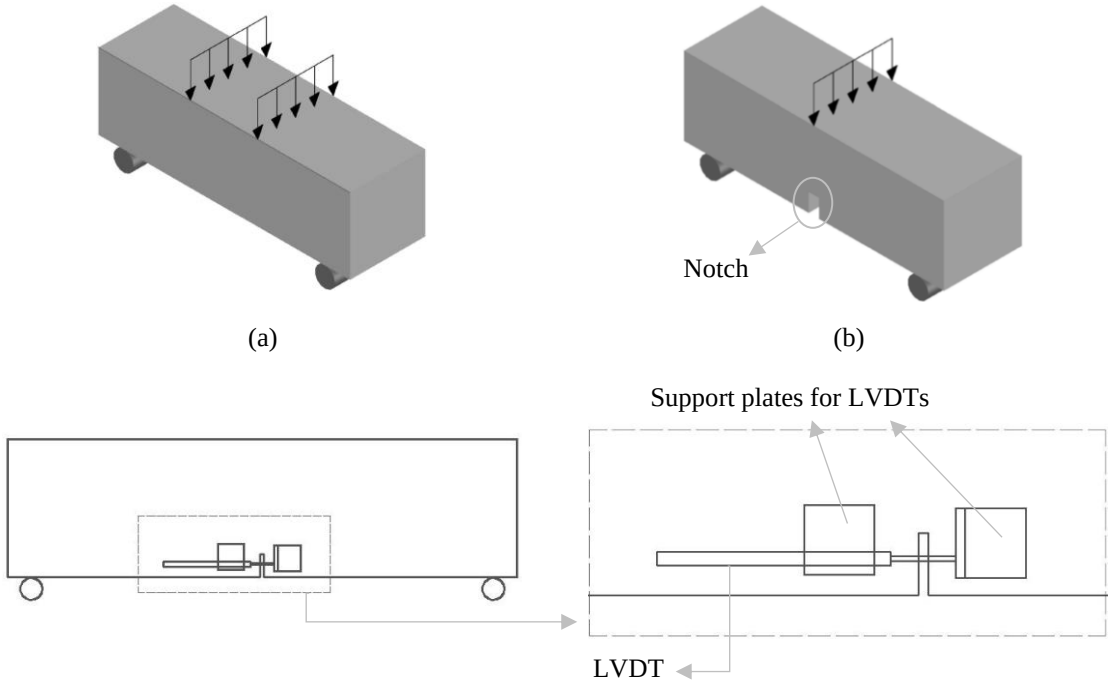
Table 3.2 – Works that address contributions on the UTT.

Work	Main Contribution
Planas *et al.* (2007)	Establishes recommendations and minimum requirements for proper performance of the UTT.
Oliveira (2010)	Proposes a direct and simple constitutive model to obtain the tensile behavior of FRC considering fiber orientation and the specific combination of matrix and fiber properties.
Cunha (2010)	Numerical simulation of the UTT with investigation at the micro and macro scale.
Salehian (2015)	Performs UTT on prismatic cores extracted from 3PBT samples and develops formulation for inverse analysis procedure to characterize the post-cracking behavior of SFRSCC.
Amin *et al.* (2018)	SFRC dogbone specimens are tested with the boundary conditions: fixed-fixed, fixed rotating, and rotating-rotating.
Qing *et al.* (2019)	Investigate the aligned steel fiber reinforced cementitious composites (ASFRC) using a uniform magnetic field formed from energized coils during casting, and the effect on the alignment of steel fibers was examined using an X-ray system and the SFRC.
Kwon *et al.* (2014), Zhao *et al.* (2019), Zhu *et al.* (2019), Blazy *et al.* (2021)	Investigated the UTT for dog bone with straight parts shape.
Van Vliet *et al.* (2000), Peagle *et al.* (2013), Deluce *et al.* (2013), Amin *et al.* (2018)	Investigated the UTT for dog bone with curve shape sample geometry.
RILEM TC 162-TDF, Cunha *et al.* (2010), Mudadu *et al.* (2018), De Smedt *et al.* (2021)	Investigated the UTT with cylindrical-shaped sample geometry.
Zhou *et al.* (1988), Salehian (2015), Qing *et al.* (2019)	Investigated the UTT for prismatic shapes sample geometry.
Islam *et al.* (2014)	Investigated the UTT for dog bone with dog bone with profile I shape.

The direct tensile test is the one that most realistically determines the tensile strength and post-cracking behavior of an SFRC sample. As the other tests that will be presented below determine this parameter indirectly, the responses from these tests are different. Therefore, it is important to emphasize that, for the purpose of comparing these different tests, it is interesting that the results are taken as a reference the UTT.

3.5.2. Bending tests

The bending tests are carried out on a prismatic-shaped specimen that is supported by two hinges. A testing machine applies a load to the upper surface of the specimen in one of two configurations, corresponding to either the Three- or Four-Point bending test (3PBT ou 4PBT) (Figure 3.9a-b). The 3PBT is also known as the Single-Edge Notch Bending (SENB).



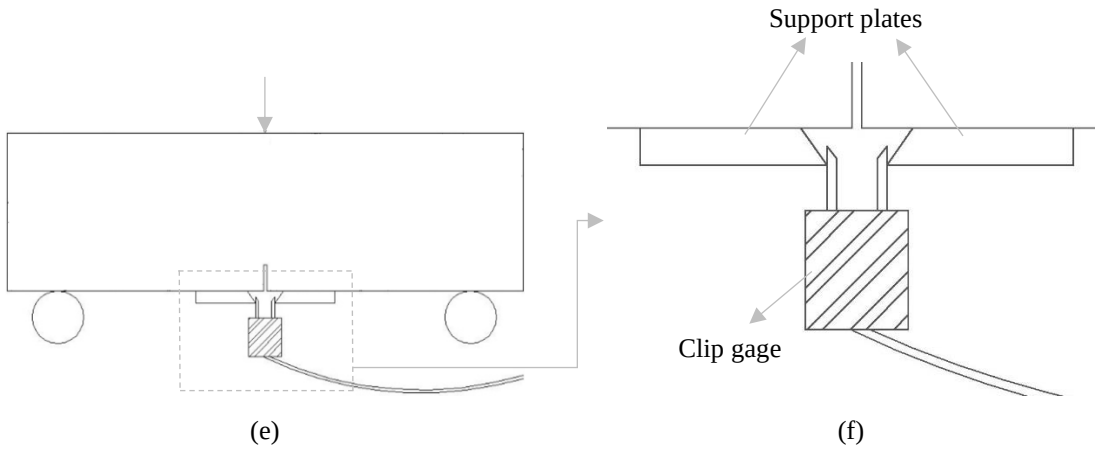


Figure 3.9 – Bending Tests: (a) Four Point Bending Test (4PBT) or (b) Three Point Bending Test (3PBT) highlighting the notch in the middle of the span, (c) sample side view with LVDT and (d) view of LVDT with backing plates, (e) sample side view with clip gage and (f) view of clip gage.

This type of test is widely used to indirectly obtain the tensile strength and to evaluate the cracking properties of the FRC (Salehian, 2015; Lameiras, 2016; Lameiras, et al., 2015; Medina, 2019; Cardoso, 2020; Figueiredo, 2011; Trindade, et al., 2020; Toledo Filho, 2001; Bencardino, et al., 2013; Yin, et al., 2019). An important feature of this test is its simplicity, which is a common feature of indirect tensile tests. The main drawback, however, is the need to employ a relatively complex behavior deduction, which is the inverse analysis procedure for test validation (Planas, et al., 2007). Another disadvantage of 3PBT is the scatter of results when compared to some other tests (Minelli & Plizzari, 2011; Conforti, et al., 2017; Medina, 2019).

In the Three-Point Bending Test (3PBT), the intermediate region presents the highest bending moment and the distribution of this moment is influenced by the loading, which occurs in a wedge shape, thus, the positioning of the notch promotes the appearance of a single mid-span crack, which allows analysis of the post-cracking behavior of the FRC in a single cross section (Salehian, 2015). In addition, the notch promotes a reduction in the dispersion of the results obtained (Medina, 2019). In the four-point bending test, there is a region subjected to pure bending (between loads), in which the formation of several cracks can occur. The use of 3PBT and 4PBT for analytical purposes in structural projects is questioned due to the dispersion of results and the differences between cracking mechanisms in tests at material and structural levels (Destrée & Mandl, 2008; Minelli & Plizzari, 2009; Medina, 2019).

Despite consisting of a more simplified approach than the UTT test, bending tests have a several limitations such as the dependence on performing an inverse analysis in order to determine the stress diagram and crack opening (Medina, 2019). If this analysis is not performed, there is a significant demand for time in the characterization performed only by the test, which is due to the variability of the mechanical properties of the FRC (TRINDADE *et al.*, 2020) and also the composite can present a behavior that is not the real one of the structures (LAMEIRAS *et al.*, 2015).

During the performance of the bending test, the load and the crack opening at the top of the notch, also referred as Crack Mouth Opening Displacement (CMOD) are monitored and the cracking strength is obtained (f_{cr}).

There are several codes that are used as a reference for 4PBT (JSCE-SF4, 1984; ASTM C1018-89, 1991; ACI 544.1R-96, 1996; DBV – Guide to Good Practice, 2007; UNI 11039-2:2003, 2003; JCI-S-003-2007, 2007; ASTM C1609, 2012) and for the 3PBT (RILEM TC 162-TDF, 2002; EN 14651, 2005; fib, 2012). In 2006, the new standard ASTM 1609 (2012) can begin to be used as an alternative to ASTM C1018-89 (1991) evaluating the flexural performance of fiber-reinforced concrete using parameters derived from the load-deflection curve (Hamad & Sldozian, 2019).

During the bending tests, there are two possible combinations of parameters for monitoring that are used: monitoring the load (*F*) with the displacement (also called deflection, δ) or with the monitoring of the load with the Crack Mouth Opening Displacement (CMOD). *F* is monitored from the universal testing machine itself or through a load cell positioned between the upper surface of the sample and the machine's piston. The CMOD is monitored by means of an Data Acquisition System and corresponds to the crack opening measured precisely in the region of the notch where the crack starts. Therefore, the use of clip gages (Planas, et al., 2007) or LVDTs (Linear Variable Differential Transducer) are usual for the CMOD monitoring (Figure 3.9c-f). One LVDT can be used on the bottom edge of the beam for CMOD monitoring (Frazão, 2019). There are also recommendations to use just one clip gage (EN 14651, 2005). But a common methodology in research is to use two LVDTs, each of which one positioned on one side of the sample, parallel to the sample direction (Lameiras, et al., 2015; Salehian, 2015; Cardoso, et al., 2021). In this methodology, the CMOD is obtained directly from the monitoring. The LVDTs can also be positioned to measure

deflection (δ) vertically (RILEM TC 162-TDF, 2002; ASTM C1609, 2012; Nour, et al., 2015; Planas, et al., 2007). In these cases, a correlation equation of these parameters can be used to obtain the CMOD. The equation (3-3) shown the correlation equation for RILEM TC 162-TDF (2002). The EN 14651 (2005) also shown a very similar equation.

$$CMOD = 1.18\delta - 0.0416 \tag{3-3}$$

Table 3.3 – References that address contributions on the 3PBT.

Reference	Main Contribution
RILEM TC 162-TDF (2002), EN 14651 (2005) and *fib* Model Code (2012)	Standardized method for 3PBT
JSCE-SF4 (1984), ASTM C1018-89 (1991), CNR-DT 204 and ACI 544.1R-96 (1996)	Standardized method for 4PBT
Minnelli *et al.* (2011), Conforti *et al*. (2017) and Medina (2019)	They found that the dispersion of 3PBT is greater than other tests such as panel tests
Planas *et al.* (2007)	Recommendations for geometry and molding criteria for samples and test setup
Salehian (2015)	Inverse analysis for 3PBT with plastic hinge model
Nour *et al.* (2015)	Inverse analysis for 3PBT with procedure based on data fitting algorithm
Carvalho *et al.* (2023a)	Developed a more rational analytical and progressive method for performing the inverse analysis procedure
Lameiras (2016)	Developed a rational numerical and progressive method for performing the inverse analysis procedure
Conforti *et al.* (2017)	Compared test methods from different standards (JSCE-SF4, 1984; ASTM C1609, 2012), refer to a post-cracking response of FRC with larger values of crack width as compared to EN 14651 (2005). The tests of these three standards are characterized by a similar result variation (CV around 0.25). Design parameters $f_{R,1}$ and $f_{R,3}$ (Model code 2010 (fib, 2012)) can be estimated from ASTM 1609 and JCI-SF4 tests.

3.5.3. Wedge Splitting Test (WST)

The Wedge Splitting Test (WST) developed by Tschegg (Tschegg, 1986; Tschegg, 1991) is a test that was developed based on the principle of applying a compressive load to a sample and resulting in the opening of cracks, in a similar way to what occurs in the Splitting Test (ST). The crack width is monitored during the test and the fracture energy of the concrete is determined. It has been proven that large samples are not required for this test (Abdalla & Karihaloo, 2003). The true specific fracture energy (G_f) of a concrete mix can be determined

by testing just a few specimens (Karihaloo, et al., 2003). The WST can be performed in cylindrical formats (Bruhwiler & Wittman, 1990), but the prismatic format is the most common. The sample is notched and has a rectangular region hollowed out at the top under which the positioning of plates coupled to rollers takes place. During the test, the wedge support moves over the rollers resulting in a tensile force component in the crack opening direction in the notch. An illustration of the WST is presented in Figure 3.10.

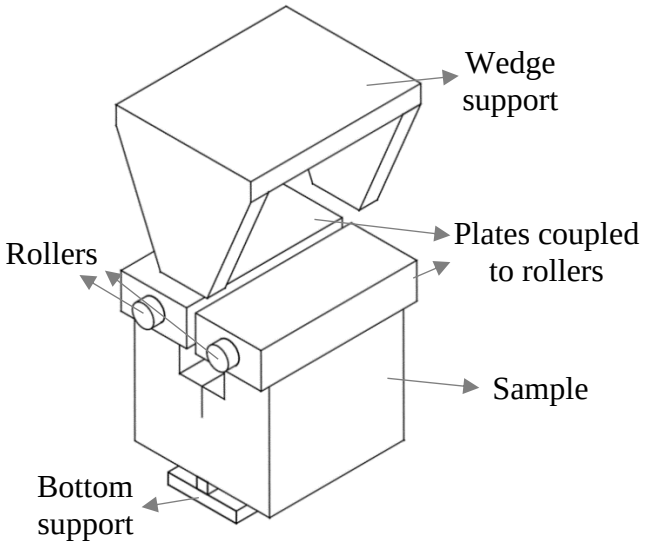


Figure 3.10 – Sample test setup for Wedge Splitting Test.

An inverse analysis procedure based on the analytical hinge model for various multi-linear softening curves is proposed (Skoček & Stang, 2008). A quad-linear curve is used and the results obtained semi-analytically are verified through FEM simulations.

Table 3.4 – Main contributions to WST.

Reference	Main Contribution
Tschegg (1986) and Tschegg (1991)	Initial conception for the WST
Bruhwiler *et al*. (1990)	WST is carried out with cylindrical shape
Abdalla *et al*. (2003)	The specific fracture energy is determined by WST comparing with 3PBT
Karihaloo *et al*. (2003)	Found that the so-called true specific fracture energy can be determined by testing just a few samples
Löfgren *et al*. (2004)	Proposed the WST for the FRC
Skoček *et al.* (2008) and Löfgren *et al.* (2005)	Proposed an inverse analysis for WST

3.5.4. Double Punch Test (DPT) and Barcelona Test (BT)

The Double Punch Test (DPT) was initially used to determine the tensile strength of concrete in cylindrical or cubic samples (Chen, 1970). It can be considered an indirect test (Monte, et al., 2023; Molins, et al., 2009; Coronel, et al., 2025). Some advantages of DPT are: the sample has reduced dimensions, the test is relatively fast and the fracture surface is considered relatively large, which reduces the dispersion of results (Molins, et al., 2009). The test is commonly employed as a quality control method for Steel Fiber Reinforced Shotcrete (Santos, et al., 2023; Santos, 2022). Repeatability and reproducibility of the residual loads were demonstrated, as well as sensitivity to parameters in the post-cracking mechanical properties of the fiber-reinforced concrete (FRC) in the Double Punch Test (DPT) (Nogueira, et al., 2021). The influence of the instability caused by matrix cracking on the determination of the residual strength in the post-crack response of FRC in the Double Punch Test (DPT) was investigated in both open-loop and closed-loop testing machines (Simão, et al., 2019). The DPT with a cube-shaped sample is used to present an efficient way to determine the orientation of fibers in a model that can be used at full scale (Pujadas, et al., 2014). This test is called Multidirectional Double Punch Test (MDPT). An empirical study (Molins, et al., 2009) was conducted involving the implementation of both DPT and bending tests on FRC specimens featuring various fiber types, concrete kinds, and fiber volume proportions. A proposed correlation between these two testing methodologies is delineated. The practical application of this correlation to FRC specimens reinforced with steel and polyolefin fibers yields highly promising outcomes. The Barcelona Test (BT) is a modification of the DPT and enhances the establishment of representative figures for the residual tensile strength and toughness of the material, with an average coefficient of variation that falls below 13% (Pujadas, et al., 2014). It has been used in other applications, such as quality control of the concrete in segments for lining the subway line (Molins, et al., 2009). For this test, an equation was proposed to determine the tensile strength as a function of the failure load and the specimen geometry (Saludes, et al., 2007). The test method consists of compressing a cylindrical sample to cause tensile stresses. The application of load is carried out through two steel punches disc shaped at the top and bottom of the sample, so that the alignment between both coincides with the position of the sample axis. The Total Circumferential Opening Displacement (TCOD) in the perimeter direction of the sample and vertical displacement between loading plates were measured. An illustration of the sample

is shown in the Figure 3.11. The solid lines represent the sample and punches. The dashed lines on fracture plane directions represent the crack lines. The another represents the hidden part of the punches and of the sample.

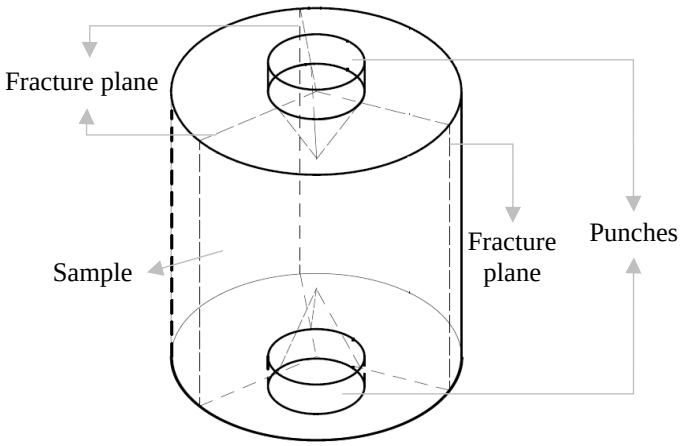


Figure 3.11 – Barcelona Test sample illustration with crack lines.

The BT has demonstrated its high suitability for the systematic evaluation of the tensile properties of FRC, but the requirement to measure the Total Circumferential Opening Displacement (TCOD) of the specimen necessitates the use of a costly circumferential extensometer (Pujadas, et al., 2013). Therefore, an extensive experimental program is undertaken to determine relationships between circumferential and axial displacement (Malatesta, et al., 2012). The results of these authors suggest the possibility of using axial displacement instead of circumferential displacement, bringing more simplicity to the test. In this same line of work, a new analytical model to convert the displacement into the TCOD is developed and validated for a wide range of FRC (Pujadas, et al., 2013). The BT has been reported to labor-intensive and technically demanding, requiring meticulous specimen preparation and the use of hydraulic presses equipped with data acquisition systems (Buttignol, et al., 2024). Moreover, it is necessary to cast the specimen in the shape required by the test configuration, which affects the representativeness of the test results.

A constitutive model was proposed for the Barcelona Test and validated through numerical simulations using finite element software, based on an experimental program with various fiber types and volume fractions (Blanco, et al., 2014).

It has been demonstrated that it is possible to predict the 3PBT based on BT with a confidence margin, despite the wide variety of fiber type, fiber content and rheology considered (Galeote, et al., 2017).

As the DPT can be considered an indirect test, it is important to develop an inverse analysis procedure for it. This procedure is proposed for the results of double punch tests (DPT) conducted on cubes (Karrer, et al., 2022).

Table 3.5 – Main contributions to DPT and BT.

Reference	Main Contribution
Chen (1970)	Development of DPT to determine the tensile strength of concrete
Saludes *et al.* (2007)	An equation was proposed to determine the tensile strength as a function of the failure load and the specimen geometry
Molins *et al.* (2009)	Proposed a correlation between DPT results and bending tests for the FRC
Malatesta *et al.* (2012)	Determined relationships between circumferential and axial displacement based on experimental results
Pujadas *et al.* (2013)	Proposed analytical model to convert the displacement into the TCOD is developed and validated for a wide range of FRC
Pujadas *et al.* (2014)	The cube-shaped sample is used to present an efficient way to determine the orientation of fibers
Blanco *et al.* (2014)	Constitutive model was proposed for the BT
Galeote *et al.* (2017)	Determines a correlation between BT and 3PBT
Simão *et al.* (2019)	Investigated influence of the instability on DPT
Nogueira *et al.* (2021)	Repeatability, reproducibility and sensitivity to parameters in the post-cracking mechanical properties
Karrer *et al.* (2022)	Perform inverse analysis procedure from the results of DPT conducted on cubes
Santos *et al.* (2023)	Use of DPT as quality control method of the steel fiber reinforced shotcrete

3.5.5. Splitting Test (ST)

As already shown, the use of UTT has important disadvantages, especially the difficulty in carrying out them. Indirect tests, such as the 3PBT, require the inverse analysis procedure to determine the tensile behavior. With a view to overcoming these difficulties, the test known as the Brazilian test or Splitting Tensile Test (STT), or simply Splitting Test (ST) (Figure 3.12a-b), is proposed by Ozyurt *et al.* (2007) and Carmona and Aguado (2012). The test was already being used to determine the characteristic tensile parameters of FRC (Nanni, 1988;

Carmona, et al., 1995). An investigation was conducted to determine the response of FRC subjected to flexural and split-tension, considering the characteristic tensile parameters (Nanni, 1991). The ST is similar to the diametral compression test used in plain concrete, the so called brazilian test, which is used to determine the characteristic tensile parameters (first crack and ultimate strengths, as well as toughness indexes) of FRC. However, the ST is aimed at the FRC, being indicated for investigating its post-cracking behavior, while the diametral compression test is indicated only for determining the tensile strength of plain concrete.

The ST can be considered simple, in addition to the fact that cores can be extracted from slabs or beams through concrete core drilling (Lameiras *et al.*, 2015). The testing carrying out occurs in such a way that a cylindrical sample in FRC is compressed in the diametrical direction and the stresses propagate in such a way that in the direction perpendicular to the plane of compression, a tensile stress occurs. In this direction, the Crack Opening Displacement (COD) is monitored as a function of the applied load by the test machine and the tensile behavior is studied. In the case of non-homogenization of concrete, the tensile stress field results in a cracking surface that is hardly uniform, so the accuracy of the tensile behavior of these cement-based materials through the crack test is questionable (Salehian, 2015).

Based on ST, Abrishambaf, Barros and Cunha (2013) proposed the Modified Splitting Tensile Test (MSTT) (Figure 3.12c-d). In this test, a notch is introduced into the sample, at the intersection between its faces and the loading plane, with the aim of inducing the formation and propagation of cracks in the region of the notch.

Based on the DEWST (Double Edge Wedge Splitting Test) and the shape of the MSTT sample, Lameiras, Barros and Azenha (2015) proposed a test with a new cylindrical sample shape with a notch similar to that present in the MSTT sample and also with the wedge-shaped adaptation of the DEWST (see Figure 3.12e-f). The purpose of introducing the new shape is to promote stress redistribution and make the intermediate section of the sample subject only to tensile stresses, overcoming the shortcomings of DEWST and MSTT by inducing even more crack formation in the compression plane, and also single crack formation.

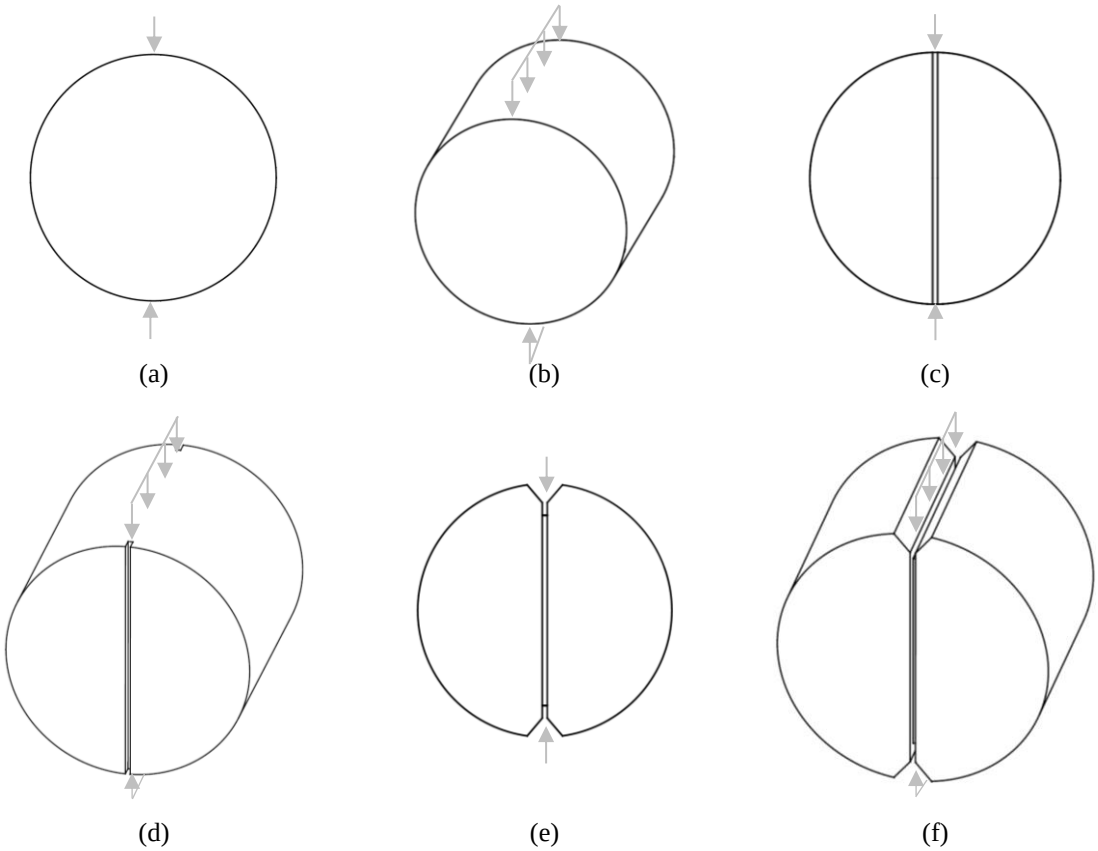


Figure 3.12 – Sample shapes for the ST (front view and three-dimensional perspective): (a) Side view and (b) Perspective view of the traditional test without notch (Ozyurt, et al., 2007; Carmona & Aguado, 2012), (c) Side view and (d) Perspective view of the MSTT test (Abrishambaf, Barros and Cunha, 2013), (e) Side view and (f) Perspective view of the test proposed by Lameiras, Barros and Azenha (2015).

Table 3.6 – Main contributions to ST.

Reference	Main Contribution
Nanni (1988)	Used the test to determine the characteristic tensile parameters (first crack and ultimate strengths, as well as toughness indexes) of FRC
Ozyurt *et al.* (2007) and Carmona *et al.* (2012)	Proposed an adaptation of the Brasilian Test to evaluate the post cracking behaviour of FRC
Abrishambaf *et al.* (2013)	Studied ST sample with straight notches in the plane of crack propagation
Abrishambaf *et al.* (2015)	Obtained σ-w relations with numerical simulations (inverse analysis) of the ST
Lameiras *et al.* (2015)	Studied ST sample with straight notches in the plane of crack propagation and with V-notch

3.5.6. Round Panel Test (RPT)

Another way to indirectly determine the tensile strength in FRC samples is through the Round Plate Bending Test (RPT). This experimental approach can be considered very effective for determining the mechanical properties of concrete, special in relation to the use of fiber reinforcement (Rambo, 2012). There are three different approaches for this test. A Square Panel Test (SPT) with a square panel sample and simple support was proposed by a standard (EFNARC, 2002). This test is performed with a square loading platen and a leaked square support (Figure 3.13a). A disk-shaped sample was employed by other authors since the 2000s (Bernard, 2000; Mobasher & Destreé, 2010). In this approach, the supports are also simple and are positioned close to the edge of the sample (Figure 3.13b). The test with this sample geometry has been called the Round Panel Test (RPT). The ASTM C 1550-05 (ASTM C1550, 2010) standard suggests different supports for the RPT. To carry out the test, the sample consists of a disc-shaped plate with a diameter of 800 mm and a thickness of 75 mm which is supported on three pivots positioned at the ends of the disk, forming a 120° inclination (Figure 3.13c) and subjected to static load, with this load and deflection being monitored. The result of a test is a load-deflection record indicating resistance to load between the onset of loading and a central deflection of at least 40 mm (ASTM C1550, 2010). Some authors (Minelli & Plizzari, 2010a; Medina, 2019; Frazão, et al., 2019; Frazão, et al., 2021) perform this test by monitoring the load and width of the three developed cracks in the fracture plane that occurs between the pivots and the center of the sample by positioning three LVDTs (Figure 3.13d), however this makes the test more complex. This approach has the advantage of determining fracture energy more accurately because this parameter is related to crack opening and not to deflection.

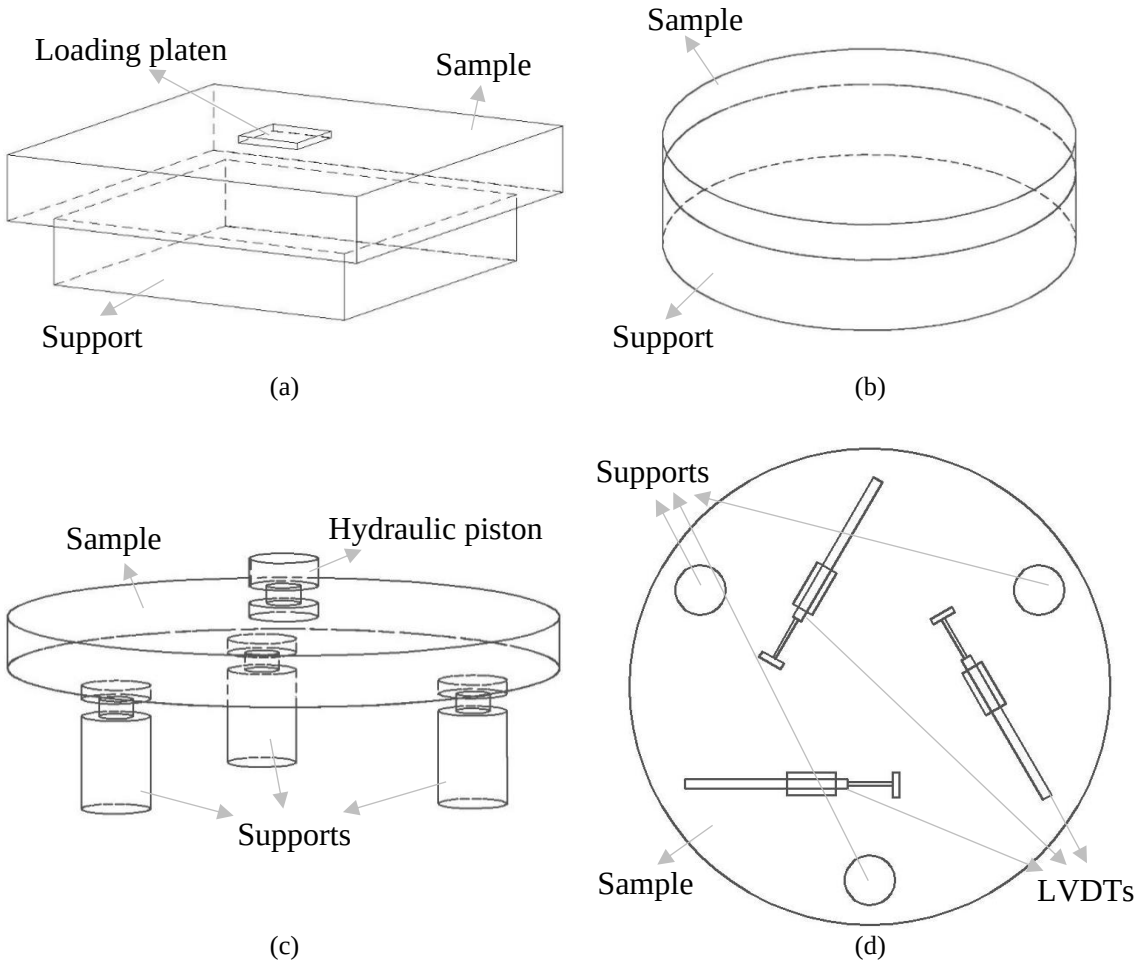


Figure 3.13 – Illustration of the samples of: (a) SPT, (b) RPT with Simple Support (RPT-WSS), (c) RPT with Three Pivots (RPT-WTP) and (d) bottom view of RPT-WTP with LVDTs.

The load and displacement are monitored on the SPT and on the RPT with simple support (RPT-WSS). The RPT with three pivots (RPT-WTP) is the most used proposal. In this case, the load is applied in the center of the disc, thus causing three regions of cracking, which total a larger cracked region than in the case of other tests used to evaluate the behavior of the SFRC, making it possible to determine the predominant orientation of the fibers and that the material can best be treated as a homogeneous and isotropic material (di Prisco, et al., 2009a). The load and Crack Mount Opening Displacement (CMOD) are monitored. The CMOD is monitored through three LVDTs positioned at the bottom of the sample in the region where cracks are expected to occur. During the test, the energy absorbed by the sample is evaluated based on the deflection of the central region. Sample performance is evaluated based on the energy absorbed when loading the plate with selected values of center

deflection. However, this characteristic makes it difficult to compare the results of other tests for the same concrete considering the different geometries of the samples in the different types of tests. Therefore, an inverse analysis procedure may be necessary. This procedure was carried out applying the plastic hinge model (Salehian, 2015) and also with the data fitting algorithm procedure (Nour, et al., 2015).

The main disadvantage of the test is that the specimen itself is too large and heavy to be handled easily and is not sized for many commonly used testing machines. Due to the difficulties in carrying out the test, especially that of mobilizing samples with significant weight, a sample of reduced dimensions was proposed (Minelli & Plizzari, 2010a; Minelli & Plizzari, 2010b; Minelli & Plizzari, 2011) for the RPT: 600 mm in diameter, 60 mm thick, weighing 40 kg. One advantage is the reduced weight of the samples, which now have a more suitable size for the use of a test machine and more reliable results (Minelli & Plizzari, 2015). This new test is known as Small Round Determinate Panel (SRDP). In addition, the most recent works on this test show a great advantage, which is the smaller dispersion of the results. This is due to the fact that the crack's surface area is much larger than in other tests, which reduces the major problem of tests for characterizing the post-cracking behavior of concrete with fibers, which is the high dispersion of the results. The Table 3.7 show papers that address contributions on this test.

Table 3.7 – Works that address contributions on the RPT and SRDP tests.

Reference	Main Contribution
Bernard (2000)	RPT trial studies highlighting single supports
ASTM C1550-05	Standardization of panels with a diameter of 800 mm
EFNARC 2002	Square Panel Test (SPT) standartization
Solleri *et al.* (2005)	It finds that SFRC samples with a larger fracture area show less dispersion
Minelli e Plizzari (2010a e 2010b)	Use of panels with a diameter of 600 mm with less weight and dispersion of results
Soltanzadeh *et al.* (2019)	The authors (Soltanzadeh, et al., 2019) tested smaller samples similar to Minelli and Plizzari (2010a and 2010b) and estimated the post-cracking response of SFRSCC using numerical approaches.
Minelli e Plizzari (2015)	Proposes an analytical methodology to determine the stress relationship with crack opening
Nour *et al.* (2015)	Performing inverse analysis for the RPT test

3.5.7. DEWST (Double Edge Wedge Splitting Test)

DEWST can be defined as a typical indirect tensile test in which a prismatic specimen with wedge-shaped openings on two opposite faces receives a compressive load (AGRA *et al.*, 2019). The test was first proposed by di Prisco *et al.* (2010). The wedge-shaped fitting is made on surfaces with a 45° inclination to the faces. The faces that present wedges correspond to the region where the load is applied (Figure 3.14). This adaptation promotes stress distribution and makes the intermediate section subject only to tensile stresses, which in this way makes the measured resistance approach a value that would be obtained if a UTT were performed (PEREIRA *et al.*, 2019).

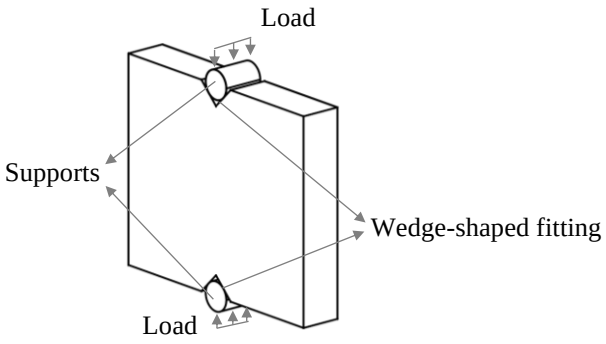


Figure 3.14 – Sample illustration for performing the DEWST.

As shown in Figure 3.14, the load is applied in the direction of the line that intersects wedges. LVDTs are placed on major faces to measure Crack Opening Displacement (COD) in the direction perpendicular to the applied load. In addition, the force applied during the test is monitored. The wedge-shaped adaptation can be performed by means of fixing metallic plates in order to minimize the friction between the roller of the equipment that applies load and the tested sample. The initial proposal of the DEWST consists of using six transducers, three positioned on one of the faces of the sample and the other three on the opposite face (di Prisco, et al., 2010; di Prisco, et al., 2013). Another test proposal consisted of a simplification using only two transducers, one positioned on each side of the sample, positioned at the middle height (Borges, et al., 2019). According to the authors, this is justified in situations of low fiber content and a softening behavior because both sides of the specimens work as rigid bodies after cracking.

The DEWST was simulated using nonlinear finite element analysis (di Prisco, et al., 2013). The authors conclude that the test does not require the inverse analysis procedure to be carried out because, despite being an indirect test, its results represent well the behavior of tensile stress versus crack opening "constitutive relationship" of the material.

An important advantage of DEWST is that it can be used as a less difficult execution alternative in relation to UTT, this is because it prevents the compressive stresses from becoming highly localized, consisting of a compression test that simulates a tensile behavior in the sample middle section (di Prisco, et al., 2010). However, making cuts to form the wedge region is not simple (Pereira, et al., 2019). Adaptations in the molding process were tested so that the mold itself contemplates the V-shaped notches (Monte, et al., 2023). According to the authors, this process simplified the test because it no longer requires

complex cuts for the proper geometry of these notches. The authors also conclude that the axial deflection can be monitored and used for the composition of the test results instead of using transducers. This further simplifies testing.

The test shows the possibility of characterizing concrete reinforced with steel fibers, allowing to determine the residual tensile strength, including associating it with different levels of cracking of the composite (Agra, et al., 2019). The test was Used the DEWST to characterize the design post-cracking parameters of fiber-reinforced concrete subjected to high temperatures (Serafini, et al., 2021).

A comparison of 3PBT with DEWST in samples of high-performance fiber-reinforced concrete it was made (di Prisco, et al., 2013) and found that in addition to DEWST allowing the investigation of tensile behavior both pre-peak and post-peak, the test proved to be a very reliable indirect test.

Table 3.8 – Works that address contributions on the DEWST.

Reference	Main Contribution
di Prisco *et al*. (2010)	First proposal for DEWST
di Prisco *et al*. (2013)	Demonstrated the reliability of DEWST compared to 3PBT with inverse analysis
Agra *et al*. (2019)	Evaluated the effects of fire on the residual tensile strength of steel fiber reinforced concrete using the DEWST
Borges *et al*. (2019)	Use of only two transducers for DEWST
Serafini *et al*. (2021)	Used the DEWST to characterize the design post-cracking parameters of fiber-reinforced concrete subjected to high temperatures
Monte *et al*. (2023)	Use shaped molds contemplating the V-shaped notches so as not to need complex cuts in the test. They conclude the possibility of performing tests with monitoring of axial deflection instead of using transducers.

3.5.8. Montevideo (MVD) and Modified Wedge Splitting Test (MWST)

The test called Montevideo (MVD) was proposed (Segura-Castillo, et al., 2018) based on tests: BT, DEWST and mainly on WST. The main advantage of this test is its simplification compared to WST. The loading device is simpler, consisting of a solid wedge. In addition, the sample only has a simple notch, avoiding the need to perform the more complex groove and notch cuts for sample preparation, as in the case of the WST. Another modification to WST (MWST) is proposed (Neuner, et al., 2022). There is also no traditional WST slot in

this approach and the wedge is similar to traditional WST. Interconnected claws are used to affix the testing apparatus. This configuration is inserted directly into the initial notch of the sample. Through the claws, the force of division is immediately conveyed into the sample via the adjacent facets of the initial notch. Additionally, a prestressing system employing steel cables positioned at the anterior and posterior facets enables the application of minor compressive prestressing on the sample, aiming to enhance the behavior of crack propagation during the test.

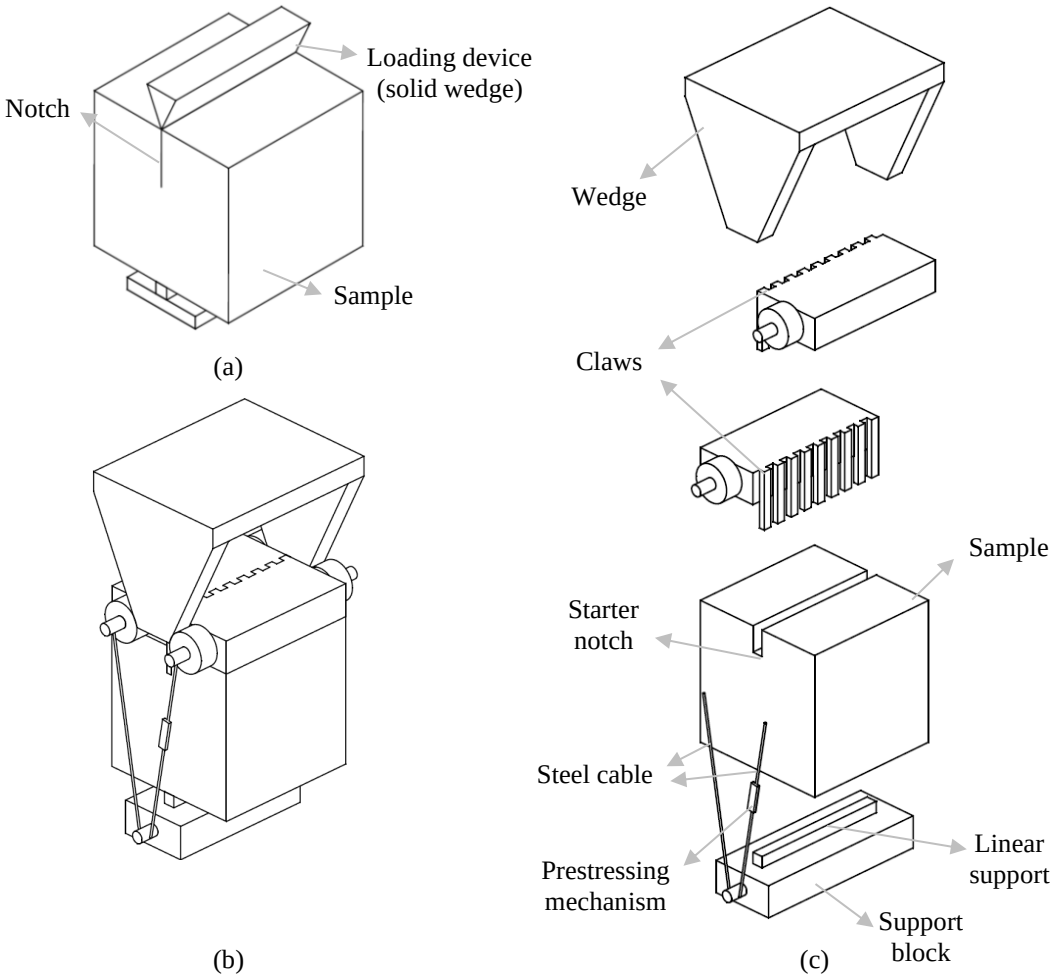


Figure 3.15 – Modifications: (a) MVD test, (b) MWST test setup, (c) Description of the elements of the MWST apparatus.

3.5.9. Disk-Shaped Compact Tension (DCT)

The Disk-Shaped Compact Tension (DCT) test was initially developed as an essential tool for evaluating the fracture resistance of asphalt mixtures, especially under low-temperature

conditions (Wagoner, et al., 2005; Wagnoner, et al., 2005). The DCT was designed as a practical method for determining the fracture energy of asphalt concrete, adapting the compact tension geometry from standard (ASTM E399-22, 2020) to bituminous materials.

The preparation of the DCT specimen involves cutting it into a semicircular shape. This extraction method is advantageous because it can be performed using a core drill, allowing specimens to be taken from actual structures. The specimen features a straight notch, and two symmetrical circular holes positioned between the notch and the specimen's perimeter. Loading pins are inserted into these holes, through which the tensile force is applied. During the test, the crack initiates at the notch and propagates in a controlled manner. The figure presents an illustration of the specimen Figure 3.16.

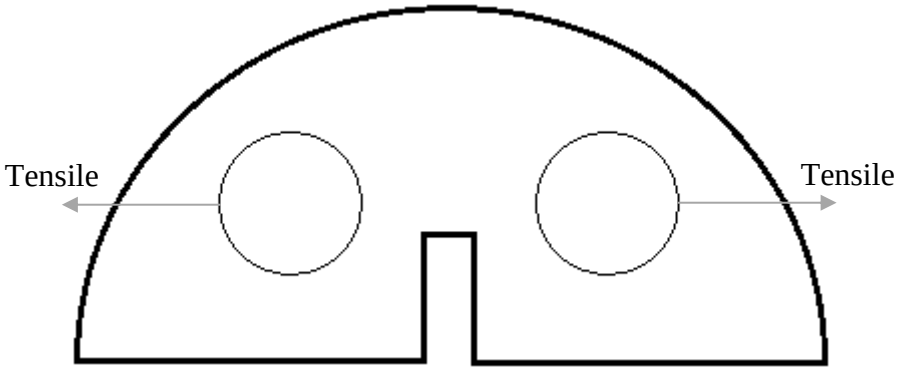


Figure 3.16 – DCT geometry.

The main motivation for the development of the DCT was the need for a reliable method to assess the fracture toughness of asphalt mixtures using cylindrical specimens extracted from field pavements or molded in the lab. The test is particularly effective in identifying the ductile-to-brittle transition behavior in asphalt mixtures under thermal stress and is highly sensitive to changes in mixture composition and loading rates. In 2007, the DCT test was officially standardized through ASTM D7313 (ASTM D7313-20, 2007). This standard outlines procedures for specimen preparation, test conditions, and methods for analyzing fracture energy.

Subsequent studies have confirmed DCT’s effectiveness in discriminating between asphalt mixtures with different cracking potentials. The DCT procedure was refined, adjustments were recommended in mixture design to increase fracture energy and proposing threshold

values to reduce the likelihood of premature cracking in pavements (Dave, et al., 2019). Thus, the use of the DCT to evaluate the influence of mix design variables on low-temperature cracking resistance, with an emphasis on the need for careful interpretation of results, has been discussed (Mandal, et al., 2019).

The DCT specimen has been adapted for use with concrete materials by introducing minor adjustments to the geometry of the loading holes and notch, as well as to the loading rate, in comparison with the ASTM D7313 standard (Amirkhanian, et al., 2012). Additionally, a cohesive zone model was effectively employed to replicate the behavior of the DCT specimen, further confirming the accuracy of the fracture parameters obtained from the experimental testing.

A test method known as the modified disk-shaped compact tension (MDCT) is introduced for assessing the specific fracture energy of concrete. While the approach builds upon earlier concepts involving compact tension specimens to investigate concrete fracture behavior, it incorporates notable changes to the specimen's geometry to prevent early failures, such as cracking or damage in the regions surrounding the loading holes (Cifuentes, et al., 2017).

In another study involving the application of the DCT test to concrete, Mode I fracture properties of cementitious materials were determined using the DCT configuration, incorporating probabilistic modeling approaches (García, 2019).

In summary, the DCT test represents a significant advancement in the characterization of fracture resistance in asphalt mixtures. Its adoption into technical standards and continued use in scientific research highlight its relevance and applicability in pavement engineering. It was one of the tests that served as a foundation for the Semi-Circular Bending Test, which will be discussed below and formed the basis for the development of the test proposed in this study.

3.5.10. Semi-Circular Bending Test (SCBT)

A Semi-Circular Bending Test (SCBT) is presented in this topic. This test is similar to 3PBT, but with sample with semicircular shape (Figure 3.17). This testing methodology enables the use of structural test specimens (di Prisco, et al., 2009), which can be readily extracted from

real structures or representative elements (more details of this type of sample are presented in the item 3.14). In this way, the experimental results of the characterization tests tend to be more representative of the concrete found in the actual structure. Additionally, the test allows the material behavior to be determined in different directions of interest, thus determining the anisotropic behavior of the material.

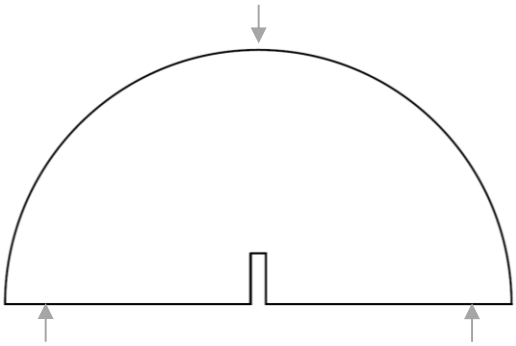


Figure 3.17 – Illustration of semicircular specimen for bending test.

The geometry of the SCBT is similar to that of the DCT. However, while the DCT specimen is subjected to tensile loading, the SCBT specimen undergoes flexural loading. Moreover, the SCBT offers the significant advantage of not requiring the drilling of loading holes; only a notch needs to be introduced. A disadvantage of the SCBT, however, is the need for inverse analysis due to the specimen being subjected to flexural loading during the test.

The SCBT is a test that can be conducted swiftly, it was initially used to evaluate the mechanical behavior of rocky materials (Lim, et al., 1994a; Lim, et al., 1994b; Aliha & Ayatollahi, 2011; Kuruppu, et al., 2014) and has been used to study properties such as tensile strength, fatigue and rupture parameters of asphalt mixtures (Arabani & Ferdowsi, 2008). For these mixtures, the test method used usually follows a technical standard recommendation (EN 12697-44, 2010). Other different materials were also studied through this test: synthetic polymers (Ayatollahi, et al., 2006), a manufactured mixture from asphalt concrete and portland cement concrete (Mirsayar, et al., 2017). However, for fiber-reinforced concrete, there is no specific standardization and literature is scarce for this test. Therefore, authors who work with FRC usually show different parameters for the samples, such as dimensions and composition of the tested material.

The SCBT was employed to evaluate the effect of loading rate on Fiber-Reinforced High-Strength Concrete (FRHSC) on different fiber types, including glass, polypropylene, and steel (Aziminezhad, et al., 2020). The test seems to be promising because it is easy to perform. Samples of this test can be obtained from structural elements through the use of concrete core drilling equipment. The Mode I fracture features of steel fiber-reinforced reactive powder concrete has also been studied (Su, et al., 2019), using the also called notched semi-circular bend test (NSCBT). Finite element simulation was carried out to investigate fracture characteristics of high-strength fiber-reinforced concrete with steel fibers (Hosseini, et al., 2023). However, there is no knowledge of the existence of tests conducted with SCBT (Semi-Circular Bending Test) with crack opening monitoring on conventional FRSCC. The main contributions, as well as the dimensions of the samples tested for works involving concrete with fibers, are presented in Table 3.9.

Table 3.9 - Contributions and dimensions of samples tested for SCBT for fiber concretes

Authors	**Contributions**	**Dimensions (span:effective height:width) [mm:mm:mm]**
Aziminezhad *et al*., 2020	Studied load rate effect on (FRHSC) on different fiber types, including glass, polypropylene, and steel.	(130:75:25)
Su *et al*. 2019	Studied the steel fiber-reinforced reactive powder concrete.	(45:30:30)
Hosseini *et al*. 2023	investigate fracture characteristics of high-strength fiber-reinforced.	(13:50:25)

It is important to emphasize that there is little knowledge regarding the application of SCBT for the characterization of the FRC, since the literature that addresses the test is scarce, therefore, the number of tests already carried out is small so far. In addition, it is still necessary to study more deeply the influence of the dimensions of the specimen on the results, which, according to the literature, is a consideration of significant importance, especially in concrete elements and FRC (Bazant, 1999) (Bazant, 1999; Lameiras et al., 2015; Abrishambaf et al., 2013). As this is a relatively new test for investigating the post-cracking behavior of the FRC, it is also important to carry out a study that addresses comparisons with the UTT, which is only possible if an inverse analysis is performed for the test.

3.6. Inverse Analysis

The direct analysis applied to the FRC consists of determining the constitutive relationship to simulate the uniaxial behavior of the material (Oliveira, 2010). The inverse analysis consists of a procedure to obtain stress-strain diagrams or stress-crack opening through interactive solutions and adjustments of experimental results through constitutive relations (Oliveira, 2010). The inverse analysis problem consists of the situation in which experimental results are available that serve to obtain input data for a direct analysis (Carvalho & Lameiras, 2023a; Ledesma Villalba, 1987; Almeida, 2006; Rauecker, et al., 2019). The inverse analysis encompasses an iterative process to ascertain parameter values that describe the direct tensile behavior, relying on the bending response. It is well-established that the selection of parameters that accurately characterize the tensile behavior of a material yields minimal discrepancies in the bending behavior.

An example of the application of inverse analysis consists of obtaining stress and crack opening diagrams using the experimental response of force-displacement in a test with samples consisting of fiber-reinforced concrete (Carvalho & Lameiras, 2023a). This application is useful, since the most indicated test to directly obtain information on post-cracking behavior is the Uniaxial Tenslile Test, which is difficult to perform (Singh, 2016). The inverse analysis procedure is depicted in the Figure 3.18a-b. The experimental F-CMOD from 3PBT serves as an input parameter. Following the completion of the procedure, the Tensile Stress vs. Crack Opening Displacement (σ-COD) is acquired (Figure 3.18a). The inverse analysis involves carrying out an interactive procedure to determine values for the parameters that describe the direct tensile behavior, based on the bending response.

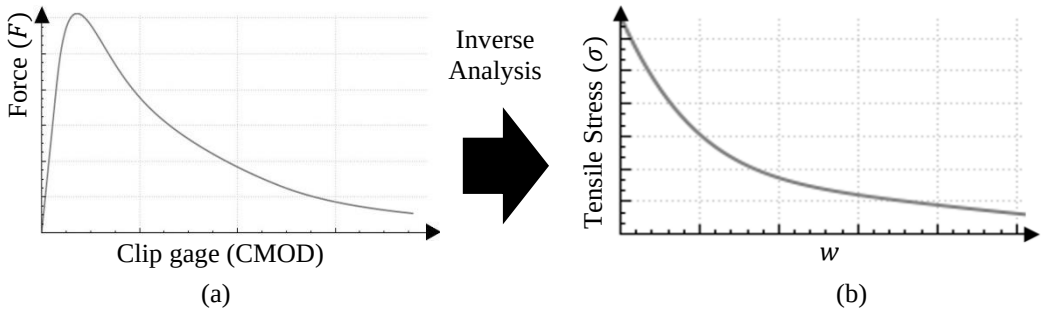


Figure 3.18 – Schematic representation of the diagrams of the inverse analysis procedure: (a) input (Force vs. Displacement or CMOD) and (b) output (Tensile Stress vs. Crack Opening Displacement. Adapted from Carvalho & Lameiras (2023).

A significant milestone in the investigation of the tensile behavior of FRC was the introduction of the fictitious crack model (Hillerborg, 1980). This model simplifies the understanding of the intricate behavior of this composite material by assuming linear relationships prior to crack formation. Moreover, the presence of cracks enables the consideration of a stress transmission mechanism bridging across the cracks. Another model (Zhang & Stang, 1998) was developed to study the behavior of FRC beams using a Three-Point Bending Test (3PBT), based on the force equilibrium in the critical section. The findings from this model lead to the conclusion that the flexural performance of FRC is significantly influenced by the relationship between Force (F) and Crack Mouth Opening Displacement (CMOD). This relationship exhibits an initial section that approximates linearity, followed by the post-cracking phase (Accornero, et al., 2022; Fantilli, et al., 2016a; Fantilli, et al., 2016b; Gorino & Fantilli, 2020). However, estimating the F–CMOD curve from this phase becomes more intricate, necessitating the utilization of complex models.

According to Carvalho & Lameiras, 2023, the inverse analysis methodology for Fiber-Reinforced Concrete (FRC) can be pursued via two distinct approaches: analytical and numerical. Within the numerical approach, essential input data encompassing geometric boundary conditions and material behavior laws are derived through numerical simulations. Nonetheless, this approach suffers from drawbacks, including the many computational interactions and the necessity to employ a numerical model, such as the Finite Element Method (FEM). Previous research has extensively employed this approach in its traditional form to investigate Steel Fiber-Reinforced Concrete (SFRC) (Cunha, 2010; Azevedo, et al., 2003; Abrishambaf, et al., 2013; Roelfstra & Wittmann, 1986; Löfgren, et al., 2004; Gao, et al., 2021; Zhang & Li, 2004), FRC incorporating recycled fibers (Frazão, 2019; Blasi &

Leone, 2022), and specimens featuring varying notch depths and sizes (Santos & Forti, 2022). Some studies have underscored the significance of analytical methodologies that focus on the incorporation of plastic hinges (Olesen, 2001; Salehian, 2015).

This encompasses various approaches that center around the optimization of parameters through probabilistic methods (Stephen, et al., 2019). Additionally, employing this numerical approach, a recent study (Lameiras, 2016) conducted an inverse analysis procedure utilizing a graphical analysis process. Initially, relationships are established to characterize the defining parameters of post-cracking behavior and boundary conditions. Subsequently, simulations utilizing an FEM-based program are executed.

For the model of the bending test of a sample with FRC behavior, when the stresses significantly exceed the cracking stress, a non-linearity of the stress-strain behavior occurs, due to the increase in the moment, and thus, the simple consideration of Constitutive relationships applied directly to the structural element have no correlation with the actual behavior of cracking and deformations (Salehian, 2015). Therefore, it is necessary to optimize these relationships, considering the behavior of this type of concrete in its post-cracking state. This subitem shows the contribution of some authors to the formation of numerical models to consider this behavior.

Zhang and Stang (1998) suggested an analytical expression witch was substantiated by FEM and experimental outcomes. The expression is currently employed as it satisfactorily predicts the load-displacement feedback for any arbitrary tensile stress vs. crack opening displacement diagram. Nonetheless, there is a deficiency of such an analytical formulation for FRC panels to the best of our understanding. The ideal bending behavior of FRC beams optimizes the bonding properties of the aggregate/matrix and fiber/matrix interfaces. The study indicated that it is possible to obtain satisfactory predictions for full structural performance in bending, such as load-CMOD and load-deflection for a sample under 3PBT.

Also based on the force balance in the critical section, Nour et al. (2011) developed an analytical model to determine the post-cracking behavior for FRC of the same thickness subjected to bending. The model was based on the Monte Carlo method and experimentally validated and the results were satisfactory.

Based on the models of Zhang e Stang (1998) and of Nour *et al.* (2011), Nour *et al.* (2015) developed an inverse analysis procedure to characterize the stress vs. Crack Opening Displacement (COD) for both the circular plate and the 3PBT beam model. The proposed methodology entails a staged analysis approach, comprising an initial parameter estimation phase followed by subsequent curve adjustment procedures. The results were experimentally validated. The analysis was carried out in three stages. In the first, an initial guess is made of the multilinear softening diagram of the sample based on the analytical response corresponding to the target curve. In the next two steps, the diagram goes through adjustment, finally, an analytical solution within an iterative process.

To determine a model for the flexural behavior of beams, several studies in the literature have relied on considering the rotation of a central element, known as the plastic hinge model (Figure 3.19). For this model, a method was developed to satisfactorily reproduce the behavior of Fiber-Reinforced Concrete (FRC) with and without conventional reinforcement (Montaignac, et al., 2012). According to the authors, the plastic hinge length (L_h) is influenced by various factors, such as the fraction, type, and volume of fibers, characteristic strength of concrete, geometry of the cross-section, presence or absence of structural reinforcement, and loading conditions. However, the conducted work concludes that employing a single value of L_h for all loading stages corresponds to favorable experimental outcomes. For FRC without conventional reinforcement, the authors used $L_h = 2h$ as the maximum crack width. Table 3.10 presents values utilized by other literature sources for L_h.

Table 3.10 – Different values of L_h adopted by the literature, adapted from Montaignac *et al*. (2012) and Salehian (2015).

L_h	Literatures
$h/2$	RILEM (2002), Massicotte (2004), Ulfkjaer *et al.* (1995), Kooiman (2000), Iyengar *et al.* (1998), Pedersen (1996)
Variable	Olesen (2001)
$2h/3$	AFGC (2002)
h	*fib* (2012), CNR (2006), Salehian (2015)
$2h$	Strack (2008), Montaignac *et al.* (2012)

Despite successfully carry out the inverse analysis, the numerical approach has some limitations, among which the following can be mentioned:

- The need to use specific computational programs for structural analysis;

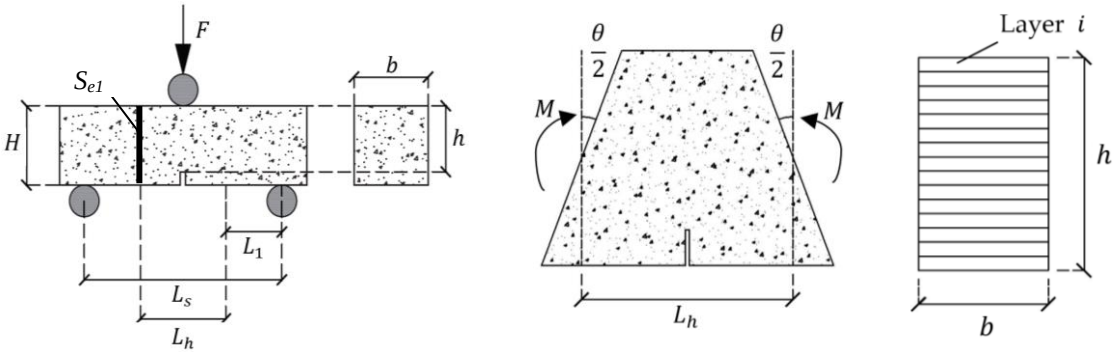
- The high computational cost;
- The significant time spent performing the inverse analysis.

In this context, the search for new ways of implementing this procedure is justified, especially in a simplified way. The following item presents an analytical model (Salehian, 2015) that will be used in this work. Next, is a methodology based on an inverse analysis strategy with graphical analysis that contributes to overcoming these disadvantages (Lameiras, 2016).

3.7. Analytical Model for Determination of (F–CMOD) Diagrams

Multiple analytical models have been developed to ascertain the behavior of the analytical relationship F–CMOD, or $(F–CMOD)_{anal}$, as evidenced by previous studies (Mobasher, et al., 2014; Cunha, 2010; Azevedo, et al., 2003; Abrishambaf, et al., 2013; Roelfstra & Wittmann, 1986; Löfgren, et al., 2005; Grünewald, 2004). For this work, a progressive model of inverse analysis was developed based in Salehian (2015) and Lameiras (2016). As such, it is described in more detail in this section. Lameiras (2016) carries out an inverse analysis method progressively making estimates of initial parameters, however, it uses a Finite Element Method (FEM) software. Salehian (2015) develops an interactive analytical method for inverse analysis, however, it does not use a strategy for estimating initial parameters. This work seeks to develop an analytical methodology for inverse analysis based on the Salehian (2015) model and using a progressive methodology with estimation of initial parameters. In this topic, the analytical model used for inverse analysis based on Salehian (2015) will be presented.

Inverse analysis for a beam under flexure is conducted based on the plastic hinge model. The flexural moment (M) induces an overall rotation (θ) at its critical cross-sections. The cross-section of the effective height element h (and full-height $H = n_e + h$) is discretized into n_L layers, with specified widths (b), thicknesses (t) (Figure 3.19), where n_e is the height of the notch. S_{e1} is the section that delimits the length of the plastic hinge, L_h .



(a) (b) (c)

Figure 3.19 – Representative scheme of the beam under the 3PBT test, highlighting: (a) overview of the test with dimensional parameters, (b) plastic hinge element with plastic hinge length (L_h), and (c) layering of the cross-section. Adapted from Carvalho & Lameiras (2023) and Salehian (2015).

The specimen cross-section is discretized into layers, each characterized by constitutive laws governing compressive and tensile behavior. The parameter L_S is the length of the beam and L_h is the non-linear hinge length. The extension (D_i^k) due to a rotation $\theta_k = k\Delta\theta$ was calculated in an computational interaction k for the i-th layer with Equation (3-4) (Figure 3.19b,c) where $\Delta\theta$ is a prestabilished constant rate:

$$D_i^k = \theta_k \times (d_i - d_{na}) \tag{3-4}$$

where d_i and d_{na} are the depth on layer i and the neutral line depth, respectively.

Having a comprehensive understanding of the compressive behavior in the inverse analysis procedure is imperative when examining a sample subjected to bending stress. In this particular investigation, the compressive behavior of FRC is characterized using an extensively researched constitutive model. The constitutive relations govern the compression force ($F_{cc,i}^k$) and tension force ($F_{ct,i}^k$) as a function of $\varepsilon_{ef,i}^k$, which corresponds to the relationship between D_i^k and L_h. For $d_i > d_{na}$, the corresponding d_i layer is below the neutral line, therefore, tensile stresses occur. In these situations and when $\varepsilon_{ef,i}^k$ surpasses the strain threshold ($\varepsilon_{ct,p}$) determined according equation (3-5) associated with the tensile strength (f_{ct}), it indicates the existence of cracks in the section. Consequently, the existing constitutive equations are not suitable to capture this behavior. In such scenarios, the equation (3-6) is established.

$$\varepsilon_{cc,p} = \varepsilon_{cc,p}^{PC} + 0.0002 W_f \tag{3-5}$$

$$F_{ct,i}^k = \sigma_{ct}(w_i^k) bt \tag{3-6}$$

Where $\varepsilon_{cc,p}^{PC}$ is the strain corresponding to the plain concrete (fib, 2012), W_f is the percentage of fibers, σ_{ct} is the tensile stress, w_i^k represents the crack opening for each layer *i* during the incremental rotation interaction k, while *t* is the thickness of individual layers. $\sigma_{ct}(w_i^k)$ is determined according (3-7) (Salehian, 2015):

$$D_i^k + \left[\frac{f_{ct} - \sigma_{ct}(w_i^k)}{E_c} - \varepsilon_{ct,p} \right] L_h - w_i^k = 0 \tag{3-7}$$

Still for $d_i > d_{na}$, but when $\varepsilon_{ef,i}^k$ is smaller or equal to $\varepsilon_{ct,p}$, we have the relation of equation (3-8).

$$F_{ct,i}^k = \sigma_{ct}(\varepsilon_{ef,i}^k) bt \tag{3-8}$$

If $d_i \le d_{na}$, the corresponding d_i layer is above the neutral line, therefore compressive forces can be obtained by equation (3-9).

$$F_{cc,i}^k = \sigma_{cc}(\varepsilon_{ef,i}^k) bt \tag{3-9}$$

$\sigma_{cc}(\varepsilon_{ef,i}^k)$ is determinated according the compression model (Barros & Figueiras, 1999a) shown in equations (3-10), (3-11) and (3-12), wich is a modification of another model (Vipulanandan & Paul, 1990) and is employed for SFRC with hooked fiber ends (hooked-end).

$$\sigma_{cc}(\varepsilon_{cc}) = f_{cc} \frac{\varepsilon_{cc} / \varepsilon_{cc,p}}{(1 - p - q) + q(\varepsilon_{cc} / \varepsilon_{cc,p}) + p(\varepsilon_{cc} / \varepsilon_{cc,p})^{\frac{1-q}{p}}} \tag{3-10}$$

$$q = 1 - p - \frac{E_{c,\sec}}{E_c},\ p + q \in]0,1[,\ \frac{1-q}{p} > 0 \tag{3-11}$$

$$p = 1 - 0.919 \exp(-0.394 W_f) \tag{3-12}$$

Where $E_{c,\sec} = f_{cc} / \varepsilon_{cc}$ is the secant modulus os elasticity os concrete (fib, 2012). f_{cc} is the compressive strenght of FRC (fib, 2012). ε_{cc} is the compressive strain of the FRC. E_c is the elastic modulus determined according to *fib* Model Code 2010 (fib, 2012), according equation (3-13) with E_c and f_{cc} in GPa and MPa, respectively.

$$E_c = 21.5 \left(\frac{f_{cc}}{10} \right)^{1/3} \tag{3-13}$$

The moment-rotation is calculated considering the balance of moments of the cross-section. A multilinear model (Hillerborg, et al., 1976) utilized to characterize the tensile behavior. This analysis is divided into pre-peak ($\sigma_{ct} < f_{ct}$) and post-peak ($\sigma_{ct} \ge f_{ct}$). In the pre-peak, if

$0 \le \varepsilon_{ct} \le \varepsilon_{cr}$, σ_{ct} is represented by the equation (3-14) and if $\varepsilon_{cr} < \varepsilon_{ct} \le \varepsilon_{ct,p}$ is represented by the equation (3-15), following a bilinear relationship.

$$\sigma_{ct}(\varepsilon_{ct}) = E_c \varepsilon_{ct} \tag{3-14}$$

$$\sigma_{ct}(\varepsilon_{ct}) = (\varepsilon_{ct} - \varepsilon_{cr})(f_{ct} - f_{cr}) / \left(\varepsilon_{ct,p} - \varepsilon_{cr}\right) + \sigma_{cr} \tag{3-15}$$

f_{cr} is the cracking strength, wich corresponds to the mean axial tensile strength (f_{ctm}) of the *fib* Model Code (2010), which is represented on equation (3-16) for concrete class less than C50/60 and on equation (3-17) for concrete class higher than C50/60.

$$f_{ctm} = 0.3\, f_{ck}^{2/3} \tag{3-16}$$

$$f_{ctm} = 2.12 \ln(1 + f_{cm}/10) \tag{3-17}$$

f_{ck} and f_{cm} are the characteristic and mean values of compressive strenght, respectively. The equilibrium condition is imposed considering the sum of forces equal to zero according to the equation (3-18).

$$\sum F_i^k = 0 \tag{3-18}$$

The bending moment (M_k) is determined according equation (3-19).

$$M_k = \sum_{i=1}^{n_t} F_i d_i \tag{3-19}$$

The Force corresponding to bending moment (F_k) at the position S_{e1} (Figure 3.19) is obtained solving the equation (3-20) (Salehian, 2015). M_k is considered constant along the length of the plastic hinge (L_h).

$$M_k = \frac{F_k (L_s - 0.5 L_h)}{4} \tag{3-20}$$

The calculation of deflection (δ_k) is determined using the virtual work method, which considers the combined contribution of both the plastic and elastic behaviors. This can be represented by equation (3-21), where the moments of inertia for the notched ($I_1 = bH^3/12$) and unnotched ($I_2 = bh^3/12$) sections, respectively.

$$\delta_k = \frac{F\left(\frac{L_s - L_h}{2}\right)^3}{6E_c I_2}\left[\left(\frac{L_s}{\frac{L_s - L_h}{2}}\right)^3 + \left(\frac{I_1}{I_2} - 1\right)\right] + \frac{L_s\theta}{4} \tag{3-21}$$

The $CMOD_{num}$ is obtained from the relationship of the equation (3-3) with the deflection calculated from the equation (3-21). The process outlined in this section is visually represented by the flowchart depicted in Figure 3.20.

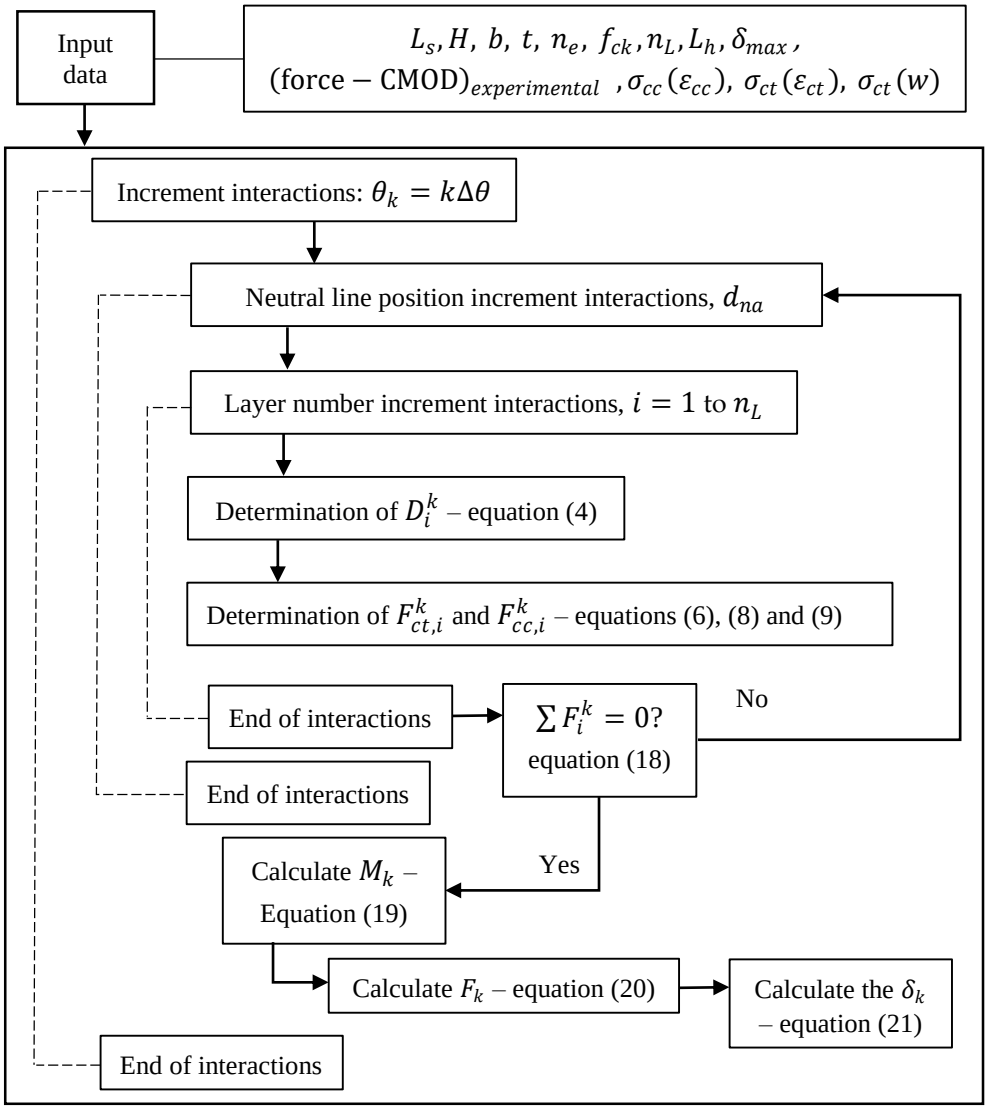


Figure 3.20 - Schematic representation of the representative model employed to characterize the post-cracking behavior of FRC and determine the *F-δ* response with adaptations (Salehian, 2015). Within this context, L_f and d_f denote the length and diameter of the fibers, respectively, while n_L=*H-h*. Additionally, $\sigma_{cc}(\varepsilon_{cc})$ represents the compressive stress derived from the modified constitutive model (Barros & Figueiras, 1999a), and $\sigma_{ct}(\varepsilon_{ct})$ is the tensile stress derived from the bilinear stress-strain relationship of *fib* Model Code 2010 (fib, 2012).

3.8. Simulation of Fiber Reinforced Concrete (FRC) with Finite Element Method (FEM)

The computational simulation of fiber-reinforced concrete (FRC) using the Finite Element Method (FEM) represents a research domain that spans from constitutive modeling to multiscale analysis. This modeling procedure necessitates the consideration of several key factors, such as fiber–matrix interaction, post-cracking behavior, and the influence of fibers on the mechanical properties of the concrete (Pasa Dutra, 2012). This section presents a discussion on this topic.

The fictitious crack model (Hillerborg, 1980; Hillerborg, et al., 1976) is fundamental for representing the post-cracking behavior in fiber-reinforced concrete. In this model, the crack is treated as a discontinuity zone where energy dissipation occurs rather than an instantaneous fracture. Concrete strength is thus attributed to a fictitious crack zone, which can propagate and evolve under additional loading. The model allows for a detailed analysis of the post-cracking phase, which is essential for simulating structures subjected to high-stress conditions. It has been widely applied to the analysis of fiber-reinforced concrete structures, such as steel fiber-reinforced concrete (SFRC), where the fiber distribution and interaction significantly influence the failure process.

The numerical scheme for crack modeling using continuous displacement fields has been applied to two-dimensional problems (Oliver, 1989). In this approach, a crack is modeled as a limiting case of two singular lines (with continuous displacements but discontinuous displacement gradients across them) that eventually coincide. An energy-based analysis within the band bounded by these lines leads to the formulation of a characteristic length, defined as the ratio of the energy dissipated per unit fracture surface area (fracture energy) to the energy dissipated per unit volume (specific energy) at a given point.

Several studies have also been conducted to analyze the interaction between steel fibers and the cementitious matrix. One of the earliest was an experimental investigation into the bond and slip characteristics of fibers embedded in concrete (Banthia & Trottier, 1994). This work was among the first to provide a detailed understanding of how deformed steel fibers affect the tensile and flexural behavior of the material, which are critical to SFRC performance. The authors proposed a theoretical model that considered the effects of fiber distribution, fiber shape, geometry, and bond properties—factors that directly impact the fracture

behavior of SFRC. The model enabled the estimation of the tensile and flexural strength of fiber-reinforced concrete by accounting for fiber contributions across different cracking stages. Additional studies focused on the bond-slip mechanisms of hooked-end steel fibers in self-compacting concrete, analyzing embedment length and the contribution of the hook to pull-out behavior (Cunha, et al., 2008; Cunha, et al., 2009). The experimental bond-slip relationships were reproduced using an analytical model, showing good agreement with the empirical results.

Large-scale SFRC slabs and shell structures have also been simulated using parametric finite element models (Gödde & Mark, 2015). The material model within the framework of an elastoplastic damage theory incorporating smeared cracking, was extended through revised equations and parameters to accommodate SFRC behavior. Plastic strains and stiffness degradation were used to represent crack-induced damage. Mesh sensitivity issues arising from strain localization phenomena were minimized through the implementation of regularization strategies.

Beam-type structures with SFRC have also been widely simulated. To represent the shear stress transfer across the cracks, the shear retention factor is applied, and its value is obtained from inverse analysis of the direct shear tests (Araújo, et al., 2010). Other finite element models have explored force–deflection and force–crack mouth opening displacement (CMOD) relationships in beams, further advancing the understanding of SFRC structural behavior under different loading scenarios. The use of coupling finite elements with a discrete and explicit representation of steel fibers can be cited (Bitencourt Jr., et al., 2019). A soft computing based study aimed to predict the shear capacity of steel fiber RC (SFRC) beams is qualified and new formulae based on gene expression programming (GEP) and nonlinear multiple regression (NMR) (Sharifi & Moghbeli, 2020). Evolutionary polynomial regression analysis (EPR-MOGA) is used to aid the development of the new model witch combines regression analysis with the AI (EPR-MOGA) to develop new correlation to predict the shear strength of steel fiber-reinforced concrete beams (Alzabeebee, et al., 2023). The effect of fiber properties and SFRC layer thickness on the flexural behavior of layered beams that undergo both compression and tension failures was used with computational simulations (Fares & Bakir, 2025).

Dog-bone specimens are casted and tested under direct and uniaxial tension já foram simuladas (Islam, et al., 2014). Finite element analyses are conducted to model the tensile

capacity of steel fiber-reinforced concrete (SFRC). The strain data are gathered employing digital image correlation technique from high-definition images and high-speed video clips. Then, the strain data are synthesized with the load data obtained from the load cell.

To perform computational simulations, constitutive models are used to represent the behavior of materials. One of the models that must be adopted is the compression model. In the simulation stage with the Diana software of this work, a specific compression model is established (Vecchio & Collins, 1993). The Total Strain Crack Model, proposed by these authors, is a widely adopted constitutive model used to simulate the nonlinear behavior of cracked concrete in finite element analyses, especially under multiaxial stress conditions. This model evolved from the principles of the Modified Compression Field Theory (MCFT), and it is specifically designed to handle the complex nature of distributed cracking in reinforced concrete structures. The MCFT is a theoretical framework for modeling the behavior of concrete subjected to shear and axial loads. Unlike traditional truss-based models, the MCFT considers concrete as a continuum with distributed cracking. It uses average stress and strain relationships for both concrete and reinforcement, considering tension stiffening, crack orientation, and the interaction between concrete and reinforcement. A three-dimensional extension of the nonlinear behavior model, based on the fundamental principles of the Modified Compression Field Theory (MCFT) and the Total Strain Crack model (Selby & Vecchio, 1995). A three-dimensional constitutive formulation capable of being applied in complex spatial analyses was developed.

In this model, the tensile damage in the lateral directions are defined: $\alpha_{l,1}$ e $\alpha_{l,2}$. The damage model assumes that the average lateral damage variable is:

$$\alpha_{lat} = \sqrt{\alpha_{l,1}^2 + \alpha_{l,2}^2} \tag{3-22}$$

The expression that accounts for the reduction caused by lateral cracking in the model is represented by:

$$\beta_{\sigma_{cr}} = \frac{1}{1 + K_c} \leq 1 \tag{3-23}$$

Where:

$$K_c = 0.27\left(-\frac{\alpha_{lat}}{\varepsilon_0} - 0.37\right) \tag{3-24}$$

ε_0 is determined by:

$$\varepsilon_0 = -\frac{f_c}{E} \tag{3-25}$$

Another model that must be adopted to perform computational simulations is crack bandwidth. For this, Govindjee's projection method is used (Govindjee, et al., 1995). In this method, the crack bandwidth is defined as the projection of the element length onto the plane of the crack. Consequently, besides the element's size, this approach also incorporates the influence of the element's shape (aspect ratio) and the crack orientation. In tension, the effective crack bandwidth is governed by the direction of the principal tensile strain and the corresponding element dimension in that direction. Similarly, in compression, the crack bandwidth is determined based on the principal compressive strain direction and the associated element length along that path.

3.9. Julia programming language

The Julia programming language was designed to address the performance limitations of interpreted languages traditionally used in scientific computing, such as Python, R, and MATLAB. Officially released in 2012, Julia was developed with the goal of overcoming the so-called "two-language problem," where researchers prototype in high-level languages and later rewrite code in low-level languages for performance (Bezanson, et al., 2012). Julia offers a unique blend of high-level syntax and low-level speed, primarily due to its just-in-time (JIT) compilation based on LLVM and its multiple dispatch system, which enables highly optimized and flexible method definitions (Bezanson, et al., 2012).

The language supports dynamic typing, metaprogramming, and native parallel and distributed computing, which make it well-suited for large-scale scientific simulations (ENCCS, 2023). Julia's ecosystem is rich with specialized libraries for numerical linear algebra, optimization, differential equations, and machine learning. For instance, packages

such as DifferentialEquations.jl, Amaru.jl and JuMP.jl demonstrate Julia's capacity to solve complex systems with high efficiency (Piembsystech, 2023).

One of Julia's main advantages is its expressiveness, which closely resembles mathematical notation, making it intuitive for researchers and engineers. Moreover, Julia offers native interoperability with C, Python, and R, allowing integration with legacy systems and other computational tools (Perkel, 2019). Recent case studies, such as the development of Trixi.jl for adaptive numerical simulations of hyperbolic PDEs, highlight Julia's performance and applicability to cutting-edge research (Ranocha, et al., 2021).

As a result, Julia has increasingly been adopted across a variety of fields, including structural engineering, computational mechanics, physics, and finance. Its high performance and open-source philosophy make it a powerful platform for developing custom finite element frameworks and conducting reproducible research in computational science.

3.10. The Amaru.jl Library for Finite Element Analysis in Solid Mechanics

Amaru.jl is an open-source finite element library written in Julia, specifically designed for the analysis of solid mechanics problems. With a focus on modularity and extensibility, the library supports both linear and nonlinear analyses in two and three dimensions. Its codebase is structured to prioritize conceptual clarity, making it particularly suitable for educational and research purposes (Durand & Silva, 2021; Durand, et al., 2023; Rodrigues & Durand, 2023).

Leveraging Julia's multiple dispatch mechanism, Amaru.jl ensures both code flexibility and computational performance. Users can define arbitrary geometries, assign material properties, apply boundary conditions, and carry out numerical simulations using built-in or user-defined constitutive models.

Due to its transparent architecture and concise syntax, Julia enables researchers to easily modify and extend its functionality (Edelman, et al., 2012). This aspect is especially relevant in academic environments where custom element formulations or new numerical methods are under investigation (Gough, 2013). Furthermore, the open-source nature of the project promotes scientific collaboration and reproducibility—key principles in modern computational mechanics research (Wilson, et al., 2014).

Amaru.jl has been employed in recent studies involving fracture mechanics, nonlinear behavior of fiber-reinforced concrete, and the development of cohesive zone models (Rodrigues & Durand, 2023; Durand, et al., 2023). Its integration with the broader Julia ecosystem also opens possibilities for coupling with optimization routines and machine learning algorithms, enhancing its versatility for advanced numerical experiments (Bezanson, et al., 2017; Innes, 2018). In this context, Amaru.jl represents a contemporary and efficient alternative to commercial finite element software, particularly in scenarios that demand complete algorithmic control, flexible modeling capabilities, and scalable performance.

This study utilized the MechSolid and MechJoint finite elements from the Amaru.jl library, with MechJoint serving as the cohesive element. The constitutive behavior was defined using the WillamWarnke, PowerYieldCrack, and AsinhYieldCrack models.

MechSolid element refers to a type of material domain that is treated as a continuous mechanical solid. This definition is essential for the finite element model, as it determines how the material will respond to the applied loads — particularly with regard to the mechanical behavior it is expected to exhibit. The MechJoint element is commonly used in the simulation of fractures and discontinuities. Its implementation requires the definition of a suitable constitutive model, among which PowerYieldCrack is one of the most frequently adopted.

The yield function is a mathematical function used to describe the point at which a material begins to undergo plastic deformations, that is, when it exceeds its elastic limit and enters a regime of permanent deformations. In general, the yield function defines the criterion for the transition between the elastic and plastic behavior of a material. It is fundamental in material models such as the plasticity model, as it indicates the moment when a material no longer returns to its original state after the application of a load.

The Willam-Warnke model (Willian & Warnke, 1974) is employed to simulate the behavior of concrete. The parameters associated with this model include Young's modulus (E), Poisson's ratio (ν), the compressive strength (f_c) and tensile strength (f_t) of concrete, and the fracture energy (G_f).

The WillamWarnke model implements a three-dimensional failure criterion commonly used for quasi-brittle materials such as concrete. It captures both compressive crushing and tensile

cracking behaviors based on a multiaxial stress state. Parameters typically include compressive and tensile strengths, cohesion, and friction angles. This model is suited for nonlinear simulations involving progressive damage under complex loading. It is especially valuable for structural concrete applications.

PowerYieldCrack is a cohesive damage model used to simulate crack initiation and propagation in quasi-brittle materials. It combines a yield function with a damage evolution law based on energy dissipation and residual tensile strength. This model is particularly effective in modeling fracture processes in fiber-reinforced concrete or along pre-defined interfaces. It allows for user-defined softening parameters and energy dissipation rates. It is often applied in studies of crack localization and structural failure.

GeoModel serves as the geometric representation in the simulations, defining the solid domain to be analyzed and providing the necessary input for mesh generation.

3.11. Inverse method for determining the stress-crack width (σ-w)

Lameiras (2016) proposed an inverse analysis method for the SFRSCC that will be described in this item and also served as an important reference for this work. Unlike Salehian (2015) model, Lameiras (2016) used a FEM-based model to generate a numerical *F-CMOD* response ($F\text{-}CMOD_{num}$). The progressive method used for determining the stress-crack width (σ-w) consists of the following steps:

Step 1: The parameters to be acquired through the inverse analysis methodology encompass: f_{ct}, σ_1, σ_2, σ_3, w_1, w_2, w_3 and w_u. They are graphically depicted in Figure 3.21. For this first step, the author considered: $w_u=L_f/8$ and the values of σ_2 and σ_3 are established in such a way that $\sigma_2/f_{ct}=1.0$ and $\sigma_3/f_{ct}=0.5$. For all stages of the procedure, it was considered: $w_1=0.2$ *mm*, $w_2=1.0$ *mm*, $w_3=2.5$ *mm*.

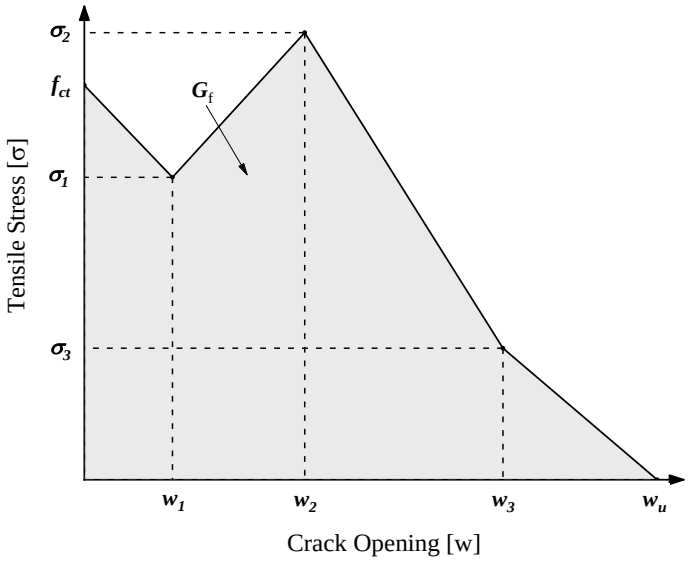


Figure 3.21 – Parameters of Inverse Analysis procedure.

Step 2: An interactive process is carried out in this step. f_{ctm} is obtained according to EN 1992-1-1 (2004) recommendations based on the maximum stress value derived from the splitting test. The parameter σ_1/f_{ct} varies by two values (0.8 and 1.2) and the parameter f_{ct}/f_{ctm} varies from 0.5 to 0.9 every 0.05. Thus, two graphs are formed (one for each σ_1/f_{ct}) with 9 curves each (one curve for each value of f_{ct}/f_{ctm}). The selection of the value of f_{ct} is performed through a graphical approach, aiming to achieve optimal alignment with the initial segment of the load-CMOD experimental curve. The value of f_{ct} and f_{ctm} obtained in this step are fixed for the following steps.

Step 3: The value of f_{ct} and f_{ctm} obtained in the previous step are fixed for this step and for the following steps. Thus, σ_1/f_{ct} is taken varying from 0.7 to 1.5 at each increment of 0.1 and σ_2/f_{ct} is established with the values: 0.8 and 1.2, respectively. Thus, 9 curves are obtained for each σ_2/f_{ct}, similarly to the previous step. With the best fit obtained with these curves in relation to the experimental F-CMOD response, the σ_1/f_{ct} ratio is graphically obtained, which is fixed for the following steps.

Step 4: The determination of σ_2/f_{ct} involves employing the identical methodology as employed in step 3, albeit with σ_2/f_{ct} being considered as the principal variable (9 values) and σ_3/f_{ct} as the secondary variable (2 values).

Step 5: The determination of σ_3/f_{ct} involves employing the identical methodology as employed in step 3 and 4, albeit with σ_3/f_{ct} being considered as the principal variable (9 values) and w_u as the secondary variable (with 2 values: $L_f/10$ and $L_f/4$).

3.12. Influence of fiber orientation on Fiber Reinforced Concrete (FRC)

The orientation of the fibers in relation to the concrete flow is an important parameter in determining their effectiveness in relation to crack opening control (Laranjeira, 2010). The conventional molding procedure of fiber-reinforced concrete (FRC) involves the addition of fibers in such a way that they become dispersed within the concrete matrix. In this process, the fibers do not exhibit a uniform orientation. However, they tend to align preferentially depending on the fresh-state properties of the concrete, the pouring technique, the geometry of the formwork, the dynamic effects like the type of vibration applied, and the overall production method (Álvarez, 2013).

In the fresh state, the flow behavior of concrete during the molding process plays a critical role in determining the orientation of the fibers (Stahli, et al., 2008; Sarmiento, et al., 2012; di Prisco, et al., 2007; Gudzulic, et al., 2019; Kooiman, 2000; Grünewald, 2004; Markovic, 2006; Martinie, et al., 2010). Fibers tend to align predominantly in the direction of the concrete flow during placement (Stahli, et al., 2008). For example, when concrete is poured from a central point above a slab-shaped mold, the fibers tend to orient themselves along the same path as the radial flow of the concrete within the mold after placement (Figure 3.22).

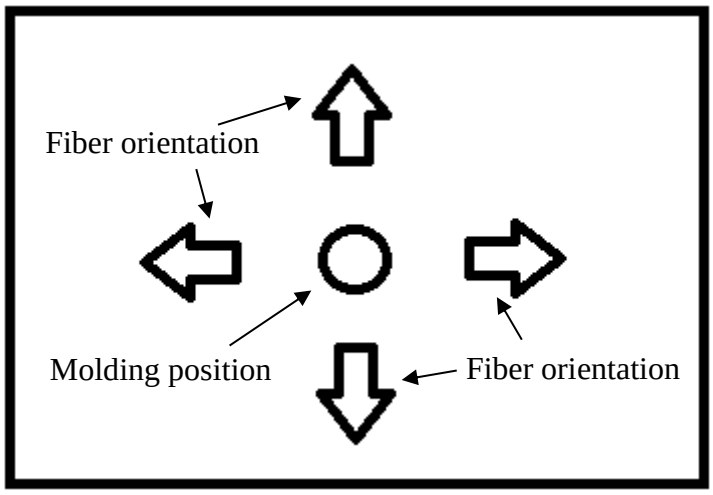


Figure 3.22 - Relationship between concrete flow orientation according to molding position and predominant fiber orientation.

To overcome the disadvantages of varying the number and orientation of fibers in the cracked section of the FRC, counting and complete determination of fiber inclinations in this region must be performed, which can be done through destructive or non-destructive methods (Laranjeira, 2010; Jones, et al., 2008; Robins, et al., 2003).

Fiber orientation was studied using SFRSCC and vibration-densified SFRC plates (Shah & Ferrara, 2008). The authors concluded that the dispersion is much greater in the SFRC and that, therefore, the SFRSCC brings improvements in the sense of better fiber distribution. This is due to factors such as greater heterogeneity of the matrix, lower workability, and greater maximum dimension of the coarse aggregate of the SFRC compared to the SFRSCC (Cunha, 2010).

Abrishambaf (2013) extracted samples from plates with dimensions 1600x1000x60 mm and extracted cylindrical cores of 150 mm in diameter and 60 mm in height, from samples for UTT and compression tests. The concrete flow during placement was taken from the center to the edge of the plate and the load for the compression test was applied in the parallel and perpendicular direction in relation to the predominant direction of the fibers as the concrete flow. To evaluate the fiber distribution and orientation, the image analysis technique was used, which consists of obtaining a high-resolution color image from the rectified and clean surface of the tested sample, then removing imperfections and adjusting the projected ellipsoidal shape of the fiber. fiber in the image. The author concludes that the distribution and orientation of the fibers influenced the results of the test: when the samples were tested with the cracking plane parallel to the concrete flow direction, they presented higher cracking parameters than in the perpendicular plane.

Lameiras (2016) developed a sandwich panel with two layers of thin SFRSCC and a small rigid foam with high thermal resistance in its core. The panel was developed to avoid the use of conventional reinforcement and allow the use of concrete elements with reduced thickness, thus resulting in panels with lower final weight. The author proposes a new test method based on the compression test to determine the fracture parameters of the SFRSCC in plates with reduced sections, and it was also found that the fiber direction influences the results. According to the author, the mechanical properties of SFRSCC determined from samples molded in small molds may not represent the behavior of the material with the same mixing ratio in the real structural element, since in these materials, the fiber orientation is strongly influenced by the molding method and shape of the elements, or wall effect (Lameiras, et al., 2015).

Continuing the studies carried out by Lameiras (2016), Medina (2019) carried out a characterization study of the post-cracking behavior of the SFRSCC in thin elements, involving different dosages of concrete and analyzing the influence of different directions of

the applied load in relation to the direction of the fibers. Square plates (cylinders being extracted from them) and circular plates of different sizes were molded, as well as prismatic beams. In those samples in which compression test, MSTT, RPT and 3PBT were performed. The author verified as results that the post-cracking parameters have greater intensity when the test is carried out with the samples presenting a fracture plane parallel to the flow lines, due to the natural tendency of fiber alignment to occur in the direction perpendicular to the flow (which is a result similar to that found by Abrishambaf et al., 2013 and Lameiras, 2015). According to the author, the average of residual tensile stresses and the average of absorption energies increased with the decrease in the thickness of the sample tested in compression test.

3.13. Wall effect

The process of placing the concrete in the molds has a significant influence on the orientation of the fibers after the FRC hardens (Abrishambaf, et al., 2015; Lameiras, 2016; Singh, 2016). The existence of surfaces (on the faces of the ends of the sample or on the shapes of the structural elements) make the orientation of the fibers parallel to these faces. In these cases, we can see the occurrence of the wall effect and also, as the FRC volume is exposed to more limits (Medina, 2019). If the region of the element is far from these faces, or from any element that induces a specific orientation, the fibers tend to be randomly distributed in the concrete matrix. In this situation, the fibers can remain perpendicular to an eventual tensile stress (Singh, 2016). Therefore, the fibers provide an improved solution for the concrete's resistance to tensile strength, contributing to increase the strength of the assembly in this region.

Different preferential fiber orientation directions may develop within the mold, depending on the boundary conditions imposed by the mold geometry and formwork constraints (Álvarez, 2013). The Figure 3.23 illustrates scenarios in which the mold walls can influence the preferential orientation of the fibers. When the mold has large dimensions and its walls are positioned far from the analyzed portion of concrete, or when no mold walls are present, the fibers tend not to exhibit a preferential orientation.

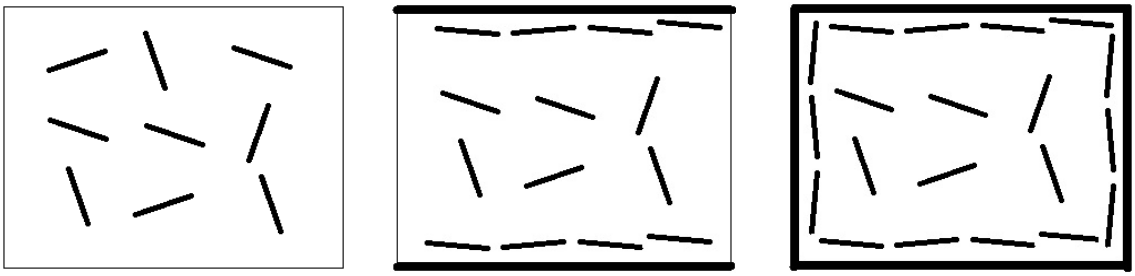


Figure 3.23 – Scenarios in which the mold walls can influence the preferential orientation of the fibers: (a) No boundaries, (b) Two boundaries and (c) Four boundaries.

Ding *et al.* (2018) performed a study involving fiber distribution. Prismatic samples were cut into eight parts on one side in the transverse direction and four parts on the other side, in the longitudinal direction (vertically and transversely). The fiber distribution ratios were then analyzed and it was observed that even excluding the parts cut from the ends of the piece, the closer to the end, the smaller the fiber distribution, which reflects the wall effect. In general, the effect was seen most intensely at a distance of 30 mm near the side surfaces and on the bottom surface of the mold.

The mechanical properties of the SFRSCC determined from samples cast in small molds may not represent the behavior of the material with the same mix ratio in the actual structural element (Lameiras, 2016).

3.14. Influence of dimensions on SFRC behavior and structural specimen

The evaluation of SFRC's the dimensions and geometry of test specimens play a pivotal role in determining the observed mechanical properties. Understanding the influence of specimen size and shape is crucial for accurate characterization and reliable application of SFRC in structural elements.

Despite the advantages of Fiber Reinforced Self-Compacting Concretes (FRSCC) like increasing ductility, strength capacity of concrete after cracking and eliminating the need for vibration, its properties are highly dependent on the shape of the structural element in which it is used and the concrete flow during the molding process (Lameiras, et al., 2015; Vrijdaghs, et al., 2020; Ferrara & Meda, 2006; Abrishambaf, et al., 2015; Cunha, 2010; Ferrara, et al., 2008). This occurs because the distribution and orientation of the fibers are influenced by the boundary conditions imposed by the molds and the flow of the concrete.

Furthermore, these wall effects caused by the molds and the flow of concrete end up triggering an anisotropic behavior of the FRC. Therefore, some studies have emphasized the importance of characterizing fiber-reinforced concretes, especially high-density ones, using a test specimen that is representative of the concrete in the structure, which can even be extracted from the structure itself (di Prisco, et al., 2009a; di Prisco, et al., 2013; Vrijdaghs, et al., 2020; Ortega-López, et al., 2022). This test specimen is commonly referred to as a "structural test specimen". Therefore, it is important that samples have a geometric shape suitable for extraction from larger structures, such as the test that will be discussed in this topic.

Furthermore, new work on new testing methods is also justified because the usual tests for the characterization of FRC have some disadvantages. The three (3PBT) and four (4PBT) point bending tests and the Round Panel Test (RPT) present execution difficulties due to the large samples (Bernard, 2000; Committee, 2002; EN 14651, 2007; CNR-DT 204, 2006). The DEWST (Double Edge Wedge Splitting Test) (di Prisco, et al., 2010; Borges, et al., 2019; Cuenca & Ferrara, 2020) has proportionally smaller samples, but its geometry is not favorable to extraction with core cutting machines. The Uniaxial Tensile Test (UTT) is the most representative test, but it is difficult to perform because it requires strict control (geometry and direction of loading) (Planas, 2007; Mudadu, et al., 2018; van Mier & van Vliet, 2002; Hordijk, 1991). The samples of these tests are usually molded in shapes separately to the real structure. It is difficult to perform the extraction of samples for these tests in the real structure due to its geometry, which is usually prismatic (3PBT, 4PBT and DEWST) or large disc-shaped (RPT) to evaluate the behavior of the FRC in the structure.

In the 1970s, studies of the scale effect were stimulated by the problems of concrete structures, for which there is a large gap between the scales of large structures (e.g. dams, reactor containments, bridges) and laboratory tests (Bazant, 1999). The representative sample of the real structure was designated with the term "structural specimen" (UNI 11188, 2004). According to Prisco *et al*. (2009), the structural deformability is acquired through the consideration of the axial distance between the transducer's axis and the lower surface of the specimen, in accordance with a plane section kinematic approach. A thin sample was used to demonstrates superior representativeness pertaining to the performance of thin (FRC) structures. Therefore, it may be designated as a structural specimen.

Prisco et al. (2004) carried out a study of the effect of the size of the dimensions in plates with a thickness of 60 mm molded with SFRC. The plates were subjected to pure bending, eccentric tensile and uniaxial tensile. The author concluded that the size of the samples had little influence on the residual strength, however, the increase in the dimensions of the plates promotes greater ductility. Therefore, the specimen must present dimensions so that it is representative of the structure to be studied.

One of the advantages of the MSCBT, which will be the object of study in this work, is the obtaining of specimens through cylindrical sample extractors. Therefore, it is possible that the specimen is extracted from a larger element, and that, therefore, it is representative of the structural element in FRC. Therefore, the study of the sample size parameters and the FRC are of paramount importance for this work.

4. METHODOLOGY

4.1. Flowchart of work activities

This work studies the Modified Semi-Circular Bending Test (MSCBT) as a proposal to investigate the post-cracking behavior of Steel Fiber Reinforced Self-Compacting Concrete (SFRSCC), and compare it with the Uniaxial Tensile Test (UTT) and the Splitting Test (ST). The Figure 4.1 show the division of the work into three major activities: Inverse Analysis (IA) algorithm for 3PBT (progressive method), IA algorithm for MSCBT (preliminary results), IA algorithm for MSCBT (validation), MSCBT (conception and sample thickness) and ST (conception).

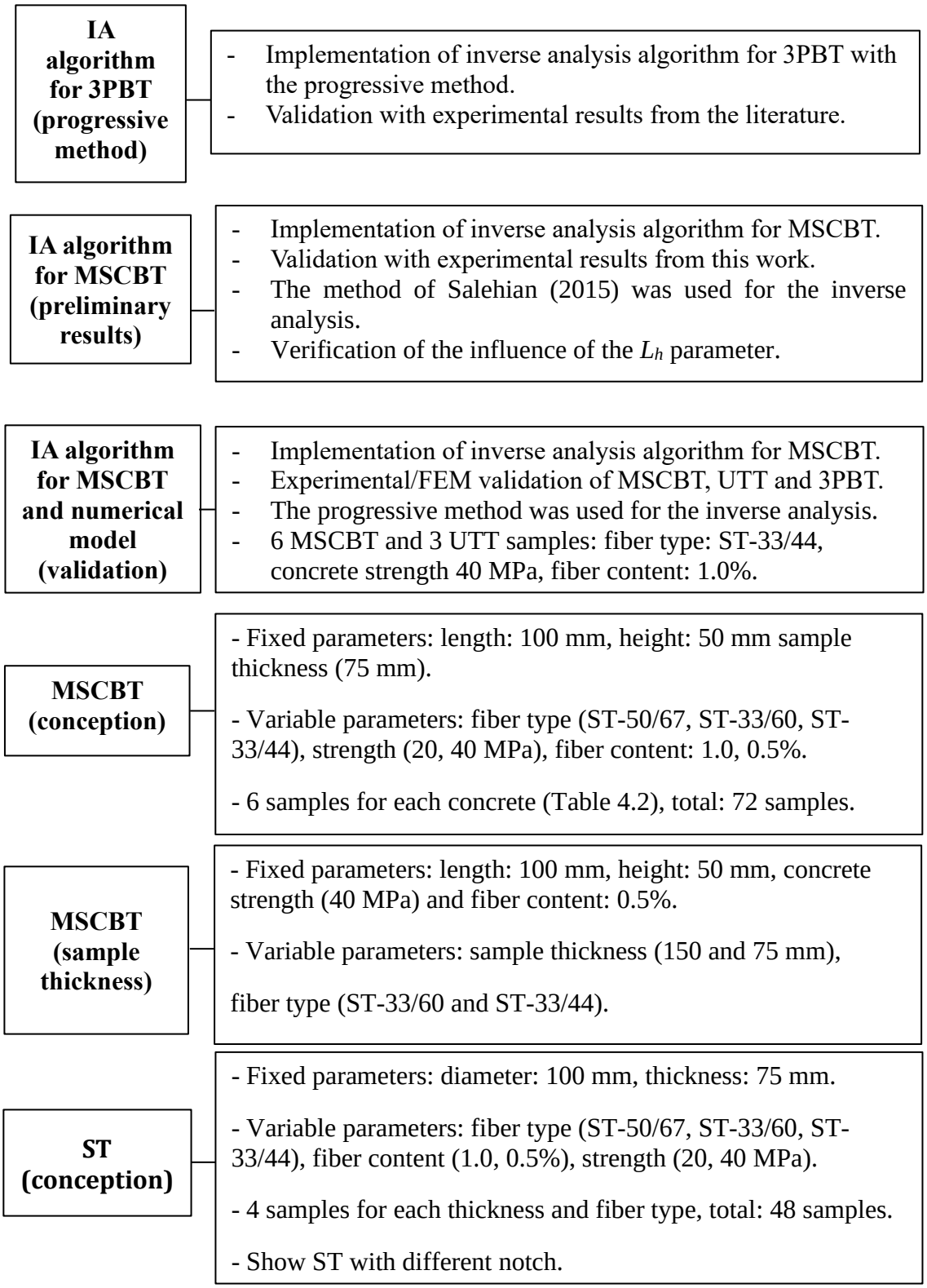


Figure 4.1 – General work flowchart.

On the IA algorithm for 3PBT (progressive method), the computational algorithm capable of performing the inverse analysis procedure in a more rational way is implemented, as well as to validate them with experimental results from the literature (Lameiras, 2016; Frazão, 2019; Nour, et al., 2015; Salehian, 2015) for the 3PBT. The algorithm was developed to determine the $F - CMOD$ curve that best fits an analytical solution based on the fixed parameters and the inverse analysis process is applied to determine the stress-opening of cracks (σ-w). The results of this work have already been published in a scientific journal (Carvalho & Lameiras, 2023a).

From the point of view of the MSCBT conception on topic IA algorithm for MSCBT (preliminary results), the tool for the inverse analysis procedure based on Salehian (2015) developed for 3PBT is applied for the MSCBT to verify the possibility of carrying out the procedure based on this type of test. A study is carried out for also verification of the influence of the L_h parameter on the results. The results of this work have already published as an international book chapter (Carvalho & Lameiras, 2023b).

On the MSCBT (conception), 48 samples are tested varying content and type of fibers and strength of concrete. On the MSCBT (sample thickness), 24 samples are tested with different thickness in order to evaluate the influence of these parameters on the FRC properties. For the ST (conception), the aim is to verify the effectiveness of this test considering its different characteristics and compare the results with traditional ST from the literature.

4.2. Characteristics of parameter monitoring equipment during tests

To carry out the tests described in this work, a servo-controlled hydraulic system possessing a maximum load capacity of 300 kN was used. Through this same equipment, the synchronized recording of the applied load and the imposed displacement will be carried out, both as a function of time. An acquisition system is intricately linked to a set comprising two Linear Variable Differential Transformers (LVDTs) and a load cell capable of accommodating loads up to 500 kN. The clip gauge is a widely used device for monitoring the CMOD in both 3PBT and UTT. It may also be suitable for the MSCBT configuration. However, it presents limitations in its measurement range, which could lead to the loss of critical data during testing. Additionally, greater care would be required during test execution to prevent the device from becoming detached due to the specimen size and test

conditions. Since this test method is still rarely applied to SFRSCC, conventional LVDTs were used in this study to ensure a more secure and stable test setup. The tests conducted in this study exhibited low loads at the beginning of the testing process. At this initial stage, the sensitivity of the load cell used is relatively low. However, since the focus of this work is on the post-cracking behavior, when the applied loads are higher, the use of this type of load cell is considered appropriate. The system is configured for monitoring the *F-CMOD* or *F-COD* parameter at a monitoring frequency rate equal to 2 Hz. The σ-w curve obtained from the tests can be considered as an approximation of the characteristic softening behavior of SFRSCC.

For the tests in this research, LVDTs of the WI-10 mm type were used. The length and thickness of the part of the equipment suitable for fixing to the plates are respectively 51.8 mm and 8 mm.

4.3. Molding characteristics of test samples

The samples for carrying out the experimental procedure of this work were obtained by extracting samples from specimens from 3PBT in the work of Cardoso (2020), which performed bending tests in 3PBT samples. Cores were extracted from 56 prismatic SFRSCC samples with dimensions 150 mm × 150 mm × 550 mm for 12 concrete compositions for steel fibers, after bending in 2 cylindrical samples of each concrete. The concrete components are shown in Table 4.1. The concretes have compressive strengths of 20 and 40 MPa. The cement contents obtained for the 20 MPa and 40 MPa concretes were approximately 400 and 510 kg/m³, respectively. These values are relatively high for the corresponding compressive strengths achieved. Such elevated contents may be attributed to possible issues related to mix design or mix procedure or cement hydration. However, since the primary focus of this study is not on mix design optimization, these values are not expected to have a significant impact on the overall research outcomes.

Table 4.1 – Concrete components to be used in the work for strength of 20 MPa and 40 MPa.

Materials	Concrete with strength of 20 MPa					
Fiber type	ST-33/60		ST-50/67		ST-33/44	
Fibers [%]	0.5	1.0	0.5	1.0	0.5	1.0

Gravel [kg/m³]	844.2	825.9	833.5	802.2	825.5	803.8
Sand [kg/m³]	627.1	613.5	619.2	595.9	613.2	597.1
Cement [kg/m³]	382.1	392.1	387.9	397.9	392.4	392.9
Water [kg/m³]	233.9	239.5	237.2	243.7	239.6	240.2
Limestone Filler [kg/m³]	244.4	251.7	248.8	280.7	251.8	286.5
Superplasticizer Additive [kg/m³]	9.0	9.2	9.1	8.0	9.2	9.5
Materials	Concrete with strength of 40 MPa					
Fiber type	ST-33/60		ST-50/67		ST-33/44	
Fibers [%]	0.5	1.0	0.5	1.0	0.5	1.0
Gravel [kg/m³]	844.4	805.1	833.6	805.7	825.6	803.1
Sand [kg/m³]	649.0	599.9	640.7	598.5	634.5	596.6
Cement [kg/m³]	505.0	515.3	512.6	514.7	518.6	520.3
Limestone Filler [kg/m³]	133.8	177.0	136.6	179.8	138.3	172.8
Water [kg/m³]	233.8	238.3	237.0	237.8	239.5	241.3
Superplasticizer Additive [kg/m³]	5.30	6.10	6.10	5.10	5.10	5.10

An axial compression test was also carried out on 4 cylindrical samples with dimensions 100 mm × 200 mm for each concrete, to determine the compressive strength. The fibers type and contents are described in Table 4.2 as well as the strength of the concrete used. The hooked-end steel fibers characteristics used in this work are shown in Table 4.3. The coarse aggregate used has a characteristic maximum diameter of 9.5 mm (gravel 0) and the sand is classified as medium sand.

Table 4.2 – Characteristics of the fibers of the samples tested according to the concrete.

Concrete	Fiber content (%)	f_{ck} (MPa)	Fiber type
C-1	0.5	20	ST-33/60
C-2	0.5	20	ST-50/67
C-3	0.5	20	ST-33/44
C-4	1.0	20	ST-33/60
C-5	1.0	20	ST-50/67
C-6	1.0	20	ST-33/44
C-7	0.5	40	ST-33/60
C-8	0.5	40	ST-50/67
C-9	0.5	40	ST-33/44
C-10	1.0	40	ST-33/60
C-11	1.0	40	ST-50/67
C-12	1.0	40	ST-33/44

Table 4.3 – Characteristics of the hooked-end steel fibers of the samples used in this research.

Fiber type	Diameter (mm)	Length (mm)	Aspect ratio (mm)
Maccaferri (ST-33/44)	0.75	33	44
Maccaferri (ST-33/60)	0.55	33	60
Maccaferri (ST-50/67)	0.75	50	67

4.4. Compressive tests and flow spread

The compressive strength was determined following the recommendations of NBR 5739 (Associação Brasileira de Normas Técnicas, 2018) using four cylinders with 100 mm in diameter and 200 mm in height, which were prepared concurrently with the 3PBT samples, using the same concrete as in the other tests, but in separate molds. These compression tests were performed after curing for 28 days under humidity control. The concrete has an average compressive strength of 35.8 MPa with a standard deviation of 0.46 and characteristic value of 35 MPa. The flow spread of SFRSCC was carried out in accordance with NBR 15823 (Associação Brasileira de Normas Técnicas, 2017). The average flow spread was 650 mm. The methodology of this topic, including the type of SFRSCC described, was applied to six samples tested under MSCBT, another three samples tested under UTT and another three tested under 3PBT. The results are presented in item 5.9.

4.5. Sample Preparation for the 3PBT

In this work, the 3PBT was performed according to the literature (Cardoso, et al., 2021). The tests were performed on four samples with the following dimensions 150 mm × 150 mm × 550 mm. The central notch is 25 mm depth, according to EN 14651 (EN 14651, 2005). The specimens underwent a curing process within a large environmental chamber featuring controlled temperature (20 ºC) and humidity (90%) for 28 days. The load cells, the LVDTs, the servo-controlled hydraulic-system and the acquisition system used in this test are described in item 4.2. The tests were carried out utilizing a servo-controlled hydraulic system, operating at a constant rate of 0.1 mm/min, under the supervision of the testing machine's internal displacement transducer. Testing was halted upon reaching a crack opening of 6 mm. For CMOD monitoring throughout the tests, an acquisition system was connected to a pair of LVDTs, positioned on each notched lateral face of the specimens. The analyzed parameters comprised the proportionality limit ($f_{fct,L}$) and the residual flexural strength f_{R1}, f_{R2}, f_{R3}, and f_{R4}, which corresponded to CMOD values of 0.5 mm, 1 mm, 2.5 mm, and 3.5 mm, respectively. The schematic representation of the sample is depicted in Figure 4.2.

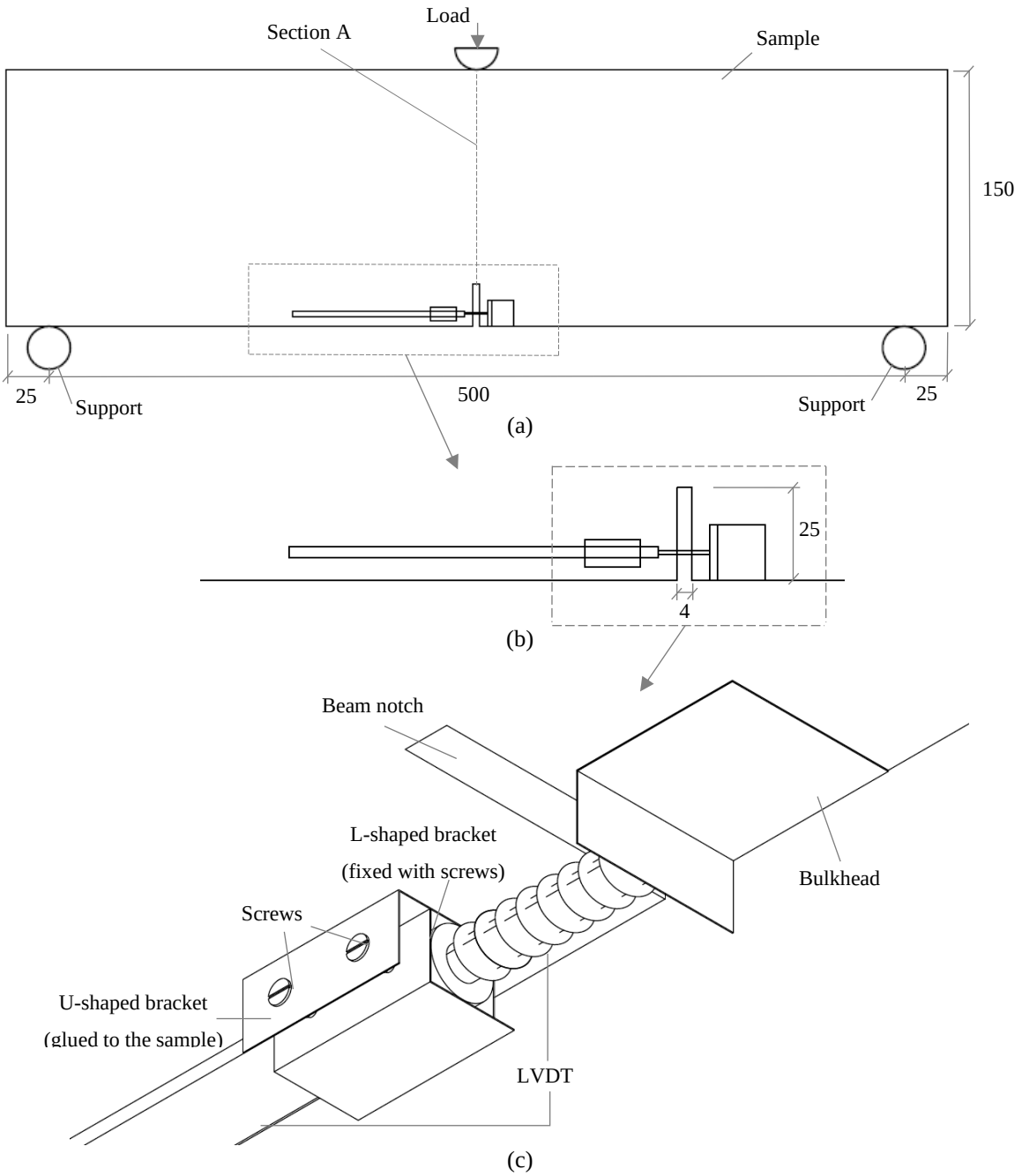


Figure 4.2 – 3PBT setup illustration (dimensions in mm): (a) overview and dimensions, (b) notch dimensions and LVDT position, (c) detail of LVDT positioning scheme.

4.6. Sample Preparation for the MSCBT

The items 4.6.1 to 4.6.8 deal with the procedures performed to obtain samples for performing the MSCBT. Some procedures are repeated to obtain samples for ST and UTT tests, as will be described in the following subsections. The load cells, the LVDTs, the servo-controlled hydraulic-system and the acquisition system used in this test are described in item 4.2.

4.6.1. Details of sample extraction

After bending, the prismatic samples were separated into two parts and presented a shape similar to that shown in Figure 4.3a. The extraction of cores in the region close to the sample separation surface was avoided due to the irregularity of the surface in this region. Some surface irregularities were found on the ends opposite this one due to molding conditions, but this only occurred in a restricted number of samples. Therefore, core extraction for the MSCBT was carried out in the intact region (after 3PBT sample division) of the sample, located between the separation surface and the end, which is opposite to it (Figure 4.3a). The projected position for the extraction of the cylinders is also depicted (Figure 4.3). Therefore, small irregularities at the edge do not influence the quality of the extracted core. A schematic of the extraction process is shown in Figure 4.3b. The resulting cylinders have a diameter of 100 mm and a height corresponding to the width of the sample from which it was extracted, that is, 150 mm.

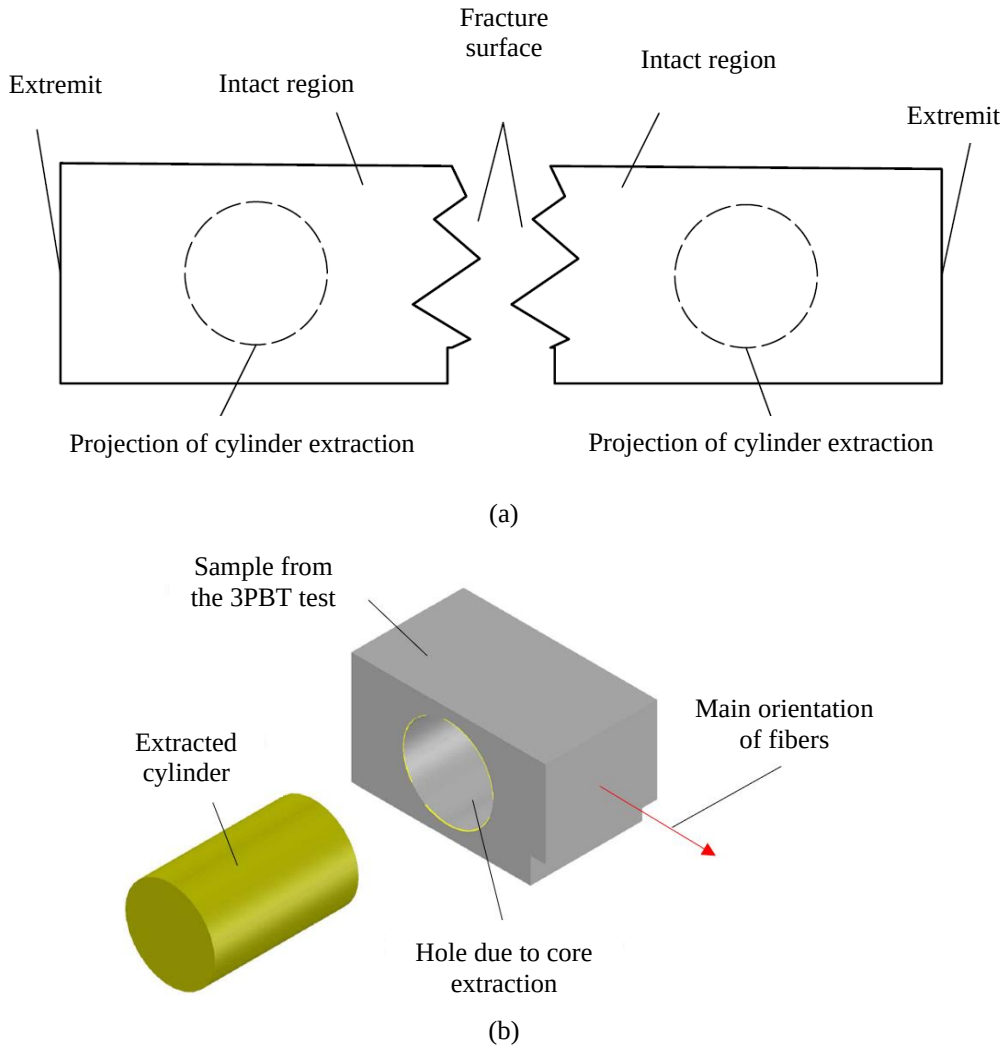


Figure 4.3 – Sample illustration: (a) after bending test and (b) after extraction of cylindrical core for MSCBT

4.6.2. Sample marking

In order to carry out the core extraction process presented in the Figure 4.3b, circular markings were made on the samples with a permanent marker for the proper direction of the core extraction process, as shown in the Figure 4.4. In addition, a straight marking is performed in the predominant direction of the axis of the 3PBT sample, to identify its axis position (y-axis) in relation to the extracted core (cylinder). This last marking is important because all the cuts made are always based on the same position in relation to this axis. The primary path of crack propagation observed in all tested samples aligns with the x-axis. The direction of casting of concrete during casting corresponds to the z-axis.



Figure 4.4 – Samples with markings for extracting cylindrical cores.

4.6.3. Cutting of samples by means of a core drilling machine

A core drilling machine was used to extract cores from samples marked with circles (Figure 4.5). The drill is a piece of equipment used in slabs, which are usually leveled during concreting. In this situation, only the equipment needs to be leveled. In this work, however, the extraction procedure was performed directly on the blocks. Therefore, an additional difficulty was encountered in carrying out the leveling of the block and the drill at the same time.

Furthermore, it was observed that when extraction is performed without additional fixation on the block, a rotational movement of the block occurs due to the large rotation capacity of the equipment. Therefore, it was necessary to find a simple way to stabilize the block during extraction. In the slab extraction procedure, this is not necessary since they are generally robust in their dimensions. A procedure that proved to be sufficiently effective was the positioning of an extra block juxtaposed to the block from which the core will be extracted. The operator positions himself on both blocks and then performs the extraction process.



Figure 4.5 – Core extraction using a drill.

4.6.4. Cutting samples by means of a concrete block cutter

In addition to extracting cores using a drill, straight cuts were made. A block cutter was used to make these cuts. The samples were fixed to the cutter table by means of a C-shaped metallic clamp and in the cylindrical samples, diametric cuts parallel to the axis were made (Figure 4.6). These samples have a width of 150 mm. Part of these samples will be used to perform MSCBT with the same width and another part will be cut again, but this time perpendicular to the axis, to obtain samples with a resulting width of 75 mm for performing MSCBT.



Figure 4.6 – Sample cuts using a block cutter performed on the sample to obtain the semicircular shape.

The Figure 4.7a-f represents the step-by-step process of extracting cores and cuts, as well as the dimensions of the nodes. The x, y and z axes represent the same directions explained in item 4.6.2. The Parts 1 and 2 from the 3PBT (Figure 4.7a) are subjected to the cylinder extraction process, which is represented in Figure 4.7b. Still in relation to this figure, the hatched circle represents the position where the core was extracted and the continuous straight line represents the reference marking for the y axis. According to the direction of continuous straight line marked, a cut (cut 1) is made, following too the direction of the cylinder axis (Figure 4.7c). Only for the 75 mm wide samples, another cut is made (cut 2) in half of the largest dimension of the sample resulting from the previous cut (Figure 4.7d). The Figure 4.7e shows the final sample with the possibility of viewing the notch and Figure 4.7f shows the dimensions of the notch.

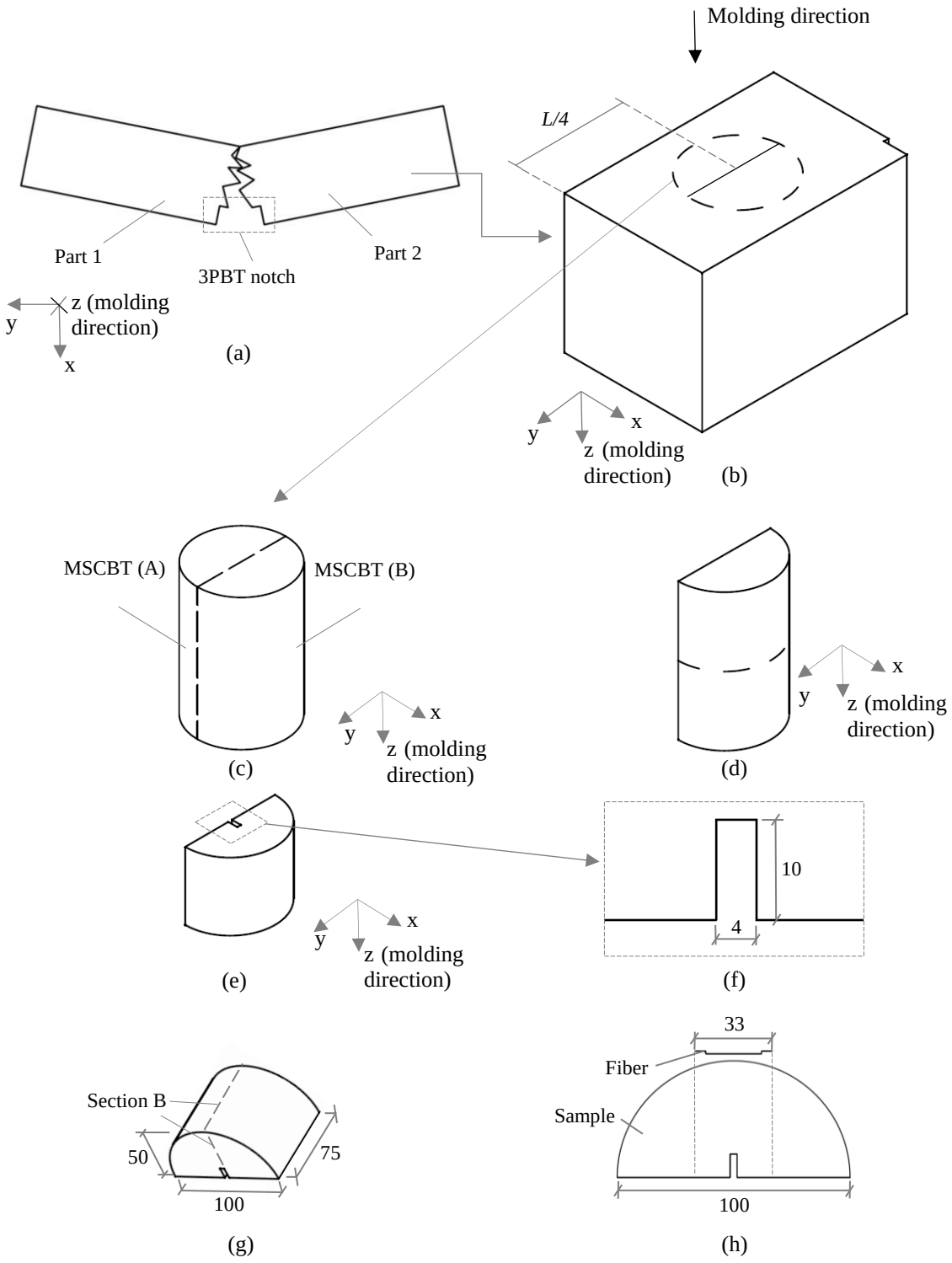


Figure 4.7 – Sample extraction and cutting procedure for MSCBT (dimensions in mm) with x, y and z axis: (a) prismatic 3PBT sample parts 1 and 2, (b) cilynders extraction of 3PBT sample part, (c) extracted cylinder with cut 1 marking, (d) resulting sample after cut 1 with cut marking 2 (performed only for 75 mm wide specimens), (e) notch cut position, (f) enlarged view of notch with dimensions, (g) final dimensions of the sample and (h) Illustration of the fiber dimension in relation to the sample.

The preferred fiber orientation for the MSCBT was selected to align with both the casting direction and the orientation of the specimens extracted for the Uniaxial Tensile Test (UTT), in order to allow a consistent and meaningful comparison between the two testing methods.

The geometry of the MSCBT sample was chosen to be compatible with the core cutting machine, enabling the extraction of specimens from the 3PBT beams with a height of 150 mm. Consequently, a direct comparison between these tests (MSCBT and 3PBT) of concrete obtained under identical molding conditions was possible. The reduced dimensions of the MSCBT sample have the advantage of facilitating test execution. Additionally, the length of the MSCBT sample (100 mm) is approximately three times the length of the fiber (33 mm). Therefore, the amount of cut fibers is minimal (Figure 4.7). It is acknowledged that as the crack propagates, it intersects more cut fibers. However, this does not impact the tensile portion of the test. Moreover, the fracture surface is minimized. Due to the reduced sample geometry, the arching effect occurs before the formation of the first crack, directing a significant portion of the load to the supports.

4.6.5. Notches

After the cuts were made with a concrete block cutting machine, the samples were again marked with a permanent marker to create notches. (Figure 4.8). The notches made consist of shallow cuts to promote a preferential position for the formation of cracks. In the case of this work, the notches had a depth of 10 mm. These cuts were made with a marble saw, given that this equipment is more practical to use and easier to set a single depth. This equipment has a maximum cutting depth of 34 mm and is therefore not suitable for making the cuts mentioned in item 4.6.4 of this text. To fix samples during cutting, a c-clamp with reinforcement on the wooden support was used. (Figure 4.8).



Figure 4.8 – Samples with markings for making notches in semicircular samples for MSCBT with emphasis on fixing with c-clamp metallic claw and marble saw for cutting.

After executing the notches, the samples obtained are presented as shown in Figure 4.9.



Figure 4.9 – Samples after making the notches for MSCBT.

Through this methodology, samples with a length of 100 mm, height of 50 mm and two thicknesses were obtained: 150 mm and 75 mm.

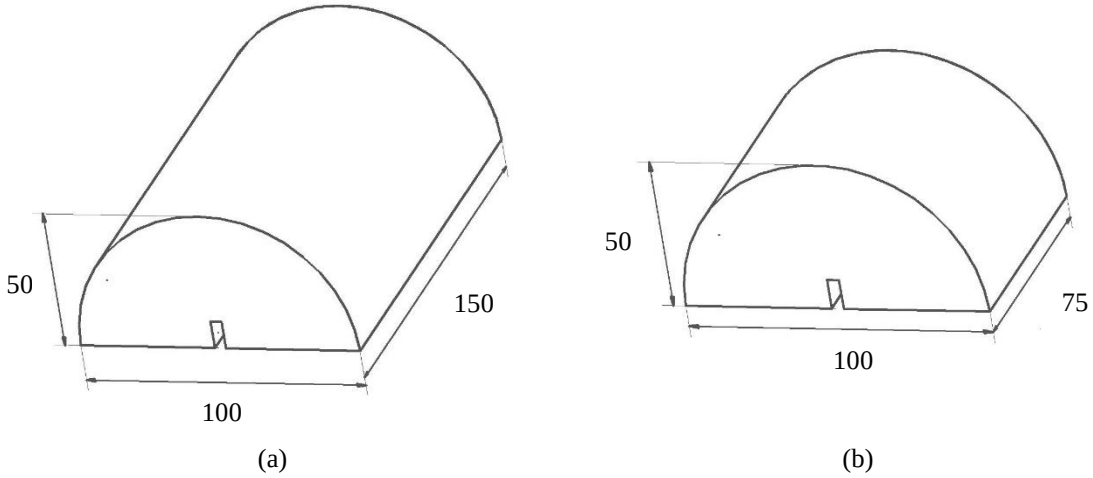


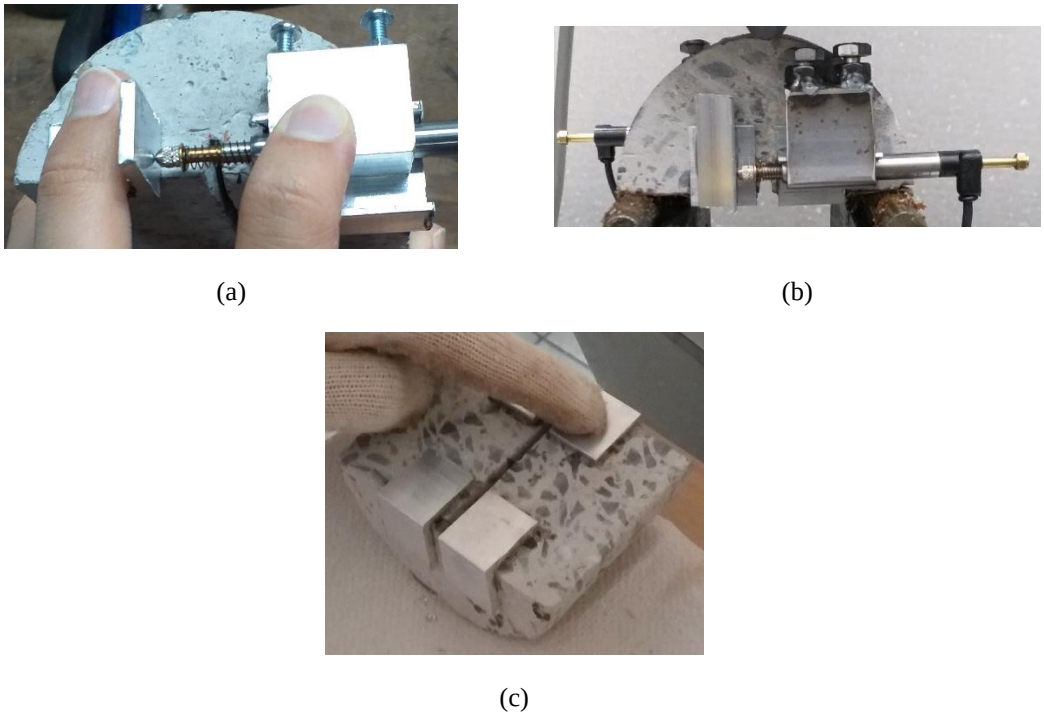
Figure 4.10 – Illustration of specimens for MSCBT after cutting (dimensions in mm): (a) specimen with a thickness of 150 mm and (b) specimen with a thickness of 75 mm

4.6.6. Preparation of plates for fixing transducers

"U" and "L" shaped metal profiles were used to fix the displacement transducers (LVDTs), as described in item 4.2 in the samples. The profiles found on the market are generally 6 meters long, a configuration that is incompatible with the samples in this work, since they have a maximum length of around 150 mm. The plates must also have a size compatible with the LVDT to be positioned.

Therefore, profiles with a width of 2 cm were selected. In the case of the metallic profile in the form of a "U", the positioning of the transducer inside is thick (8 mm) also allowing a space inside for the positioning of iron nuts (one on the inside and another on the outside) and an adjustable length of fixing screws. The profiles were cut in lengths of 2 cm. This dimension proved to be sufficient for measuring the crack mouth opening (Crack Mouth Opening Displacement – CMOD) during the MSCBT for both the undeformed and the deformed configuration. Two cut "U" profiles were selected and a side flap of each one of them was drilled for the passage of screws using a bench drill. The iron nuts (internal and external) were glued around these holes with epoxy glue with high adhesion power in order to speed up the instrumentation of the tests. Since this way, it would not be necessary to manually fix the iron nuts for threading the screws. Initially, aluminum plates and two screws with a diameter of 5 mm were used. This instrumentation is shown in Figure 4.11a. However, it was observed that when tightening the screws, there was a tendency for the plate to slide

in relation to the same due to its reduced medium. In addition, the reduced dimensions of the iron nuts limited the bonding surface, making their fixation difficult. These factors made the fixation process last around twenty minutes. In order to speed up the process, the aluminum plate was replaced by a steel plate and screws with a diameter of 10 mm and hexagons were used. The use of steel plate allowed the tolerance of the iron nuts to them and the diameter of the hexagonal screws were satisfied. In addition, considering the reduced total height of the MSCBT sample (5 cm), the hex keys facilitate the passage of screws. This new form of instrumentation is illustrated in Figure 4.11b.



(a) (b)

(c)

Figure 4.11 – Illustration of fixation plates: (a) aluminum plates glued to the sample passing through the lower end of the sample and plate with threading for screws of 5 mm in diameter; (b) sample ready for testing with steel plates with hexagonal screws of 10 mm in diameter; (c) initial placement of larger plates.

With the exception of the plates on which the bolt nuts were positioned, the cut plates were glued to the specimens. Initially, on each side of each sample, an “L”-shaped plate and a “U”-shaped plate were glued, in order to maintain the same glued area of both (Figure 4.11a). However, it was observed that the use of this procedure could result in contact between fixation plates or transducers and the supports, which could affect the reading of the transducers. In addition, in this design, the gluing area is located on the lateral region of the sample, distributed along the height of the plate. Therefore, the value recorded by the

transducers may differ from the actual CMOD values, since the propagation of cracks occurs in the direction of the sample height. So, it was decided to glue four support plates in an “L” shape on each of the semicircular faces of the sample (Figure 4.11b-c). Initially, four 20 mm wide sheets with 25 mm side flaps are glued together, keeping the glue area only at the bottom of the sample (Figure 24c). Then, over the region of these plates that are on the side of the sample, plates with 30 mm in length and 12 mm side flaps are glued in order to keep one of them in the height direction and the other in the length direction. In sequence, the LVDTs and the plate with threading for the screws are positioned and a combination between the plate with nut/screw and the plate glued to the sample performs the process of fixing the transducers to the samples. The final scheme is shown in Figure 24b.

4.6.7. Preparation of support for the test

For the MSCBT, the same support for the 75 mm and 150 mm wide samples was made using welded solid steel pieces. Two sheets were cut for each arrangement of the following dimensions: 25.4x40x150 mm (type 1) and 25.4x120x150 mm (type 2). In addition, three cylinders of 12.7 mm in diameter and 150 mm in length were cut. A type 2 plate was welded to two type one plates, which in turn were welded to two cylinders, forming the basis for the MSCBTs. For the proper positioning of a load cell on the sample, a support was made for it as follows: a second type 2 plate is welded to another cylinder so that it is centered. To carry out the test, the sample is positioned on the base. The support is positioned over the sample. The load cell is positioned above this support. A schematic is shown in Figure 4.12.

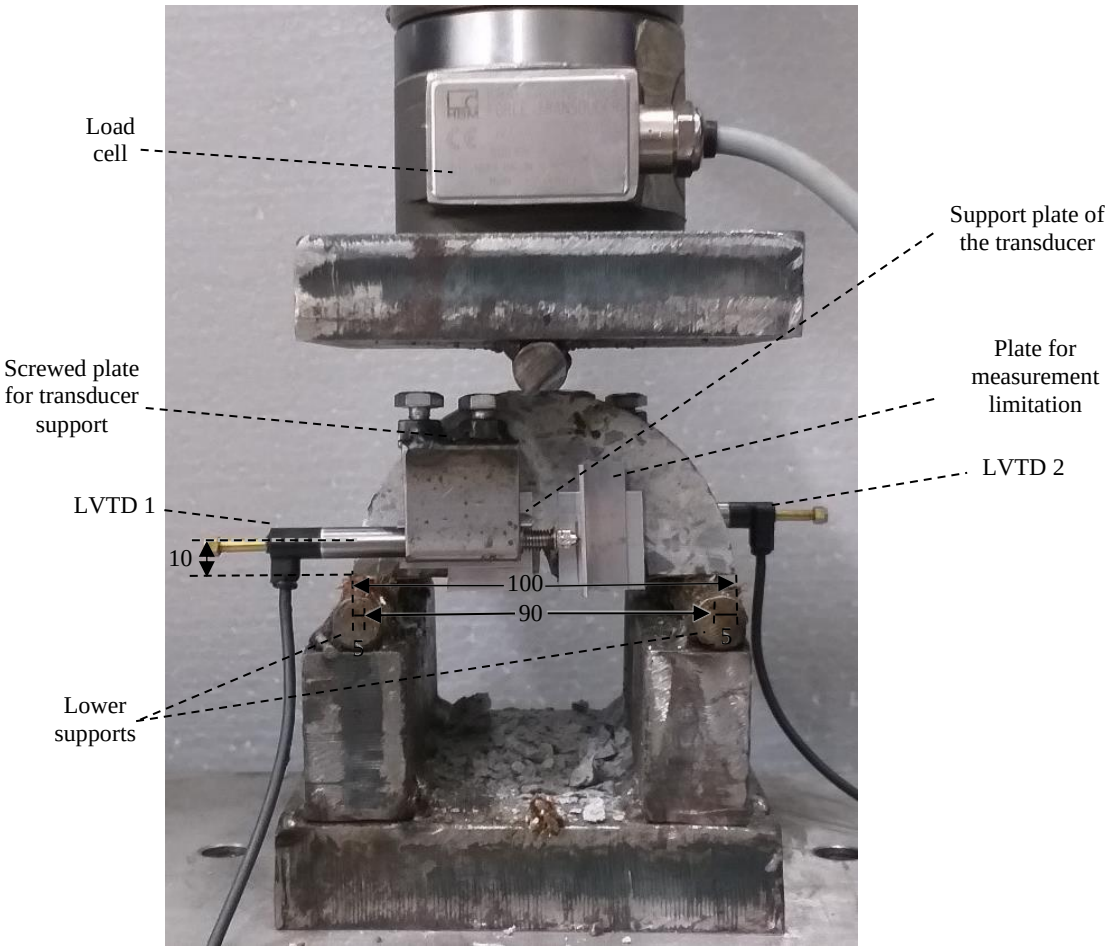


Figure 4.12 – Scheme for performing the MSCBT (dimensions in mm).

To make this condition viable, a Teflon tape was glued to the base of the sample. Grease was placed on the surface of the teflon tape to further minimize the effect of friction. These two elements promote the sliding of the sample when it is requested by horizontal forces, thus idealizing the support of the first type. The total length of the sample is 100 mm and the span is 90 mm. The LVDT is positioned 10 mm measured vertically from the base of the sample. An illustration of these elements is presented in Figure 4.13.

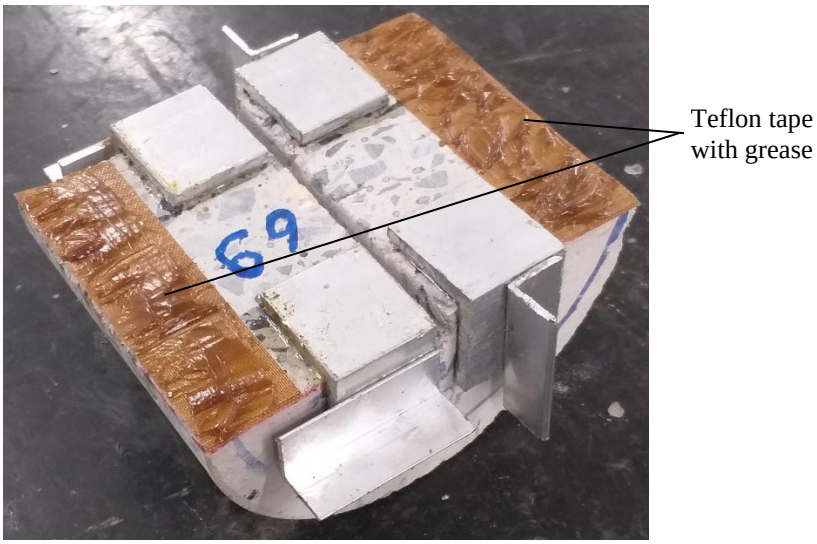


Figure 4.13 – Bottom view of sample for MSCBT highlighting teflon tape and grease placement.

4.6.8. Monitoring throughout the test

The monitoring of displacements during the MSCBT was performed using two linear displacement transducers (LVDT), each one of them positioned on each of the semicircular faces of the tested sample (Figure 4.12). This equipment was positioned transversely to the predominant direction of crack propagation in order to monitor the CMOD throughout the test. The MSCBT were performed with a constant speed of 0.2 mm/min deflection increment. The load was applied in the central region, in the upper part of the sample (Figure 4.12), in order to cause flexion in the sample, which remains in a supported condition.

4.7. Sample preparation for UTT

The items 4.7.1 to 4.7.8 treat with the procedures performed to obtain samples for performing the UTT. Some procedures are the same used to obtain samples for ST and MSCBT, as will be described in the following subsections. With this methodology, 9 samples were obtained to perform the UTT in this work.

4.7.1. Choice of sample extraction position

Among the samples in the after bending state (as explained in item 4.6.1 and showed in Figure 4.3a), those who presented minor imperfections at the ends were selected for cutting and obtaining final samples for the UTT. The location chosen for the extraction of the initial sample was along the edge (Figure 4.2a), according to Salehian (2015). The initial sample

was divided into four parts according to careful marks made on the samples with a permanent marker as described in the next subsection (4.7.2). The sample cutting process is presented in item 4.7.4. The final samples show dimensions 140×70×70 mm Figure 4.14b. Notches were made on two opposite faces of the samples, with a depth of 10 mm and a thickness of 4 mm (Figure 4.14b-c). Due to the known difficulty of performing the UTT, some of the general recommendations for Planas et al. (2007), as shown in the item 3.3.1 of this work. In addition, the methodology has aspects similar to those of Cunha (2010) and Salehian (2015).

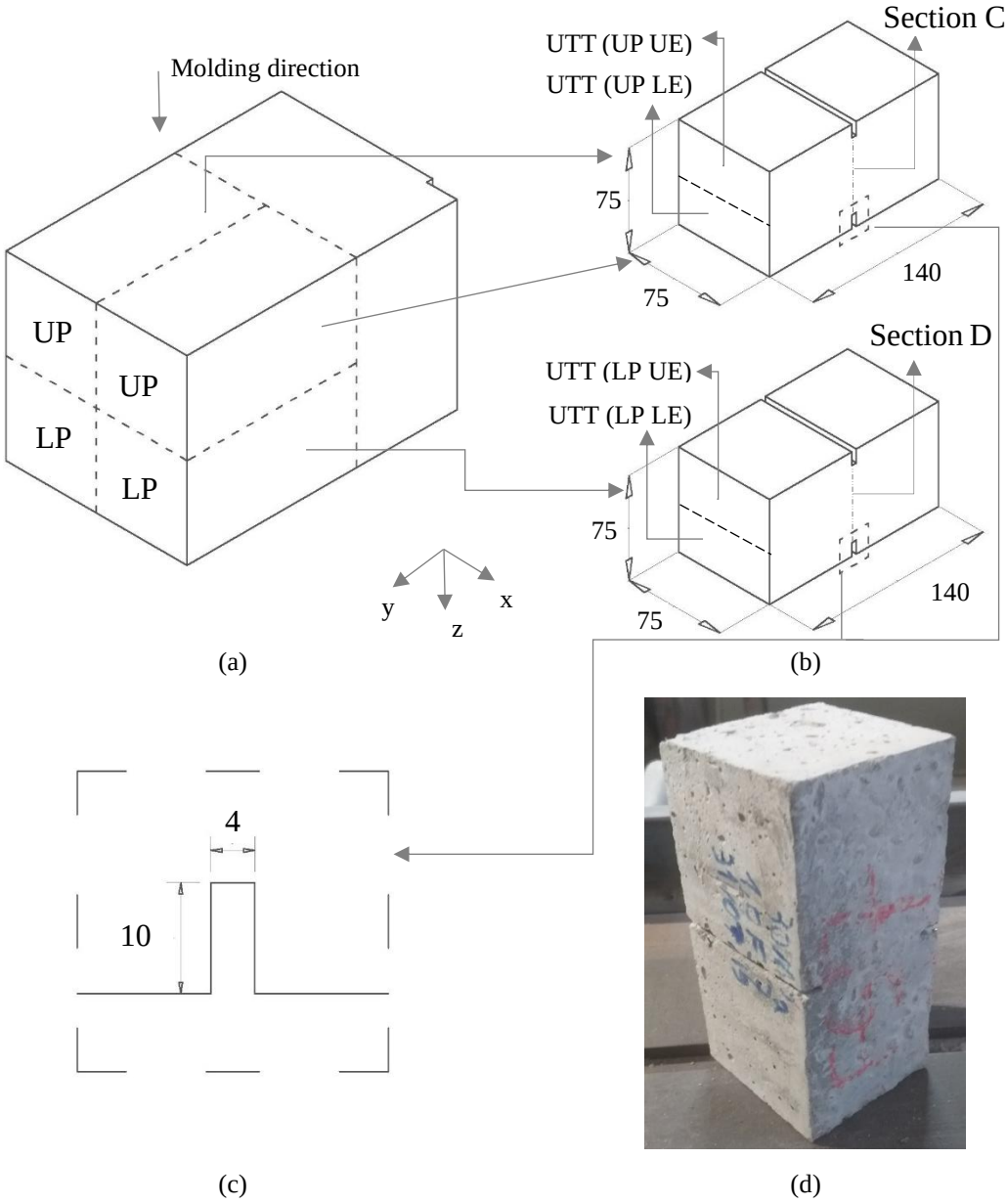


Figure 4.14 – Cutting process to obtain sample for UTT (dimensions in mm): (a) 3PBT half samples scheme, (b) Final UTT sample with dimensions (z-axis represents the molding direction and y-axis represents the

predominant orientation of the fibers), (c) Notch scheme with dimensions, (d) Final sample illustration for UTT.

Care was taken so that the cuts were made in such a way as to keep the final sample always in the same direction, taking as reference (Figure 4.14a-b):

- The direction in which the concrete was poured during molding (z-axis);
- The axis of the 3PBT sample, which corresponds to the axis of the final UTT sample (y-axis);
- The predominant direction of crack propagation during the 3PBT sample test (x-axis).

4.7.2. Sample marking

Before executing the cuts illustrated in Figure 4.14a, marks were made on the samples with a permanent marker for the proper direction of the cut. The shapes of the markings were straight (Figure 4.15) and the extracted samples shown the prismatic shape.



Figure 4.15 – Samples with line markings for core extraction in prismatic shape to obtain samples for UTT.

4.7.3. Cutting of samples by means of a core extraction

As the UTT test was performed on prismatic samples, the core extraction procedure using a drill was not performed to obtain these samples.

4.7.4. Cutting samples by means of a block saw

The prismatic cores were extracted using a block saw for straight cutting, according to Figure 4.16a-c. The samples were fixed to the cutter table by means of a metallic c-clamp (Figure 4.16a-d). First, a perpendicular cut to the axis is performed to separate the fractured sample part to be discarded and maintain the final sample height of 140 mm (Figure 4.16a), which makes the remaining part lighter and easier to handle for the cuts. Next, the second and third cuts are made following the markings on the faces of the sample (Figure 4.16b and Figure 4.16c, respectively).



(a)



(b)



(c)

Figure 4.16 – Cuts in samples using a block saw. (a) first cut of the prismatic sample (discard fractured part of the sample), (b) second cut of the prismatic sample, (c) third cut of the prismatic sample.

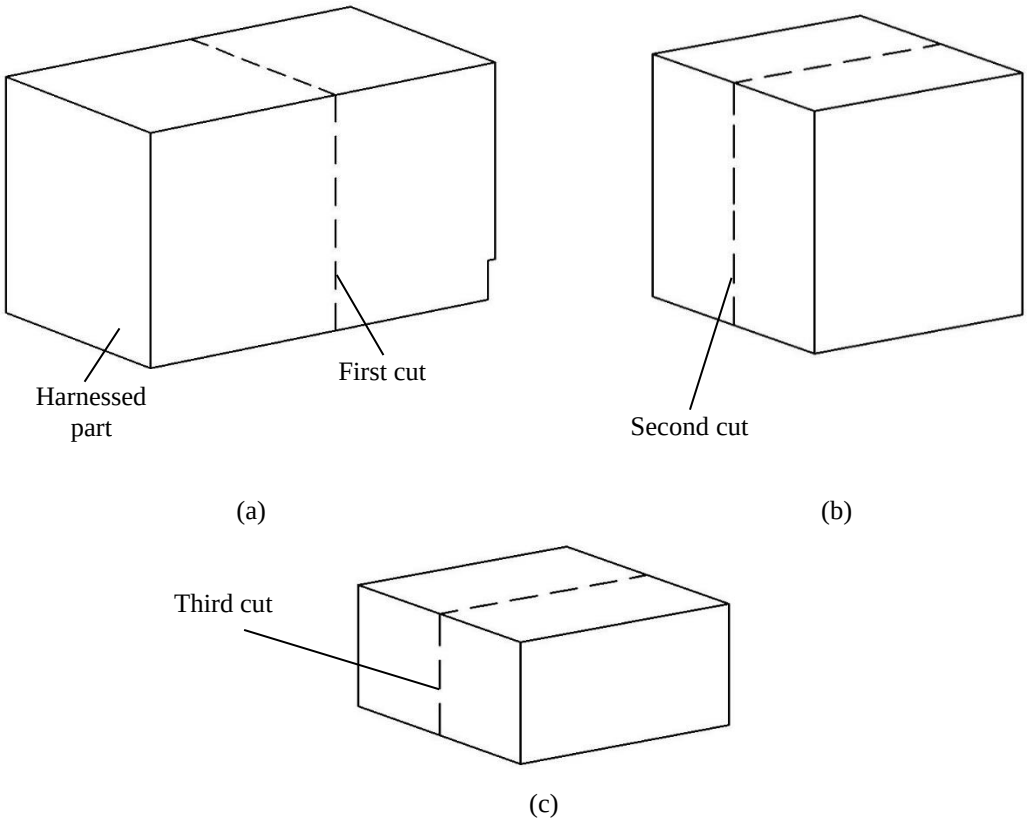


Figure 4.17 – Schematic illustration of the cuts for obtaining a sample for the UTT test: (a) First cut, (b) second cut and (c) third cut.

After the cuts, straight markings are made to make notches on two opposite faces of the sample (Figure 4.18). These markings are carried out according to the positioning in relation to the x, y and z axes shown in the Figure 4.14b.



Figure 4.18 – Sample for UTT with markings for making notches.

4.7.5. Making of notches

After marking the notches (Figure 4.18), the notches are made with a marble saw, as already showed in the Figure 4.8. On the Figure 4.19 the illustration of the sample with the finished notch is shown. In the case of this work, the notches were 10 mm deep and 4 mm wide. The marble saw was used because this equipment is more practical to use and easier to set a single depth.



Figure 4.19 – Prismatic sample with notch for UTT test execution.

4.7.6. Preparation of plates for fixing transducers

In each surface where the notches were implemented, a displacement transducer was strategically placed to observe the Crack Opening Displacement (COD). Unlike the procedure performed for the MSCBT, just two "L"-shaped fixation plates were securely affixed to each surface of the sample. The plates have dimensions as described in the item 4.6.6. One of these plates functioned as a support for the transducer, accompanied by a "U"-shaped plate containing threaded screws (as described in the item 4.6.6), composing the fixation system. The second plate was utilized as a travel limiter during the monitoring process. Specifics regarding these components are visually depicted in Figure 4.20.

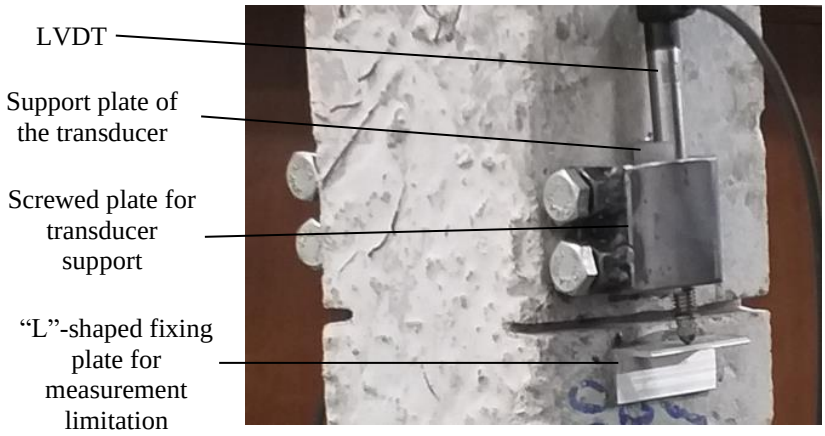
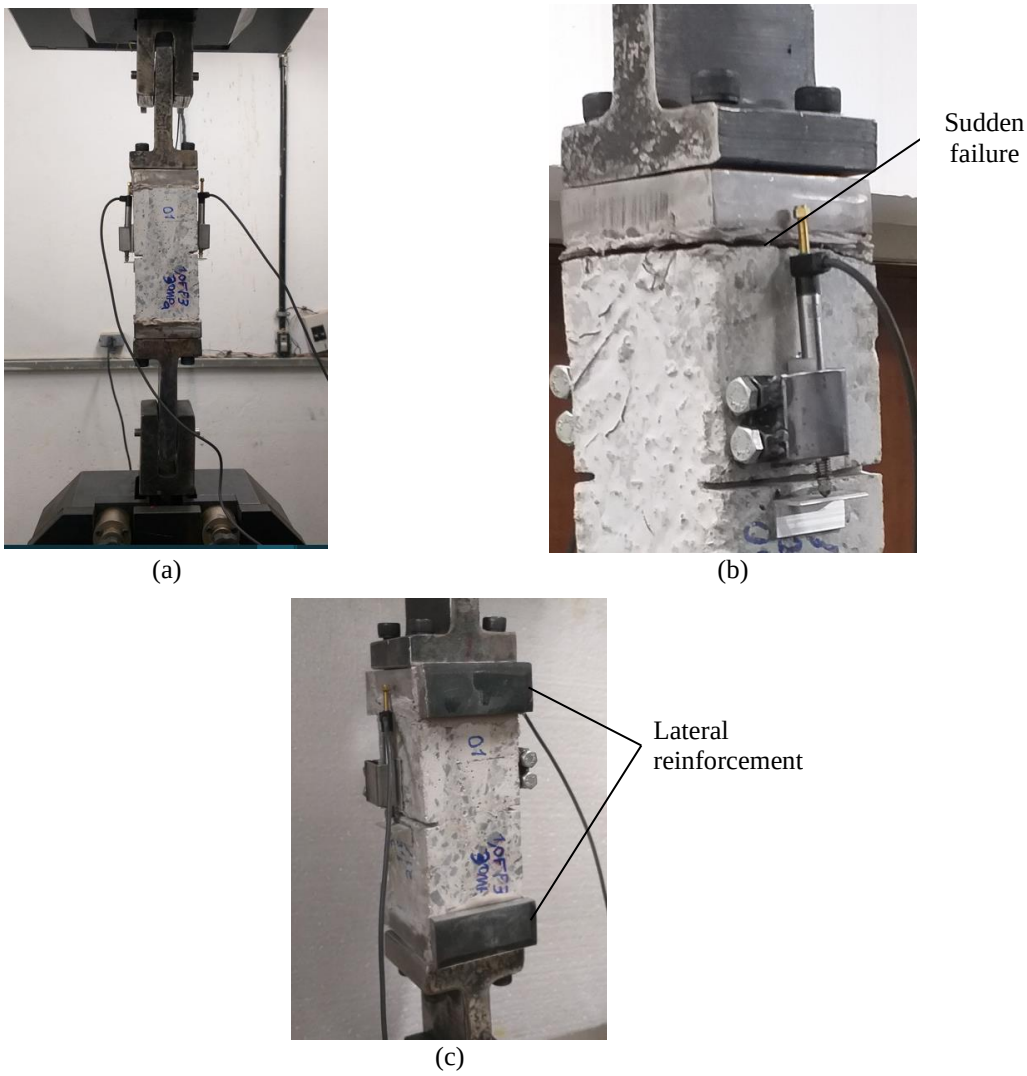


Figure 4.20 – Detail illustration of plates for fixing transducers for monitoring CMOD during UTT test.

4.7.7. Characteristics of the apparatus for carrying out the test

The UTT was conducted utilizing a servo-controlled hydraulic system, as described in item 4.2. Given that the adjustment of the displacement rate was based on the displacement of the load machine piston rather than the LVDT measurement, a displacement rate of 0.03 mm/min was stipulated for displacements up to 3 mm. For displacements exceeding this threshold, a rate of 0.1 mm/min was adopted. This latter rate aligns with the existing literature on the subject (Cunha, 2010; Salehian, 2015; RILEM TC 162-TDF, 2002). The σ-w (where w represents the Crack Opening Displacement, COD) curve was obtained under the assumption of uniform stress distribution across the cross-section of the specimen during the entire test, and the negligible influence of specimen geometry on the stress-crack opening curve (Hillerborg, et al., 1976; Planas, et al., 2007). Consequently, the material properties acquired from the uniaxial tension tests are regarded as accurate representations of the material properties, and the σ-w obtained from these tests can be considered an approximation of the distinctive softening behavior exhibited by SFRSCC. Within each of the tensile grips of the testing apparatus, a hinge mechanism was established by affixing a U-shaped plate to a rectangular plate through welding. The U-shaped plate features a perforation that allows for the insertion of a solid pin, effectively interconnecting it with a T-shaped component in a designated configuration. The T-shape itself incorporates apertures at its base, facilitating the passage of structural screws, which are threaded into rectangular plates. Notably, these plates exhibit a non-threaded surface on the opposite side and are securely bonded to the specimen using a high-adherence epoxy structural adhesive known

as Sikadur 32. The scheme is shown in Figure 4.21a. A detailed schematic of the final test setup can be found in Figure 4.21a-c.



(a) (b) (c)

Figure 4.21 – Illustration of the UTT setup: (a) Perspective of the setup with emphasis on Demonstration without reinforcement of side plates, transducers and fitting in the test machine's claws; (b) Highlight for sudden rupture in the glue region; (c) View of the reinforcement of the side plates

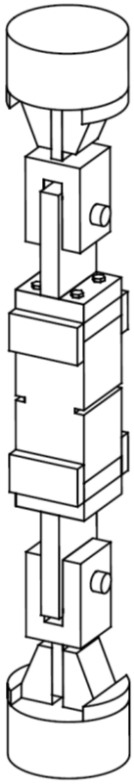
After an initial battery of tests, this initial methodology was found to be inefficient due to a high tendency for sudden rupture in the region close to the glue (Figure 34b). This occurrence prevents adequate monitoring of the COD, since the transducers monitor the opening of cracks only in the notch region.

Therefore, it was decided to use a new methodology to increase the contact surface between the sample and the plates by means of the glue. The execution of a lateral reinforcement was

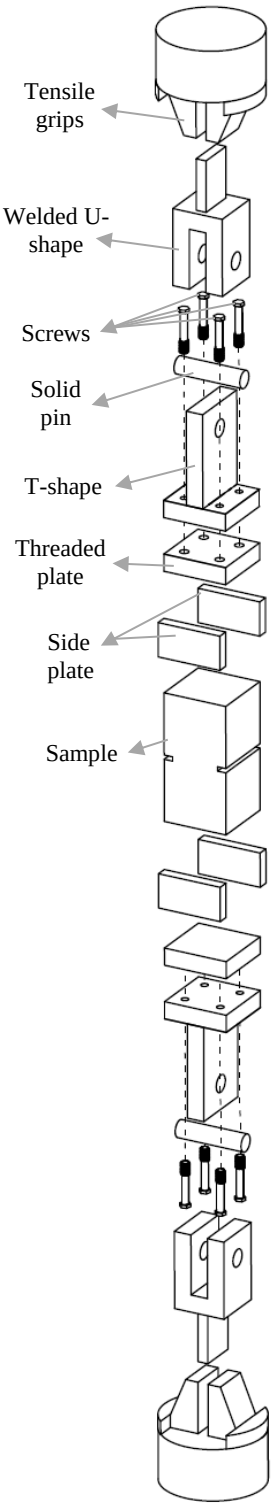
made possible, executed by gluing plates on the faces that do not have transducers (Figure 4.21c). These plates have a height of only 40 mm, a thickness of 12.7 mm and a width of 75 mm, and were positioned at the end of the sample. Therefore, they do not significantly disturb the stress state in the notch region, which is where the COD is monitored. These sheets are glued in such a way as to keep their bonding surface in contact with the threaded sheet (which is glued to the sample at the top and bottom) and with the sample. This last methodology proved to be viable and with a high success rate, since the bonding surface was increased, thus minimizing the occurrence of inadequate failure modes for monitoring the COD. This was the definitive methodology adopted for carrying out the tests in this work. An overview of the sample with this definitive methodology is shown in Figure 4.22a. A schematic with the indication of the names of the parts and details of the fixing brackets are presented in Figure 4.22b. In Figure 4.22c, a schematic of the assembled system is shown.



(a)



(b)



(c)

Figure 4.22 – Illustration of experimental apparatus for performing the UTT: (a) overview, (b) scheme of the assembled system and (c) scheme detailing the parts of the system.

4.7.8. Monitoring throughout the test

The monitoring of displacements during the UTT was carried out by means of two linear displacement transducers (LVDT), each one of them positioned on each of the lateral faces of the tested sample. (Figure 4.21a-c). This equipment was positioned transversely to the predominant direction of crack propagation in order to monitor the CMOD throughout the test. The TD tests were performed at a constant displacement increment of 30 μm/min, which consists of a speed lower than that specified by TC 162-TDF (2002), up to a displacement of 3 mm. After reaching this CMOD value, the rate was increased up to 100 μm/min until the end of the test. The load was applied so that it occurs parallel to the sample, in order to produces tensile to this sample.

4.8. Preparation of samples for the ST

The items 4.6.1 to 4.6.4 deal with the procedures performed to obtain samples for performing the ST. Some procedures are the same used to obtain samples for UTT and/or MSCBT tests, as will be described in the following subsections.

4.8.1. Extraction of sample

The extraction position, the marking and the extraction process itself of the cores for performing the ST were the same as those carried out for the MSCBT. This process was presented in item 4.6.1. The Figure 4.3 shows a schematic of the process.

4.8.2. Sample cutting

“V”-shaped notches (V-notch) were made for the samples used for the ST tests in this work, according to Lameiras (2016). The sample with this notch shown in the Figure 3.12b. This type of notch provides better direction for the crack so that the chances are greater that it will occur entirely in the sample region between the support plates for the transducers. This is the region where COD monitoring can be performed by transducers (Figure 4.23).

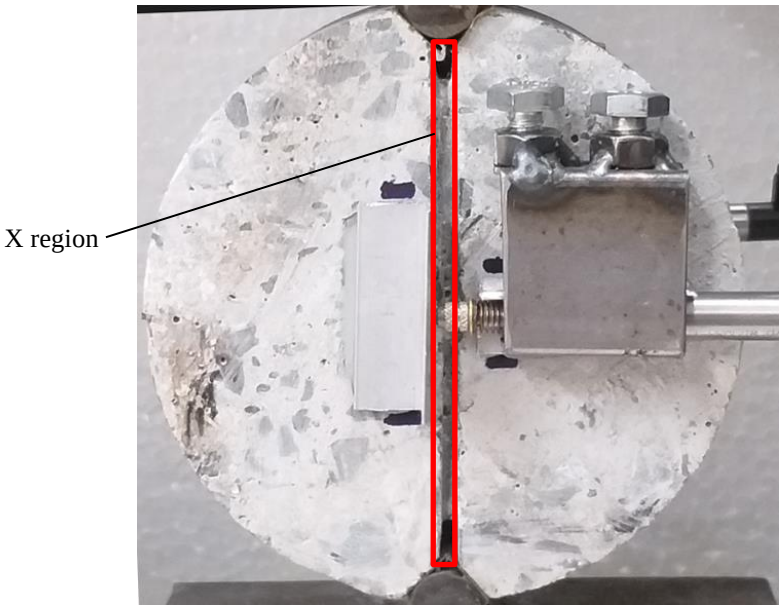


Figure 4.23 – Illustration of the sample for the ST test with emphasis on the sample region between the support plates for the transducers (X region).

A block saw was used to make these cuts for the V-notch. Initially, markings were carefully made on the samples for a better direction of the cuts (Figure 4.24).

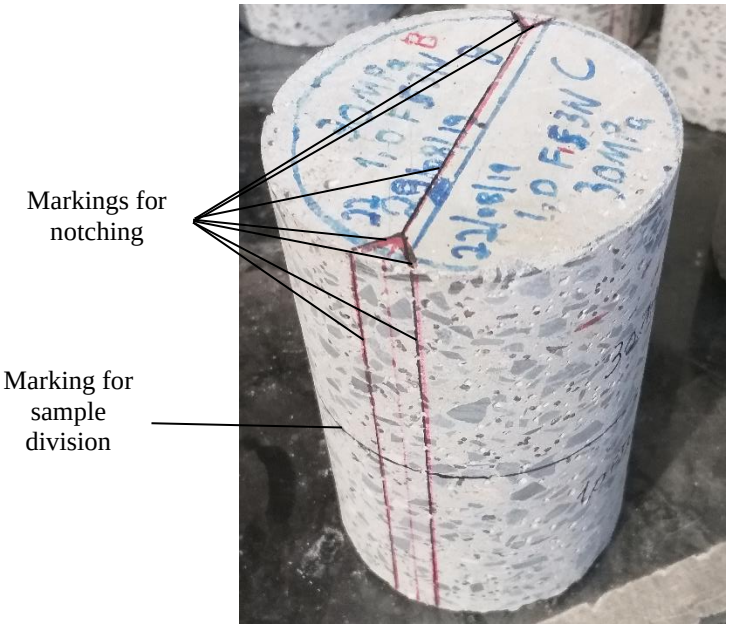


Figure 4.24 – Marking for orientation of cuts in sample for ST test.

Despite the aforementioned advantages, some difficulties were found in the execution of this type of notch. This is due to the cylindrical geometry of the sample, the shape of the notch

(in the form of a “V”) and the fact that the notch is performed on a surface with curvature. There was a need for a flat support surface, both for making the markings and for making the cuts. Therefore, the wooden board of the block cutter needed to be replaced by another one with a more regular surface for a better orientation of the sample. The sample had to be well fixed to the plate to avoid possible rotation of the sample during the execution of the cut. For this, a metallic fastener was welded to the side of the plate. An angle bracket was welded to the other side of the plate to assist in the orientation and fixation of the sample during cutting. In addition, a plate was welded to the base of the equipment in order to control the cutting depth limit of the equipment. The Figure 4.25 illustrates sample attached to the block saw table.



Figure 4.25 – Fixing the sample to the block saw table.

After performing the V-notch, a straight notch similar to that performed in the conventional ST is performed at the base of the V-notch. As this cut had a smaller depth, it was performed with a marble saw. The final sample presented a final form similar to a work in the literature (Lameiras, et al., 2015). The detail of the final sample used in this work with the notches executed is shown schematically in the Figure 3.12c and in illustration in Figure 4.26. In addition to the cuts for making the notches, the samples were also cut at half height perpendicular to the axis (Figure 4.24). Therefore, each 150 mm high core extracted with the drill to carry out ST tests was divided into two (Figure 4.27) so that the final sample is 75 mm high. The sample marking for this type of cut is also shown in the Figure 4.24.



Figure 4.26 – Sample for performing the ST after cuts with emphasis on straight notches.



Figure 4.27 – Samples for carrying out the ST test after performing cuts for notches and after division.

The shape and dimensions of the sample after carrying out each cutting step for the execution of the notches, as well as the schematic representation of these steps, including the dimensions are presented in the Figure 4.28a-d.

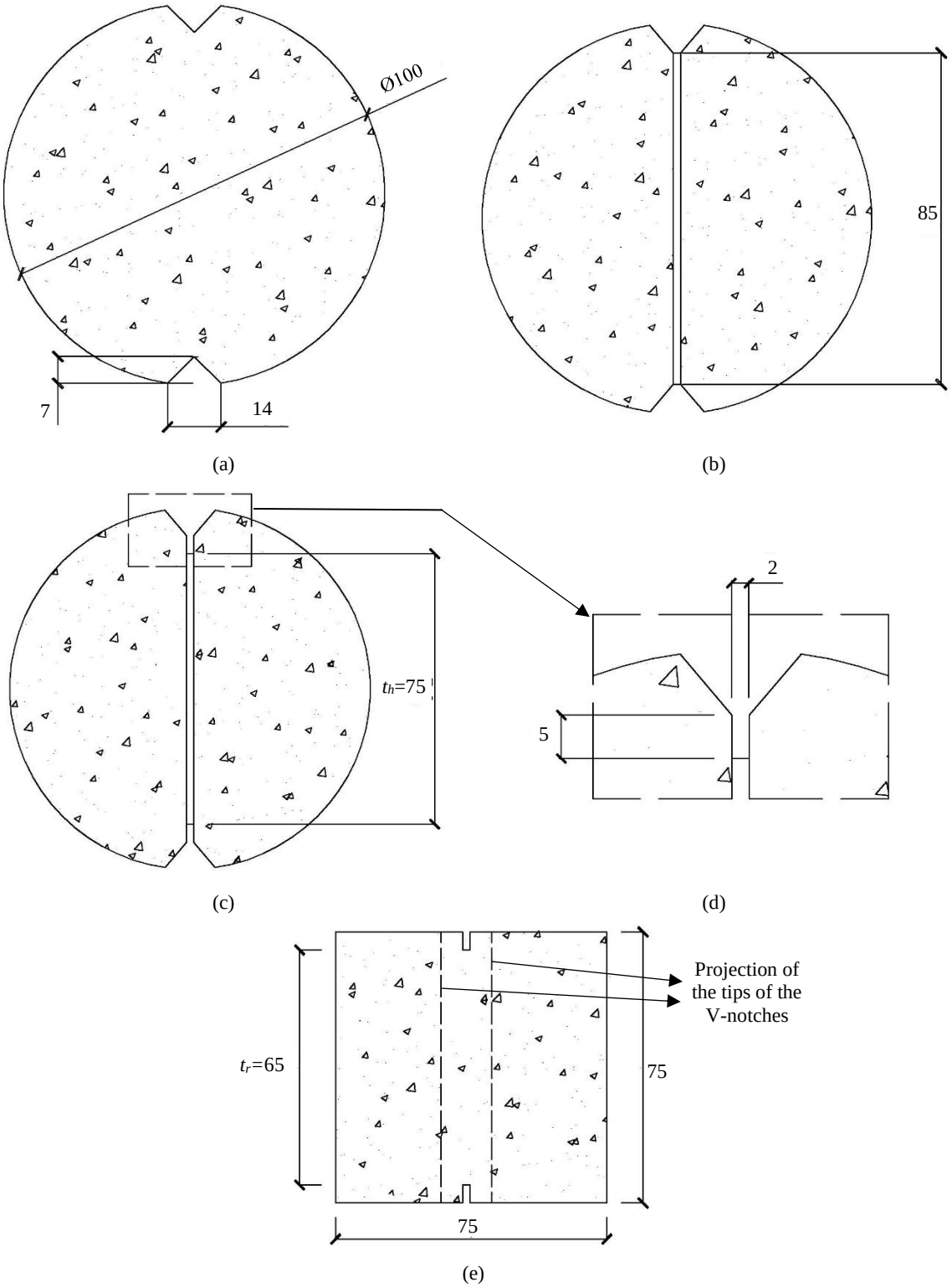


Figure 4.28 – Schemes with dimensions and steps of notch cuts for ST samples (dimensions in mm): (a) first step, (b) second step, (c) third step, (d) detail of the depth and thickness of the straight notch with dimensions and (e) top view of the sample with projection of the tips of the V-notches.

Teflon tape was glued to the surface of the V-notch and then greased to minimize friction on the load-applying surface and promote better crack direction (Figure 4.29).

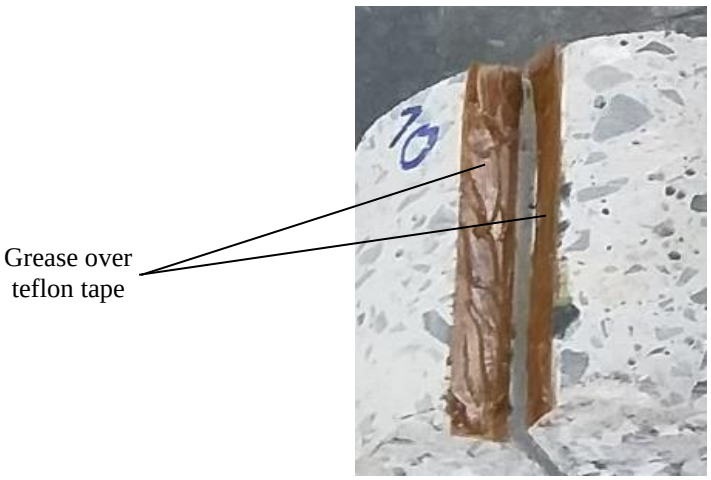


Figure 4.29 – Illustration of a sample for the ST, highlighting the teflon tape glued and grease on its surface.

4.8.3. Preparation of plates for fixing transducers and support system

To fix the transducers, two “L” profiles were glued to each of the circular surfaces of the resulting sample (Figure 4.30) and the profile “U” with threaded screws complement the fixation of the transducers in a similar way to that performed for the UTT, as shown in item 4.7.6. The dimensions of the plates presented in item 4.6.6 proved to be sufficient.

For the support system, two steel plates were cut with the following dimensions: 25.4x75x120 mm (ST1). These plates were welded in their central region to two other rectangular plates with dimensions: 12.7x75x12.7 mm (ST2). These plates were welded, along their largest dimension, to cylinders (ST3) with a diameter of 12.7 mm and a length of 75 mm, resulting in two pieces. During the test, one of them was positioned at the base of the universal press (described in item 4.2) with the cylinder part facing the upper side. The sample is positioned on this piece so that the steel cylinder maintains contact with the greased Teflon tape in the V-notch region. The other piece is positioned over the sample, also keeping the steel cylinder in the V-notch region. On top of this part, the load cell is positioned (described in item 4.2). Above this, the load application point of the press is located. The test scheme is shown in Figure 4.30.

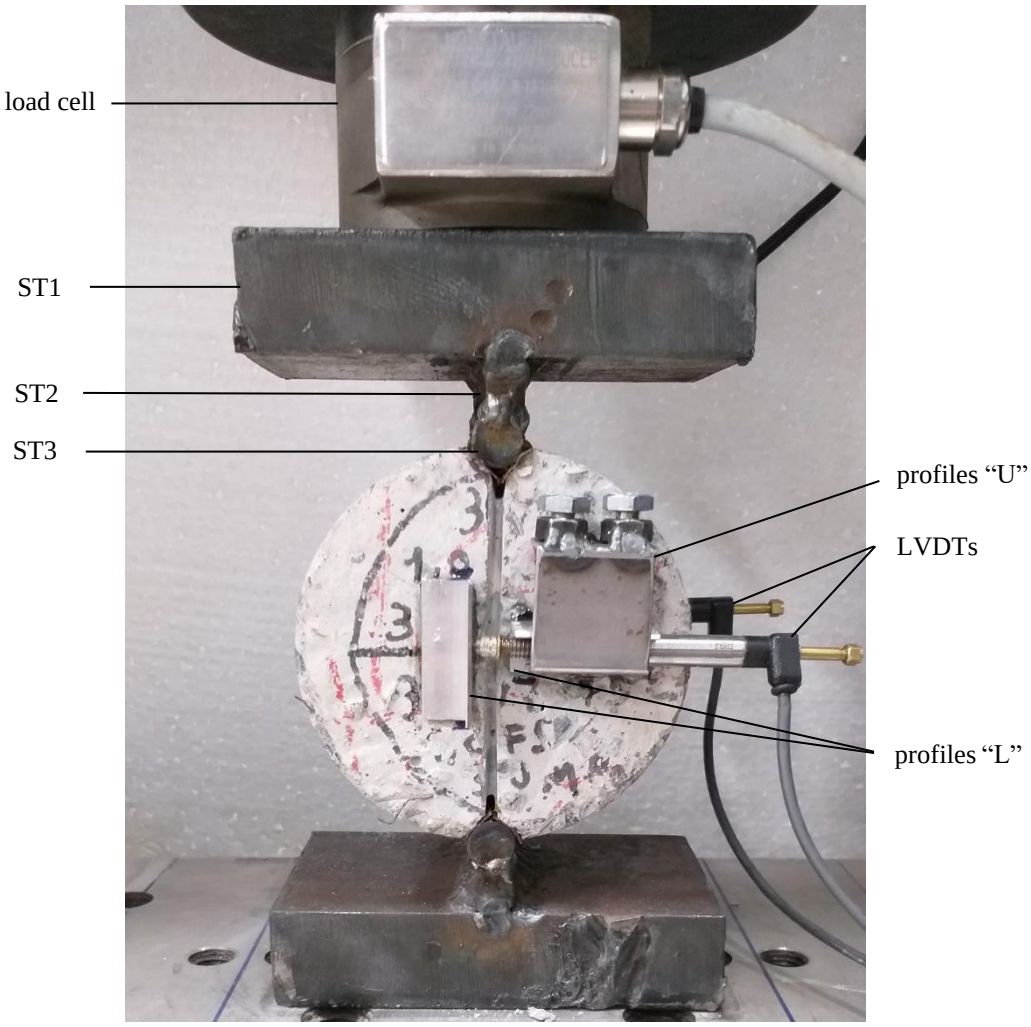


Figure 4.30 – ST test setup.

4.8.4. Monitoring throughout the test

The monitoring of displacements during the ST was carried out by means of two linear displacement transducers (LVDT), each one of them positioned on each of the lateral faces of the tested sample (Figure 4.30). This equipment was positioned transversely to the predominant direction of crack propagation in order to monitor the COD throughout the test.

The compressive load was applied in the central region, at the top of the sample (Figure 4.30), in order to cause the sample to split. The test was performed with a displacement rate of 1.0 μm/s until reaching a displacement of 3 mm and 4.0 μm/s for the rest of the test. This displacement rate was similar to that already used (Lameiras, 2016), being only slightly lower for displacement between 2 and 3 mm, where the author used 2 μm/s.

4.9. IA algorithm for 3PBT (progressive method)

The inverse analysis procedure, which has been extensively examined in existing literature (Mobasher, et al., 2014; Löfgren, et al., 2005; Gao, et al., 2021; Blasi & Leone, 2022; Santos & Forti, 2022; Stephen, et al., 2019; Ding, et al., 2022; Zhang & Ju, 2011; Matos, et al., 2021; Nour, et al., 2015) has limitations. One notable limitation is the considerable computational processing time associated with implementing numerical or analytical models. Therefore simplifications, as proposed in this study, are necessary because the traditional procedure may involve a substantial number of parameter combinations to be computed across all analyzed levels. Additionally, usual procedures typically involve the consideration of the complete *F-CMOD* curve, further contributing to the demanding computational requirements for generating the σ-w (tensile-crack opening displacement) response.

This study introduces a novel and simplified approach to the inverse analysis procedure. In conventional inverse analysis procedures, input data is typically selected randomly or without a specific criterion, resulting in a high computational cost. In contrast, this study determines the input parameters based on the fiber length, which is considered one of the influencing factor on the tensile behavior of FRC (Meng, et al., 2021; Mehta & Monteiro, 2006; Singh, 2016) and also one of the characteristic variations of the MACCAFERRI fibers used in this study. Furthermore, the fiber length is related to the crack opening limit, as very small fibers do not allow for significant crack openings during the test. Moreover, the proposed inverse analysis procedure is conducted progressively, initially determining the parameters that govern the initial segment of the σ-w response. Subsequently, the remaining parameters are adjusted. It is acknowledged that the initial parameters: f_{ct}, σ_1, σ_2 and σ_3 of the σ-w response have a more pronounced graphical impact on the *F-CMOD* curve respectively in the following regions of the *F-CMOD* diagram: before w_1, in the vicinity of w_1, near w_2, and near w_3, as observed graphically by previous research (Lameiras, 2016). The methodology presented in this study enhances computational efficiency by recognizing that the initial parameters of σ-w solely affect a specific portion of the *F-CMOD* curve. Consequently, each set of parameters for the σ-w response curve is adjusted by considering the difference between the experimental *F-CMOD* and the numerical *F-CMOD* up to a given CMOD value. The conventional inverse analysis procedures employed in other studies (Nour, et al., 2015; Salehian, 2015; Salehian & Barros, 2015) are also integrated into the

estimation of the initial parameters. Thus, the proposed approach advocates for a step-wise determination of the parameters, starting with the adjustment of the initial section of the σ-w curve and subsequently calculating the error (between the analytical and experimental response) for only a specific part of the curve and following a similar procedure for other parts of the curve. This process significantly reduces the number of program steps required.

Although the work conducted (Lameiras, 2016) to estimate initial parameters, it has the limitation of relying on a proposal based on the Finite Element Method (FEM). On the other hand, an analytical method for inverse analysis was used (Salehian, 2015); however, no systematic estimation of the initial parameters was established. Hence, this study makes a significant contribution by integrating the strengths of both studies, utilizing an analytical methodology alongside a progressive estimation of initial parameters. This combined approach has the potential to substantially reduce the computational cost associated with inverse analysis.

4.9.1. The Conception of Inverse Analysis

The primary objective of the inverse analysis procedure is to determine the stress values σ_1, σ_2, and σ_3 according to the respective crack openings w_1, w_2 and w_3 (Figure 3.21). These parameters correspond specific points on the σ-w diagram, which is generated through the application of the inverse analysis procedure. These points play a crucial role in defining the post-cracking behavior of fiber-reinforced composites (FRC) under direct tensile loading, exhibiting a quadrilinear response. To initiate the analysis, it is essential to estimate these values as an initial step within the algorithm.

Figure 4.31 depicts a flowchart illustrating the stepwise execution of the inverse analysis procedure. The procedure is carried out incrementally to ascertain the σ-w relationship using a multilinear model. However, this study introduces an alternative approach specifically tailored for a quadrilinear response.

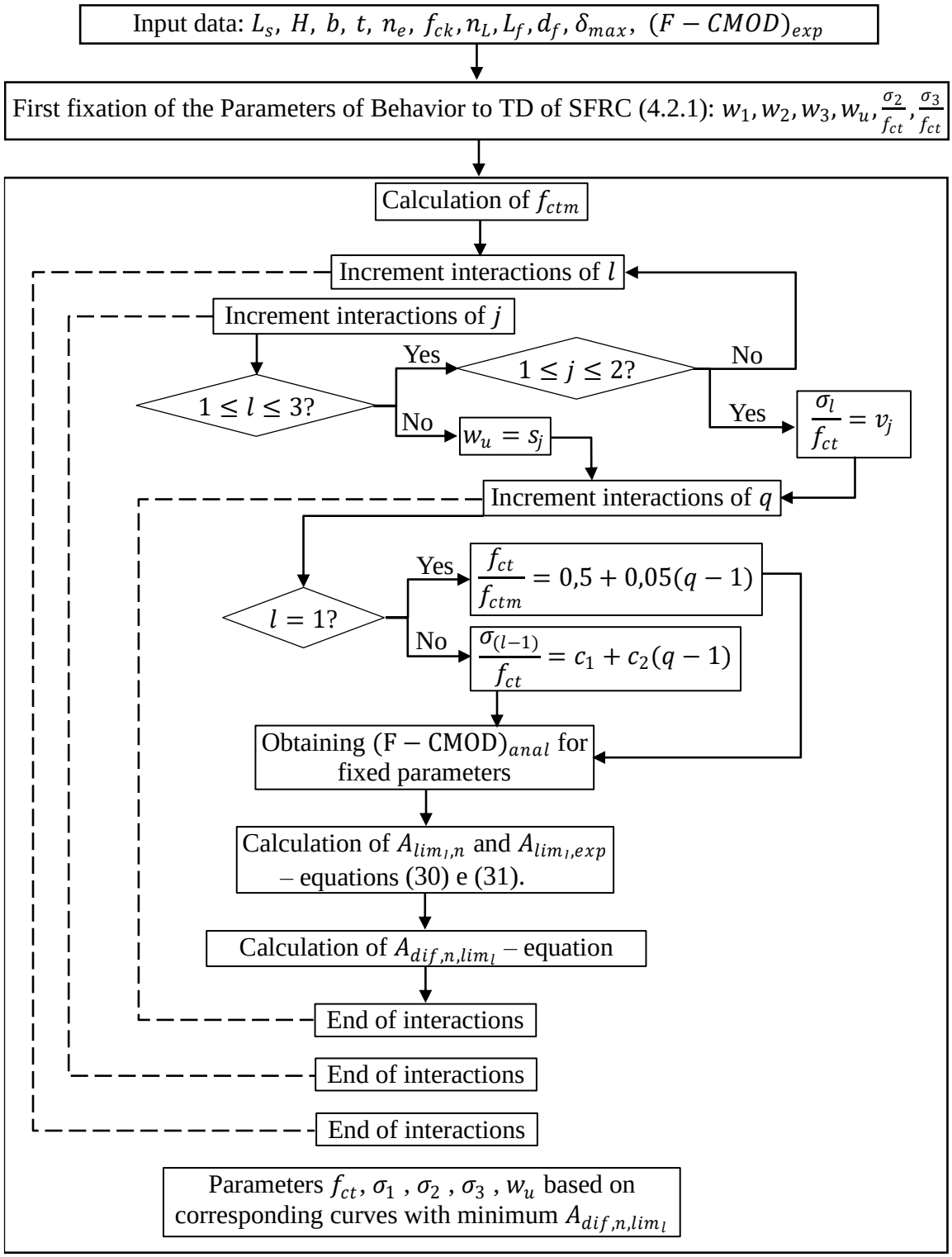


Figure 4.31 - Flowchart detailing the procedure for determining the parameters σ_1, σ_2, σ_3, w_1, w_2, w_3, w_u to perform the inverse analysis procedure.

The program initiates with several input parameter to execute the inverse analysis procedure, outlined as follows:

- Geometric parameters of the sample: span (L_S), height (h), width (b), and notch depth (n_e=H–h), as depicted in Figure 3.19.
- Concrete characteristics: tensile strength (f_{ct}) and compressive strength (f_{ck}) of the fiber-reinforced concrete (FRC) are necessary. The average tensile strength (f_{ctm}), determined according to *fib* Model Code 2010 (fib, 2012).
- Fiber parameters: length (L_f) and diameter (d_f);
- To calculate the error between the analytical and experimental response, the $(F\text{-}CMOD)_{\exp}$ curve (experimental results of 3PBT) must be included as input data. Additionally, the maximum deflection (δ_{max}) should be provided.

In the Figure 4.31, the following notations are employed:

- The index "l" varies from 1 to 4, representing the incremental interactions of the steps in which each variable is fixed.

- The index "j" varies from 1 to 3, denoting the incremental interactions for the determination of s_j, which corresponds to the predetermined values for w_u for the interactions.
- The index "q" varies from 1 to 13, signifying the incremental interactions of the steps in which the values of f_{ct}, σ_1, σ_2, σ_3 are determined.
- v_j represents to the values fixed for the relations σ_1/f_{ct}.
- $A_{lim1,n,i}$ represents the area of the i-th segment of the n-th analytical curve (Figure 4.31).
- $A_{lim1,exp,i}$ represents the area of the i-th segment of the n-th experimental curve (Figure 4.31).
- $A_{dif,n,lim1}$ is the differences between each of the n areas of the analytical response and the experimental response (Figure 4.31).

The estimation of the tensile parameters is conducted, and subsequently, the bending response is analyzed. It is assumed that the parameter set characterizing the tensile behavior of the material yields the minimum error between the analytical and experimental response in the bending behavior. The $(F\text{-}CMOD)_{anal}$ diagrams are obtained analytically using the methodology based on (Salehian, 2015), following the flowchart illustrated in Figure 3.20.

The inverse analysis procedure is then employed to determine the stress-crack opening (σ-w) relationship.

4.9.2. Initial Parameters Determination

This study proposes the implementation of an inverse analysis approach, utilizing a strategic selection of initial parameters that exert a significant influence on the post-cracking behavior of fiber-reinforced composites (FRC). By employing an analytical model, the *F-CMOD* curve is subsequently generated. Thus, this procedure establishes a more rational approach. In the analytical methodology, fracture mechanics parameters related to the tensile behavior of the FRC, such as crack opening (w) and the corresponding stress (σ), are predetermined (as shown in Figure 3.21). Subsequently, the algorithms iterating through a series of steps to identify the parameters that effectively solve the inverse problem and determine the σ-w response, aiming to minimize the error between the analytical and experimental *F-CMOD* response. To mitigate computational burden, a strategy inspired by the previous experience (Lameiras, 2016) is adopted. Initially, certain initial tensile parameters (σ-w) are strategically estimated.

The parameters w_1 and its corresponding σ_1 depend on the fiber content and, in the case of hook-anchored fibers, also on the hook length and curvature (Marcalikova, et al., 2020; Cajka, et al., 2020; Katzer & Domski, 2012; Sucharda, et al., 2017; Alani & Beckett, 2013; Alani & Beckett, 2012). Lameiras (2016) fixed the parameters $w_1=0.2$, $w_2=1.4$ and $w_3=2.5$ *mm*, as explained in item 3.8. Based on this previous experience, the present study adopts a simplified approach to determine these parameters according to the fiber length (L_f). By dividing the fiber length used by Lameiras by a constant, the parameter w_1 adopted by the author is obtained ($L_f/175=0.2$ *mm*$=w_1$). Therefore, it was established that the values would be constant throughout all the inverse analysis procedure, but dependent on the fiber length (L_f). Therefore, w_1 was determined in this study according to equation (4-1):

$$w_1 = \frac{L_f}{175} \tag{4-1}$$

The initial estimate for the w_u was conducted in accordance with L_f value: $w_u=\eta(L_f/4)$. The orientation factor (η) for IURD (isotropic uniform random distribution) of 0.5 was considered because it is commonly used for 3D geometric shape elements (Krenchel, 1975;

Soroushian & Lee, 1990; Cunha, 2010; Stroeven & Hu, 2006). $L_f/4$ is the average statiscal embedded length of a fiber crossing an active crack. However, for SFRSCC, it is anticipated that the value of η may be slightly different because in the self-compacting concrete cast in beams, as carried out in this research, there is a preferential orientation for the fibers. For SFRSCC 3PBT beams, a value between 0.7 and 0.9 has already been determined for η (Cunha, 2010). However, a value of η=0.5 was adopted throughout this study. This leads to the equation (4-2):

$$w_u = \frac{L_f}{8} \tag{4-2}$$

The parameter w_p, according to equation (4-3), was established for the generic representation of the parameters w_2, w_3, ... Still on equation (4-3), $(w_u\text{-}w_1)/(nb\text{-}1)$ is the difference between two consecutive parameters w_p, as illustrated in Figure 4.32. p is the index of w_p and varies from 2 to $nb\text{-}1$. nb represents the number of branches of the diagram shown in the Figure 4.32.

$$w_p = w_1 + \frac{w_u - w_1}{nb - 1} \times (p - 1) \tag{4-3}$$

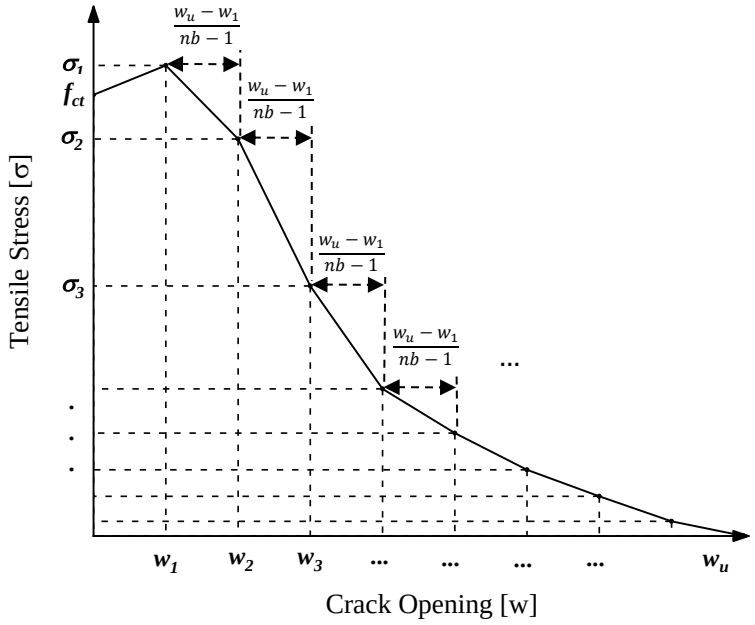


Figure 4.32 - Illustration of the point generalization process for the inverse analysis procedure.

Despite this generalization presented, the quadrilinear model was used in this work, because previous works (Matos, et al., 2021; Frazão, et al., 2022; Salehian & Barros, 2015) were successful to model the post cracking behavior of different types of SFRC. Following this model, the parameter w_1 is determined according equation (4-1) and the parameters w_2 and w_3 are determined according to the equations (4-4) and (4-5), respectively. These equations were easily derived by ensuring that the intervals from w_1 to w_2, from w_2 to w_3, and from w_3 to w_u were equal. The parameter w_u was initially estimated according to equation (4-2), in this step. In this step and in the next step (f_{ct} determination), the following values were set: σ_2/f_{ct}=1.0, σ_3/f_{ct}=0.5.

$$w_2 = w_1 + \frac{w_u - w_1}{3} \tag{4-4}$$

$$w_3 = w_1 + \frac{w_u - w_1}{3} \times 2 \tag{4-5}$$

4.9.3. f_{ct} determination

In the current stage, the algorithm determines the value of tensile strength (f_{ct}). Subsequently, f_{ctm} is calculated following the recommendations provided by *fib* Model Code (2010). The analytical model is then employed to establish the relationship between $\sigma_1/f_{ct}= v_1$, as well as between $\sigma_1/f_{ct}= v_2$. In this step, the variable σ_1/f_{ct} is considered the secondary variable, while f_{ct}/f_{ctm} is the primary variable. The values of the secondary variable (v_1 and v_2) are set at 20% above and below the unit value for this and subsequent steps within the methodology. Specifically, v_1 is assigned a value of 0.8, while v_2 is set to 1.2.

The range chosen for the f_{ct}/f_{ctm} ratio was [0.5-1.1], with variations occurring at each specific step. The step size for variation was chosen as 0.05, which is half of the step size employed in subsequent steps. This decision was based on the observed increased sensitivity of the obtained curves to the f_{ct}/f_{ctm} variable, considering that it is the primary variable in this particular step. The part of this range that is between 0.5 and 0.9 results in f_{ct} values that are very different from f_{ctm}. Since the f_{ctm} is an estimate that should be close to the f_{ct} (fib, 2012). However, this is was considered due to the presence of notches in the specimens, where the maximum stress can be significantly lower than the cracking stress. This is because stresses

tend to concentrate around the notch area (Lameiras, 2016). Comparisons made with previous studies (Nour, et al., 2015; Salehian, 2015; Frazão, 2019) confirmed that the range from 0.9 to 1.1 was also applicable for certain types of concrete. Thus, we have:

$$\frac{f_{ct}}{f_{ctm}} = 0.5 + 0.05(q - 1) \tag{4-6}$$

The range of q is from 1 to 13, as indicated in the flowchart depicted in Figure 4.31.

The subsequent step involves evaluating the obtained curves to identify the one that best corresponds to the initial segment of the diagram. This evaluation is conducted by comparing the experimental $(F\text{-}CMOD)_{exp}$ values with the analytical $(F\text{-}CMOD)_{anal}$ values, as outlined in Section 4.9.7. A graphical representation of this procedure can be observed in Figure 4.33. In this particular case, the first interval is defined as the range between 0 and w_1, as it is heavily influenced by the f_{ct}/f_{ctm} relationship. The solid lines in the graph correspond to the analytical $(F\text{-}CMOD)_{anal}$ values, while the dashed line represents the experimental $(F\text{-}CMOD)_{exp}$ values. Subsequently, the algorithm computes the area beneath each $(F\text{-}CMOD)_{anal}$ curve within this range and compares it with the estimated area beneath the $(F\text{-}CMOD)_{exp}$ curve, as elaborated in Section 4.9.7.

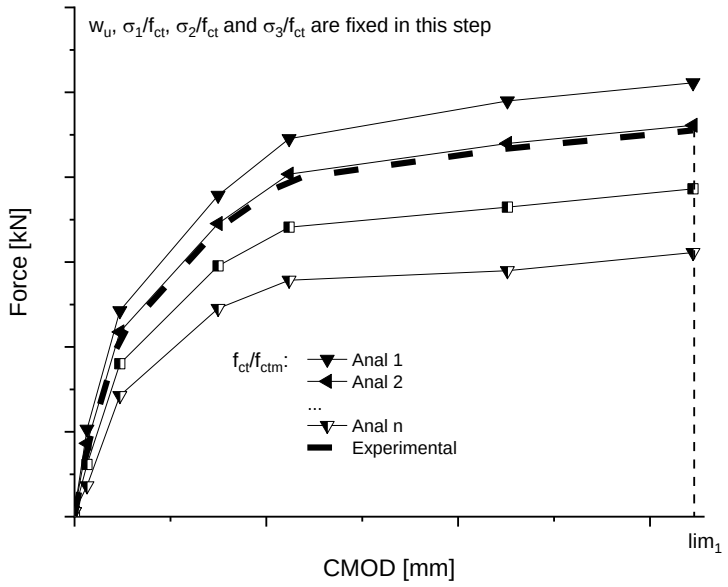


Figure 4.33 – The branch for calculating the area of CMOD between 0 and lim_1.

4.9.4. σ_1 / f_{ct} determination

Besides the initially specified parameters, the ratio f_{ct}/f_{ctm}, which was previously determined because f_{ct} and f_{ctm}, are the values obtained from the previous step. In this stage, interactively, the interval values [0.4–1.6] to σ_1/f_{ct} with a step doubled concerning the previous step (0.1). Consequently, we have the equation (4-7).

$$\frac{\sigma_{(l-1)}}{f_{ct}} = c_1 - c_2(q-1) \tag{4-7}$$

The variable q spans from 1 to 13, as indicated by the flowchart presented in Figure 4.31. In this particular step, the constants c_1=0.4 and c_2=0.1 are employed. The primary variable of interest is the ratio σ_1/f_{ct}, while the secondary variable is σ_2/f_{ct}, which assumes the values v_1 and v_2, as outlined in previous step. By means of this iterative process, the optimal value of σ_1/f_{ct} that best aligns with the obtained curves $(F\text{-}CMOD)_{exp}$ vs. $(F\text{-}CMOD)_{anal}$ is determined considering the smallest error between then. This procedure is depicted in Figure 4.34 as a general illustration. In this context, the selected range is significantly influenced by the σ_1/f_{ct} relationship. The solid lines represent the analytical responses $(F\text{-}CMOD)_{anal}$, while the dashed line represents the experimental response $(F\text{-}CMOD)_{exp}$. Subsequently, the algorithm calculates the area beneath each of the $(F\text{-}CMOD)_{anal}$ curves within this range and compares it with the estimated area under the $(F\text{-}CMOD)_{exp}$ curves, as elaborated in Section 4.7.7.

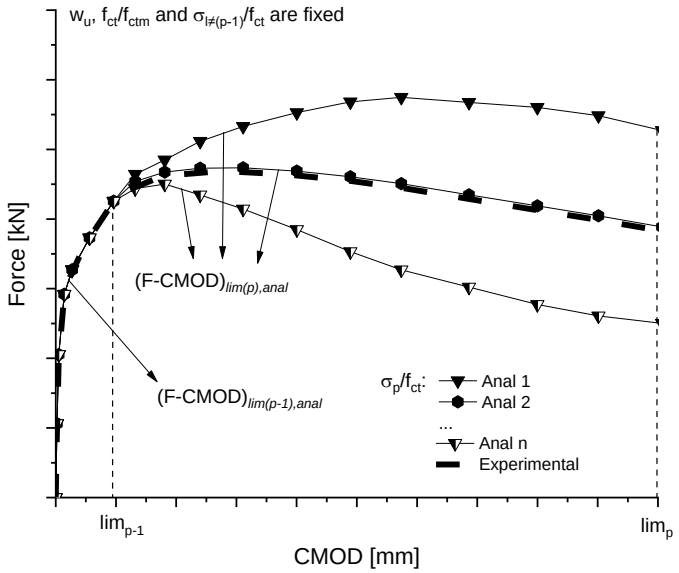


Figure 4.34 – The branches for calculating the areas of CMOD between lim_{p-1} and lim_p are established.

4.9.5. σ_2/f_{ct} determination

A similar procedure as in the previous step is conducted to determine σ_2/f_{ct}. However, in this case, σ_2/f_{ct} becomes the primary variable, while σ_3/f_{ct} serves as the secondary variable, assuming the values v_1 and v_2, as described in Section 4.7.3. The parameter σ_1/f_{ct} is held constant and is the same to the value of the previous step. Moreover, the parameters f_{ct}/f_{ctm} (as per the outcome of Section 4.7.3) and $w_u=L_f/8$ remain fixed in this step. Additionally, the same values of c_1 and c_2 established in the previous step are utilized, and Equation (4-7) can be employed to determine the value of σ_2/f_{ct}.

4.9.6. σ_3/f_{ct} determination

A similar procedure as in the previous step is conducted to determine σ_3/f_{ct}. However, in this case, σ_3/f_{ct} becomes the primary variable. The equation (4-2) was useful as an initial estimate for w_u. The orientation factor (η) for IURD (isotropic uniform random distribution) of 0.5 was considered because it is commonly used for 3D geometric shape elements (Krenchel, 1975; Soroushian & Lee, 1990; Cunha, 2010; Stroeven & Hu, 2006). $L_f/4$ is the average statiscal embedded length of a fiber crossing an active crack. However, for SFRSCC, it is anticipated that the value of η may be slightly different because in the self-compacting concrete cast in beams, as carried out in this research, there is a preferential orientation for the fibers. For SFRSCC 3PBT beams, a value between 0.7 and 0.9 has already been determined for η (Cunha, 2010). Therefore, in the σ_3/f_{ct} determination stage of this work, the algorithm was designed to investigate the following values of w_u: $s_1=L_f/10$, $s_2=L_f/4$, $s_3=L_f/8$. w_u serves as the secondary variable. The parameters f_{ct}/f_{ctm}, σ_1/f_{ct}, and σ_2/f_{ct} remain unchanged from Sections 4.7.3, 4.7.4, and 4.7.5, respectively. After evaluating different values, it was determined that $c_1=0.3$ and $c_2=0.1$ demonstrate greater compatibility between the analytical and experimental responses in this stage. Consequently, σ_3/f_{ct} is computed using Equation (4-7).

4.9.7. Choice of the Best Fit Curve

A routine was developed to calculate the area under curve of the $F-CMOD$ diagram to select the curve that best fits the previous steps. For this, the diagram is divided into nb branches. In this step, it was considered that a considerable number of sections can increase the computational effort and a small number can lead to inaccurate results. Therefore, it was

decided to increase the refinement concerning the number of stretches only in the region close to the peak.

The choice of CMOD limits to calculate the areas that fit each of the parameters is a significant choice assembled in the procedure proposed in this study. It is observed that these parameters would influence the $F-CMOD$ curve more until the limits of CMOD are reached in (Lameiras, 2016). Thus, the limits established by the author were used. Considering the applied quadrilinear model, these limits will be $lim_1=L_f/175$, $lim_2=L_f/70$, $lim_3=L_f/17.5$ and $lim_4=L_f/10$.

An illustration of the area calculation for this procedure is shown in Figures Figure 4.33 and Figure 4.34. For the first step (described in Section 4.9.3), the response areas $(F-CMOD)_{anal}$ (represented by the continuous lines: Anal 1, Anal 2, ... Anal n) and $(F-CMOD)_{exp}$ (represented by the thicker dashed line) are calculated for CMOD between 0 and lim_1. The sections areas of the diagram for each of the n curves, corresponding to analytical solutions and experimental response (exp) are calculated using Equation (4-8):

$$A_{\boldsymbol{lim_1},(n\ ou\ exp),i}=\frac{|F_{i+1}+F_i|\times|CMOD_{i+1}-CMOD_i|}{2} \tag{4-8}$$

To obtain the analytical and experimental curve areas, the sum presented in Equations (4-9) and (4-10) are performed. The areas of the n analytical curves and the experimental curve contained between 0 and lim_1:

$$A_{lim_1,n}=\sum_{i=1}^{m}A_{lim_1,n,i} \tag{4-9}$$

$$A_{lim_1,exp}=\sum_{i=1}^{m}A_{lim_1,exp,i} \tag{4-10}$$

where m is the number of sections, $A_{lim_1,n,i}$ is the area of the i-th section of the n-th analytical curve, and $A_{lim_1,exp,i}$ is the area of the i-th experimental curve section. The procedure is applied for the $(F-CMOD)_{lim_1,anal}$ and $(F-CMOD)_{lim_1,exp}$ response.

The equation (4-11) expression gives the differences between the n areas of the analytical and experimental response:

$$A_{dif,n,lim_1}=\left|A_{lim_1,n}-A_{lim_1,exp}\right| \tag{4-11}$$

Among the n curves, the one with the lowest value of $A_{dif,n}$ corresponds to the analytical response $(F - CMOD)_{lim_1,anal}$ in the region between 0 and lim_1.

The same procedure is performed for the other sections of the diagram: between lim_1 and lim_2, between lim_2 and lim_3, and between lim_3 and lim_4, i.e., between lim_{p-1} and lim_p. An illustration of the procedure is shown in Figure 4.34.

As described, for each determination step of an individual parameter (f_{ct}, σ_1, σ_2, σ_3, w_u), two (or three, in the case of w_u) sets of curves are obtained, one for each secondary parameter. Likewise, for any of these sets, there will be an A_{dif,n,lim_p} corresponding to the secondary parameters. Among these, the algorithm selects the one that presents the slightest difference between the obtained areas of the analytical and experimental response.

At the end of this process, a $(F - CMOD)_{anal}$ curve is obtained. This curve approximates the $(F - CMOD)_{exp}$ response obtained through the 3PBT, as shown in Figure 4.35. For the respective $(F - CMOD)_{anal}$ found, the curve representing the tensile behavior $(\sigma - w)_{anal}$ is obtained.

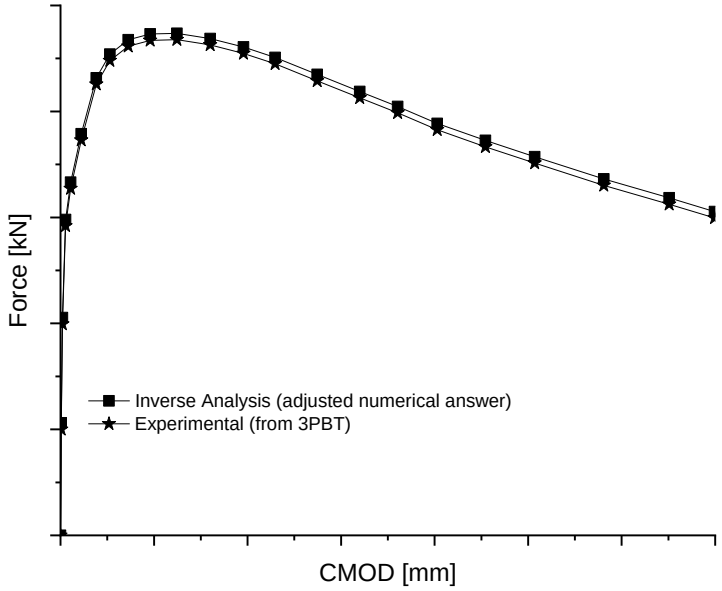


Figure 4.35 – Answer $(F - CMOD)_{anal}$ vs. $(F - CMOD)_{exp}$.

4.9.8. Validation of the Inverse Analysis Procedure

The methodology presented in the previous steps establishes the $(\sigma - w)_{anal}$ diagram. Then, $(\sigma - w)_{anal}$ and $(F - CMOD)_{anal}$ results from inverse analysis performed with experimental validation of four types of FRC from different studies were selected for its

validation. Three of the concretes used in the literature were reinforced with conventional steel fibers (hooked-end - HE) and one with recycled steel fibers with variable end shapes and dimensions. In addition, the concretes presented different types: self-compacting (SFRSCC) and conventional (SFRC), with different f_{ck} values and fiber form factors. These characteristics are described in Table 4.4.

Table 4.4 – Characteristics of the analyzed fibers and concretes.

Author	Denomination	f_{ck} [MPa]	f_{ct} [MPa]	Fiber Length / Diameter [mm/mm]	Fiber	Concrete
(Lameiras, 2016)	SFRSCC B	55	2.23	35/0.55	Steel, HE	SFRSCC
(Salehian, 2015)	C45-f90	45	2.4	35/0.55	Steel, HE	SFRSCC
(Frazão, 2019)	RSFRC1%_2	45	3.34	23/0.22	Recycled	SFRSCC
(Nour, et al., 2015)	FRC60-1	60	3.26	60/0.75	Steel, HE	SFRC

The casting of the samples from the consulted literature (Frazão, 2019; Lameiras, 2016; Nour, et al., 2011; Salehian, 2015) was performed according to the standardization (EN 14651, 2005). All notched beam samples were molded with 600 × 150 × 150 mm^3.

These studies were chosen because they show results of the inverse analysis procedure compatible with the methodology developed in this study for comparison purposes. A similar process of inverse analysis by parts to (Lameiras, 2016) was used, despite using FEM. Therefore, this feature differs from the one in this study, which used an analytical methodology. Thus, it is possible to investigate the difference between FEM and analytical methodology when comparing their results with those developed here.

An analytical methodology has already been used (Salehian, 2015), but the inverse analysis procedure with piecewise process has not been applied. Recycled fibers have been investigated (Frazão, 2019), although most studies have used the usual steel fibers. Distinct from the other consulted authors, an SFRC was used (Nour, et al., 2015), and their model was based on (Zhang & Stang, 1998) and consequently presented some differences in the analytical methodology of (Salehian, 2015).

For all these consulted literatures (Frazão, 2019; Lameiras, 2016; Salehian, 2015; Nour, et al., 2015), the f_{ct} parameter is different. The fibers present different values of L_f and d_f. The f_{ck} variation range (45–60 MPa) contemplates a very usual situation when considering

conventional SFRC structures. Thus, it is possible to compare the methodology of this study in these different situations and use concretes with typical characteristics.

4.10. IA algorithm for MSCBT (preliminary results)

This item deals of a preliminary application of Modified Semi-Circular Bending Test (MSCBT) to determinate the post-cracking behaviour of SFRSCC. Four specimens of concrete C-3 (Table 4.2) underwent testing utilizing the proposed test configuration. Additionally, a methodology was implemented to execute the inverse analysis procedure, utilizing the test results, and thereby estimating the direct tensile behavior of the concrete. The inverse analytical analysis procedure without the progressive method, commonly employed for 3PBT specimens, was utilized for SCBT samples dimensions and employed to estimate the direct tensile behavior of the tested SFRSCC (Salehian, 2015), described in item 3.7. Furthermore, an investigation was conducted to assess the impact of employing two distinct values for the nonlinear hinge length (L_h) within the inverse analysis procedure: $L_{h1}=H/2$ as literature (RILEM TC 162-TDF, 2002; Massicotte, 2004; Ulfkjaer, et al., 1995; Kooiman, 2000; Iyengar, et al., 1998; Pedersen, 1996) and $L_{h2}=H$ (fib, 2012; CNR-DT 204, 2006; Salehian, 2015), respectively as.

L_h	Literatures
$h/2$	RILEM (2002), Massicotte (2004), Ulfkjaer *et al.* (1995), Kooiman (2000), Iyengar *et al.* (1998), Pedersen (1996)
Variable	Olesen (2001)
$2h/3$	AFGC (2002)
h	*fib* (2012), CNR (2006), Salehian (2015)
$2h$	Strack (2008), Montaignac *et al.* (2012)

In this investigation, the sample preparation is according described in item 4.6 and illustrated in Figure 4.7a-f, however the final dimensions of the sample were: width: 150 mm, height: 45 mm, length: 90 mm and span of 80 mm. Therefore, the cut of the Figure 4.7d was not performed. In addition, the notch was approximately 3 mm wide, due to the use of a different disk.

4.11. General Information on the Numerical Simulation Tools Used in this work

Two approaches were employed for numerical simulations. The first consisted of a preliminary numerical simulation for C-12 concrete, conducted for the MSCBT with 75 mm

thick specimens using DIANA software (as described in section 4.12 and results with in section 5.9.2). The second approach did not employ the DIANA software; instead, it involved more comprehensive numerical simulations conducted using the Amaru library in the Julia programming language (described in section 4.13 and with results shown in 5.9.3 and 5.9.4) for C-10, C-11, and C-12 concretes, which were tested through UTT, MSCBT (samples with 75 mm thickness), and 3PBT tests.

4.12. Diana numerical model for MSCBT (simulation)

In this section, the preliminary numerical simulation performed for C-12 concrete in the context of the MSCBT using 75 mm thick specimens and the DIANA software is described. A numerical framework employing the Finite Element Method (FEM) is utilized to corroborate the inverse analysis procedure. The software is employed to delineate the configuration of the notched MSCBT specimen geometry and its corresponding supports. Subsequently, the ensuing data was employed as the input:

- The concrete characteristics: While it is customary to employ the value of 0.2 for the Poisson ratio (ν) (Hosseini, et al., 2023; Ahmad & Lagoudas, 1991; Doyon-Barbant & Charron, 2018; Huo, et al., 2021), the fib Model Code 2010 (fib, 2012) specifies that this parameter may range from 0.14 to 0.26. It has already been shown that the fiber content exerts an influence on the Poisson ratio, furthermore a value of 0.15 was obtained (Carrillo, et al., 2019) for a fiber content close to that used in this study (1%). Therefore, the same value for Poisson ratio was utilized in this study. The same value was employed for the software tutorial used in this work (DIANA FEA, 2022). The Young's Modulus (E_c) of 36,267.6 N/mm² was determined according the equation (3-13) from standardization (fib, 2012). The crack orientation was stabilished according a specific methodology (fib, 2012; DIANA FEA, 2022). Axial compression tests were performed to determine the average compressive strength: 35 MPa.
- For modeling purposes, the tested sample is regarded as a composite. Thus, the fiber and concrete matrix elements are treated as a single entity, requiring considerations for both tensile and compressive behavior. The constitutive model Total Strain Crack (Vecchio & Collins, 1993; Selby & Vecchio, 1995; DIANA FEA, 2022) was

employed for the compression behavior. The tensile behavior of SFRSCC was modeled by inputting the average Stress (σ) vs. Crack Opening Displacement (COD) obtained experimentally from the UTT on the finite element software. The tensile curve taken as a reference for the model was in accordance with the *fib* Model Code 2010 (fib, 2012). The Govindjee's projection method (Govindjee, et al., 1995; DIANA FEA, 2022) was used for crack bandwidth specification.

- For w_u, a slightly higher value than the estimate of the equation (4-2) is expected in the case of self-compacting concrete, as discussed in the section 4.9.6. Consequently, a value of 6 mm was employed for numerical simulation, as it aligns closely with the average of values utilized in the inverse analysis of this study ($L_f/10$, $L_f/8$, $L_f/4$) and is consistent with values reported in the literature (Lameiras, 2016).
- The compression fracture energy is an input parameter in the numerical model employed. The Stress vs. displacement relationship in compression was estimated in accordance with the constitutive relationships of *fib* Model Code (fib, 2012) according to equation (4-12), for $|\varepsilon_c| < |\varepsilon_{c\,lim}|$. Where ε_c is the compression strain, $\varepsilon_{c\,lim}$ is the ultimate strain, $\eta=E_{ci}/E_{c1}$, $k=\varepsilon_c/\varepsilon_{c1}$, ε_{c1} is the strain at maximum compressive stress, E_{c1} is the secant modulus from the origin to the peak compressive stress.

$$\sigma_c = -\frac{f_{cm}(k\eta - \eta)}{[1 + (k-2)\eta]} \tag{4-12}$$

- The steel Young's Modulus (E_s) on the supports: 200,000 N/mm².

In a finite element model, mesh convergence criteria are essential to ensure that the results obtained are not dependent on the discretization of the domain, that is, that they are independent of the size and shape of the mesh elements. These criteria are established to assess whether the numerical solution approaches the true solution as the mesh is refined.

The simulations conducted using the DIANA software are preliminary in this study. Since the results obtained using mesh recommendations from the literature (DIANA FEA, 2022) were satisfactory, a more in-depth analysis of mesh refinement and convergence criteria was not carried out within this approach. However, the approach involving the Julia

programming language and the Amaru library was conducted using more refined convergence criteria.

To ensure the adequacy of the mesh, a decision was made to employ a finer mesh in the specific region anticipated for crack propagation. In other words, in the vicinity of the central portion of the sample span, specifically within the region extending from the apex of the notch to the highest point of the sample. The total number of elements used for the mesh was 756. A mesh size of 2 mm was selected for the discretization of the sample geometry. The chosen mesh type is Hexa/Quad. In the initial support, solely the vertical displacement was constrained, while at the second support, both horizontal and vertical displacements were constrained. Furthermore, rotation is set to free on both supports. The mesh illustration is showed in Figure 4.36. A configuration of eight nodes per element was implemented. A mesh size of 0.5 mm was adopted for the mid-span boundary (20% of the central length of the specimen, which corresponds to 25 mm), which corresponds to the region within the sample where crack propagation is anticipated. These values were chosen in proportion to those suggested (DIANA FEA, 2022), taking into consideration the dimensions of the sample utilized in this study.

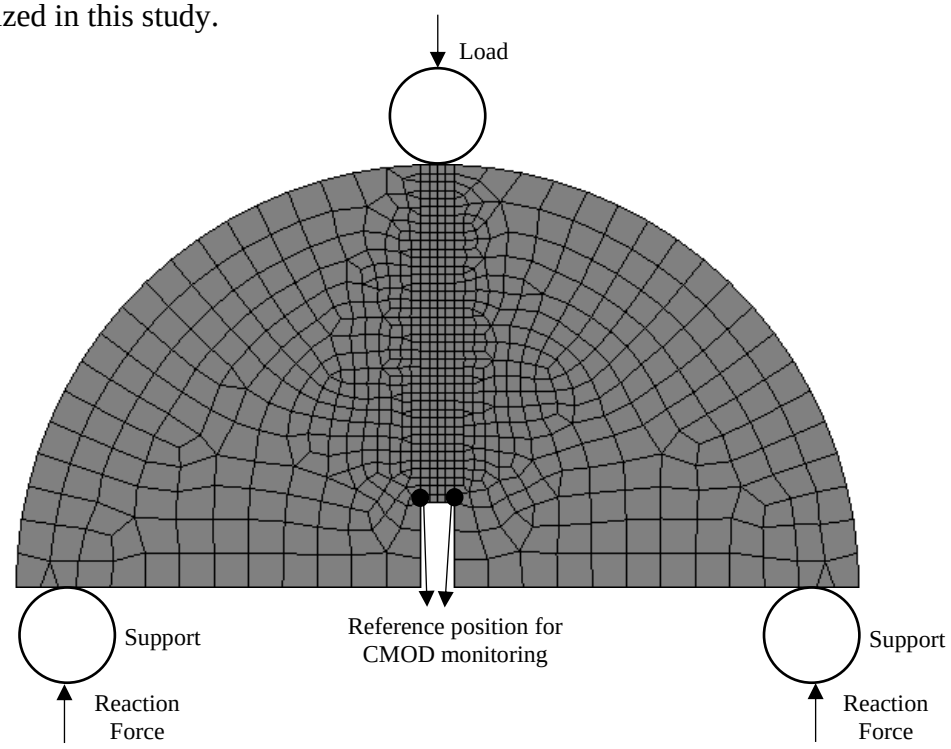
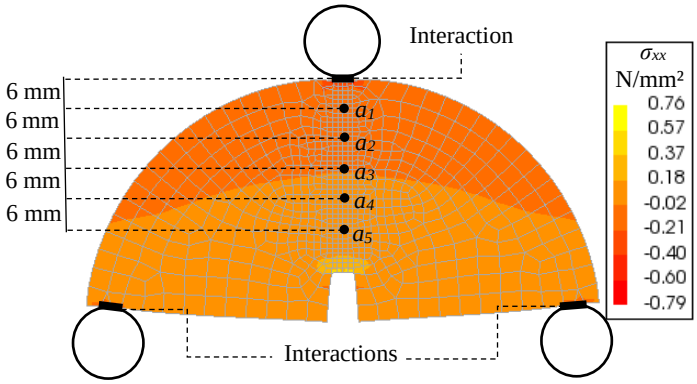
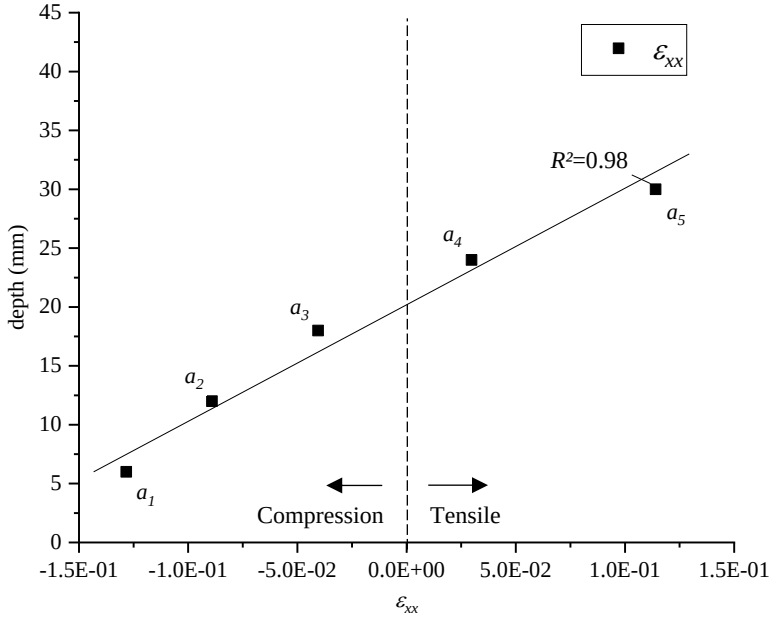


Figure 4.36 – Mesh used to the FEM-based model to simulate the MSCBT with the two notches marked with circles which was taken as a reference for determining the CMOD.

The deformed configuration of the sample and the stress distribution is shown in Figure 4.37a for a load equal to 44 N. This result is quite compatible with the model presented in the literature (DIANA FEA, 2022). The points (a_1, a_2, a_3, a_4, and a_5) are at distances of 6, 12, 18, 24 and 30 mm from the top of the sample, respectively. The deformations (ε_{xx}) vs. the depth of these points are shown graphically in Figure 4.37b. It is observed that the increase in ε_{xx} deformations varies almost linearly (R^2=0.98) according to the elevation of each point. This means that the Euler-Bernoulli theory is applicable for this stress level. Furthermore, compression is observed in the at the top edge of the sample and tensile in the notched region. Therefore, the use of the progressive inverse analysis model presented in this work is quite suitable for MSCBT, since this model is usually used for 3PBT.



(a)



(b)

Figure 4.37 – Results of linear elastic model corresponding to a load equal to 44 N: (a) Color map of the strain (ε_{xx}) distribution in the specimen (dimensions in mm); (b) Strain distribution along the notched section (a_1 *to* a_5) section.

During the analysis stage, the Newton-Raphson iterative method was employed. The processing steps for the model were determined based on incremental displacements (DIANA FEA, 2022). A number of 200 initial steps were performed, each with an increment of 0.0005 mm. Next, the following increments are adopted for the respective steps: 100 steps each with an increment of 0.001 mm, 200 steps each with an increment of 0.005 mm, 100 steps each with an increment of 0.03 mm.

The model employed to conduct the analysis of the MSCBT used the Finite Element Method (FEM) software. According to the symbology used in the Figure 3.19, which deals with the 3PBT, the following dimensions are established for the MSCBT in the FEM model: L_s=90 mm, h=40 mm, H=50 mm and b=75 mm.

The constituent materials used in the composition of the concrete used in this study are shown in Table 4.1 for fiber type ST-33/44, hooked-end, with content of 1% (volume) and concrete of 40 MPa were used in this work. This type of fiber was chosen because its length is in the range of 30 to 35 mm, which is recommended for Shotcrete applications (Arcelor Mittal, 2010). The nominal Young's modulus and nominal unit weight of the fibers are 210 MPa and 7850 kg/m³, respectively.

4.13. Numerical model for MSCBT using the Amaru library

The following section describes the characteristics of the numerical model used with the Amaru library in this study.

The numerical analysis of quasi-brittle materials like concrete requires a suitable model to capture both deformation and crack propagation. This study employs a continuous–discontinuous approach, integrating linear bulk elements with nonlinear cohesive elements (Durand & Silva, 2019) which will be described in this section. Since the formulation of cohesive finite elements is well established (Durand & Silva, 2021; Durand & Silva, 2019; Beer, 1985; Plesha, et al., 1989; Hird & Kwok, 1989; Roy & Dodds, 2001; Jin, et al., 2003). A two-dimensional version employing a Coulomb-based plasticity model was also presented in another study (Durand & Silva, 2021). Cohesive elements need a complex constitutive model capable of accurately predicting crack formation and propagation, as well as the corresponding openings.

4.13.1. Cohesive Elements

In the Amaru library employed in this study, the cohesive element formulation is based on the isoparametric element, which will be detailed in this section. A schematic representation of a zero-thickness joint element with four nodes and a length of b is illustrated in Figure 3.1.

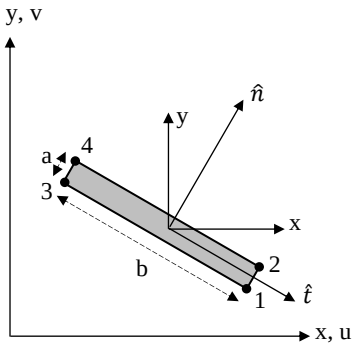


Figure 4.38 – Four-node 2D cohesive element with zero thickness ($a = 0$).

By defining $\bar{u}$, $\bar{v}$ as the relative displacements in the local coordinate system ($\bar{x}$,$\bar{y}$) and ($\bar{u}$,$\bar{v}$) as the relative displacements in the global coordinate system (x,y), the relative displacement vector in the global coordinate system can be expressed as:

$$\mathbf{W} = \mathbf{T}\,\mathbf{N}\,\mathbf{U} \tag{4-13}$$

where the relative displacement vector is given by $\mathbf{W} = (u \quad v)^T$, while **T** denotes the transformation matrix, which can be expressed as:

$$\mathbf{T} = \begin{bmatrix} n_1 & n_2 \\ t_1 & t_2 \end{bmatrix} \tag{4-14}$$

where n_1 and n_2 represent the components of the vector $\hat{n}$ in the (x,y) coordinate system, while t_1 and t_2 correspond to the components of the vector $\hat{t}$ in the same coordinate system, as illustrated in Figure 3.1. The interpolation function matrix **N** can be expressed as:

$$\mathbf{N} = \begin{bmatrix} -N_1 & 0 & -N_2 & 0 & N_1 & 0 & N_2 & 0 \\ 0 & -N_1 & 0 & -N_2 & 0 & N_1 & 0 & N_2 \end{bmatrix} \tag{4-15}$$

The negative sign in the first half of matrix **N** is essential for computing the differences between displacements. The interpolation functions of the cohesive element are defined to match the shape of the facets of the adjacent solid elements. For instance, in the case of a linear triangular element, the shape functions of the cohesive element correspond to those of a two-node bar element. Similarly, for a linear tetrahedral element, the shape functions of the joint element are equivalent to those of a three-node triangular element. Finally, the nodal displacement vector **U** is given by:

$$\mathbf{U} = (u_1 \ v_1 \ u_2 \ v_2 \ u_3 \ v_3 \ u_4 \ v_4)^T \tag{4-16}$$

Equation (4-14) can be rewritten in an incremental form as follows:

$$\Delta\mathbf{W} = \mathbf{T}\,\mathbf{N}\,\Delta\mathbf{U} \tag{4-17}$$

Where $\Delta\mathbf{W}$ is the vector of incremental relative displacements, while $\Delta\mathbf{U}$ represents the vector of incremental nodal displacements. The joint stress vector $\boldsymbol{\sigma}$ is obtained through the following equation:

$$\boldsymbol{\sigma} = \mathbf{D}\,\mathbf{W} \tag{4-18}$$

where the matrix **D** represents the constitutive matrix, which can be either elastic ($\mathbf{D}^e$) or elasto-plastic ($\mathbf{D}^{ep}$), depending on the characteristics of the interface to be simulated. Eq. (39) can be rewritten in an incremental form as follows:

$$\Delta\boldsymbol{\sigma} = \mathbf{D}\,\Delta\mathbf{W} \tag{4-19}$$

where $\Delta\boldsymbol{\sigma}$ represents the increment vector of the joint stress. The joint element stiffness matrix $\boldsymbol{K}$ is obtained through the matrix **D** and the matrix **B**, which can be calculated as $\mathbf{B} = \mathbf{T}\,\mathbf{N}$. Thus, the stiffness matrix can be determined using the following equation:

$$\boldsymbol{K} = \int_{l} \mathbf{B^T\ D\ B\ dL} \tag{4-20}$$

where l represents the length of the joint element. This formulation can be extended to obtain surface cohesive elements, which are used in 3D analyses.

4.13.2. Cohesive Zone Model

There is a damage zone that occurs near the crack, known as the Fracture Process Zone (FPZ). The FPZ is responsible for stress transfer, which tends to close the crack faces (Kumar & Barai, 2011). This capability decreases as the distance between the fracture faces increases (Figure 4.39). The model for the FPZ considered in this work, follows the same approach as presented in the literature (Silva, 2021; Silva, 2017). Several micro-failure mechanisms, such as the matrix of microcracks, interface delamination, and crack branching, contribute to energy consumption during crack propagation, as well as to stress transfer within the FPZ.

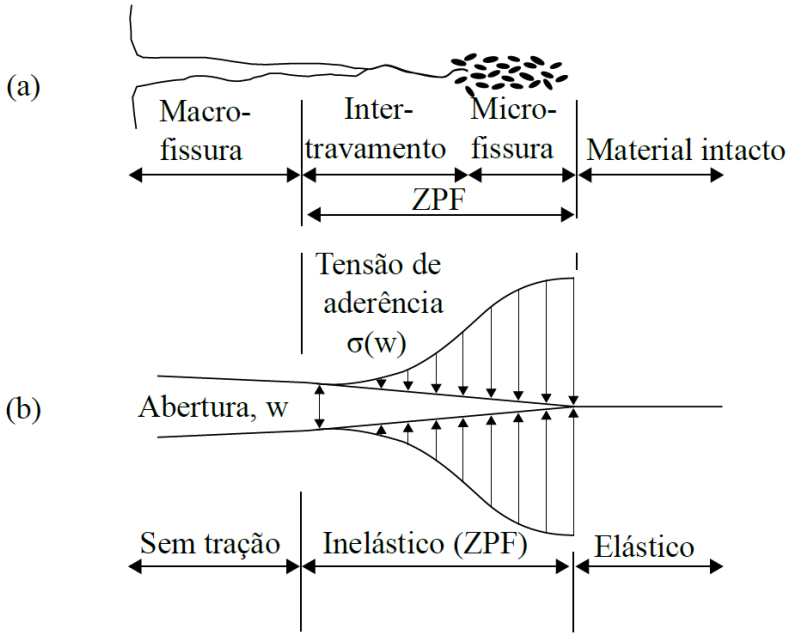


Figure 4.39 – Representation of the crack in quasi-brittle materials: (a) Fracture process zone and (b) Distribution of cohesive stress within the FPZ. Adapted from Silva (2021).

A detailed description of fracture in quasi-brittle materials must account for the tortuous crack path, three-dimensional crack profile, and inelastic response within the fracture

process zone (FPZ) (Bazant & Jaime, 1998). The FPZ is characterized by cohesive stress $\sigma(w)$, which decreases decreases from the maximum value (tensile strength, f_t, when $w = 0$) as the crack opening w increases. $\sigma(w)$ reaching zero at the critical crack opening w_c. A schematic representation is shown in Figure 4.40.

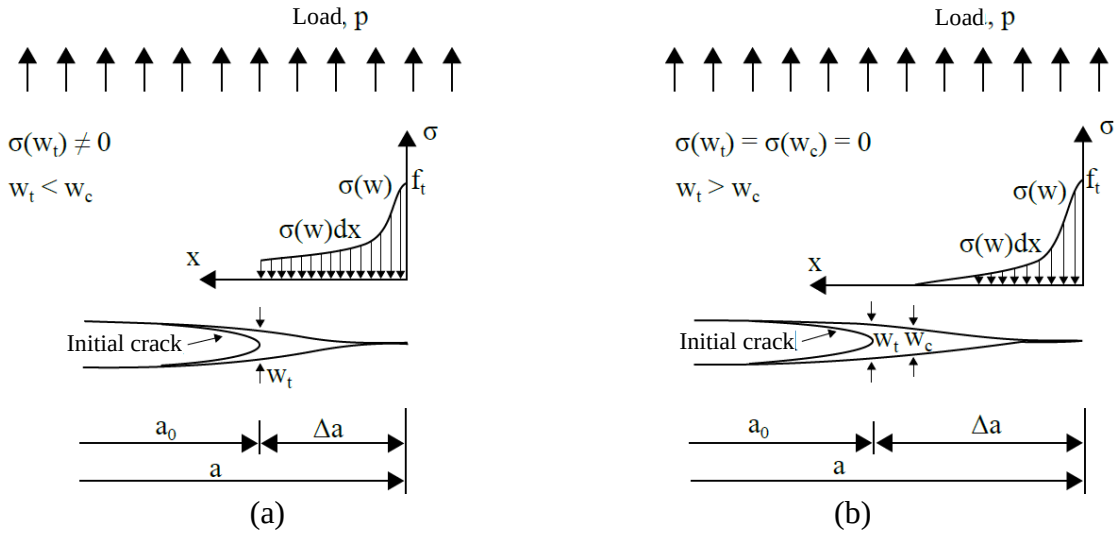


Figure 4.40 – Idealization of fracture in quasi-brittle materials: (a) cohesive crack with crack surfaces in contact ($w_t < w_c$), and (b) cohesive crack with partial separation of crack surfaces ($w_t \geq w_c$). Adapted from Bazant and Planas (1998) and Silva (2021).

When a quasi-brittle material with a crack is loaded, the energy release rate G_f consists of two components: the cracking energy release rate G_{Ic}, related to material fracture, and the energy required to overcome the cohesive stress G_σ. The total energy balance is expressed as:

$$G_f = G_{Ic} + G_\sigma = G_{Ic} + \int_0^{w_t} \sigma(w)dw \qquad (4\text{-}21)$$

Where w_t is the separation displacement at the initial crack tip. Different fracture mechanics models consider either one of these terms. The Griffith-Irwin approach assumes $G_\sigma = 0$, while the Dugdale-Barenblatt model assumes $G_{Ic} = 0$. The fictitious (cohesive) crack approach, illustrated in Figure 2.9, models crack propagation through a cohesive zone ahead of the crack tip, where energy dissipation is fully characterized by the stress-displacement relation. In this case, the total energy release simplifies to:

$$G_f = \int_0^{w_t} \sigma(w)dw \qquad (4\text{-}22)$$

This condition is valid for structures with constant unit thickness, and crack initiation occurs when the principal tensile stress reaches the material's tensile strength f_t.

4.13.3. Power Yield Crack

The Power Yield Crack Model is a constitutive model to predict cracks through the opening of cohesive elements. One of the models for the yield function (Durand, et al., 2023) is defined as follows:

$$f(\sigma, \sigma_{max}) = \beta(\sigma_{max})(\sigma_n - \sigma_{max}) + \left(\frac{\tau^2}{{f_t}^2}\right)^{\alpha} = 0 \qquad (4\text{-}23)$$

The highest tensile strength, σ_{max}, observed during the analysis is employed as the internal softening variable. σ_n is the normal stress acting on the plane. τ is the shear stress. α is an input parameter that helps create a curved (exponential) yield function, which envelops the tensile and compressive Mohr circles defined by the tensile strength f_t and compressive strength f_c. Meanwhile, β is utilized to adjust the size of the yield function based on σ_{max} and is calculated as:

$$\beta(\sigma_{max}) = \beta_{res} + (\beta_{ini} - \beta_{res}) + \left(\frac{\sigma_{max}}{f_t}\right)^{\theta} \qquad (4\text{-}24)$$

where θ is a parameter that defines how fast the yield function is modified. β_{res} is the residual value of the β function. The initial value (β_{ini}) for β is given by

$$\beta_{ini} = \frac{\left(\frac{{\tau_t}^2}{{f_t}^2}\right)^{\alpha}}{f_t - \sigma_t} \qquad (4\text{-}25)$$

Where:

$$\sigma_t = \frac{2\alpha f_t + \alpha f_c - f_c - \sqrt{\alpha^2 f_c^2 - 4\alpha^2 f_c f_t + 4\alpha^2 f_t^2 - 2\alpha f_c^2 + f_c^2}}{4\alpha - 2} \qquad (4\text{-}26)$$

$$\tau_t = \sqrt{\alpha(2\sigma_t - f_c)(f_t - \sigma_t)} \qquad (4\text{-}27)$$

The point (σ_t, τ_t) in Figure 4.41 represents the location where the compressive Mohr's circle intersects with the initial yield envelope.

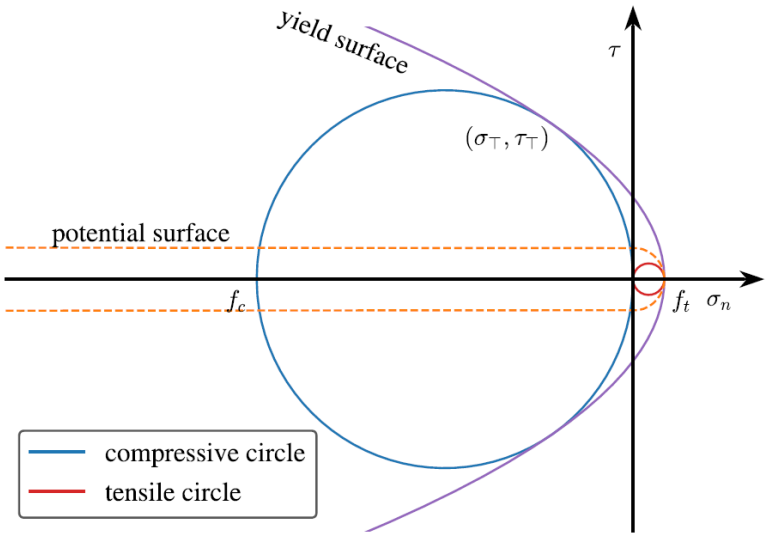


Figure 4.41 – Yield and potential plasticity functions, together with the compressive and tensile Mohr's circles. Adapted from Durand et al. (2023).

While the yield function describes the critical point at which a material begins to undergo plastic deformations, the plastic potential function, on the other hand, is associated with the plastic flow and defines the direction in which the plastic deformations will evolve once the yield function has been reached. For this work, the plastic potential function (Figure 4.41) is given by the composite function:

$$g(\boldsymbol{\sigma}, \sigma_{max}) = \begin{cases} \tau^2 - \sigma_{max}^2 = 0 & \text{for } \sigma_n \leq 0 \\ \sigma_n^2 + \tau^2 - \sigma_{max}^2 = 0 & \text{for } \sigma_n > 0 \end{cases} \qquad (4\text{-}28)$$

The Power Yield Crack Model has been successfully applied to the study of prestressed beams (Durand, et al., 2023).

4.13.4. Asinh Yield Crack

The Asinh Yield Crack model is another constitutive approach for cohesive elements, in which the inverse hyperbolic sine function is used for the yield criterion, which is written as:

$$f(\boldsymbol{\sigma}, \sigma_{max}) = f(\sigma_n, \tau, \sigma_{max}) = \tau - \beta(\sigma_{max}) \operatorname{asinh}\left(\alpha \frac{\sigma_{max} - \sigma_n}{f_t}\right) \qquad (4\text{-}29)$$

Where:

$$\tau = \sqrt{{\tau_1}^2 + {\tau_2}^2} \qquad (4\text{-}30)$$

$$\boldsymbol{\sigma} = \langle \sigma_n, \tau_1, \tau_2 \rangle \qquad (4\text{-}31)$$

$$\beta(\sigma_{max}) = \beta_{res} + (\beta_0 - \beta_{res}) \left(\frac{\sigma_{max}}{f_t}\right)^{\theta} \qquad (4\text{-}32)$$

τ is the resultant of shear stresses in the plane of the cohesive element. $\boldsymbol{\sigma}$ is the stress vector

The plastic potential function is the same as the Power Yield Crack model.

4.13.5. Willam-Warnke model

In the simulations conducted using the Amaru library in this study, the nonlinear behavior of concrete was represented using the Willam-Warnke model with hardening. This model is an extension of the original Willam-Warnke model, which is used to describe the behavior of concrete under different types of loading, such as tension, compression, and shear. The Willam-Warnke model is particularly useful for representing the nonlinear behavior and failure of concrete, taking into account aspects such as microcracking and plasticity. In the context of nonlinear hardening, the model is modified to include a relationship that describes the increase in the material's strength after it begins to plastically deform. This model is

frequently used in finite element simulations to analyze the behavior of concrete structures under different loading conditions, including high deformation scenarios, and to predict the point of failure or collapse.

The Willam-Warnke model has a yield criterion, which is a criterion primarily used to model the mechanical behavior of brittle materials, such as concrete and rocks. It is a three-dimensional extension of the Mohr-Coulomb criterion, designed to capture the influence of hydrostatic stress on material behavior. The Drucker-Prager criterion is also used for brittle materials but the Willam-Warnke criterion is more flexible and provides a better approximation of the behavior of concrete, especially for triaxial stress states. The yield function of the Willam-Warnke yield criterion is given by:

$$f(\boldsymbol{\sigma}, \varepsilon_p) = \rho - \frac{\rho_0}{\xi_0} r(\theta)(\xi_0 - \xi) = 0 \qquad (4\text{-}33)$$

Where

$$\xi_0 = \sqrt{3}\frac{f_b f_t}{f_b - f_t} \qquad (4\text{-}34)$$

$$\rho_0 = \sqrt{2}\frac{f_c \xi_0}{f_c - \sqrt{3}\xi_0} \qquad (4\text{-}35)$$

$$r(\theta) = \frac{2(1-e^2)\cos(\theta) + (2e-1)\sqrt{4(1-e^2)\cos^2(\theta) + 5e^2 - 4e}}{4(1-e^2)\cos^2(\theta) + (2e-1)^2} \qquad (4\text{-}36)$$

ρ represents the measure of the deviatoric stress, ξ is the spherical stress radius, θ is the Lode angle and f_b is the biaxial strength wich was set to match the uniaxial compressive strength f_c.

4.13.6. Comparing simulations with experimental results

The methodology for the simulations described in this chapter was developed using the Julia programming language and Amaru library (https:// github.com/NumSoftware/Amaru). The MEF analysis for UTT, MSCBT and 3PBT will be delineated. The procedures were carried out for concretes C-10, C-11, and C-12, which exhibit the characteristics presented in the

Table 4.2. The obtained results, along with a comparison to the experimental outcomes of UTT, are presented in section 5.9.

The same Inverse Analysis algorithm developed for the 3PBT described in item 4.9 was used to carry out the procedure for the MSCBT. However, due adjustments were made regarding the different geometry of the MSCBT sample. The dimensions that were different were the span, the height and thickness of the sample and the depth and thickness of the notch. The dimensions are shown in the Figure 4.10b and the test setup is shown on Figure 4.12. Thus, the thickness of the MSCBT sample is 75 mm. These considerations are suitable to be realized because the MSCBT sample is under bending during the test, in the same way as the 3PBT sample. Therefore, the principles of inverse analysis (Carvalho & Lameiras, 2023a) are applicable.

Softening and hardening behaviors were observed in the experimental results. Material stiffness can contribute to these two behaviors in the process of crack formation and initial propagation. Two models were used for the analysis through FEM. The cohesive elements were modeled using the approach proposed by Durand et al. (Durand, et al., 2023). The Willam-Warnke model (Willian & Warnke, 1974) was used to account for the behavior of concrete considering elasto-plastic behavior.

For the approach using the Julia programming language with the Amaru library, presented in this section, a brief mesh convergence study was carried out. Initially, the Refined Mesh Length (RML) along the specimen where a more refined mesh would be applied was determined. The refinement was set to a value corresponding to 20% of the total length of each specimen (Table 4.5). Based on the mesh refinement study, convergence of the results was observed. Accordingly, the general element size (GES) values were established as 8 mm, 3.5 mm, and 2 mm for the 3PBT, MSCBT, and UTT tests, respectively, according to the corresponding specimen dimensions. In the mesh refinement region, the element length was obtained by multiplying the GES by a Reduction Coefficient (RC) of 0.3 for MSCBT and UTT. For the 3PBT test, a smaller coefficient (0.1) was adopted, as is commonly used for this type of test (Salehian, 2015; Lameiras, 2016). To represent all sample geometries of the tests, an unstructured mesh was generated using tetrahedral elements, and joint elements were added between them. The mesh is generated by extruding the 2D geometry along the z-axis (parallel to the sample axis as shown in the Figure 4.42), creating a symmetrical three-dimensional model. The RML, GES, RC, number of Bulk elements, Cohesive elements, and

Nodes for the UTT, 3PBT, and MSCBT tests are presented in the Table 4.5. The illustration of the mesh models used is presented in Figure 4.42.

Table 4.5 – Finite element models elements and nodes for UTT, 3PBT and MSCBT.

Test	RML [mm]	GES [mm]	RC [mm]	Bulk elements	Cohesive elements	Nodes
UTT	28	3.5	0.3	1308	1117	2656
3PBT	110	8	0.1	5887	9587	21126
MSCBT	20	2	0.3	2114	1913	4408

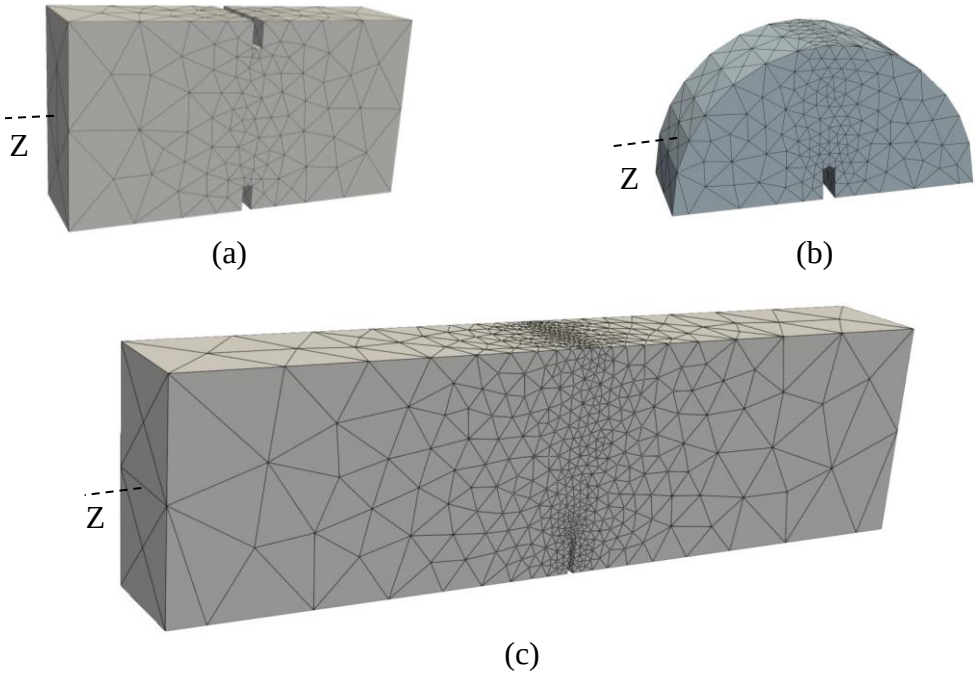


Figure 4.42 – Illustration of the mesh models used for the simulations with the Julia programming language: (a) for the UTT, (b) for the MSCBT, and (c) for the 3PBT.

The numerical model is constructed using the GeoModel function to define the geometry of the specimen. A set of discrete points is introduced using the addpoint! function, capturing the shape of the FRC sample. The spatial distribution of these points ensures that the geometry closely resembles experimental specimens used in mechanical characterization tests.

To ensure numerical accuracy, a mesh refinement strategy is applied in the central region where fracture is expected. The following key steps are performed:

- Definition of boundary points (12 for 3PBT, 14 for UTT, 22 for MSCBT, the latter being the most complex), forming a closed polygon that represents the sample cross-section.
- Use of the addpath! function to define the sample perimeter by sequentially linking these points.
- Local refinement of the mesh using an adaptive criterion, specifically targeting the region where significant stress concentrations are anticipated.

The three-dimensional structure is generated using the pull! function, extruding the 2D profile along the out-of-plane axis, creating a solid model with a thickness of half the total thickness, considering symmetry (75 mm for 3PBT and 37.5 mm for UTT and MSCBT).

To accurately simulate fracture, cohesive elements are inserted in a predefined fracture process zone. This is accomplished using the insert_cohesive_elements! function, which selectively introduces interface elements within the specified domain on the notch region. These elements capture the softening behavior associated with crack propagation in concrete materials.

The cohesive zone model (CZM) follows a nonlinear traction-separation law, incorporating a path function to define the stress-displacement relationship. The degradation of stiffness in the cohesive elements is dictated by an energy-based approach, ensuring a realistic representation of fracture processes.

Two different material models are implemented to represent the bulk and joint regions:

- Bulk Material: The continuum domain follows the Willam-Warnke failure criterion, a three-parameter model suitable for concrete and quasi-brittle materials. The material properties are in the Table 4.6.
- Cohesive Zone Model: The fracture process is described using the Power Yield Crack Model, with a damage evolution function defined via PathFunction, which define evolution laws for material properties as a function of a control variable—typically strain, displacement, or crack opening. The model incorporates: Initial tensile strength; Softening parameterization to ensure numerical stability; Stress-dependent energy dissipation mechanisms. The parameters defining post-cracking behavior were taken from direct tensile tests. Based on this tensile stress–strain curve, a smoothing procedure is applied using the Bezier curve that best

approximates the observed behavior. The parameters (characteristic points of this curve) are then incorporated into the Julia routine, which employs the Amaru library to generate the Finite Element model used to simulate the behavior of the analyzed test.

Table 4.6 – Material properties of simulations according to the concrete type.

Constitutive model	Concrete type	E [×10³ MPa]	ν	f_c [MPa]	f_t [MPa]	f_b [MPa]	ζ	α	γ	θ
Power Yield Crack	C-10	36.3	0.2	45.6	3.4	-	5	0.51	0.05	1.2
	C-11	36.3	0.2	42.2	3.1	-	5	0.51	0.05	1.2
	C-12	36.3	0.2	35.8	2.9	-	5	0.51	0.05	1.2
William Warnke	C-10	36.3	0.2	45.6	3.4	4.08	-	-	-	-
	C-11	36.3	0.2	42.2	3.1	3.72	-	-	-	-
	C-12	36.3	0.2	35.8	2.9	3.48	-	-	-	-

The finite element model is subjected to appropriate boundary conditions to replicate the experimental setup. Fixed constraints at to restrict displacement for 3PBT (x=25, y=0 mm) and for MSCBT (x=5, y=0 mm), and at the symmetrically opposite point, a simple support is established. For UTT, fixed constraints at restrict displacement and bending moment on: x=0, y=0 mm.

The results are logged at predefined points, particularly at positions corresponding to linear variable differential transformers (LVDTs), ensuring direct comparison with experimental data. Control points were defined according to the gluing position of the LVDT fixing plates to monitor displacements during the simulation.

The results of these simulations are presented in Section 5.9.3.

4.13.7. Parametric study

In this chapter, a procedure for a parametric study involving numerical simulations will be described, conducted to investigate modifications in the sample geometry concerning notch depth and sample length.

The ratio between the span and the effective height (discounting the notch length) of the experimentally tested MSCBT sample (Figure 4.12), as described in section 9.1, is 2.25 (L/H = 90/40). This ratio was used to accommodate the possibility of extracting specimens from the 3PBT prisms, which have a height of 150 mm and a width of 150 mm. However, this geometry is not compatible with the behavior of typical beams (L/H > 2.5). Therefore, this

subsection describes a parametric study based on computational simulations to verify the influence of this ratio on the semicircular sample.

The simulations were performed with a constant thickness of 75 mm. If the span (90 mm) were maintained for the simulations, the height of the sample would be significantly reduced, which would increase the dispersion of the results and cause many fibers to be cut in the tensile zone. The studied relationships are presented in the Table 4.7, along with the corresponding sample dimensions and assigned notations.

Table 4.7 – Dimensions and notations of simulations performed varying notch size and sample length.

Notation	Effective Span [mm]	Span [mm]	Effective height [mm]	Full-height [mm]	Notch depth [mm]	Thickness [mm]	Effective Span / Effective height	Effective height × Thickness [mm²]
S-150-13	140	150	62	75	13	75	2,26	4650
S-150-19	140	150	56	75	19	75	2,50	4200
S-150-24	140	150	51	75	24	75	2,75	3825
S-150-28	140	150	47	75	28	75	2,98	3525
S-200-16	190	200	84	100	16	75	2,26	6300
S-200-24	190	200	76	100	24	75	2,50	5700
S-200-31	190	200	69	100	31	75	2,75	5175
S-200-37	190	200	63	100	37	75	3,02	4725

The Figure 4.43 shows an illustration of the different configurations tested for the simulations.

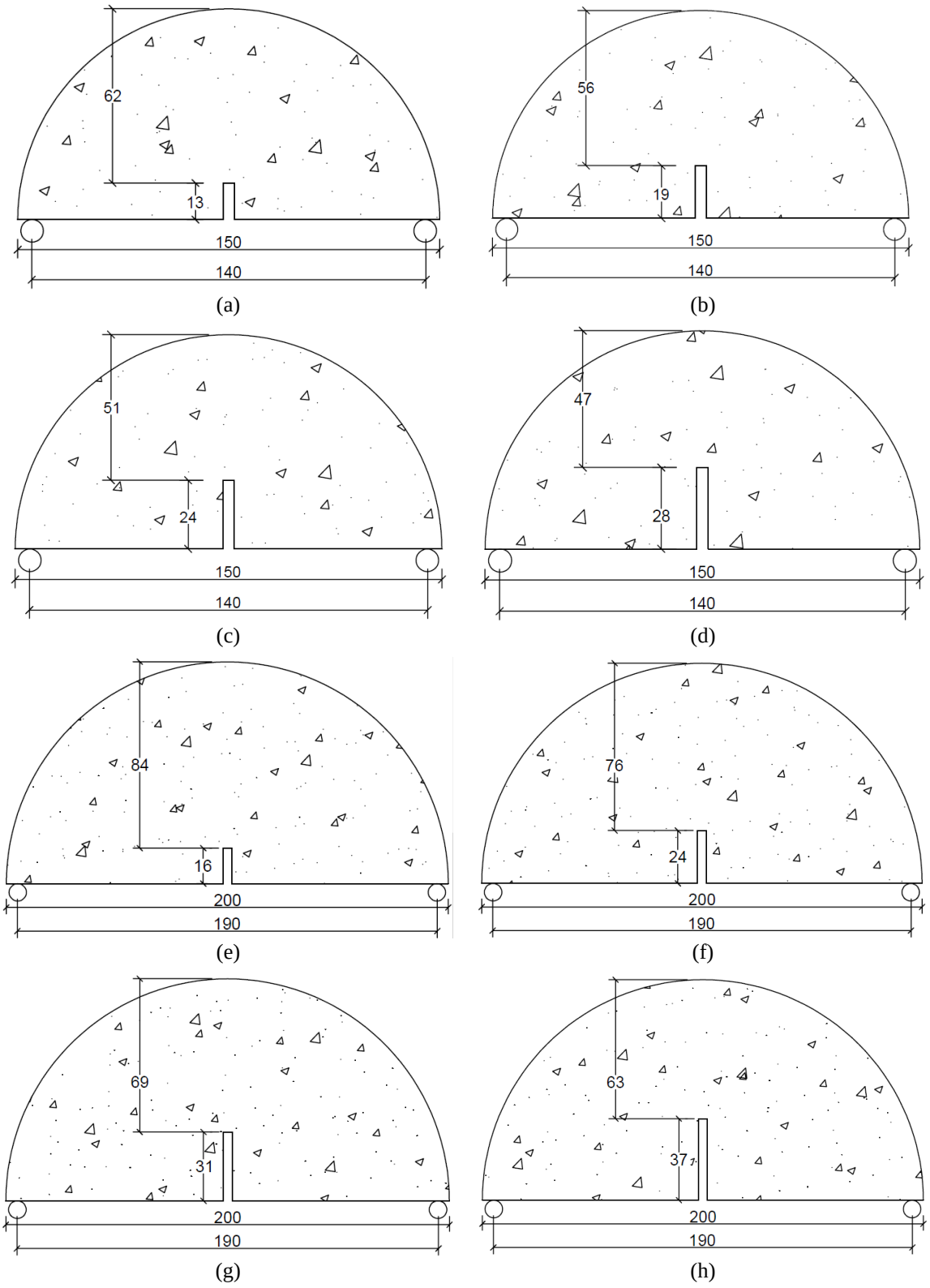


Figure 4.43 – Illustrations of the geometries used in the MSCBT simulations, including notch dimensions, span, and effective span.

The simulation procedure performed is similar to that described in item 4.13.1. However, some modifications were necessary:

- Therefore, 22 boundary points were defined for the semi-circular shape.

- The type of concrete (C-10) was kept fixed. Differently from the comparative analysis with the experimental results, in which concretes C-10, C-11 and C-12 were studied.

- Adjustments were made to the position of the LVDTs and supports due to changes in the sample geometry and notch position.

The number of Bulk elements, Cohesive elements, and Nodes for the MSCBT simulations with varying notch depth and sample length are presented in the Table 5.1.

Table 4.8 – Finite element models elements and nodes for MSCBT simulations with varying notch depth and sample length.

Test	Bulk elements	Cohesive elements	Nodes
S-150-13	2349	1516	3677
S-150-19	2333	1380	3442
S-150-24	2319	1499	3715
S-150-28	2232	1327	3354
S-200-16	4820	2257	5633
S-200-24	4148	1535	4120
S-200-31	4561	1769	4702
S-200-37	4340	1437	4009

The illustration of the mesh models used is presented in Figure 4.44.

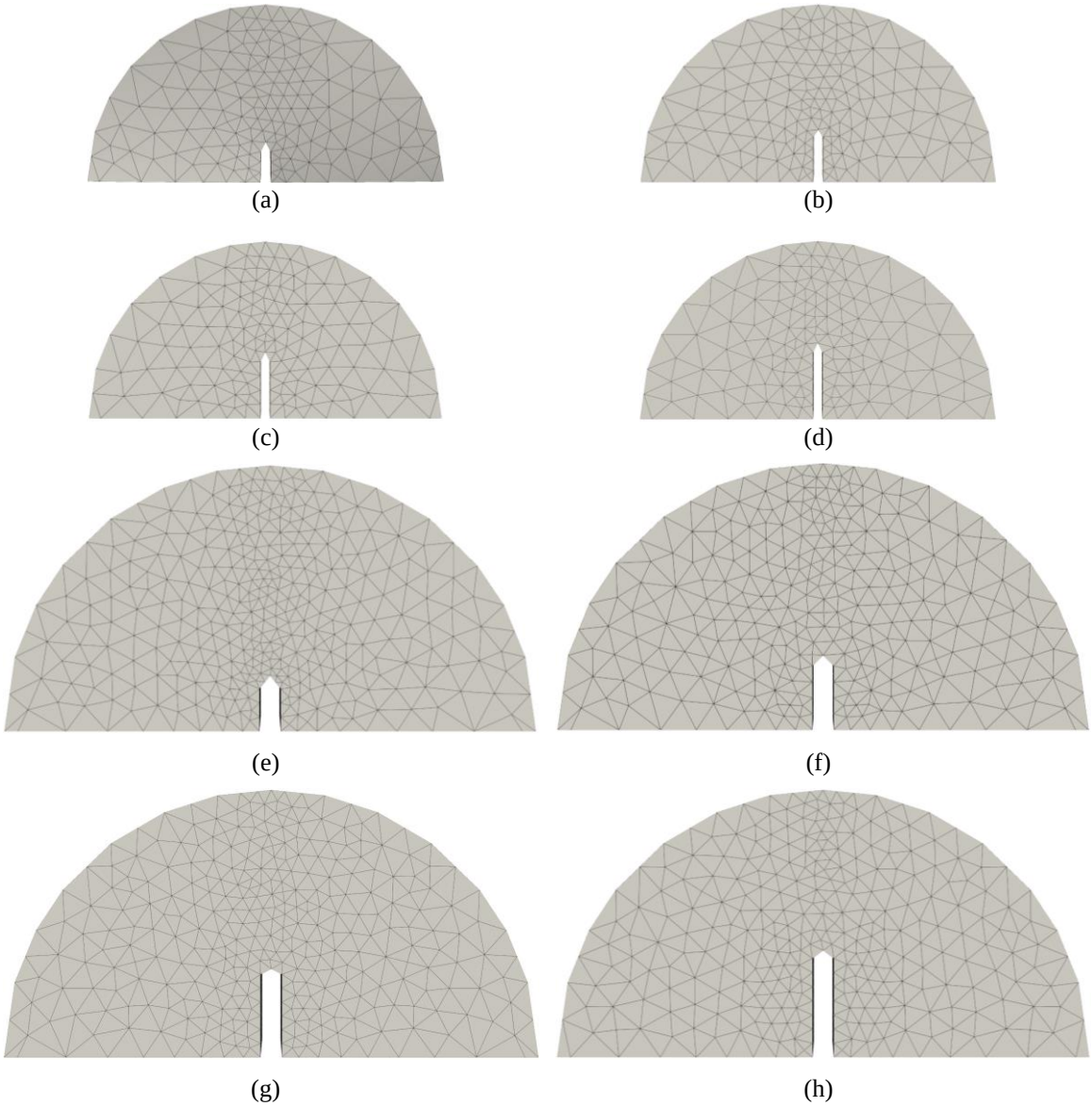


Figure 4.44 – Mesh models for MSCBT simulations: (a) S-150-13, (b) S-150-19, (c) S-150-24, (d) S-150-28, (e) S-200-16, (f) S-200-24, (g) S-200-31 and S-200-37.

The results of these simulations are presented in Section 5.9.3.

4.14. MSCBT (conception)

Despite the contributions made to the SCB and MSCBT, a study of the MSCBT involving concretes with different characteristics and at the same time performing CMOD monitoring for SFRSCC has not yet been carried out. This work aims to contribute to this gap. The MSCBT is used including Crack Mouth Opening Displacement (CMOD) monitoring to determine the properties of Steel-Fiber Reinforced Self-Compacting Concrete (SFRSCC). It

is of relevance in this work, to study the design of the MSCBT, as well as the possibility of this test representing the post-cracking behavior of the SFRSCC considering the different characteristics of the studied concrete. Therefore, a broad experimental program for this test was carried out in this work. For samples with a width of 75 mm, 72 samples were tested in MSCBT, 6 for each of the 12 types of concrete described in Table 4.2. Therefore, 3 types of fibers with different lengths and diameters (ST-50/67, ST-33/60, ST-33/44), two concrete resistance classes (20 and 40 MPa) and two fiber contents (0.5 and 1.0%) were evaluated. The results of the methodology described in this section are presented in section 5.4.

4.15. MSCBT (sample thickness)

The adequate size of the sample for carrying out the tests is an important parameter for the tested sample to be considered representative of the behavior of the studied concrete, as already discussed in item 4.6. Therefore, this work also sought to evaluate the effect of a greater thickness for the MSCBT test sample. For this, samples with a thickness of 150 mm were tested and compared with the results obtained for a thickness of 75 mm.

For this analysis, among the fibers studied in this work, the shortest lengths (ST-33/44 and ST-33/60) were selected for a content of 0.5%. Concrete with the highest strength class (40 MPa) was chosen. Therefore, the types of concrete chosen to carry out the thickness study were C-7 and C-8, as shown in Table 4.2. For each of these types of concrete, 6 samples were tested with a width of 150 mm. The obtained results were compared with those of samples using the same types of concrete, albeit with a thickness of 75 mm, which are the same as those previously tested as described in 4.14.

In total, the study of sample thickness would involve testing 24 samples, 12 for each thickness (75 and 150 mm).

4.16. ST (conception)

The ST is known to have a number of advantages, especially because it is a relatively easy test to perform. Hence, this work sought to perform ST for a later comparison with the MSCBT results. Therefore, 4 samples were tested with ST for each of the 12 types of

concrete presented in Table 4.2. The sample preparation process is carried out as explained with details in item 4.7. A total of 48 ST samples have already been tested in this work.

4.17. Fiber counting procedure for 3PBT, MSCBT and ST

The fiber counting procedures according to the different types of tests will be described and the results obtained are shown in this item. The counting methodology used in this study was similar to that employed in the literature (Lameiras, 2016)e. The fiber was considered effective when it was broken or when its visible length was, at least, two times larger than the length of the hooked part of fiber. For 3PBT, the count was carried out by dividing the fractured section of the sample into three parts with the same cross sectional area: lower part - 3PBT (B), middle part - 3PBT (M) and upper part - 3PBT (U) according to the test configuration (section A which can be seen from the 3PBT sample in Figure 4.2a and detailed in Figure 4.45a). For the MSCBT, the count was carried out considering the entire section B (Figure 4.7g and Figure 4.45b) of the tested sample because this sample has a smaller cross-sectional area. There are two sample extraction positions in relation to the 3PBT core: MSCBT (A) and MSCBT (B), as shown in Figure 4.7c. In these two positions, the molding direction is parallel to the width of the sample. Therefore, a greater concentration of fibers in the tensile region of the sample caused by the molding conditions during the test is not expected. Thus, no differentiation is made between MSCBT (A) and MSCBT (B) in the analysis of the results of this study. For the Uniaxial Tensile Test (UTT), one of the specimens selected was obtained from the Lower Portion (LP) of the 3PBT sample in alignment with the molding direction, while the remaining two specimens were retrieved from the Upper Portion (UP), according to Figure 4.14a. For each UTT sample, two regions were counted separately: Upper Edge (UE) and Lower Edge (LE). Therefore, these samples are presented with the notations: UTT (LP LE), UTT (UP LE), UTT (LP UE) and UTT (UP UE), according to Figure 4.14b.

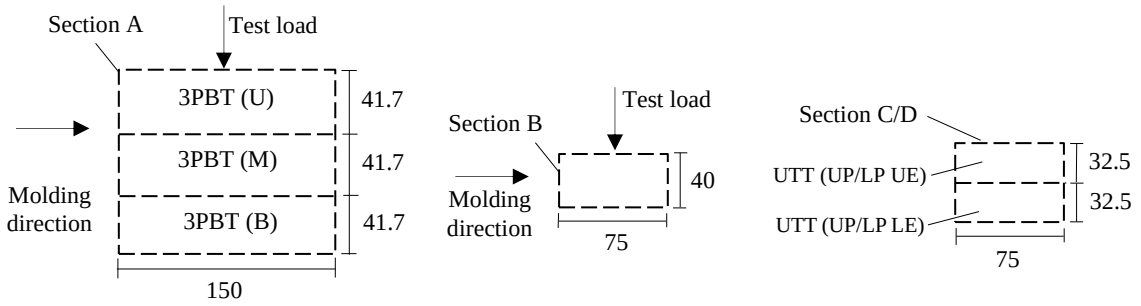


Figure 4.45 – Fiber count on section of the samples (the section corresponding to the notch area did not have fibers counted, therefore it is not illustrated) according to test load direction and molding direction for: (a) 3PBT, (b) MSCBT and (c) UTT. UTT (UP UE) and UTT (UP LE) correspond to Section C. UTT (LP UE) and UTT (LP LE) correspond to Section D.

5. RESULTS

In this section, the results obtained so far with this work will be presented. All the tests foreseen for this thesis have already been carried out, as presented in the methodology item of this text. As part of the results have not yet been analyzed, the results referring to the flowchart on the Figure 4.1 will be presented: IA algorithm for 3PBT (progressive method), IA algorithm for MSCBT (preliminary results) and IA algorithm for MSCBT (validation).

5.1. IA algorithm for 3PBT (progressive method)

The algorithm in this study was used to verify the post-cracking behavior of the concretes presented in Table 4.4. This study's inverse analysis methodology achieves the results discussed in this section. The $(F-CMOD)_{anal}$ curves obtained through the proposed procedure were compared with the results obtained experimentally by the respective references. All the curves obtained analytically through the implemented algorithm were very close to the experimental curves. The errors between the analytical and experimental F-CMOD response found were less than 10%.

The illustration of the detailed parameters determination steps for the curves $(F-CMOD)_{anal}$ will only be shown for the SFRSCC B concrete from (Lameiras, 2016). The discussions of this analysis can be found in section 4.9. The results of the final $F-CMOD$ diagrams are presented in this section. The inverse analysis (σ-w) was compared to the consulted authors.

5.1.1. Determination of f_{ct}

In this step, the analytical model was processed for the f_{ct}/f_{ctm} relations presented in Section 4.9. Figure 5.1 shows the results for the secondary parameter $\sigma_1/f_{ct}=0.8$ and Figure 5.2 for $\sigma_1/f_{ct}=1.2$. In Figure 5.1, secondary parameter has a lower value than the one seen in Figure 5.2. As a result, there is a trend towards a lower slope for the curves obtained by the algorithm for the different simulated f_{ct}/f_{ctm} about the dashed curve (experimentally validated by (Lameiras, 2016). For better curves visibility obtained through the analytical model, the interval with the CMOD ranges from 0 to $L_f/175$ was selected to determinate the areas, as indicated in Section 4.9, Figure 5.1 and Figure 5.2.

After executing the step described in Section 4.9, the algorithm shows the error found between analytical and experimental curve for the two situations of σ_1/f_{ct}. For the ratio $\sigma_1/f_{ct} = 0.8$, among the corresponding f_{ct}/f_{ctm} parameters, as shown in Figure 5.1, the smallest error was 5.2%. However, for the ratio $\sigma_1/f_{ct} = 1.2$ (Figure 5.2), the smallest error was 2.6%. This result was obtained for the curve corresponding to $f_{ct}/f_{ctm} = 0.55$. This curve indicates good compatibility with the dashed curve. The algorithm selected this curve to compose the result in the interval corresponding to this step. There is a significant sensitivity of the results obtained for $(F - CMOD)_{anal}$ when changing f_{ct}/f_{ctm}.

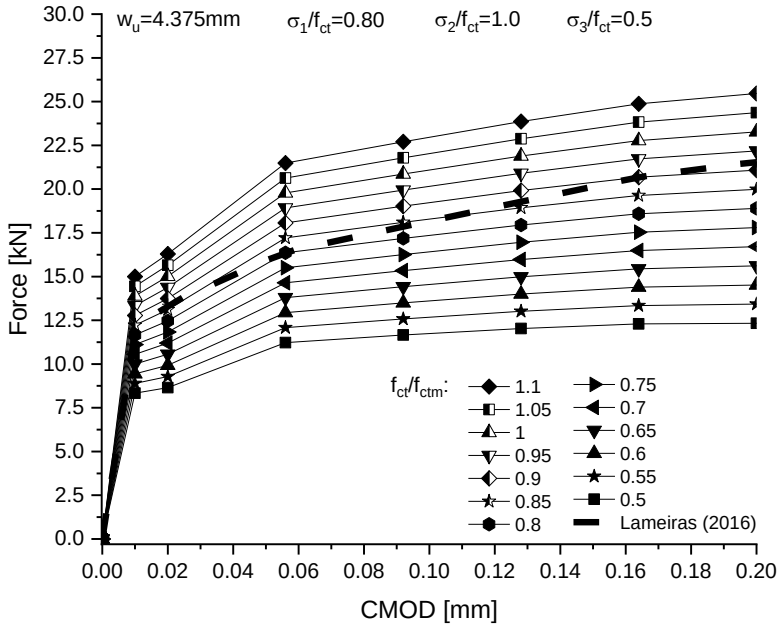


Figure 5.1 – Inverse analysis - determination of f_{ct} for σ_1/f_{ct}=0.8 compared with experimental result (Lameiras, 2016).

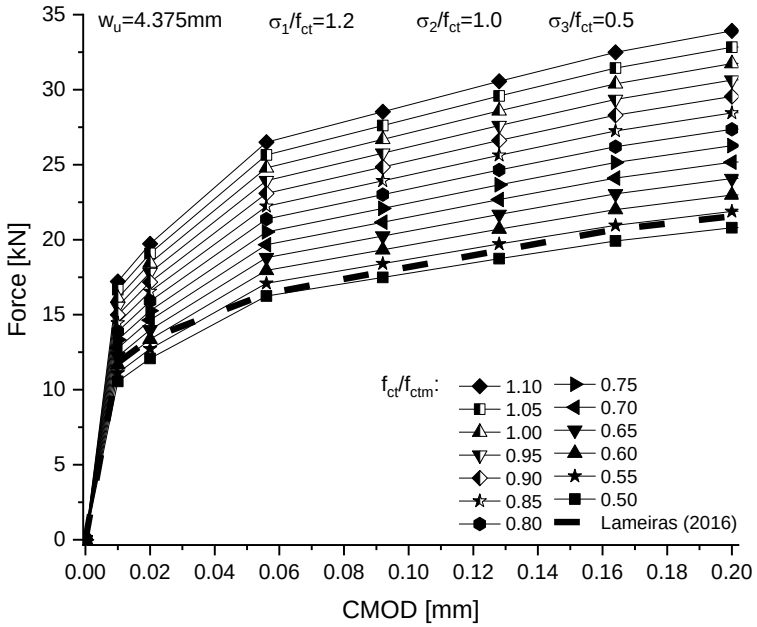


Figure 5.2 – Inverse analysis—determination of f_{ct} for $\sigma_1/f_{ct} = 1.2$ compared with experimental result (Lameiras, 2016).

5.1.2. Determination of σ_1

The analytical model was processed for the different σ_1/f_{ct} ratios in this step, according to Section 4.9. The results are shown in Figure 5.3 and Figure 5.4. For better visibility of the curves obtained through the analytical model, the interval with the CMOD varying from 0

to $L_f/70$ was selected to estimate the areas, as described in Section 4.9. For CMOD between 0 and 0.02 mm, the presented diagram is influenced by the previous step since the f_{ct} parameter is fixed, and its influences the initial section of the curve. Therefore, this curve is compatible with the experimental response. After $CMOD = 0.01\ mm$, the influence of the σ_1/f_{ct} variation is verified. The observation described in the previous item can be carried out regarding the secondary parameter (which in this step is σ_2/f_{ct}). However, it is possible to verify less sensitivity of the results obtained concerning the variation of this parameter, which can be seen by comparing Figure 5.3 with Figure 5.4 considering the slope of the curve.

For the $\sigma_2/f_{ct} = 0.8$ ratio, among the corresponding f_{ct}/f_{ctm} parameters, as shown in Figure 5.3, the smallest error between the analytical and experimental F-CMOD response was 1.1% for the $\sigma_1/f_{ct} = 1.2$ ratio. The algorithm selected this curve to compose the result in the interval corresponding to this step. For the relation $\sigma_2/f_{ct} = 1.2$ (Figure 5.3), the slightest error was obtained for the curve corresponding to $\sigma_1/f_{ct} = 0.8$. In Figure 5.3. The curve with this relation is the one that comes closest to the validated result (dashed curve). Based on the association found by the model, the difference between areas of the analytical response to the experimental one was significantly lower, which would not seriously compromise the proposed methodology.

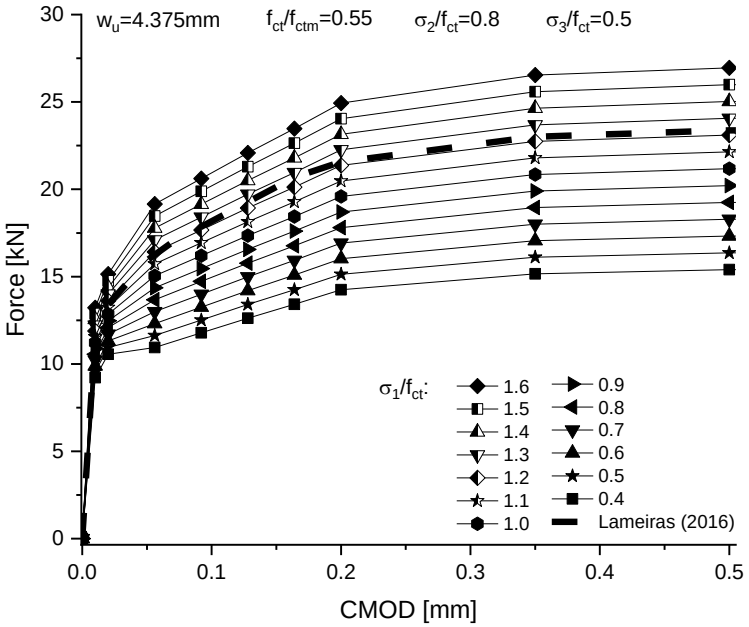


Figure 5.3 – Inverse analysis - determination of σ_1 for $\sigma_2/f_{ct} = 0.8$ compared with experimental result (Lameiras, 2016).

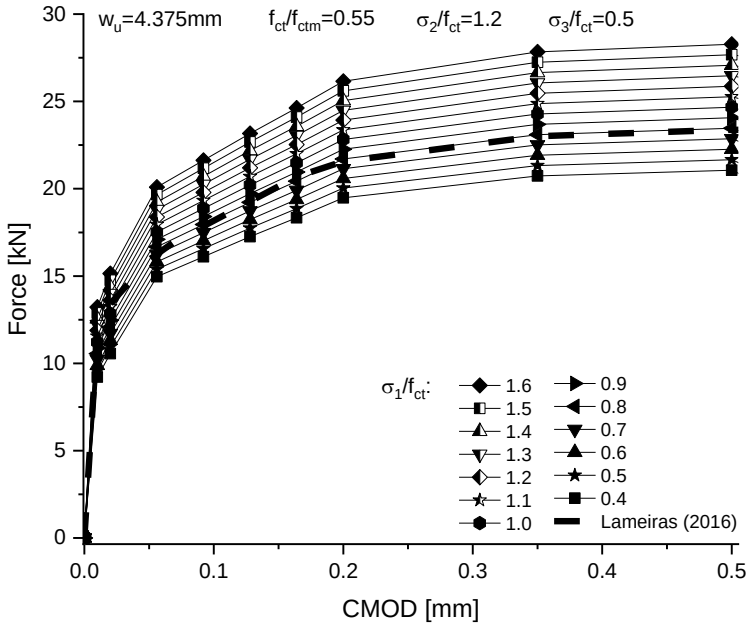


Figure 5.4 – Inverse analysis - determination of σ_1 for $\sigma_2/f_{ct} = 1.2$ compared with experimental result (Lameiras, 2016).

5.1.3. Determination of σ_2

The results of this step are presented in Figure 5.5 (secondary variable: $\sigma_3/f_{ct} = 1.2$) and in Figure 5.6 ($\sigma_3/f_{ct} = 0.8$). The interval was selected in these figures with the CMOD varying from 0 to $L_f/17.5$ and for prediction of areas, as described in Section 4.9. A more significant influence of this variable is observed from $CMOD = 0.8$, where the $\sigma_3/f_{ct} = 1.2$ curve tends to present larger load values, which can be explained by the bigger value of the σ_3/f_{ct} ratio in this situation. The smallest error between the analytical and experimental F-CMOD response found in this step is 0.6%, which was obtained for the relation $\sigma_3/f_{ct} = 0.8$ and $\sigma_2/f_{ct} = 0.8$. In the interval between 0 and 0.2 mm, the section of the curve obtained in the previous step is shown. Between 0.2 and 2 mm, the diagram section influenced by the parameters of this step analysis is shown.

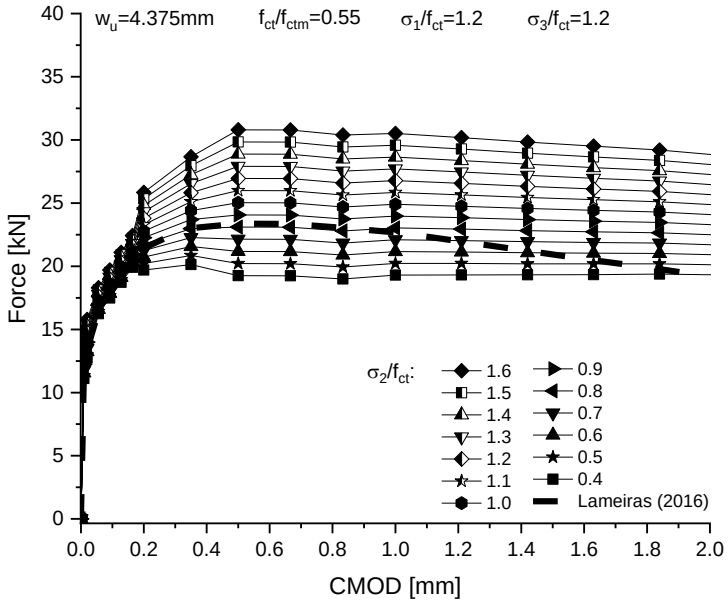


Figure 5.5 – Inverse analysis—determination of σ_2 for $\sigma_3/f_{ct} = 1.2$ compared with experimental result (Lameiras, 2016).

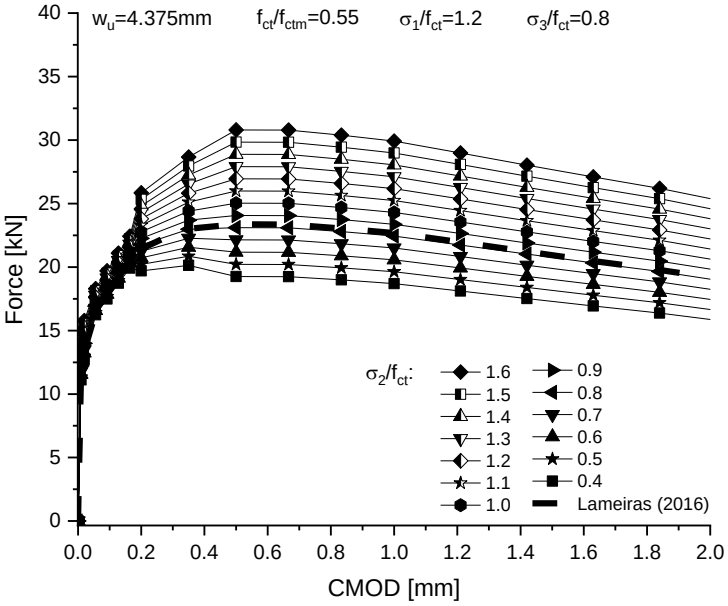


Figure 5.6 – Inverse analysis - determination of σ_2 for $\sigma_3/f_{ct} = 0.8$ compared with experimental result (Lameiras, 2016).

5.1.4. Determination of σ_3

The results of this step are shown in Figures 58-59, which were generated for w_u corresponding to $L_f/8$, $L_f/10$, and $L_f/4$, respectively, as described in Section 4.9. The visualization interval was selected in these figures with the CMOD varying from 0 to

$L_f/17.5$ and for calculation of areas, as defined in Section 4.9. The diagrams showed minor differences between them. The most significant differences occur for $CMOD > 2.5$, which is already a high value to evaluate the structural behavior of FRC. The most negligible contrast between the analytical and experimental areas is for $w_u = 4.375$ mm and $\sigma_3/f_{ct} = 0.7$.

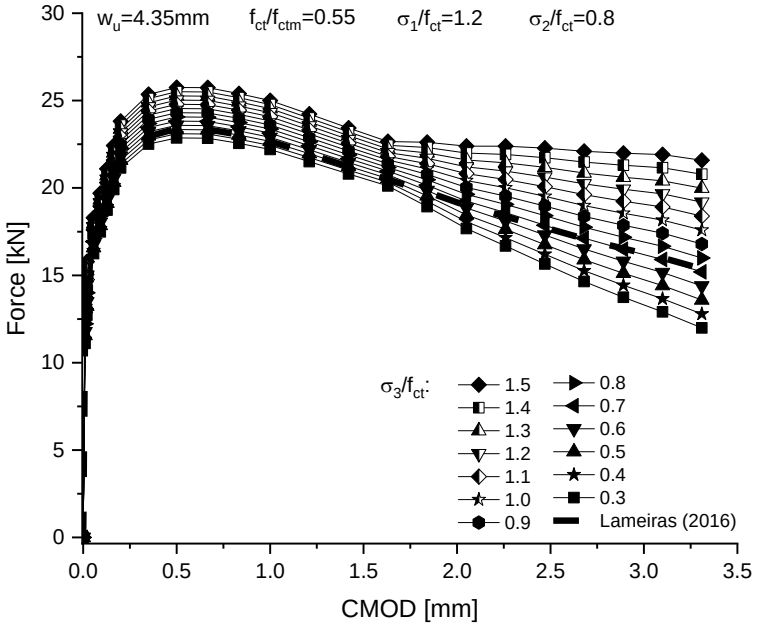


Figure 5.7 – Inverse analysis - determination of σ_3 for $w_u = 4.375$ mm compared with experimental result (Lameiras, 2016).

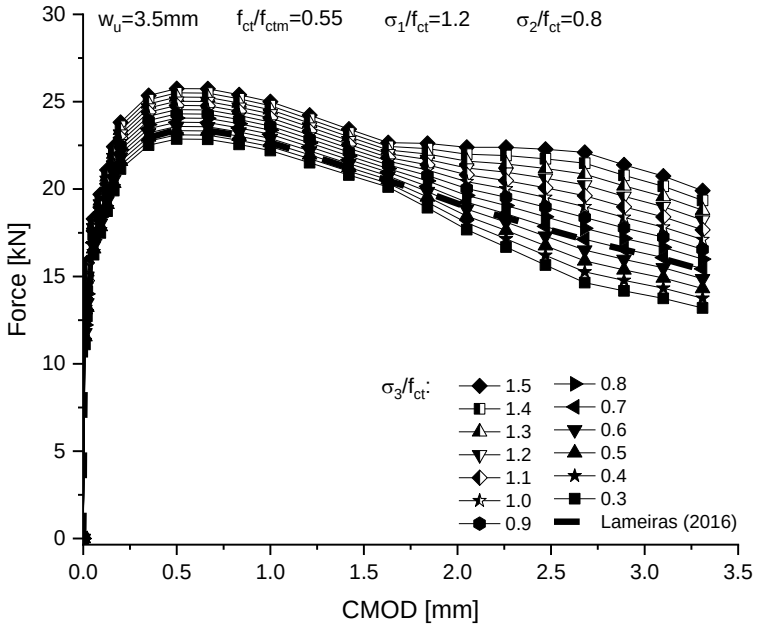


Figure 5.8 – Inverse analysis - determination of σ_3 for $w_u = 3.5$ mm compared with experimental result (Lameiras, 2016).

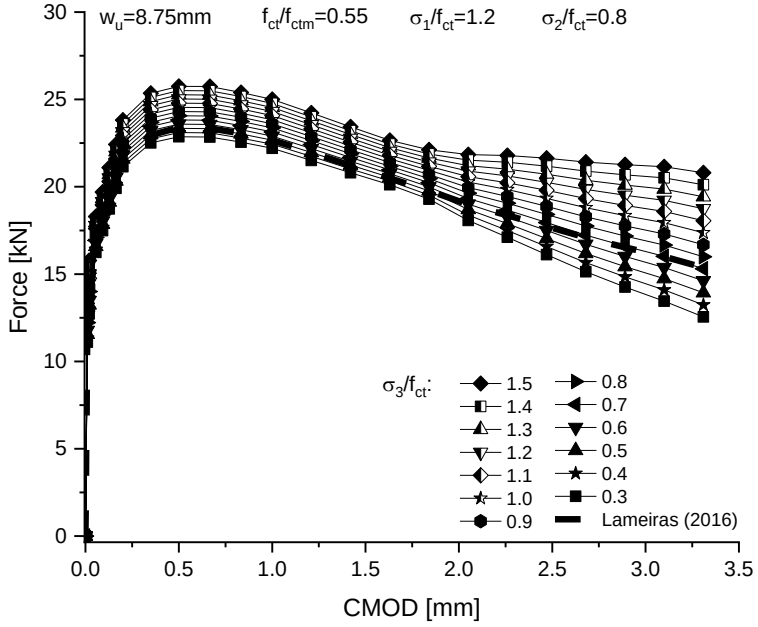


Figure 5.9 – Inverse analysis - determination of σ_3 for $w_u = 8.75$ mm compared with experimental result (Lameiras, 2016).

From the results presented in Figure 5.1 to Figure 5.9, it is possible to verify that for each situation (determination of f_{ct}, s_1, s_2, and s_3), a curve approaches the experimental response with a relatively small error between the analytical and experimental F-CMOD response (less than 10%). This fact indicates that Equations (4-6) and (4-7) well represent the variation

of the parameters and that the values of q, c_1, and c_2 were sufficient for the behavior expression.

When the secondary variable changes, i.e., Figure 5.1 vs. Figure 5.2, Figure 5.3 vs. Figure 5.4, Figure 5.5 vs. Figure 5.6, Figure 5.7 vs. Figure 5.8, and Figure 5.9, it is observed that there is sensitivity for this variable, mainly for f_{ct}, s_1, s_2, and s_3. For the variable w_u, the sensitivity is lower (Figure 5.7 to Figure 5.9). Lameiras (2016) reached a similar conclusion.

5.1.5. $F-CMOD$ Full Diagram

Figure 5.10 shows the final $F - CMOD$ diagram obtained through the analytical model for the inverse analysis and the experimental result presented (Lameiras, 2016). The determined results are close, as shown in the initial sections of the diagrams from Figures 54-60. The same approach of this study was applied to concretes C45-f90, RSFRC1%_2, and FRC60-1 (Frazão, 2019; Lameiras, 2016; Salehian, 2015; Nour, et al., 2015). The results for these concretes are presented from Figures 61-64.

The analytical model used to obtain the $F - CMOD$ curves proved to be quite adequate, even with varying characteristics of concrete and fibers. Satisfactory results were noticed even for RSFRC1%_2, which has a different type of fiber (steel fiber recycled from tires). In determining the compression behavior, the model (Salehian, 2015), which this study used to generate the $F - CMOD$ curves, employs the model described (Vipulanandan & Paul, 1990) later modified (Barros & Figueiras, 1999a) to represent $\sigma_{cc} - \varepsilon_{cc}$. This model includes equations formulated for hooked-end steel fibers. Although these equations were not calibrated for a different type of fiber; however, the results were satisfactory. This evidence is explained because the compressive behavior of the composite has less influence on the post-cracking behavior.

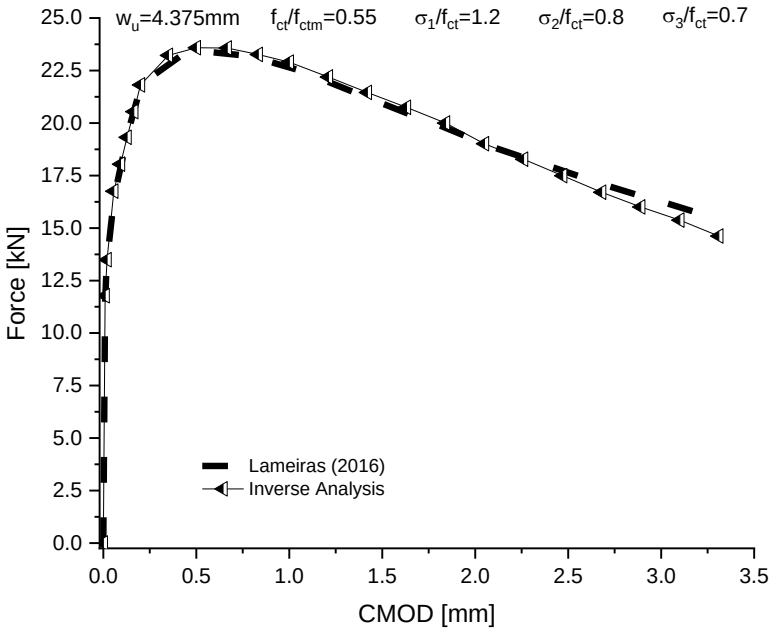


Figure 5.10 – Force–CMOD diagram for SFRSCC B concrete compared with experimental resul (Lameiras, 2016).

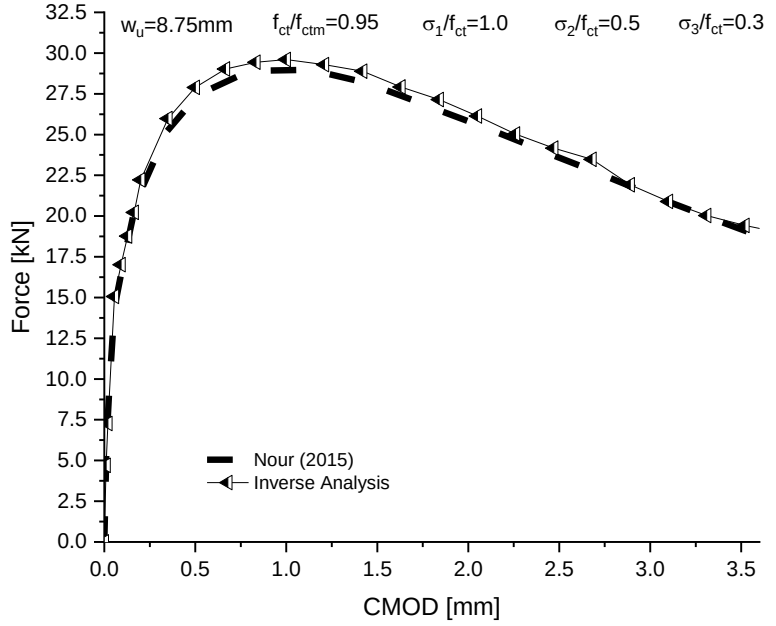


Figure 5.11 – Force–CMOD diagram for FRC60-1 concrete compared with experimental result (Nour, et al., 2015).

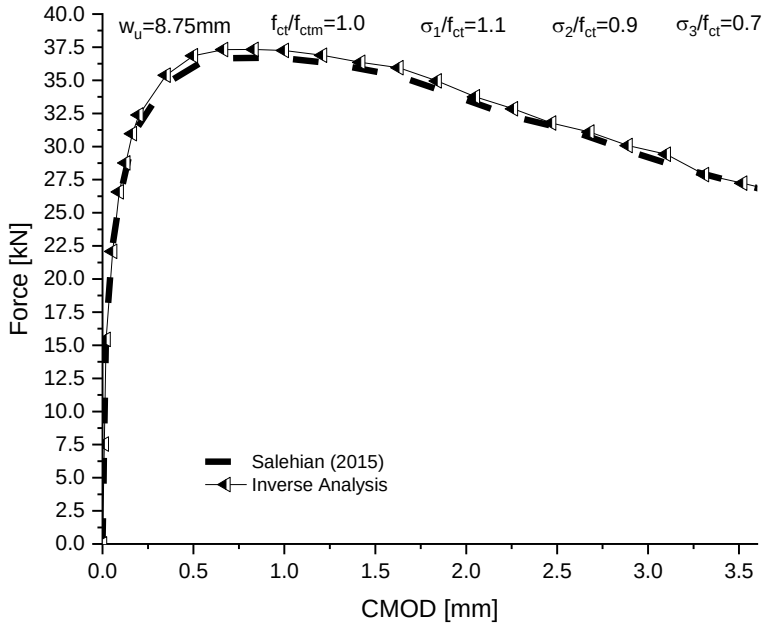


Figure 5.12 – Force–CMOD diagram for C45-f90 concrete compared with experimental result (Salehian, 2015).

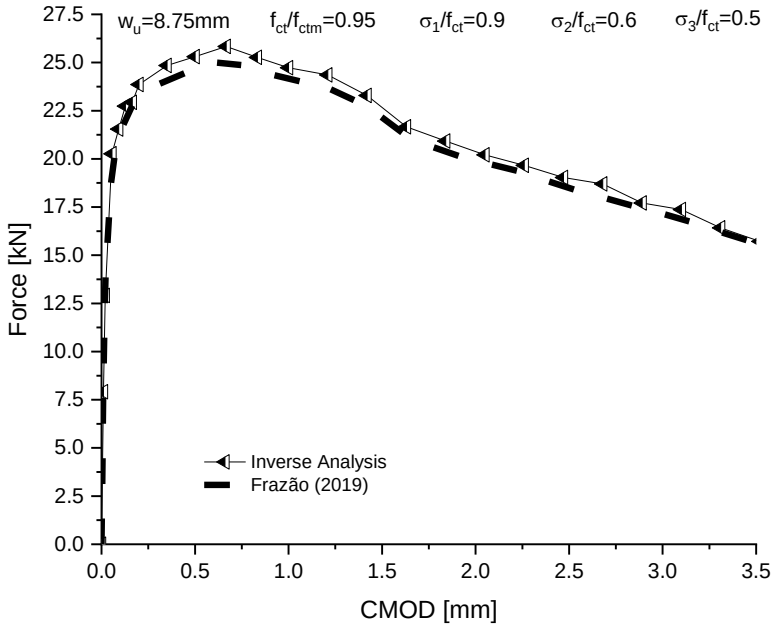


Figure 5.13 – Force–CMOD diagram for RSFRC1%_2 concrete compared with experimental result (Frazão, 2019).

5.1.6. Inverse Analysis

As a final result of the inverse analysis using the approach of this study, the $\sigma - w$ diagrams are presented in Figures 72-75. The values of $\sigma_1, \sigma_2, \sigma_3, w_1, w_2, w_3$ and w_u are shown in Table 5.1. For these parameters, the consulted authors used different values from the

literature. For comparison purposes, these parameters were graphically collected from these references, and the values found through the determined approach are presented.

Table 5.1 – Parameters from the inverse analysis for different FRC types.

Concrete	Reference	f_{ct} [MPa]	w_1 [mm]	σ_1 [-]	w_2 [mm]	σ_2 [-]	w_3 [mm]	σ_3 [-]	w_u [mm]
SFRSCC B	This work	2.45	0.20	2.94	1.59	1.96	2.98	1.71	4.38
	(Lameiras, 2016)	2.23	0.20	2.90	1.40	1.71	2.80	0.95	4.38
C45-f90	This work	3.79	0.20	4.17	1.59	3.41	2.98	2.65	8.75
	(Salehian, 2015)	3.60	0.20	3.92	1.50	3.25	2.50	2.36	5.83
RSFRC1%_2	This work	3.60	0.13	3.24	1.05	2.16	1.96	1.80	5.75
	(Frazão, 2019)	3.34	0.10	3.20	0.95	2.07	1.80	1.67	5.00
FRC60-1	This work	3.30	0.34	3.30	2.72	1.65	5.11	0.99	15
	(Nour, et al., 2015)	3.26	0.30	3.16	2.40	1.49	4.80	0.82	11.44

The parameters f_{ct}, σ_1, σ_2 and σ_3 shown average percentage differences of 6%, 3%, 9% e 30%, respectively. The highest percentage difference is observed for σ_3 when compared to σ_1 and σ_2 because σ_3 corresponds to a higher value of crack opening (w_3) resulting in a greater influence of fiber randomness concerning quantity, distribution, and orientation. The same can be explained when comparing the average percentage differences of σ_2 with σ_1.The w_u in this study presented the same value as reported in the literature (Lameiras, 2016) for SFRSCC B because the cited literature employed a similar methodology to estimate w_u based on the same L_f. For RSFRC1%_2 concrete, the w_u parameter exhibited the highest perceptual difference compared to the procedure conducted in this study (>70%). This can be justified by the use of recycled fibers and the inverse analysis procedure employed by the literature (Frazão, 2019) which differs from the approach taken in this study. In the cases of C45-f90 and FRC60-1, the percentage differences were 50% and 23%, respectively. w_u was obtained by extending linear trend lines from the linear portion of the Stress vs. COD diagram to the corresponding $\sigma_u = 0$. Moreover, it should be noted that w_u occurs only for high crack openings, and therefore, it is associated with the contribution of fibers to resist stresses. Consequently, this parameter is subject to greater uncertainties in computational models due to the randomness associated with factors such as the quantity, orientation, and distribution of fibers, which vary in each tested sample. Furthermore, a study (Cunha, 2010) conducted a comparison between using w_u only up to 3.5 mm and up to 12 mm , revealing significant differences.

The f_{ctm} was calculated according to fib Model Code (fib, 2012) for concrete C45-f90 and according to EN 1992-1 for concrete SFRSCC B. This resulted in slightly different values for this parameter. However, this did not significantly affect the results up to $COD = 1.4$ mm since the value of f_{ct} determined in this study was also higher.

Some differences between the studies in the literature and the results were found here, explained by the studies using different FRC behavior models. First, the values used for w_1, w_2, and w_3 in the literature were different from those applied based on the methodology employed here. When this difference was significant, some interpolations were performed to compare with closer w values (Table 5.1). Sensitivity can be observed in the variation of parameters w_1, w_2, and w_3.

The Tensile vs. Crack width are shown in Figure 5.14 to Figure 5.17, for the considered concretes compared to the literature results. Generally, it is possible to observe a reasonable agreement between the results. In addition, the FRC behavior model used in this study is validated by the literature. In turn, the acceptable feasibility of using the methodology of this study can be stated.

Compared with different inverse analysis procedures, the process carried out has the advantage of establishing consistent criteria as a function of fiber length to then determine the parameters w_1, w_2, and w_3. Furthermore, the progressive method of determining the inverse analysis parameters leads to quick and efficient processing of the developed algorithm.

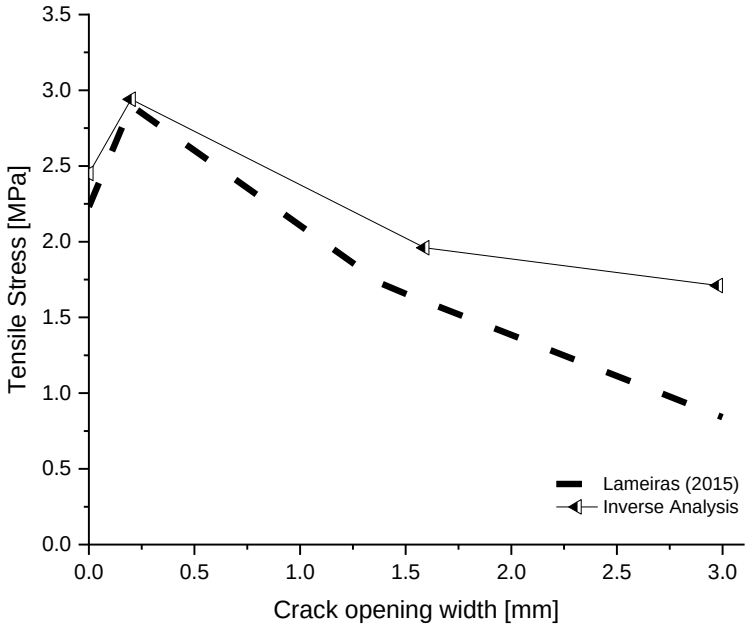


Figure 5.14 – Stress–COD diagram obtained through inverse analysis for concrete SFRSCC B compared with experimental result (Lameiras, 2016).

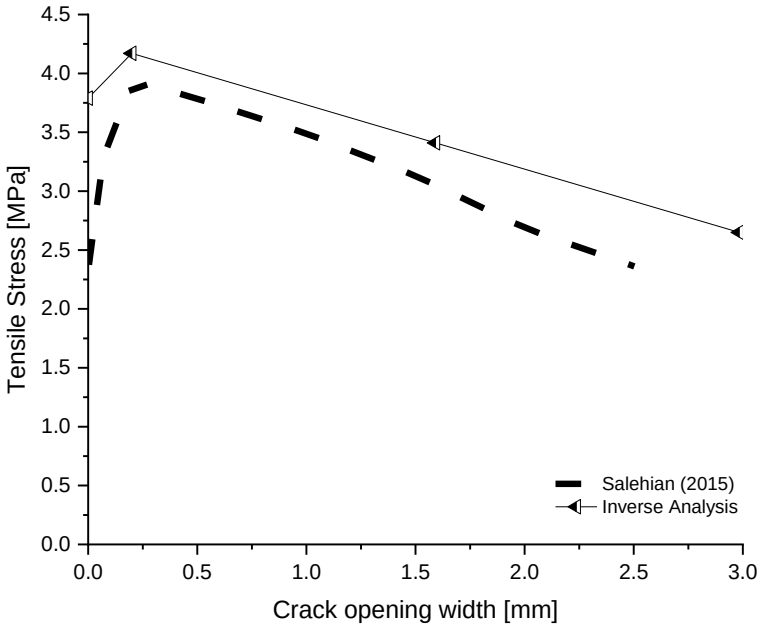


Figure 5.15 – Stress–COD diagram obtained through inverse analysis for concrete C45-f90 compared with experimental result (Salehian, 2015).

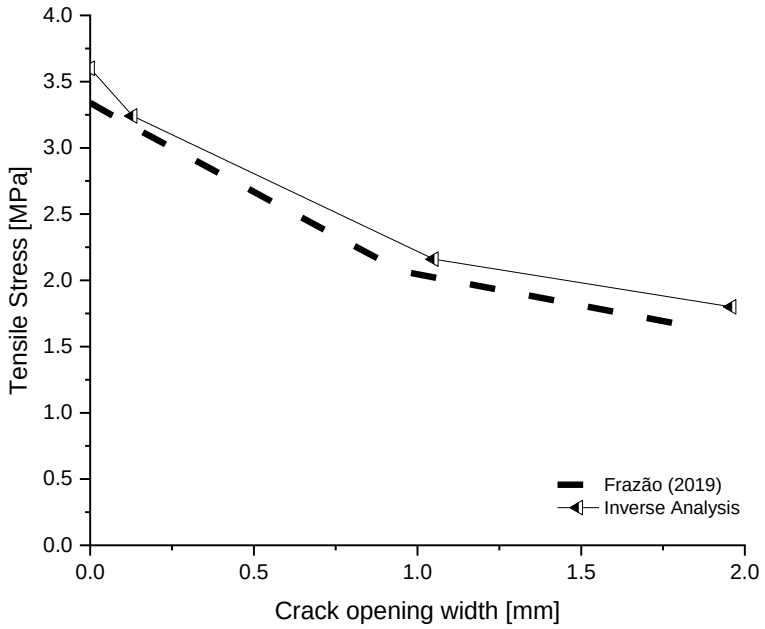


Figure 5.16 – Stress–COD diagram obtained through inverse analysis for concrete RSFRC1%_2 compared with experimental result (Frazão, 2019).

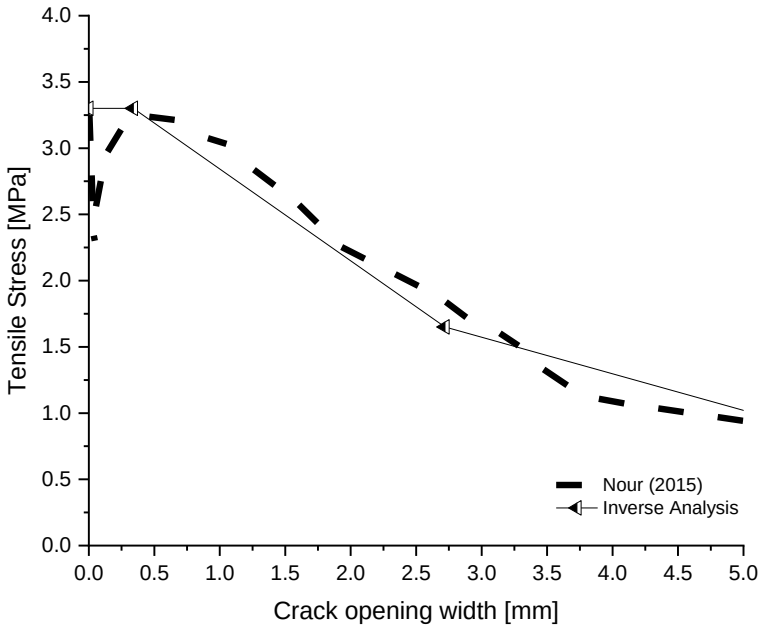


Figure 5.17 – Stress–COD diagram obtained through inverse analysis for concrete FRC60-1 compared with experimental result (Nour, et al., 2015).

5.1.7. Discussions

This work proposes a methodology for performing the inverse analysis procedure. A computational algorithm is developed based on a well-validated analytical model for the behavior of FRC. Criteria for determining parameters are adopted as a function of fiber length, which is an essential factor for the tensile behavior of this type of concrete.

A progressive procedure for parameter estimation is proposed. The methodology proved to be quick (the analyses were performed in less than two minutes) and effective in determining stress vs. COD. The procedure is adequately validated by comparing the results obtained with different literature and for different types of concrete and fibers with various characteristics. The results indicated a sensitivity of the developed algorithm to the inverse analysis parameters.

The curves obtained are similar to the experimental responses in the literature, even with the relatively simple methodology to perform the inverse analysis procedure employed in determining $F - CMOD$ and $\sigma - w$.

With the development of this study, it is possible to conclude that:

- The inverse analysis can be performed with the procedure proposed, obtaining results compatible with the experimental response, considering a margin of error between the analytical and experimental $F - CMOD$ response of less than 10%;
- The algorithm developed in this study employs a methodology that features a reduced number of iterations compared to conventional inverse analysis methodologies (Salehian, 2015; Nour, et al., 2015), providing faster processing;
- This procedure does not require FEM software.

As a proposal for future studies, applying the procedure used in this study for larger structures and applying this methodology in other types of bending tests are recommended.

5.2. Compressive tests

The experimental determination of the compressive strength (f_{cm}) followed the prescribed methodologies outlined in NBR 5739 (Associação Brasileira de Normas Técnicas, 2018).

The average compressive strength results (f_{cm}) from four of the tested samples are shown in the Table 5.2.

Table 5.2 – average compressive strength results (f_{cm}) in MPa for each type of concrete.

Symbology	C-1	C-2	C-3	C-4	C-5	C-6	C-7	C-8	C-9	C-10	C-11	C-12
f_{cm} [MPa]	24.5	23.7	23.8	24.7	22.1	22.6	43.3	41.9	37.7	45.6	42.2	35.8

5.3. 3PBT

Since the samples used for the UTT, MSCBT, and ST tests in this study were extracted from the 3PBT specimens from a work by the same research group as this thesis (Cardoso, et al., 2021), this section is dedicated to presenting the results obtained from the tests conducted on the 3PBT samples.

In most three-point bending tests, a single primary crack was observed, particularly in concretes with lower fiber volumes. In specimens where fibers provided minimal reinforcement, the crack tended to be nearly vertical. In isolated cases, multiple cracks developed in the load application region.

The Figure 5.18a-f show the results for the 3PBT *F-CMOD* (Force vs. Crack Mouth Opening Displacement) for concretes with 20 MPa, according to the symbology of Table 4.2. The gray hatch represents the envelope (for 95% of confidence level) that corresponds to the area between Upper Bound (U.B.) and Lower Bound (L.B.). The solid black line corresponds to the average of the experimental results.

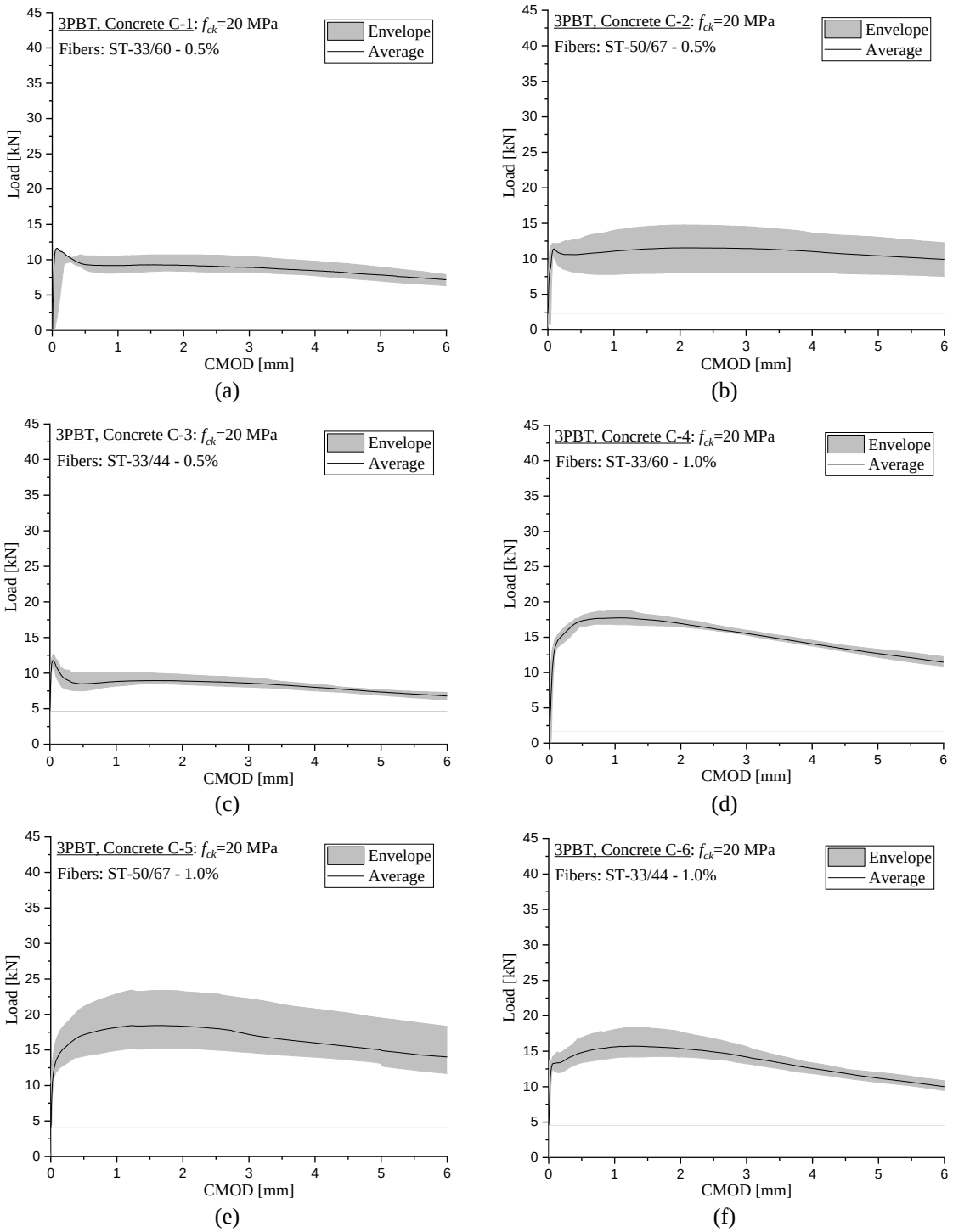


Figure 5.18 – *F-CMOD* results for 3PBT samples for concretes with 20 MPa: (a) C-1, (b) C-2, (c) C-3, (d) C-4, (e) C-5 and (f) C-6. Adapted from Cardoso (2021).

The Figure 5.19a-f shows the *F-CMOD* results for concretes with 40 MPa. The average of the experimental results and the area between Upper Bound (U.B.) and Lower Bound (L.B.) presents the same form of representation as the Figure 5.19a-f, with the solid line and the hatched area, respectively.

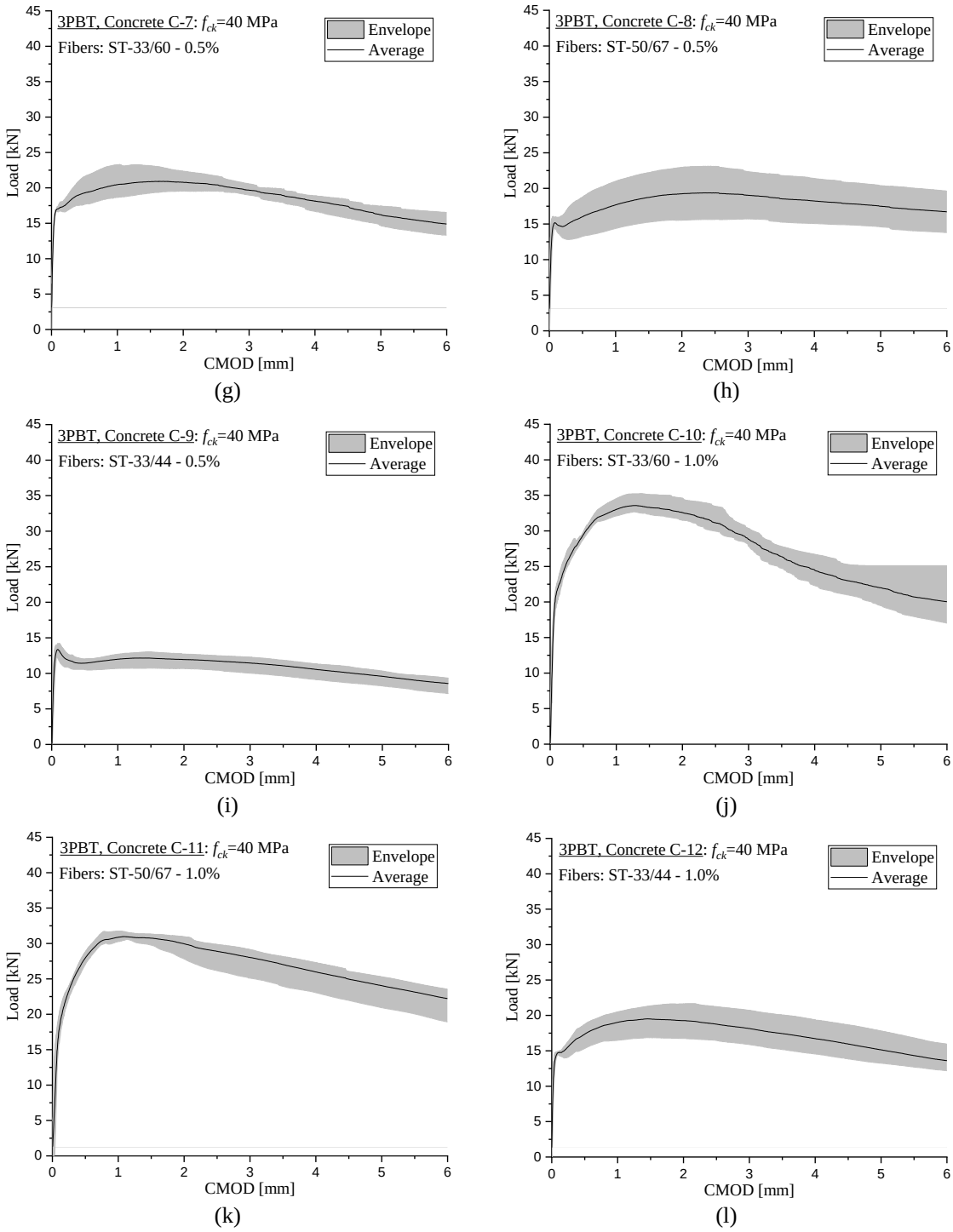


Figure 5.19 – *F-CMOD* results for 3PBT samples for concretes with 40 MPa: (a) C-7, (b) C-8, (c) C-9, (d) C-10, (e) C-11 and (f) C-12. Adapted from Cardoso (2021).

The Table 5.3 presents the post-cracking parameters for the 3PBT. The residual strengths (f_{r1}, f_{r2}, f_{r3} and f_{r4}) correspond to CMOD values (fib, 2012): 0.5, 1.5, 2.5, and 3.5 mm. The

values of $f_{fct,L}$ and f_{ct} are also presented. The $f_{fct,L}$ is determined according to the fib Model Code 2010 (fib, 2012), with equation (3-2). The f_{ct} was estimated at 70% of the $f_{fct,L}$ (Cardoso, et al., 2021).

Table 5.3 – Values obtained (Average and CoV.) from 3PBT for: Residual strengths (f_{r1}, f_{r2}, f_{r3} and f_{r4}), $f_{fct,L}$ and f_{ct}. Adapted from Cardoso (2021).

Concrete Mix	Avg./CoV.	$f_{fct,L}$ [MPa]	f_{ct} [MPa]	Residual Flexural Strength			
				f_{r1} [MPa]	f_{r2} [MPa]	f_{r3} [MPa]	f_{r4} [MPa]
C-1	Avg.	3.07	2.15	3.06	3.07	3.02	2.86
	CoV	16.9%	16.9%	8.5%	10.5%	10.8%	9.8%
C-2	Avg.	3.68	2.58	3.69	4.01	4.05	3.95
	CoV	4.4%	4.4%	20.1%	24.3%	24.0%	23.3%
C-3	Avg.	3.76	2.63	2.72	2.86	2.81	2.66
	CoV	8.1%	8.1%	12.6%	8.1%	6.6%	5.1%
C-4	Avg.	3.92	2.75	5.73	5.58	5.07	4.57
	CoV	10.4%	10.4%	4.4%	4.9%	5.7%	7.8%
C-5	Avg.	3.97	2.78	5.48	5.89	5.77	5.28
	CoV	14.8%	14.8%	18.9%	20.1%	18.2%	19.4%
C-6	Avg.	4.17	2.92	4.74	5.01	4.77	4.28
	CoV	6.6%	6.6%	10.3%	11.6%	8.6%	5.8%
C-7	Avg.	5.17	3.62	6.17	6.68	6.54	6.06
	CoV	2.4%	2.4%	9.0%	7.9%	4.7%	4.1%
C-8	Avg.	4.87	3.41	5.52	6.48	6.73	6.40
	CoV	3.9%	3.9%	9.6%	11.2%	10.8%	10.0%
C-9	Avg.	4.10	2.87	3.66	3.88	3.75	3.54
	CoV	6.1%	6.1%	5.6%	8.3%	7.8%	9.0%
C-10	Avg.	5.28	3.69	9.42	10.66	9.96	8.44
	CoV	10.7%	10.7%	1.6%	3.9%	5.2%	4.8%
C-11	Avg.	4.07	2.85	8.95	9.84	9.24	8.65
	CoV	37.7%	37.7%	2.9%	2.3%	6.3%	7.6%
C-12	Avg.	4.41	3.08	5.82	6.31	5.94	5.46
	CoV	6.2%	6.2%	3.6%	7.9%	12.5%	15.2%

Significant result dispersion was observed due to non-uniform fiber distribution, consistent with prior studies (Correal & Herrána, 2018; Banthia, et al., 2014; Carrilo, et al., 2017;

Conforti, et al., 2017). However, concretes with ST-33/60 fibers exhibited reduced variability.

For 20 MPa concretes reinforced with ST-50/67 fibers, post-cracking strength increased significantly, with f_{r1} rising by 48.51% and f_{r3} by 42.47%. In 40 MPa concretes, these increases were 62.14% and 37.30% for a fiber volume increase from 0.5% to 1.0%. A higher compressive strength further enhanced these values, with f_{r1} and f_{r3} gains reaching 63.32% and 72.62% at 1.0% fiber content. These findings align with the literature (Venkateshwaran, et al., 2018), who highlighted the role of matrix strength in fiber anchorage and activation.

Similarly, increasing ST-33/44 fiber content from 0.5% to 1.0% in 20 MPa concrete led to f_{r1} and f_{r3} improvements of 74.26% and 69.75%, respectively, while for 40 MPa concrete, these values increased by approximately 59%. When keeping fiber content constant and increasing compressive strength, f_{r1} and f_{r3} rose by 34.56% and 33.45% (0.5% fiber) and by 22.78% and 24.53% (1.0% fiber).

Comparisons between ST-33/44 and ST-33/60 fibers indicated that the latter provided superior residual strength due to its higher aspect ratio, corroborating a result already found (Abbass, et al., 2018).

ST-33/60 fiber was presented the best performance for the f_{r1} and f_{r3} parameters. This can be justified by the fact that this type of fiber has a higher number of fibers per gram and a high aspect ratio, which already has a relationship established with the residual resistances (Kwan & Chu, 2018; Abbass, et al., 2018). Secondly, the concretes with ST-50/67 fiber also presents good results due to its larger size that guarantees effective anchoring in the matrix. The ST-33/60 fiber presents better residual strength results than the ST-33/44 because, although these fibers have the same size, the ST-33/60 has a larger aspect ratio, which contributes to greater strength. Similar conclusions are found in the literature (Cardoso, et al., 2021).

Comparing the average f_{r1} and f_{r3} of concretes with different strength classes, it is observed that concretes with 40 MPa present, on average, values 55% and 65% higher than concretes with 20 MPa for f_{r1} and f_{r3}, respectively.

5.4. MSCBT (conception)

The experimental result of the large-scale experimental study, according described in the section 4.14, involving 72 MSCBT samples with 12 concrete mixes for SFRSCC (Table 4.2) is presented in this section. Concretes vary in two strength classes (20 and 40 MPa) and fibers vary in two volumes (0.5 and 1.0%) and three types (ST-33/60, ST-33/44 and ST-50/67). Considering these different characteristics, the F-CMOD diagrams of these concretes are compared in order to verify the sensitivity of the test to these parameters. For this comparison, the area under the diagram is considered.

A linear regression process is carried out with the results. The test indicated that it is promising because showed sensitivity for SFRSCC parameters such as increasing the volume of fibers and strength of concrete, as well as diferents type of fiber in concrete. The bending behavior and failure modes occurred as expected for 3PBT with a good success rate.

5.4.1. Concrete Mixture

The molding carachteristics of the concrete used in this research are described in section 4.3 and the concrete components are shown in Table 4.1. Maccaferri steel fibers are used in this work. The characteristics of diameter (d), length (l) and aspect ratio (l/d) of each fiber type are described in the Table 4.3.

5.4.2. Compressive tests

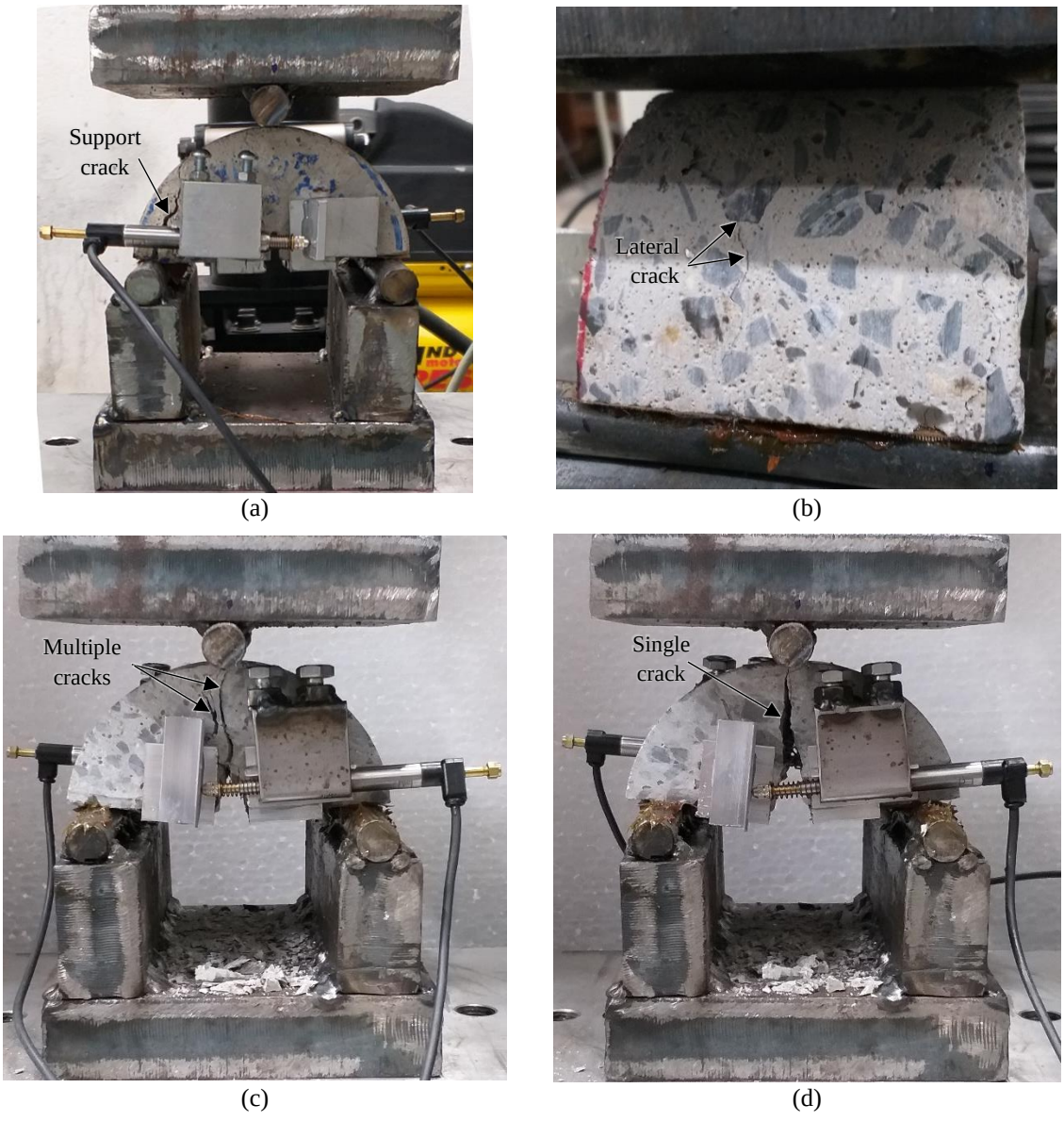
The experimental determination of the compressive strength (f_{cm}) is described in 5.2 and the results are shown in the Table 5.2.

5.4.3. *F-CMOD* results (MSCBT)

The procedure for obtaining samples for the MSCBT is carried out as described in item 4.6.

The first samples tested for the MSCBT showed irregularity on the underside surface. This caused stress concentrations during the test and resulted in an unexpected failure mode, with cracks occurring outside the notch region. Some of these irregular cracks occurred from the support (Figure 5.20a), others in a direction approximately transverse to the notch, on the lateral face of the sample (Figure 5.20b) and others with multiple crack (Figure 5.20c). Samples with these characteristics corresponded to 7% of the total tests. Therefore, they

were discarded from the analyses. In most tested samples for MSCBT (more than 90%), the rupture mode occurred with the appearance of a single crack from the notch to the top of the sample (Figure 5.20d). In general, the behavior of the tested samples was similar to that of a beam in bending with a notch, as occurs with the 3PBT. A small compressed area is observed at the top of the sample.



(a) (b)

(c) (d)

Figure 5.20 – Illustration of the types of cracks during the MSCBT: (a) Support crack, (b) Lateral crack, (c) Multiple cracks, and (d) Single crack.

The Figure 5.21a-f show the results for the MSCBT *F-CMOD* for concrete with 20 MPa and the Figure 5.22a-f show the results for concrete with 40 MPa, according to the symbology of Table 4.2. The gray hatch represents the envelope (for 95% of confidence level) that

corresponds to the area between Upper Bound (U.B.) and Lower Bound (L.B.). The solid black line corresponds to the average.

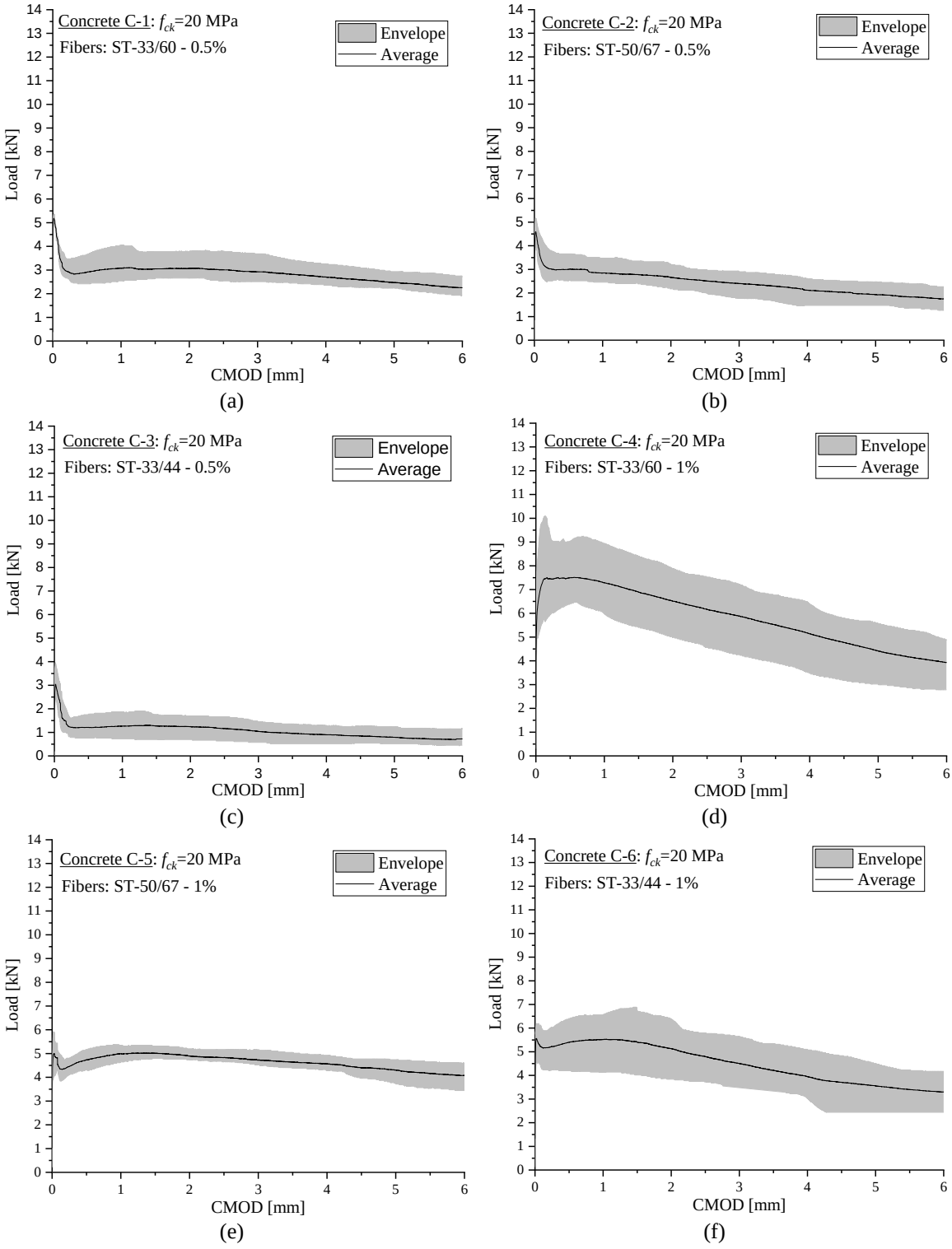


Figure 5.21 – *F-CMOD* results for MSCBT samples with a thickness of 75 mm for concretes with 20 MPa: (a) C-1, (b) C-2, (c) C-3, (d) C-4, (e) C-5 and (f) C-6.

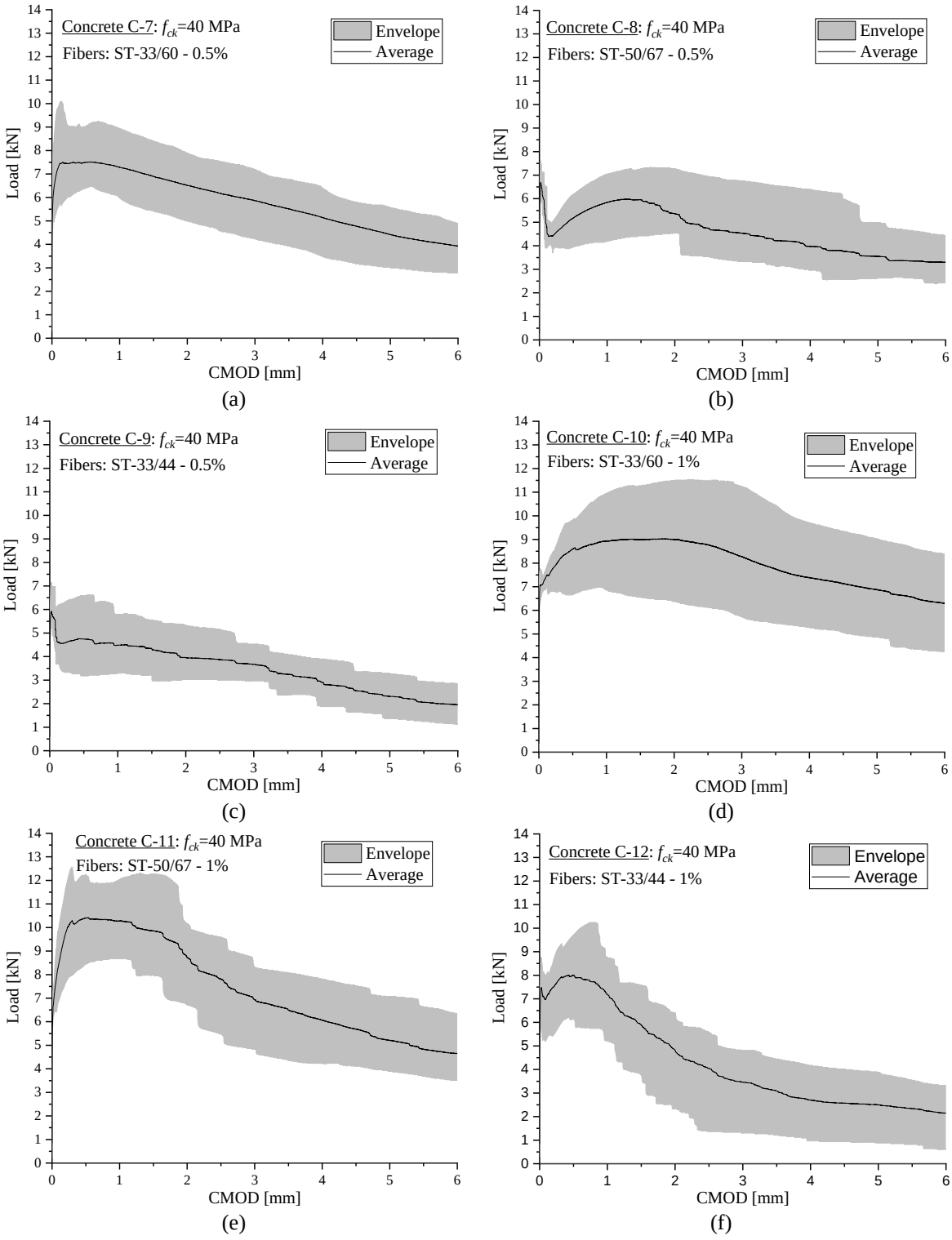


Figure 5.22 – *F-CMOD* results for MSCBT samples with a thickness of 75 mm for concretes with 40 MPa: (a) C-7, (b) C-8, (c) C-9, (d) C-10, (e) C-11 and (f) C-12.

The tested samples corresponding to concretes which has the highest percentage by volume of fibers (1.0%) presented a better performance. The evidence of this fact can be visualized

graphically through diagrams of concretes with the same strength and fiber type, but different fiber contents. Comparing the diagrams of the concretes: C-1, C-2, C-3, C-7, C-8, C-9, which present a volume of 0.5% of fibers and, respectively, the same strengths and type of fibers of concretes: C-4, C-5, C-6, C-10, C-11, C-12, it is possible to verify this fact. Thus, the MSCBT demonstrated sensitivity when there is variation in the fiber volume parameter. This is an important characteristic for using the test, since it is already expected that the increase in fiber volume in the range of values studied in this work will generate, as a consequence, a greater performance of the SFRSCC (Lameiras, 2016; Cardoso, et al., 2021).

When viewing the values for the areas of the F-CMOD diagrams, the same conclusion can also be seen when these same concretes are compared. The Table 5.4 shows these areas for each type of concrete (C-1, C-2, C-3, ..., C-12) for the average (Avg.), upper bound (U.B.) and lower bound (L.B.). The Avg. corresponds to the average between the results of the specimens tested for each type of concrete. The L.B. and the U.B. correspond to the result obtained from the sample that presented the lowest and highest load value, respectively, for each type of concrete according to a confidence coefficient of 95%. The Table 5.4 also shown the absolute difference between Avg. and the respectives U.B. and L.B. in absolute values (abs.) and percentages (%) for each type of concrete.

Table 5.4 – Average (Avg.), upper bound (U.B.) and lower bound (L.B.) values for the areas of the *F-CMOD* diagrams for each type of concrete.

areas [kN.mm]	C-1	C-2	C-3	C-4	C-5	C-6	C-7	C-8	C-9	C-10	C-11	C-12
U.B.	20.8	17.8	9.1	43.0	30.1	33.2	43.0	37.4	27.7	60.7	55.1	34.2
Avg.	16.9	14.5	6.3	34.8	27.7	26.9	34.9	27.2	20.8	47.4	44.4	25.5
L.B.	14.7	11.5	3.8	26.1	25.7	20.2	26.1	20.7	15.0	34.5	33.5	13.7
Avg.–L.B. (abs.)	2.3	3.1	2.6	8.8	2.1	6.7	8.8	6.6	5.9	13.0	10.9	11.8
Avg.–L.B. (%)	13.4	21.1	40.8	25.2	7.4	24.9	25.2	24.1	28.1	27.3	24.5	46.1
U.B.–Avg. (abs.)	3.9	3.3	2.8	8.1	2.4	6.3	8.1	10.2	6.9	13.2	10.7	8.7
U.B.–Avg. (%)	22.7	22.8	44.0	23.3	8.5	23.5	23.3	37.4	33.0	27.9	24.1	34.1

From the Table 5.4, can be seen that the Avg. differed less than 30% from U.B. and L.B., with the exception of concretes C-3 and C-12. Differences of this order of magnitude can also be found in the literature (Lameiras, 2016; Cardoso, et al., 2021) for the 3PBT. Although this level of variability might initially appear significant, it was considered relatively low, particularly when contextualized by the performance of the traditional Three-Point Bending

Test (3PBT), which demonstrated a comparable degree of dispersion despite involving a substantially larger fracture surface. This outcome was somewhat unexpected, as the reduced fracture area in the MSCBT specimens was anticipated to result in greater sensitivity to fiber distribution and orientation, thereby increasing the scatter in the measured responses.

Several factors may account for this lower-than-expected dispersion. Firstly, the MSCBT configuration may inherently promote a more stable and localized crack propagation mechanism, mitigating the influence of heterogeneous fiber distribution within the cross-section. Additionally, the semi-circular geometry and the notch position may induce a more consistent stress field in the fracture process zone, thereby reducing variability. These findings suggest that, under controlled conditions, the MSCBT may offer a reliable alternative to conventional flexural testing methods, even when performed on specimens with smaller fracture areas. Further investigation into the underlying mechanisms governing fracture consistency in MSCBT could yield valuable insights for standardizing and optimizing this testing methodology.

The observed relationships between the average area of *F-CMOD* diagram for each kind of concrete analyzed in this study and the average number of effective fibers per cm^2 at the fracture surface of MSCBT specimens are depicted in Figure 5.23. The R^2 parameter of 0.72 found in this study is consistent with the ranges reported in the literature for 3PBT in similar concretes: 0.51 to 0.78 (Lameiras, 2016) and 0.38 to 0.72 (Cardoso, 2020). This confirms the sensitivity of MSCBT to the fiber content parameter.

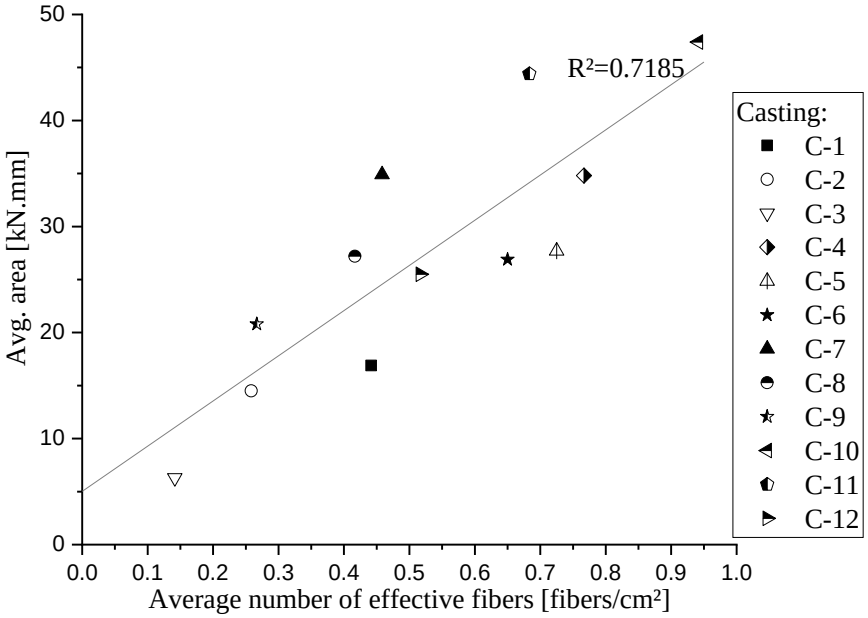


Figure 5.23 – Relationships between the average number of effective fibers per square centimeter and the average area of F-CMOD diagram for each kind of concrete.

The results of the 3PBT are typically analyzed with residual strengths (fib, 2012), which are obtained according to equation (3-1). The linear regression process has been previously employed to determine representative equations for different types of concrete based on experimental results of the 3PBT (Cardoso, et al., 2021). However, the usual method for determining residual strengths (fib, 2012) in the 3PBT may not be directly applicable for the MSCBT, given the geometric differences and the fact that this is a newly proposed test. In this study, instead of using residual strengths, linear regression was performed based on the loads monitored during the test corresponding to CMOD (fib, 2012) values: 0.5, 1.0, 2.5, and 3.5 mm. The average load for each CMOD (F_1, F_2, F_3 and F_4) and for each type of concrete are presented in the Table 5.5. In the same table, values of $f_{fct,L}$ and f_{ct} are also presented. $f_{fct,L}$ is determined according to the *fib* Model Code 2010 (fib, 2012), with equation (3-2). f_{ct} was estimated at 70% of the $f_{fct,L}$ (Cardoso, 2020).

Table 5.5 – Parameters $f_{fct,L}$, f_{ct}, F_1, F_2, F_3 and F_4 determined experimentally for MSCBT with thickness 75mm.

Concrete		$f_{fct,L}$ [MPa]	f_{ct} [MPa]	Loads			
				F_1 [kN]	F_2 [kN]	F_3 [kN]	F_4 [kN]
C-1	Avg.	3.93	2.75	2.91	3.05	3.01	2.82
	CoV.	5.21%	5.21%	18.14%	16.82%	18.83%	15.82%
C-2	Avg.	3.29	2.30	3.01	2.79	2.52	2.29
	CoV.	19.97%	19.97%	11.74%	11.68%	14.71%	17.34%
C-3	Avg.	3.30	2.31	1.20	1.27	1.16	0.96
	CoV.	18.50%	18.50%	34.28%	35.78%	34.23%	30.06%
C-4	Avg.	4.33	3.03	7.50	6.90	6.16	5.51
	CoV.	20.40%	20.40%	14.86%	15.36%	16.64%	17.19%
C-5	Avg.	4.04	2.83	4.74	5.01	4.83	4.65
	CoV.	13.56%	13.56%	9.31%	5.04%	4.68%	6.38%
C-6	Avg.	2.96	2.07	5.41	5.41	4.79	4.21
	CoV.	17.66%	17.66%	15.43%	18.06%	16.80%	19.10%
C-7	Avg.	4.66	3.26	7.36	7.51	7.06	6.54
	CoV.	6.62%	6.62%	29.25%	28.32%	20.97%	17.73%
C-8	Avg.	4.56	3.19	6.16	6.86	4.50	4.20
	CoV.	3.27%	3.27%	18.94%	21.21%	23.43%	29.29%
C-9	Avg.	4.33	3.03	4.74	4.35	3.87	3.25
	CoV.	1.53%	1.53%	29.80%	22.45%	24.80%	23.43%
C-10	Avg.	4.74	3.32	8.59	9.00	8.78	7.74
	CoV.	5.80%	5.80%	17.38%	22.53%	25.54%	27.53%
C-11	Avg.	4.76	3.33	10.41	9.86	7.81	6.50
	CoV.	3.48%	3.48%	14.79%	18.69%	22.97%	23.89%
C-12	Avg.	4.51	3.16	8.00	5.89	4.04	3.09
	CoV.	6.20%	6.20%	18.52%	26.35%	45.49%	47.69%

F_1, F_2, F_3 and F_4 are determined experimentally. Avg. is the average of the tested samples. CoV. is the Coefficient of Variation.

For the parameters $f_{fct,L}$, f_{ct}, F_1, F_2, F_3 and F_4, lower values are found for concretes with 20 MPa (C-1, C-2, C-3, C-4, C-5 and C-6) when are compared, respectivelly to concretes with 40 MPa (C-7, C-8, C-9, C-10, C-11 and C-12). The exception occurs only when comparing C-6 with C-12 for F_3 and F_4. This can be justified by the high dispersion found precisely in these two parameters for concrete C-12 (exceeding 45%). The MSCBT sample is subject to bending during the test. Then, the greater resistance to compression (concretes with 40 MPa) contributes to the better behavior of the compressive region of the sample during the test, making the sample present a better performance (Salehian, 2015; Carvalho & Lameiras, 2023a; Carvalho & Lameiras, 2023b).

When concretes with different fiber content are analyzed for the F_1, F_2, F_3 and F_4 parameters (Table 5.5), it appears that for the same concrete strength and fiber type, the performance is better for concretes with higher fiber content. This can be observed by comparing, respectively, the parameters obtained for the concretes: C-1, C-2, C-3, C-7, C-8, C-9 (with 0.5% of fiber content) with the concretes: C-4, C-5, C-6, C-10, C-11, C-12 (with 1.0% of fiber content). The exception occurs only when comparing C-9 and C-12 for F_4. This can be justified by the high dispersion found for this parameter for C-12, as previously explained. This result is also quite expected, because the increase in fiber content (concretes with 1.0% of fiber content) tends to result in improvement the post-cracking behavior of the SFRSCC.

Still analyzing concretes with different fiber contents, it is verified that when we compare concretes C-3 with C-6, there is no increase in the f_{ct} and $f_{fct,L}$ parameters for concretes with higher fiber contents. Although the C-6 has higher fiber content, it does not have higher values for f_{ct} and $f_{fct,L}$. This is because these parameters are more influenced by concrete strength than fiber content.

Analyzing the different types of fibers studied, the concretes with ST-33/60 fiber was presented the best performance for the F_1, F_2, F_3 and F_4 parameters. This can be justified by the fact that this type of fiber has a higher number of fibers per gram and a high aspect ratio, which already has a relationship established with the residual resistances (Kwan & Chu, 2018; Abbass, et al., 2018). Secondly, the concretes with ST-50/67 fiber also presents good results due to its larger size that guarantees effective anchoring in the matrix. The ST-33/60 fiber presents better residual strength results than the ST-33/44 because, although these fibers have the same size, the ST-33/60 has a larger aspect ratio, which contributes to greater strength. Similar conclusions are found in the literature (Cardoso, et al., 2021).

5.4.4. F_i equations

After obtaining the results of the *F-CMOD* diagrams, a linear regression procedure was performed using the least squares method to determine equations that fit the parameters F_i. For this, the equations of Domski and Katzer (Domski & Katzer, 2020) were used, as also already done by Cardoso, Lameiras and Capuzzo (Cardoso, et al., 2021). However, these authors relied on 3PBT using $f_{r,i}$. In this work, the procedure is performed for the MSCBT using F_i.

From the procedure, four equations are determined, one for each F_i, which are set as a function of the volume of fibers, the aspect ratio and the square root of the concrete compressive strength. The sum of the product of these parameters multiplied by coefficients, equated to each of the F_i determines the model equations. The coefficients are determined by applying the procedure.

In this work, the equations obtained for F_1, F_2, F_3 and F_4 that characterize the post-cracking behavior of the SFRSCC are presented (equations (5-1)-(5-4)). For these equations, the r^2 statistical measures obtained were respectively: 0.81, 0.76, 0.63 and 0.52. The fact that these values are decreasing is expected since randomness factors such as fiber orientation and quantity in the sample sections have a greater effect at more advanced loading stages. Although these values were not very high, the r^2 parameter for SFRSCC in the order of 0.5 can be found in the literature (Lameiras, 2016) for 3PBT with similar concretes.

$$F_1=2.209(f_c)^{0.5}+0.005(l_f/d_f)+3.215(W_f)-11.357 \quad (5\text{-}1)$$

$$F_2=2.145(f_c)^{0.5}+0.045(l_f/d_f)+2.584(W_f)-12.714 \quad (5\text{-}2)$$

$$F_3=1.721(f_c)^{0.5}+0.046(l_f/d_f)+2.039(W_f)-10.412 \quad (5\text{-}3)$$

$$F_4=1.440(f_c)^{0.5}+0.044(l_f/d_f)+1.421(W_f)-8.539 \quad (5\text{-}4)$$

In wich:

F_1, F_2, F_3 and F_4 are the predicted loads referring to the crack openings of 0.5 mm, 1.5 mm, 2.5 mm and 3.5 mm, respectively;

l_f is the fiber length;

d_f is the fiber diameter;

W_f is the fiber volume;

f_c is the compressive strength of the concrete.

The equations (5-1)-(5-4) obtained with the model were used to determine the predicted loads for the concretes in this work, using the values in Table 4.2 for l_f, d_f, W_f and f_c as input data. A comparison between these results, as well as the error found between the predicted (pred.) and experimental (exp.) values are presented in the Table 5.6.

Table 5.6 – Predicted and experimental values of the parameters F_1, F_2, F_3 and F_4, as well as error (between predicted and experimental values) for MSCBT.

Concrete	-	F_1 [MPa]	F_2 [MPa]	F_3 [MPa]	F_4 [MPa]
C-1	exp.	2.91	3.05	3.01	2.82
	pred.	2.19	2.47	2.33	2.24
	error	24.63%	18.95%	19.87%	20.33%
C-2	exp.	1.20	1.27	1.16	0.96
	pred.	2.28	2.79	2.64	2.52
	error	90.83%	119.17%	121.09%	163.71%
C-3	exp.	3.01	2.79	2.52	2.29
	pred.	2.46	2.01	1.79	1.66
	error	18.19%	28.01%	40.35%	27.47%
C-4	exp.	3.04	3.04	2.70	2.37
	pred.	4.06	3.98	3.52	3.07
	error	33.64%	30.87%	15.73%	29.83%
C-5	exp.	4.52	4.78	4.61	4.43
	pred.	2.43	2.85	2.69	2.51
	error	46.10%	40.43%	40.52%	43.29%
C-6	exp.	4.22	3.88	3.47	3.10
	pred.	4.35	3.48	2.95	2.44
	error	3.27%	10.27%	29.93%	21.13%
C-7	exp.	7.36	7.51	7.06	6.54
	pred.	6.29	6.36	5.45	4.81
	error	14.62%	15.30%	26.02%	26.49%
C-8	exp.	5.17	5.95	4.73	4.22
	pred.	6.13	6.47	5.60	4.97
	error	18.53%	8.77%	8.29%	17.81%
C-9	exp.	4.74	4.35	3.87	3.25
	pred.	6.04	5.35	4.47	3.83
	error	27.37%	22.91%	5.81%	17.91%
C-10	exp.	8.59	9.00	8.78	7.74
	pred.	8.71	8.38	7.04	5.96
	error	1.43%	6.88%	18.02%	23.02%
C-11	exp.	10.05	9.49	7.45	6.13
	pred.	8.46	8.36	7.09	6.01
	error	15.73%	11.97%	29.46%	2.03%
C-12	exp.	8.00	5.54	3.69	2.59
	pred.	7.66	6.59	5.44	4.47
	error	4.30%	18.84%	31.97%	72.77%

The average error found between predicted and experimental values for parameters F_1, F_2, F_3 and F_4 was approximately 30%. For concrete C-2, the error was quite high (exceeding 90%). Excluding this type of concrete from the analysis, the average error drops to 22.48%. The average errors for F_1, F_2, F_3 and F_4 were 24.89%, 27.70%, 32.25%, and 38.82%, respectively. The increase in error as F_i increases is justified by the influence of the randomness in fiber orientation and distribution, which is more pronounced at higher loading stages because the contribution of fibers to the strength is greater at these stages. Except for C-2 and C-5 concretes, high errors of the magnitude of 40% were not found. The literature (Cardoso, et al., 2021) presents an average error a little lower (around 10%) for 3PBT and an error of around 40% was also found for a given type of concrete (Lameiras, 2016).

5.4.5. Discussions

In this topic, an experimental study on 72 samples of the MSCBT is carried out. Two classes of concrete resistance (20 and 40 MPa), three types of fibers (ST-33/60, ST-50/67 and ST-33/44), as well as two fiber contents (0.5% and 1.0%) are tested. The main conclusions of this work were the following:

- It was shown that the performance of the MSCBT showed consistent results for the characterization of the post-cracking behavior of the SFRSCC.

- The MSCBT was presented as a test with sensitivity to the parameters: concrete strength, fiber type and fiber content. Samples in which these parameters were different showed variations on the load during the test parameters of the studied concretes.

- Concrete with higher fiber content, or with fiber types with a higher aspect ratio (ST-33/60 and ST-50/67) or/and smaller diameter and length (ST-33/60), showed better performance. The fiber type that presented the worst performance (ST-33/44) has a larger diameter and a smaller length and, consequently, a smaller aspect ratio. These results are already expected for bending results like 3PBT.

- The presented results show great similarity between the MSCBT and the 3PBT because bending of the sample occurs in both tests. The intensities of the loads monitored during the test, presented values lower than those expected for the 3PBT. This result was already expected, since the size and amount of fibers in the MSCBT sample section are smaller.

- The MSCBT proved to be easy to perform because the final samples are small in size and light, which facilitates the transport and preparation of the samples.

- The crack propagation mode is as expected in most of the samples tested, corresponding adequately to the occurrence of bending in the sample.

- MSCBT samples have been shown to be easily drilled out of larger structures using techniques already known to construction professionals. This makes the test results more representative of the actual structure when compared to 3PBT.

5.4.6. Comparing MSCBT with 3PBT

This section presents a brief comparison between the 3PBT and MSCBT parameters for C-12 concretes, which are used as a reference for the subsequent inverse analysis procedure. The Table 5.7 shows the results obtained from the concrete parameters for 3PBT in relation to the average (Avg.) and Coefficient of variation (CoV.). The $f_{fct,L}$ and f_{ct} showed low variation (approximately 14%) in relation to the results obtained for F_1, F_2, F_3 and F_4 the MSCBT (see Table 5.5). The parameters f_{r1}, f_{r2}, f_{r3} and f_{r4} depend on the amount of fibers in the cross section of the tested sample. This amount depends a lot on the molding conditions and may vary significantly from one sample tested to another, even for the same concrete. For MSCBT, the amount of fibers in the section was higher. This reflected in higher values of f_{r1}, f_{r2} and f_{r3} for MSCBT compared to 3PBT (see Table 5.7).

Table 5.7 – Residual flexural strength of the concretes determined for 3PBT as recommended by fib Model Code 2010 (fib, 2012).

	$f_{fct,L}$ [MPa]	f_{ct} ($0.7f_{ct,L}$) [MPa]	Residual flexural tensile strength [MPa]			
			f_{R1}	f_{R2}	f_{R3}	f_{R4}
Avg.	4.41	3.08	5.82	6.31	5.94	5.54
CoV.	6.2%	6.2%	3.6%	7.9%	12.5%	15.2%

5.5. Uniaxial Tensile Tests (UTT)

In this section, the experimental results of the Uniaxial Tensile Tests (UTT) are showed. The UTT is also known as the Double Edge Notched Tension (DENT) when the specimen has two notches on opposite sides. The test samples were obtained in accordance with the

procedure showed in section 4.7. The test setup, as well as the sample geometry, are also described in that item.

5.5.1. Concrete Mixture

During the execution of the UTT, the implementation difficulties described in 3.5.1 arose and have also been reported in the literature (Planas, 2007; Mudadu, et al., 2018; van Mier & van Vliet, 2002; Hordijk, 1991). Therefore, fifteen samples had to be tested to obtain three successful monitoring samples of F-CMOD for each of the three different types of concrete tested, totalizing nine successful samples. The six samples that did not yield successful tests were excluded from the analysis. In these cases, the cracks were either single or multiple, but all were concentrated in the notch region, ensuring that the test was not compromised. From these samples, four exhibited cracks near the supports, thus outside the notched region, making CMOD monitoring impossible (Figure 5.24a). This may have been caused by molding conditions specific at the location where the crack occurred. The other two samples exhibited significant curvature (Figure 5.24b), which may have been caused by the non-uniform distribution of cracks in the notched section. The concretes tested were C-10, C-11, and C-12, which are presented in the Table 4.2. These concretes differ by the types of fibers used, which are, respectively: ST-33/60, ST-50/67, and ST-33/44. The molding carachteristics of the concrete used in this research are described in section 4.3 and the concrete components are shown in Table 4.1. The characteristics of the fiber type used are described in the Table 4.3. Considering these different characteristics, the σ-*COD* diagrams of these concretes are compared to verify the sensitivity of the test to these parameters. For this comparison, the area under the diagram is considered.



(a) (b)

Figure 5.24 – Peculiar behaviors observed during the execution of the UTT: (a) Crack outside the notch position, and (b) Sample curvature.

5.5.2. Compressive tests

The experimental determination of the compressive strength (f_{cm}) is described in 5.2 and the results are shown in the Table 5.2.

5.5.3. Tensile vs. *COD* results (UTT)

The envelope for a 95% confidence level and average of the tensile stress versus COD diagrams of the three samples tested are shown in Figure 5.25a-c for the concretes C-10, C-11 and C-12, respectively. At the beginning of the diagram, the tensile stress versus COD relationship is practically vertical for all concretes tested. For concrete C-12, a significant variation in tensile (from 2 to 3.2 N/mm²) can be seen for COD between 0.05 and 0.3 mm. This variation is not uncommon and can been observed in other researches (Nour, et al., 2015), that used concrete with similar characteristics. The mean difference between the areas under the average curve and under the upper bound and under the lower bound curves was 9%. Thus, the results obtained can be considered very satisfactory and representative of the tensile behavior of the studied concrete, especially considering that UTT is difficult to perform (Planas, 2007; Mudadu, et al., 2018; van Mier & van Vliet, 2002; Hordijk, 1991).

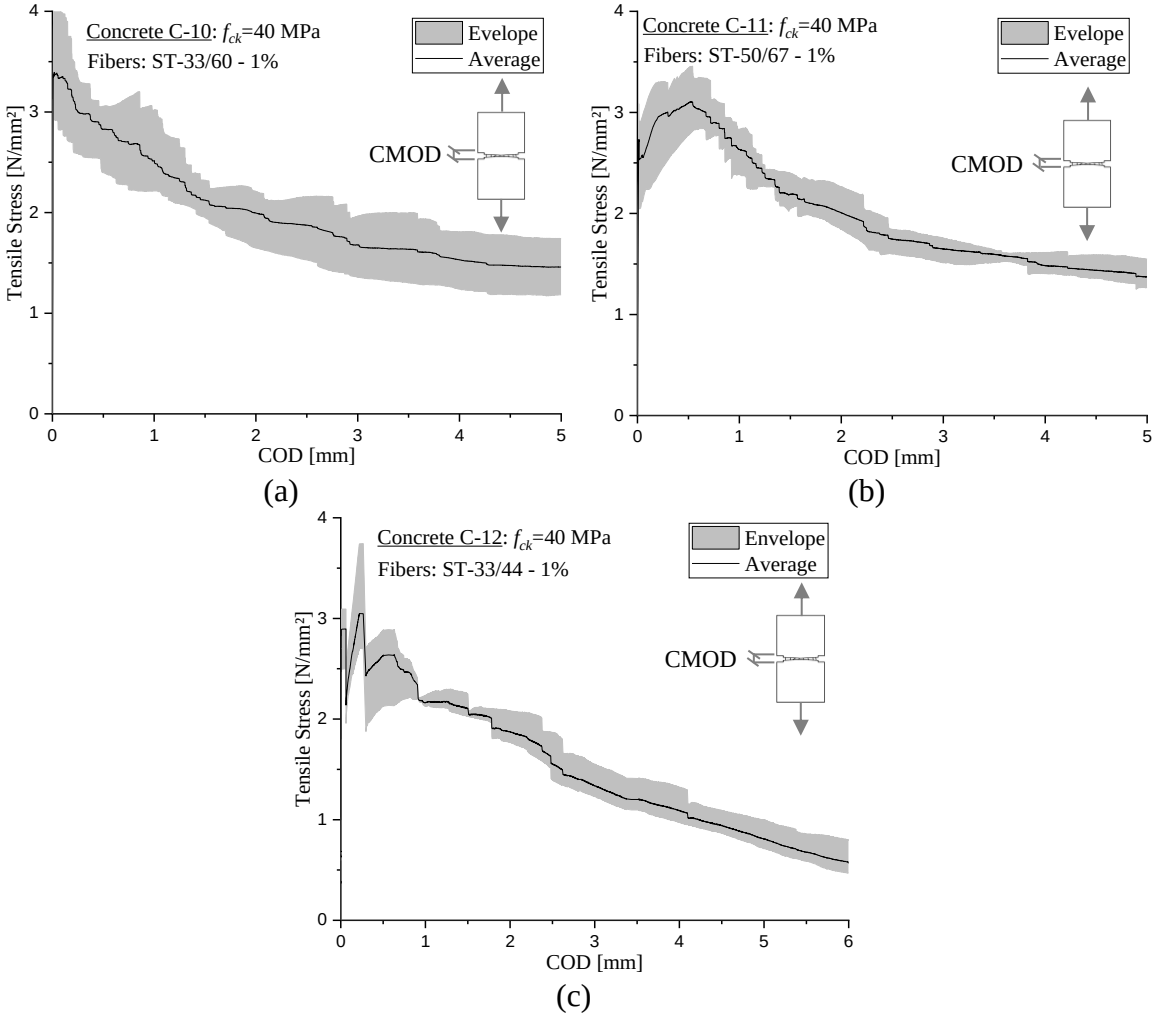


Figure 5.25 – Average and envelope form experimental curves Tensiles Stress versus COD for UTT results molded with the concretes: (a) C-10, (b) C-11 and (c) C-12.

The Table 5.8 shown Average (Avg.), upper bound (U.B.) and lower bound (L.B.) values for the areas of the Tensiles Stress versus COD diagrams for UTT, according to the diagrams in Figure 3.20. For the three types of concrete studied, the percentage difference between the U.B. and the L.B. relative to the Avg. was less than 20%. This is a dispersion compatible with a UTT test when compared to results reported in the literature (Amin, et al., 2018; Donnini, et al., 2020; Shi, et al., 2020). The exclusion of samples that did not yield successful tests during COD monitoring contributed to low dispersion. The results obtained can be considered very satisfactory and representative of the tensile behavior of the studied concrete, especially considering that UTT is difficult to perform (Planas, 2007; Mudadu, et

al., 2018; van Mier & van Vliet, 2002; Hordijk, 1991). Considering the parameter of the Avg. area of the Tensile vs. COD diagram (Table 5.8), the tests conducted with concretes C-10, C-11, and C-12 showed, respectively, the following performances: best, intermediate, and worst. The same result was obtained for the MSCBT and ST tests as presented in sections 5.3 and 5.5. Despite this, concretes C-10 and C-11 exhibited very similar Avg. areas under the diagram (differing by approximately 1%) for UTT. These results can be attributed to the fact that the aspect ratio of the ST-33/60 and ST-50/67 fibers are close to each other and greater than that of the ST-33/44 fiber.

Table 5.8 – Average (Avg.), upper bound (U.B.) and lower bound (L.B.) values for the areas of the Tensile Stress versus *COD* diagrams for UTT.

areas [kN.mm]	C-10	C-11	C-12
U.B.	11.6	10.8	10.2
Avg.	10.0	9.9	9.0
L.B.	8.4	9.1	8.2
Avg.–L.B. (abs.)	1.6	0.8	0.8
Avg.–L.B. (%)	16.0%	8.3%	8.9%
U.B.–Avg. (abs.)	1.6	0.9	1.2
U.B.–Avg. (%)	15.7%	8.8%	13.3%

Considering the test conditions for the UTT, the tensile stress during the test is usually assumed to be uniformly distributed over the fracture surface. Therefore, the fracture energy (G_f) was calculated and subsequently compared with the amount of fibers in the section. The fiber counting procedure was conducted as described in section 4.17. The Figure 5.26 presents G_f as a function of the effective number of fibers.

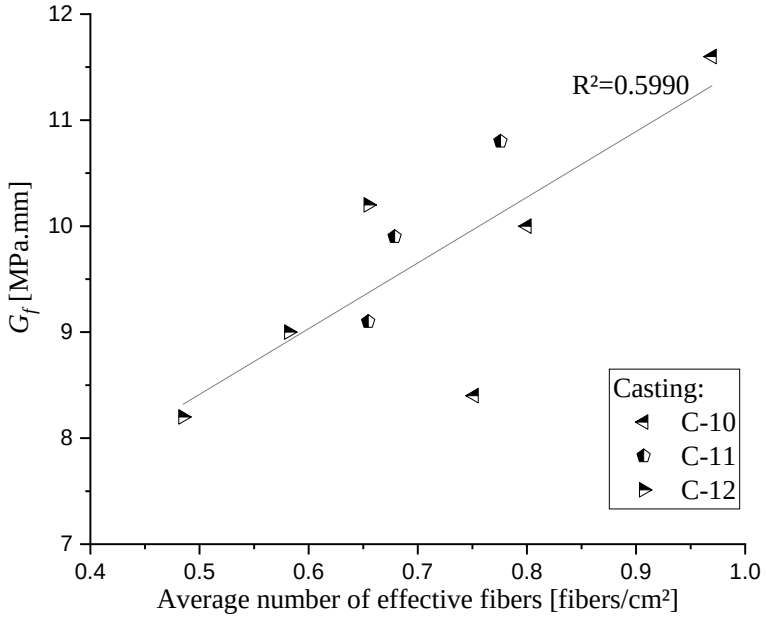


Figure 5.26 - Relationships between the average number of effective fibers and the toughness.

The average number of effective fibers counted in the sections of the tested UTT samples ranged from 0.5 to 1 fibers/cm². A smaller variation and a higher mean were found when compared to the variations found for ST (0.02 to 1 fibers/cm²) and MSCBT (0.1 to 1 fibers/cm²). This can be explained by the fact that all UTT samples tested had a fiber content of 1%, while for ST and MSCBT, concretes with fiber contents of 0.5% and 1% were tested. This low variation in fiber content in UTT contributed to a consequently low variation (8 to 12 MPa.mm) in the G_f values (Table 21). Additionally, it can be observed that the increase in the average number of effective fibers counted in the section is associated with a higher G_f. Therefore, the UTT performed with the methodology used in this study showed sensitivity to the parameter average number of effective fibers. This is an important characteristic for using the test, since it is already expected that the increase in fiber volume in the range of values studied in this work will generate, as a consequence, a greater performance of the SFRSCC (Lameiras, 2016; Cardoso, et al., 2021).

5.5.3.1. Discussions

In this topic, an experimental study on 9 samples of the UTT is carried out. Three types of fibers (ST-33/60, ST-50/67 and ST-33/44) are tested for class of concrete resistance of 40 MPa and the fiber content of 1.0%. The main conclusions of this work were the following:

- It was shown that the performance of the UTT showed consistent results for the characterization of the post-cracking behavior of the SFRSCC.

- The UTT was presented as a test with sensitivity to the parameters: fiber type and fiber content. Samples in which these parameters were different showed variations on the G_f values of the studied concretes, when they are obtained using the fib Model Code 2010 equations from 3PBT.

- The type of UTT used was able to determine that concretes with the types of fibers having higher aspect ratios (ST-33/60 and ST-50/67) exhibited similar performance to each other and superior performance compared to the concrete with the ST-33/44 type fiber.

5.6. ST (conception)

In this topic, the obtained results for the Splitting Test (ST) will be presented. The procedure for sample acquisition for this test is elucidated in section 4.8, wherein the methods for notch cuts and the affixing of support plates for LVDTs (Linear Variable Differential Transformers) to monitoring Crack Mouth Opening Displacement (CMOD) to determine the properties of Steel-Fiber Reinforced Self-Compacting Concrete (SFRSCC), as well as the test setup, are detailed.

Despite the contributions already made with samples for the ST for SFRSCC involving the V-notch (Lameiras, et al., 2015), only one type of concrete was tested by these authors (considering a single concrete strength, fiber type and fiber content). Furthermore, the sample thickness (60 mm) and cylinder diameter (150 mm) are greater than this research (sample thickness: 75 mm, cylinder diameter: 100 mm). The dimensions of the V-notch are proportionally larger than those employed in this study. The details of dimensions are shown on Figure 4.28. Despite the mentioned differences, the approach to the ST is grounded in the work of these authors.

5.6.1. Concrete Mixture

A total of 48 samples, 4 for each of 12 concrete mix (Table 4.2), were tested, varying in two fiber volume percentages (0.5% and 1.0%), three fiber types (Table 4.3) and two average strengths for the concrete (20 MPa and 40 MPa). The test indicated that it is promising because showed sensitivity for SFRSCC parameters such as increasing the volume of fibers and strength of concrete, as well as diferents type of fiber in concrete. The materials used for concrete mix for ST are the same for the MSCBT (decribed in item Table 4.1). Considering that the same types of concrete were used, the compression tests of the item 5.4.2 can be taken as a reference.

5.6.2. Compressive tests

The experimental determination of the compressive strength (f_{cm}) is described in 5.2 and the results are shown in the Table 5.2.

5.6.3. *F-COD* results (ST)

The ideal condition for ST is that cracks would propagate on the central surface through a single crack at the location of the straight notches (Figure 5.27a). This occurred effectively for the majority of the samples (43 out of 48). One of the forty-eight tested samples exhibited cracks from the notched-V region to sample periphery (see Figure 5.27b), leading to significantly deviated crack paths. Two of the forty-eight tested samples exhibited cracks from the notched-V region to for the LVDT bonding region, causing a compromised reading due to the lack of LVDT fixation (Figure 5.27c). Two out of the forty-eight tested samples exhibited transverse cracks (Figure 5.27d). The cracks that deviated from the expected behavior occurred due to torsion caused by irregularities on the surface of the V-notch or due to vertical misalignment only for some tested samples, or due to molding conditions. This caused stress concentrations during the test and resulted in an unexpected failure mode, with cracks occurring outside the notch region. Samples with these characteristics corresponded to a low percentage of the total tested samples (10%) of the total tests. Therefore, they were discarded from the analyses.

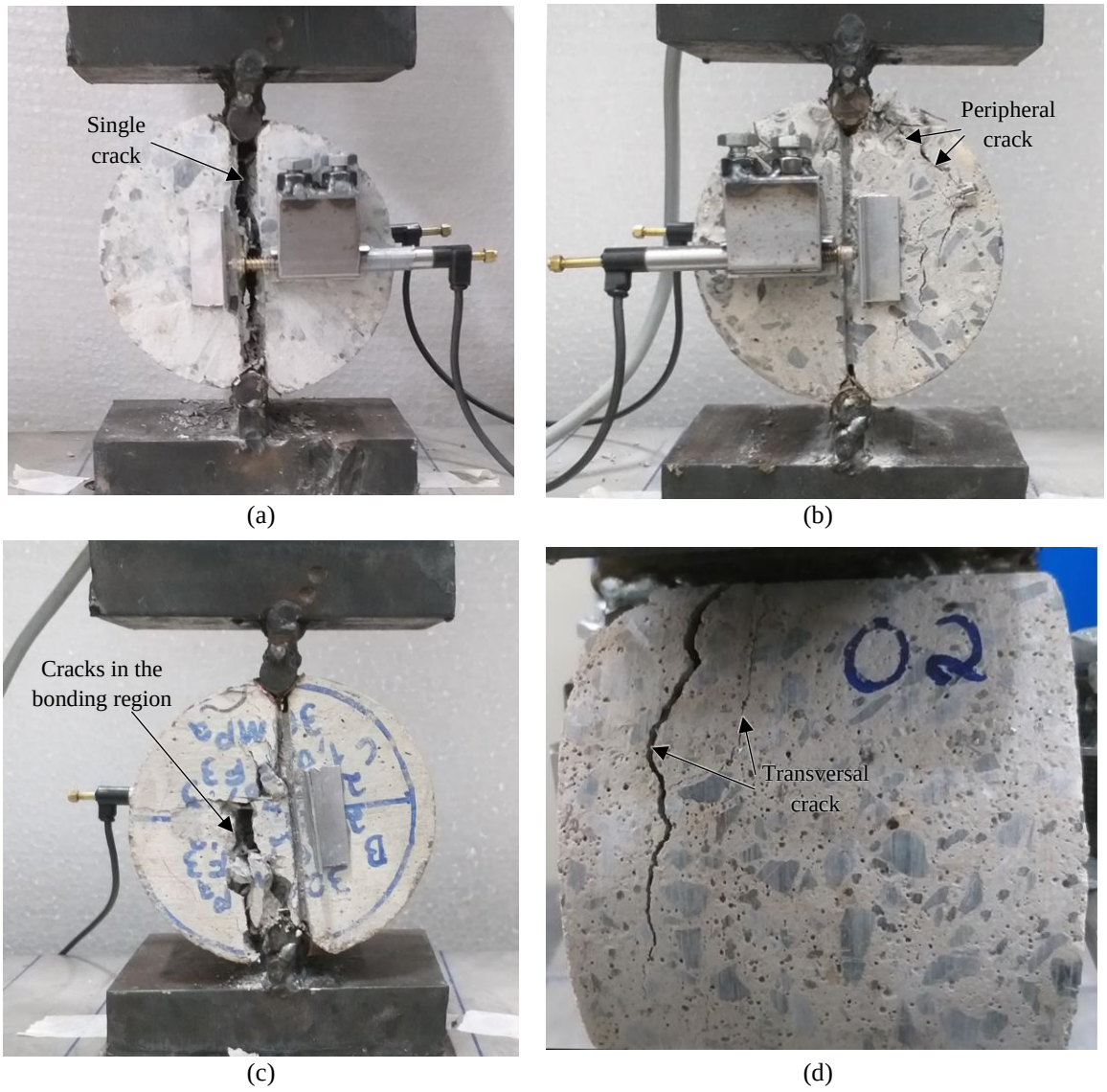


Figure 5.27 – Illustration of the types of cracks during the ST: (a) Single crack, (b) Peripheral crack, (c) Cracks in the bonding region and (d) Transversal crack.

During ST, *F-COD* monitoring is conducted. Based on the this data, the splitting tensile stress ($\sigma_{t,split}$) versus crack width curves was obtained. The crack width corresponds to the average of the values obtained during the test, and $\sigma_{t,split}$ is determined from the following equation (Lameiras, et al., 2015):

$$\sigma_{t,split} = \frac{2 \cdot P}{\pi \cdot t_r \cdot t_h} \tag{5-5}$$

On equation (5-5), P is the compressive load. In this work, t_r and t_h are dimensions of effective fracture area after the v-notches and straight notches, as shown in Figure 4.28. In order to simplify the representation of the results, $\sigma_{t,split}$ will be represented simply as σ. The

Figure 5.28 show the results for the ST *σ-COD* for concrete with 20 MPa and the Figure 5.29 show the results for concrete with 40 MPa, according to the symbology of Table 4.2. In both situations, results were presented for COD up to 3 mm similarly to the literature (Lameiras, et al., 2015).

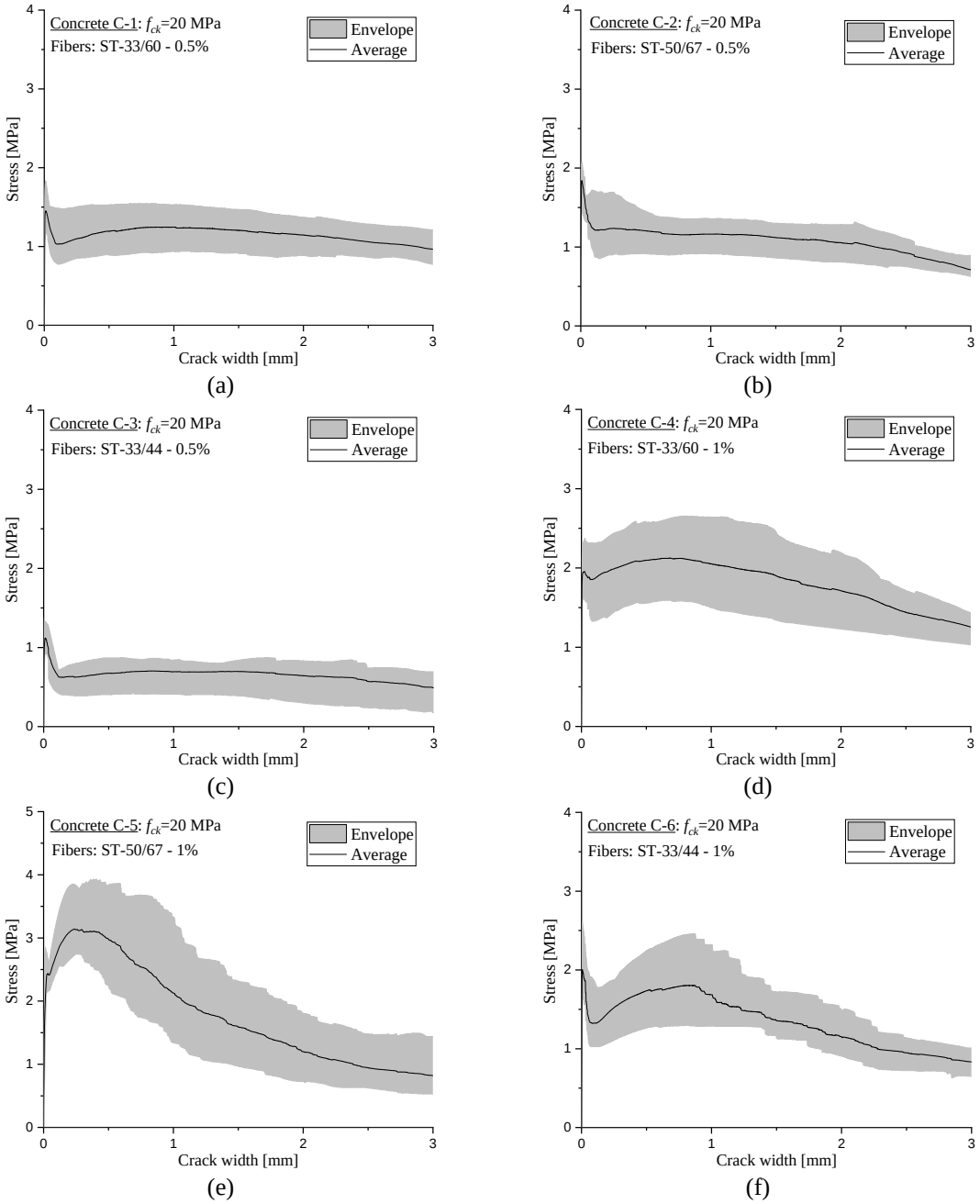


Figure 5.28 – *σ-COD* results for ST for concretes with 20 MPa: (a) C-1, (b) C-2, (c) C-3, (d) C-4, (e) C-5 and (f) C-6.

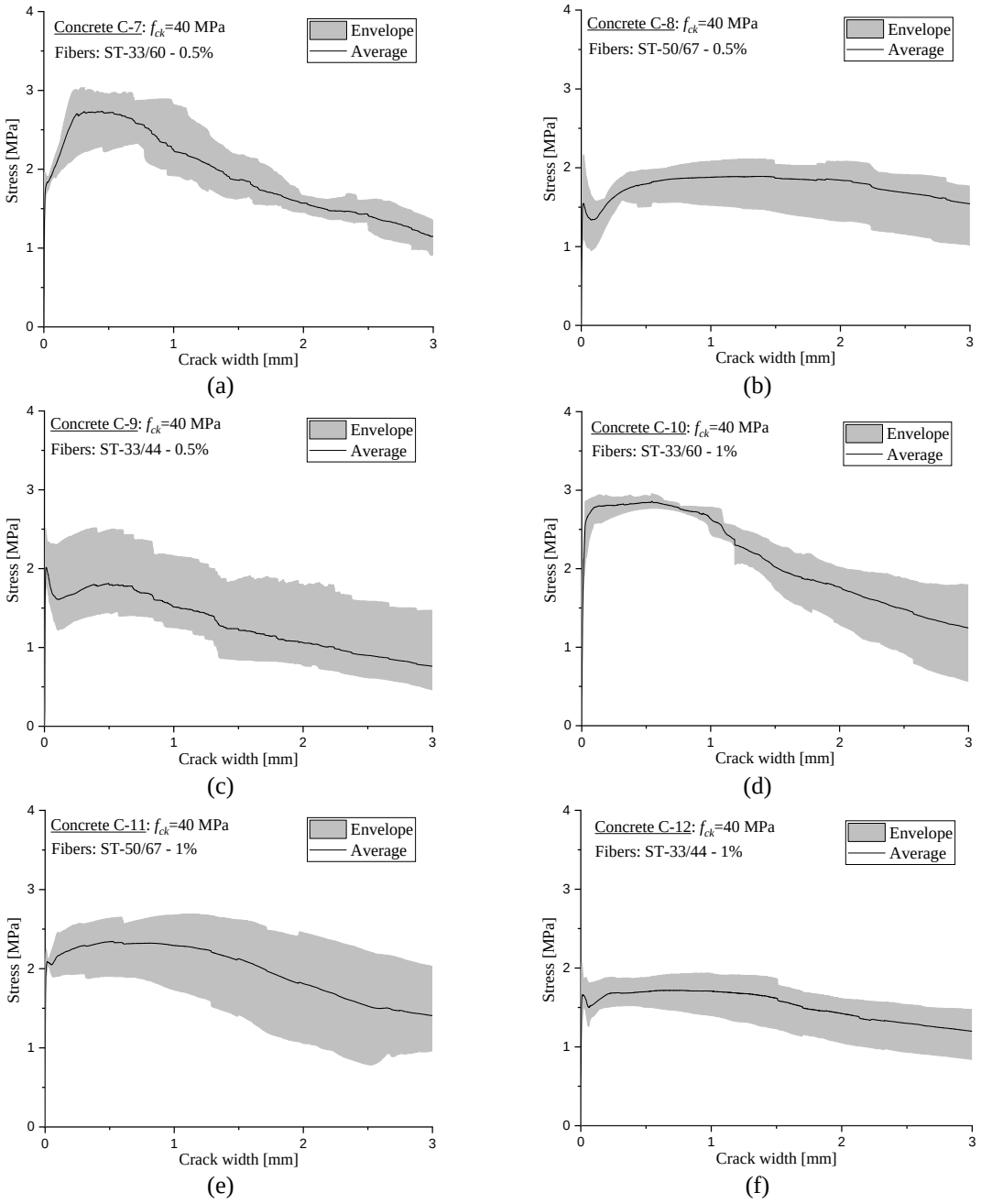


Figure 5.29 – *σ-COD* results for ST for concretes with 40 MPa: (a) C-7, (b) C-8, (c) C-9, (d) C-10, (e) C-11 and (f) C-12.

The Table 5.9 shows the areas of the *σ-COD* results according to Figure 5.28 and Figure 5.29 for each type of concrete (C-1, C-2, C-3, ..., C-12) for the average (Avg.), upper bound (U.B.) and lower bound (L.B.) values. The Avg. corresponds to the average between the results of the specimens tested for each type of concrete. The L.B. and the U.B. correspond to the result obtained from the sample that presented the lowest and highest load value,

respectively, for each type of concrete according to a confidence coefficient of 95%. The Table 5.9 also shown the absolute difference between Avg. and the respectives U.B. and L.B. in absolute values (abs.) and percentages (%) for each type of concrete.

Table 5.9 – Average (Avg.), upper bound (U.B.) and lower bound (L.B.) values for the areas of the *σ-COD* diagrams in kN.mm for each type of concrete.

	C-1	C-2	C-3	C-4	C-5	C-6	C-7	C-8	C-9	C-10	C-11	C-12
U.B.	4.3	3.9	2.5	6.7	7.6	7.2	6.6	5.9	5.9	7.1	7.4	5.2
Avg.	3.4	3.2	2.0	5.4	5.3	4.0	5.8	5.3	3.9	6.3	5.9	4.6
L.B.	2.7	2.5	1.0	4.0	3.7	3.1	5.0	4.0	2.9	5.3	4.2	3.6
Avg.–L.B. (abs.)	0.8	0.7	0.9	1.4	1.6	0.9	0.8	1.3	0.9	1.0	1.7	0.9
Avg.–L.B. (%)	23.0	21.9	46.7	25.8	30.5	22.1	13.4	23.7	24.0	15.6	29.4	20.6
U.B.–Avg. (abs.)	0.8	0.7	0.5	1.3	2.3	3.2	0.9	0.6	2.1	0.8	1.5	0.7
U.B.–Avg. (%)	24.1	21.0	26.7	24.7	42.3	80.5	14.8	12.1	53.0	12.0	24.5	14.5

The tested samples corresponding to concretes which has the highest percentage by volume of fibers (1.0%) presented a better performance. The evidence of this fact can be visualized graphically through diagrams of concretes with the same strength and fiber type, but different fiber contents (Figure 5.28a-f and Figure 5.29a-f) and also when comparing the average values of the areas of the *σ-COD* diagrams (Table 5.5). Comparing the diagrams of the concretes: C-1, C-2, C-3, C-7, C-8, C-9, which shown a volume of 0.5% of fibers and, respectively, the same strengths and type of fibers of concretes: C-4, C-5, C-6, C-10, C-11, C-12, which shown a volume of 1.0% of fibers, it is possible to verify that the average area of the diagrams is higher for the 1.0% fiber content. The average percentage increase in the diagram area was 27% for the concretes with 1.0% of fibers when compared to the concretes with 0.5% of fibers. Thus, the MSCBT demonstrated sensitivity when there is variation in the fiber volume parameter. This is an important characteristic for using the test, since it is already expected that the increase in fiber volume in the range of values studied in this work will generate, as a consequence, a greater performance of the SFRSCC (Lameiras, 2016; Cardoso, et al., 2021). When viewing the values for the areas of the *σ-COD* diagrams, the same conclusion can also be seen when these same concretes are compared.

Concretes with a strength of 40 MPa (Figure 5.29a-f) exhibited a greater area under the diagrams in the figures than those with 20 MPa (Figure 5.28a-f). This can be observed by respectively comparing the graphs of concretes C-1 to C-6, that has 20 MPa, with those of

concretes C-7 to C-12, that has 40 MPa. The same can be done when comparing the Avg. area values shown in Table 5.9. This is justifiable, as the increase in matrix strength contributes to the improved post-cracking behavior of concrete (Domski & Katzer, 2020; Cardoso, et al., 2021). The average percentage increase in the diagram area was 28%, considering this difference in resistance for the concretes studied. Therefore, the test also showed sensitivity for this parameter.

Concretes with fiber type ST-33/60 (concretes C-1, C-4, C-7 and C-10) shown higher areas of the diagrams (Figure 5.28a-f and Figure 5.29a-f). This can be justified by the fact that this type of fiber has a higher number of fibers per gram and a high aspect ratio (Kwan & Chu, 2018; Abbass, et al., 2018). Secondly, the concretes with ST-50/67 fiber (concretes C-2, C-5, C-8 and C-11), and finally, concretes with fiber type ST-33/44 (C-3, C-6, C-9 and C-12). Concretes with ST-33/60 fiber exhibited an average area 6% higher than concretes with ST-50/67 fiber, which showed an average area 40% higher than concretes with ST-33/44 fiber. The explanations for this performance are the same as those explained for the MSCBT in this work. Similar conclusions are found in the literature (Cardoso, et al., 2021).

From the Table 5.4, the diference form Avg. to U.B. and L.B. is less than 30%, with the exception of concretes C-3, C-5, C-6 and C-9. Considering all concretes studied, the average difference between the Avg. with U.B. and with L.B. was 29% and 25%, respectively. The experimental scattering was anticipated in stress-crack width curves due to the local dispersion and orientation of fibers (Ferrara, et al., 2012; di Prisco, et al., 2013; Lameiras, et al., 2015). The Figure 5.30 illustrates the relationships between the average number of effective fibers and toughness, according to the areas of the σ-*COD* diagrams (G_F). The parameter R^2=0.7616 was slightly higher (<10%) than that found in literature that employed a similar test (Lameiras, et al., 2015).

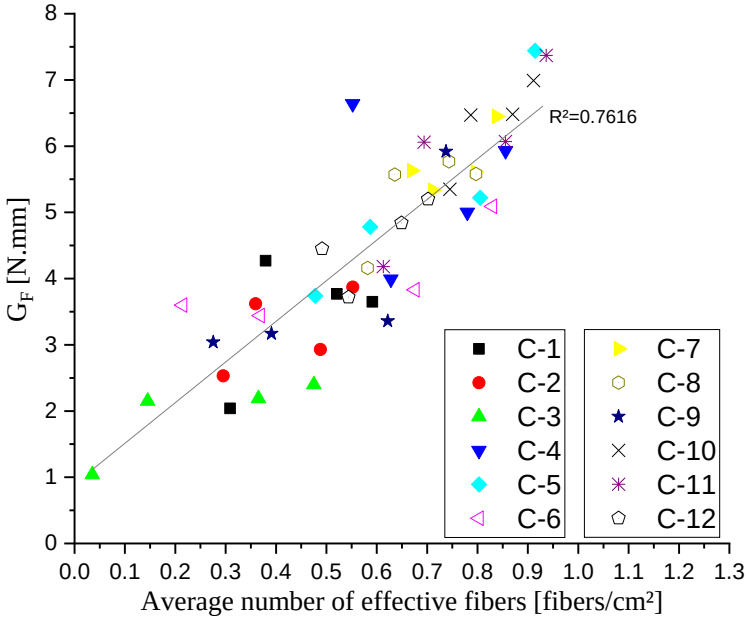


Figure 5.30 - Relationships between the average number of effective fibers and the toughness.

When concretes with different fiber content are analyzed for the f_{R1}, f_{R2}, f_{R3} and f_{R4} parameters of the Table 5.5, it appears that for the same concrete strength and fiber type, the performance is better for concretes with higher fiber content. This can be observed by comparing, respectively, the parameters obtained for the concretes: C-1, C-2, C-3, C-7, C-8, C-9 (with 0.5% of fiber content) with the concretes: C-4, C-5, C-6, C-10, C-11, C-12 (with 1.0% of fiber content). This result is also quite expected, since these parameters are more related to the post-cracking behavior of the SFRSCC, which is significantly influenced by the fiber content variation studied in this work.

Still analyzing concretes with different fiber contents, it is verified that when we compare concretes C-3 with C-6, there is no increase in the f_{ct} and $f_{fct,L}$ parameters for concretes with higher fiber contents. Although the C-6 has higher fiber content, it does not have higher values for f_{ct} and $f_{fct,L}$. This is because these parameters are more influenced by concrete strength than fiber content.

Analyzing the different types of fibers studied, the concretes with ST-33/60 fiber was presented the best performance for the f_{R1}, f_{R2}, f_{R3} and f_{R4} parameters. This can be justified by the fact that this type of fiber has a higher number of fibers per gram and a high aspect ratio, which already has a relationship established with the residual resistances (Kwan & Chu, 2018; Abbass, et al., 2018). Secondly, the concretes with ST-50/67 fiber also presents

good results due to its larger size that guarantees effective anchoring in the matrix. The ST-33/60 fiber presents better residual strength results than the ST-33/44 because, although these fibers have the same size, the ST-33/60 has a larger aspect ratio, which contributes to greater strength. Similar conclusions are found in the literature (Cardoso, et al., 2021).

5.6.4. Discussions

In this topic, an experimental study on 72 samples of the MSCBT is carried out. Two classes of concrete re-sistance (20 and 40 MPa), three types of fibers (ST-33/60, ST-50/67 and ST-33/44), as well as two fiber contents (0.5% and 1.0%) are tested. The main conclusions of this work were the following:

- It was shown that the performance of the MSCBT showed consistent results for the characterization of the post-cracking behavior of the SFRSCC.

- The MSCBT was presented as a test with sensitivity to the parameters: concrete strength, fiber type and fiber content. Samples in which these parameters were different showed variations on the residual strength parame-ters of the studied concretes, when they are obtained using the fib Model Code 2010 equations from 3PBT.

- Concrete with higher fiber content, or with fiber types with a higher aspect ratio (ST-33/60 and ST-50/67) or/and smaller diameter and length (ST-33/60), showed better performance. The fiber type that presented the worst performance (ST-33/44) has a larger diameter and a smaller length and, consequently, a smaller form factor. These results are already expected for bending results like 3PBT.

- The presented results show great similarity between the MSCBT and the 3PBT because bending of the sample occurs in both tests. The intensities of the loads monitored during the test, as well as the fr parameters, presented values lower than those expected for the 3PBT. This result was already expected, since the size and amount of fibers in the MSCBT sample section are smaller.

- The MSCBT proved to be easy to perform because the final samples are small in size and light, which facili-tates the transport and preparation of the samples.

- The rupture mode is as expected in most of the samples tested, corresponding adequately to the occurrence of bending in the sample.

- MSCBT samples have been shown to be easily drilled out of larger structures. This makes the test results more representative of the actual structure when compared to 3PBT.

5.7. MSCBT (sample thickness)

In this section, the results of the MSCBT tests conducted on samples with a thickness of 150 mm will be showed. These results are compared with those obtained for the 75 mm thick samples.

The procedure for sample acquisition for this test is elucidated in section 4.6. In this topic, the methods for notch cuts and the affixing of support plates for LVDTs (Linear Variable Differential Transformers) to monitoring Crack Mouth Opening Displacement (CMOD) to determine the properties of Steel-Fiber Reinforced Self-Compacting Concrete (SFRSCC), as well as the test setup, are detailed. In the approach presented in this section, the results of 26 samples tested with concrete with a strength of 40 MPa and a fiber content of 0.5%, varying in thickness (75 and 150 mm), were analyzed. For the 75 mm thicknesses, 6 samples of concrete C-7 (with ST-33/60 type fiber) and another 6 samples of concrete C-9 (with ST-33/44 type fiber) were tested, as described in section 5.4. Seven samples with thickness of 150 mm were also tested for each of concretes C-7 and C-9. The classification of the concretes (C-7 and C-9) is shown in the Table 4.2. The materials used for concrete mix for the MSCBT are decribed in item 4.3. The compression tests of the item 5.2 can be taken as a reference.

5.7.1. MSCBT - F-CMOD results

The ideal condition for MSCBT is that a single crack would propagate from the notch to the top of the sample, where the load is applied. This occurred effectively for the majority (9 of 16) of the samples with 150 mm of thickness, according showed on Figure 5.31a. 2 others of these 16 samples exhibited cracks with slight deviations or multiple cracks that could still be monitored by the LVDTs during the test (Figure 5.31b). The last 4 of the 16 samples exhibited cracks transverse to the sample that could not be monitored by the LVDTs and were disregarded for analysis in this study (Figure 5.31c). These cracks occurred due to torsion caused by irregularities on the bottom surface of the MSCBT sample or due to vertical misalignment. This caused stress concentrations during the test and resulted in an unexpected failure mode, with cracks occurring outside the notch region. The samples with

a thickness of 150 mm exhibiting these cracking characteristics showed a slightly higher percentage (25%) compared to the samples for the ST (10%) and to the MSCBT with 75 mm of thickness (7%). This is justified by the greater thickness and consequently, larger support surface area of the MSCBT samples with 150 mm when compared to the MSCBT samples with 75 mm, resulting in greater stress concentration effects due to sample irregularities. The ST used in this study exhibits a tendency towards the occurrence of an ideal crack propagation orientation due to the V-notch and straight notches. This resulted in a low incidence of transverse cracks, similar to the MSCBT samples with 75 mm.



(a) (b)

(c)

Figure 5.31 – Illustration of the types of cracks during the MSCBT with a thickness of 150 mm: (a) Single crack, (b) Peripheral crack, (c) Transversal crack (bottom view of the sample).

During MSCBT, *F-CMOD* monitoring is conducted. The Figure 5.32a show the results obtained for MSCBT samples with 150 mm of thickness for concrete C-7 and the Figure 5.32b show the results for concrete C-9. In both situations, results were presented for CMOD up to 6 mm similarly to the literature (Lameiras, et al., 2015). For the 75 mm of thickness,

the results of the concretes C-7 and C-9 are show on Figure 5.33a and Figure 5.33b, respectively.

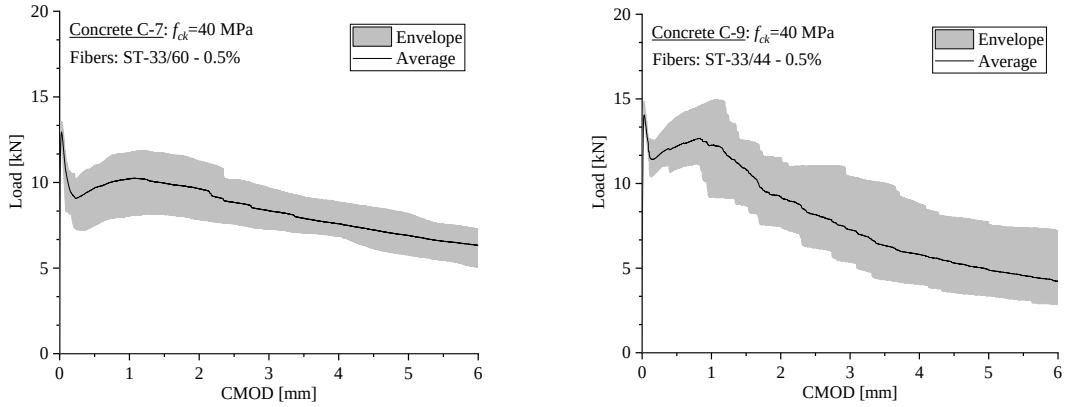


Figure 5.32 – *F-CMOD* results for MSCBT samples with 150 mm of thickness: (a) for concrete C-7 and (b) for concrete C-9.

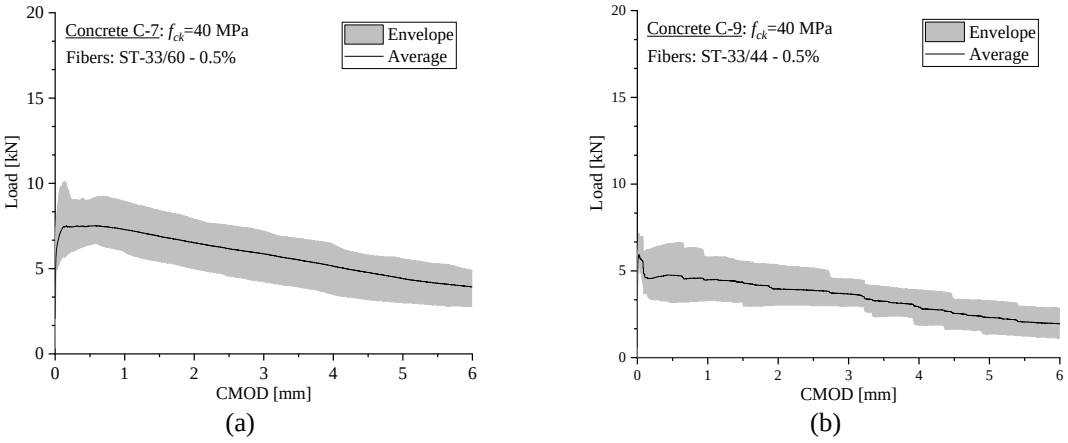


Figure 5.33 – *F-CMOD* results for MSCBT samples with 75 mm of thickness: (a) for concrete C-7 and (b) for concrete C-9.

The Table 5.10 shows the areas of the *F-CMOD* results according to Figure 5.32a-b and Figure 5.33a-b for each type of concrete (C-7 and C-9) for the average (Avg.), upper bound (U.B.) and lower bound (L.B.) values. The Avg. corresponds to the average between the results of the specimens tested for each type of concrete. The L.B. and the U.B. correspond to the result obtained from the sample that presented the lowest and highest load value, respectively, for each type of concrete according to a confidence coefficient of 95%. The

Table 5.10 also shown the absolute difference between Average (Avg.), and the respectives Upper Bound (U.B.) and Lower Bound (L.B.) in absolute values (abs.) and percentages (%) for each type of concrete.

Table 5.10 – Average (Avg.), upper bound (U.B.) and lower bound (L.B.) values for the areas of the *F-CMOD* diagrams in kN.mm for each thickness and each type of concrete for MSCBT.

Concrete	C-7	C-9	C-7	C-9
Thickness [mm]	75	75	150	150
U.B.	43.0	27.7	58.5	63.0
Avg.	34.9	20.8	50.5	47.4
L.B.	26.1	15.0	42.3	36.7
Avg.–L.B. (abs.)	8.8	5.9	8.2	10.7
Avg.–L.B. (%)	25.2	28.1	16.3	22.6
U.B.–Avg. (abs.)	8.1	6.9	8.0	15.5
U.B.–Avg. (%)	23.3	33.0	15.9	32.7

The average areas found (Table 5.10) for the samples tested with a thickness of 150 mm exceeded those of the 75 mm thick by 44.9% (for C-7 concrete) and 127.9% (for C-9 concrete). This can be justified by the fact that the greater thickness contains a higher number of fibers in the section of the samples, which contribute to the post-cracking performance. Thus, the MSCBT demonstrated sensitivity when there is variation in the thickness of the sample. For the 150 mm samples, the averages of the percentage differences Avg.–L.B. and U.B.–Avg. (Table 5.10) for the studied concretes are 19.4% and 24.3%, respectively. For the 75 mm samples, the averages were 26.7% and 28.1%, respectively. Thus, the dispersion of the samples was compatible for the SFRSCC (Lameiras, 2016; Cardoso, et al., 2021).

For both the 75 mm and 150 mm thick samples, the area under the *F-CMOD* diagram was greater for C-7 concrete compared to C-9. This can be attributed to the type of fibers used: ST-33/60 in C-7 concrete, and ST-33/44 in C-9 concrete. The ST-33/60 fiber has a higher aspect ratio, and concretes with this type of fiber tend to have a greater number of fibers per unit volume of concrete, which consequently influences better performance (Kwan & Chu, 2018; Abbass, et al., 2018; Cardoso, et al., 2021). The 75 mm thick concretes with this type of fiber also showed better performance, as previously explained in section 5.4.3.

The Figure 5.34 illustrates the relationships between the average number of effective fibers and the area of the *F-CMOD* diagram. The parameter R^2=0.6677 aligns with what is

presented in the literature for the 3PBT (Lameiras, et al., 2015; Cardoso, 2020). It is found that the increase in fiber content corresponds with an increase in the area of the F-CMOD diagram. This is also observed for the samples with a thickness of 75 mm (section 5.4) of this work. Thus, the MSCBT with samples of 75 mm and 150 mm thickness proved to be sensitive to variations in the parameter: fiber content.

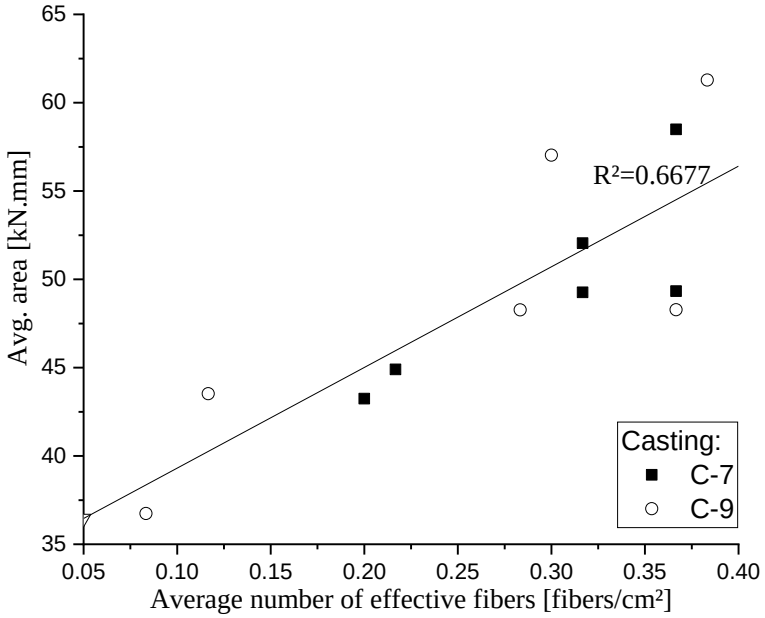


Figure 5.34 - Relationships between the average number of effective fibers and the area under *F-CMOD* diagram.

5.7.2. Discussions

In this topic, an experimental study on 16 samples of the MSCBT is carried out. These samples have three types of fibers (ST-33/60, ST-50/67 and ST-33/44), a single class of concrete resistance (40 MPa) as well as a single fiber content (1.0%). The main conclusions of this work were the following:

- It was shown that the performance of the MSCBT showed consistent results for the characterization of the post-cracking behavior of the SFRSCC.

- The MSCBT was presented as a test with sensitivity to the fiber type and fiber content. Samples in which these parameters were different showed variations on the area of the *F-CMOD* diagram.

- The casting with higher fiber content, or with fiber types with a higher aspect ratio and smaller diameter (ST-33/60), showed better performance when compared to the samples with fiber ST-33/44. These results are already expected for bending tests like 3PBT.

- The presented results show great similarity between the MSCBT and the 3PBT because bending of the sample occurs in both tests. The intensities of the loads monitored during the test, as well as the area of the *F-CMOD* diagram, presented values lower than those expected for the 3PBT. This result was already expected, since the size and amount of fibers in the MSCBT sample section are smaller.

- Even the 150 mm thick MSCBT samples proved to be easy to perform because the final samples are small in size and lightweight, which facilitates the transport and preparation of the samples.

- The rupture mode is as expected in most of the samples tested, corresponding adequately to the occurrence of bending in the sample. However, a higher percentage of test failures was found for the samples with a thickness of 150 mm (25%) compared to the samples with a thickness of 75 mm (7%).

- MSCBT samples have been shown to be easily drilled out of larger structures. This makes the test results more representative of the actual structure when compared to 3PBT.

5.8. IA algorithm for MSCBT (preliminary results)

This item presents the results of a preliminary study on the application of the inverse analysis procedure to the MSCBT, as shown in the item 4.10. A procedure already applied to the 3PBT (Salehian, 2015) is enhanced for the experimental MSCBT, which was carried out in four specimens of concrete C-3 (Table 4.2). For this preliminary study, the samples used presented the geometry similar to the Figure 4.7f-h, except for the length, height, width dimensions, which instead of 100 mm, 50 mm and 75 mm (Figure 4.7g), were 90 mm, 40 mm and 150 mm, respectively. The cut of the Figure 4.7d was not performed. For the inverse analysis procedure, the following values were used for the nonlinear hinge length (L_h): $L_{h1}=H/2$ and $L_{h2}=H$.

The MSCBT experimental results are shown in Figure 5.35a-b. In Figure 5.35a, the results for CMOD in the 0-6 mm range are shown. In Figure 5.35b, the results for the CMOD in the

0-0.2 mm interval are shown in order to promote visualization of the initial section of the diagram.

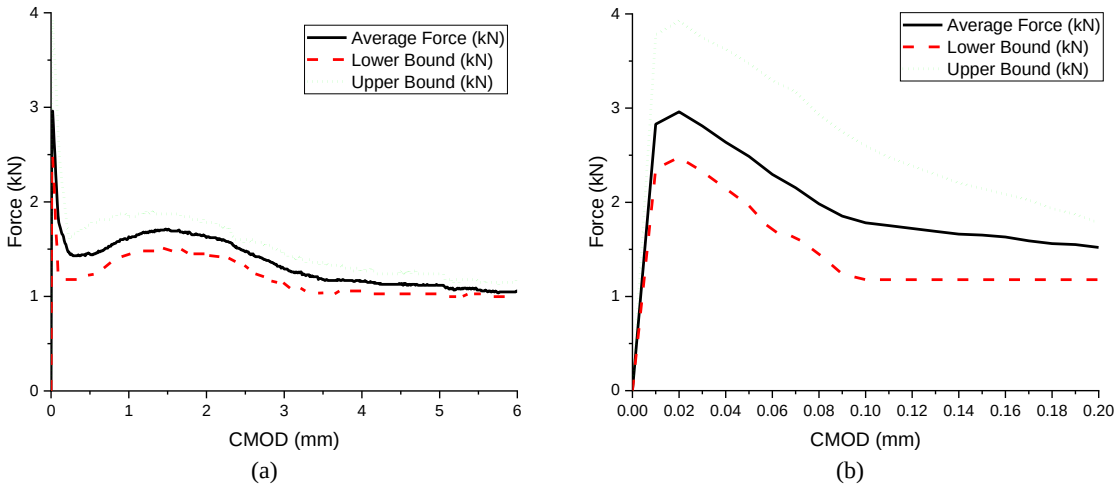


Figure 5.35 – Experimental results for F–CMOD response for the SCB specimens: average, upper and lower bound: (a) CMOD: 0-6 mm and (b) CMOD: 0-0.2 mm. Adapted from (Carvalho & Lameiras, 2023b).

In the Figure 5.35a-b, the solid line represents the meaning among the tested samples. The dotted line represents the results with the highest values found according to a 95% confidence level (upperbound). For the same confidence level, the dashed line represents the lowest values found (lowerbound). The average difference between the peaks of the upper and lower bound diagrams in relation to the average of the experimental results is 33% and 16%, respectively. This difference is razonable if taked into account the anisotropy with SFRSCC and the fact that the MSCBT has a low load due to the dimensional characteristics of the sample. Observing the results of the literature that utilized 3PBT and concretes with similar characteristics (Lameiras, 2016; Cardoso, 2020), smaller differences were found (8% and 7%, respectively) for same type of concrete (Cardoso, 2020), and greater differences are found (48% and 35%, respectively) for similar type of concrete (Lameiras, 2016).

Considering in terms of area, the average between the area differences between the upperbound and lowerbound diagrams to the average for the MSCBT were 13% and 14%, respectively. When we compare with the literature results for 3PBT for upperbound and lowerbound, respectively, we find 37% and 35% (Lameiras, 2016) for a similar concrete and 8% and 9% (Cardoso, et al., 2021) for the same concrete. Considering the fact that the

fracture surface is smaller for MSCBT compared to 3PBT, we can consider the dispersion found to be quite coherent for the MSCBT results in relation to the 3PBT. Therefore, we can consider that there was a relatively low dispersion in this parameter for the studied concrete.

In Figure 5.36, the σ–w results are shown for the analytical responses obtained through the inverse analysis procedure of this work.

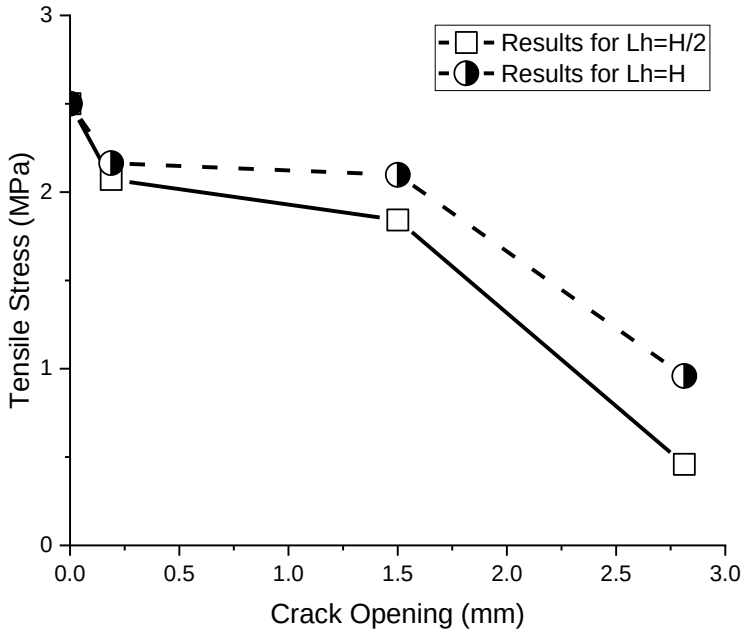


Figure 5.36 – σ – w results for the analytical responses obtained through the inverse analysis procedure of this work.

The Table 5.11 illustrates the value of the areas under the Tensile Stress vs. Crack Opening diagrams as well the percentage difference between the two responses.

Table 5.11 – Area under Tensile Stress vs. Crack Opening diagrams for $L_{h1}=H/2$ and $L_{h2}=H$ and percentage difference between them.

Parameter	$L_h = H / 2$	$L_h = H$	Difference (%)
Area (MPa·mm)	4.50	5.24	16.44

The results indicate that there is no larger difference when applying the inverse analysis procedure with different values for L_h. This fact can be verified by different authors (RILEM TC 162-TDF, 2002; Ulfkjaer, et al., 1995; Kooiman, 2000; Iyengar, et al., 1998; Pedersen,

1996; Salehian, 2015), who performed the inverse analysis procedure successfully from the different values of L_h studied in this work.

The inverse analysis procedure provides as a response the $\sigma - w$ values that represent the tensile behaviour of the studied SFRSCC (Salehian, 2015). The values of the defining parameters of the $\sigma - w$ diagram are presented in Table 5.12. The results showed good agreement with each other, indicating low variation when L_h is changed considering the values used by the literature (*H/2* and *H*). This shows a low influence of this parameter on the inverse analysis procedure. This reflects agreement between the *F–CMOD* and $\sigma - w$ results of the model proposed in this work and a potential use of the tool for the SCB test.

Table 5.12 – Parameters of the $\sigma - w$ diagram after inverse analysis procedure.

L_h	f_{ct} [MPa]	w_1 [mm]	σ_1 [MPa]	w_2 [mm]	σ_2 [MPa]	w_3 [mm]	σ_3 [MPa]
H/2	2.5	0.19	2.07	1.50	1.84	2.81	0.46
H	2.5	0.19	2.16	1.50	2.10	2.81	0.96

The comparison amid experimental data and the outcomes derived from inverse analyses evinced the commendable efficacy of the methodology in ascertaining the constitutive tensile properties. $\sigma - w$ opening relationship of SFRSCC. All utilized non-linear hinge lengths (*H/2* and *H*) demonstrated commendable congruity with the experimental findings. The chosen values exhibited compatibility with literature pertaining to the three-point bending test. Nonetheless, it is essential to acknowledge that this study represents a preliminary investigation, necessitating additional examinations and experimental validation of the aforementioned approach, including comparative assessments with tensile tests.

5.9. IA algorithm for MSCBT and 3PBT and numerical model (simulation)

This section includes the results obtained according to the methodology described in item 4.12.

5.9.1. Inverse Analysis

This section presents the results of the inverse analysis procedure for MSCBT and 3PBT for concrete C-12. The analytical response of the Load-CMOD diagram obtained during the use of the algorithm for performing the inverse analysis for MSCBT procedure is shown in

Figure 5.37. When compared with the average experimental results of MSCBT, the difference between the areas under the curves is approximately 4% and a good agreement can be observed between them. A more effective agreement can be observed mainly in the initial part of the diagram, when a behavior close to linear-elastic is verified. This occurs because the constitutive models are more realistic when the material presents this behavior.

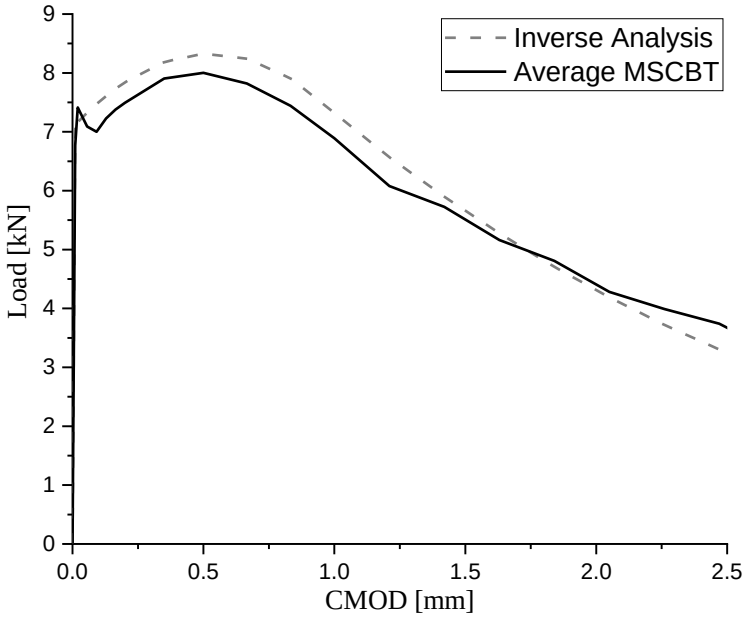


Figure 5.37 – Load-CMOD for MSCBT: comparison between average experimental and inverse analysis.

The response of the Load-CMOD diagram obtained through the inverse analysis for 3PBT procedure for C-12 concrete is shown in Figure 5.38. When compared with the average experimental results of 3PBT, the difference between the areas under the curves is approximately 7% and a good agreement can be observed between them.

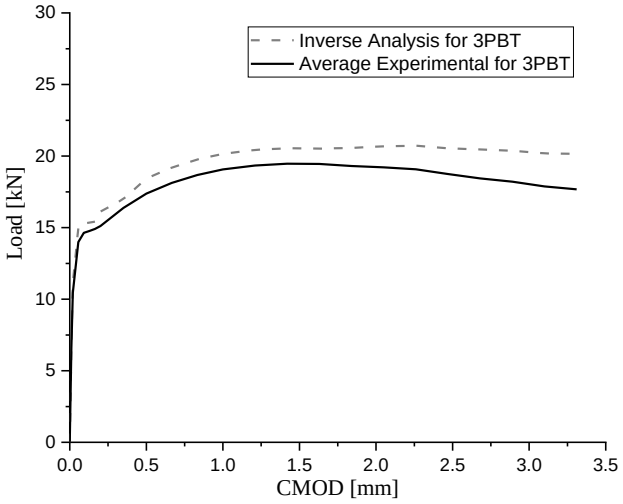


Figure 5.38 – Load-CMOD for 3PBT: comparison between average experimental result and inverse analysis result.

In Figure 5.39, the results Tensile Stress versus COD of the inverse analysis procedure using the methodology proposed in this work are presented for MSCBT and 3PBT. The average of the UTT experimental results is presented in the same graph for comparison. Considering that the quadrilinear model was used, the algorithm response points are presented. A difference of approximately 8% between the areas under the inverse analysis for MSCBT and average UTT experimental diagrams is found. The difference between the areas of the 3PBT and UTT diagrams is approximately 5%. Comparing MSCBT and 3PBT, the difference between the areas of the diagrams is approximately 12%.

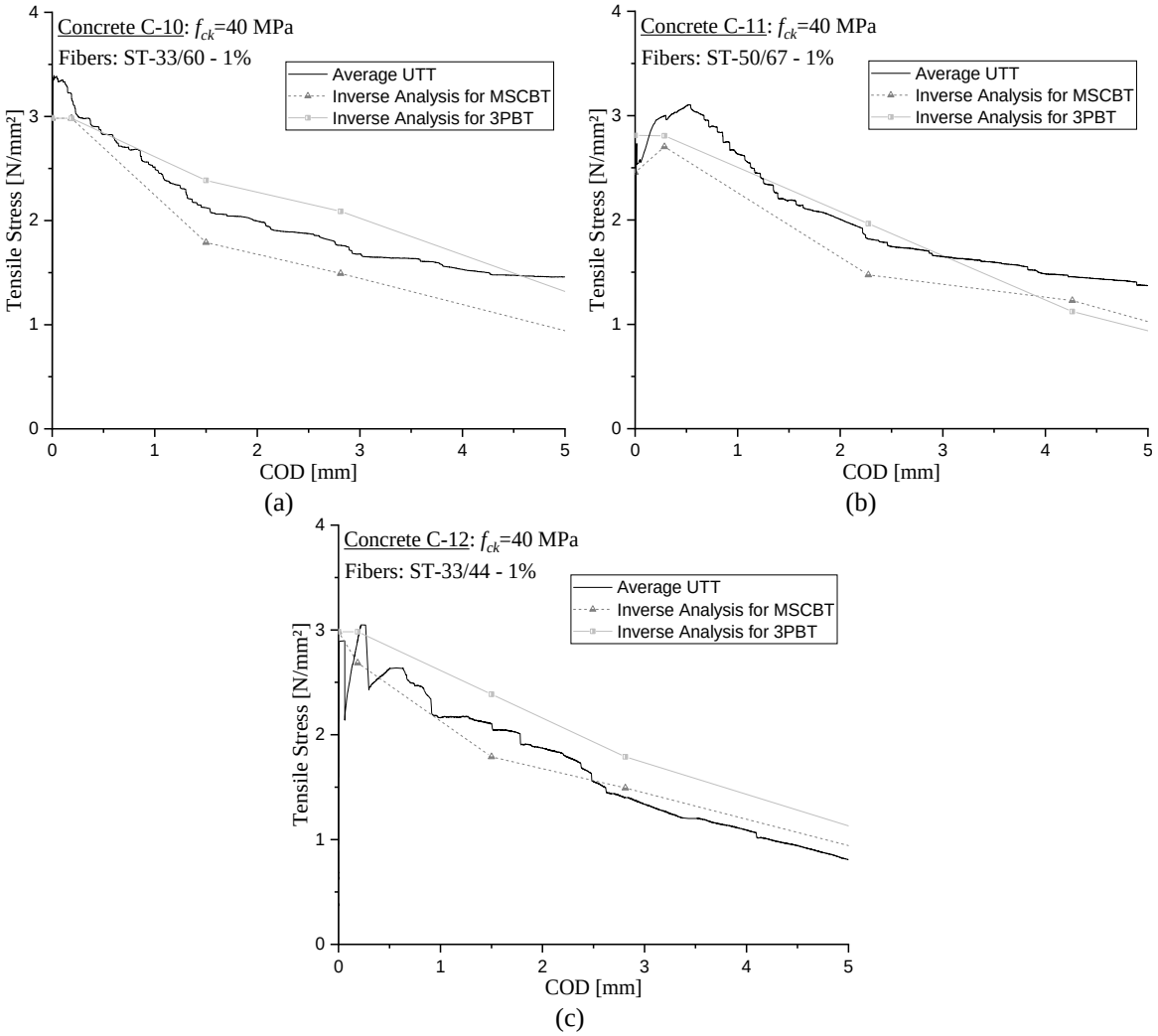


Figure 5.39 – Tensile Stress versus COD, average UTT experimental and inverse analysis results for MSCBT and 3PBT for concretes: (a) C-10, (b) C-11 and (c) C-12.

Given the minor disparities observed, it is conceivable to ascertain that the outcomes obtained from the employed inverse analysis technique hold substantial validity in characterizing the tensile characteristics of the investigated concrete, encompassing both the MSCBT and the 3PBT.

The fracture parameters that define the average behavior of SFRSCC obtained by inverse analysis of MSCBT and of 3PBT are in Table 5.13, including the fracture energy (G_f) calculated up to 3.5 mm. A difference of approximately 14% is found between the value of G_f in this work for MSCBT and in a previous work carried out by Lameiras (Lameiras, 2016), in which an SFRSCC with similar characteristics was used. The small difference found

indicates that the UTT result in this work and also the inverse analysis procedure was successful applied for MSCBT.

Table 5.13 – Fracture parameters for the average behavior obtained by inverse analysis of MSCBT and 3PBT.

Concrete	Type of IA	f_{ct} [MPa]	w_1 [mm]	σ_1 [MPa]	w_2 [mm]	σ_2 [MPa]	w_3 [mm]	σ_3 [MPa]	w_u [mm]	G_f [N.mm]
C-10	IA of 3PBT	2.98	0.19	2.98	1.50	2.39	2.81	2.09	8.25	8.37
	IA of MSCBT	2.98	0.19	2.98	1.50	1.79	2.81	1.49	8.25	6.81
C-11	IA of 3PBT	2.81	0.29	2.81	2.27	1.96	4.26	1.23	12.5	7.64
	IA of MSCBT	2.45	0.29	2.70	2.27	1.47	4.26	1.23	12.5	6,60
C-12	IA of 3PBT	2.98	0.19	2.98	1.50	2.39	2.81	1.79	8.25	7.98
	IA of MSCBT	2.98	0.19	2.98	1.50	1.79	2.81	1.49	8.25	6.58

5.9.2. Numerical simulation with Diana FEA

The Figure 5.40 shows the numerical *load-CMOD* results obtained through the FEM software up to *CMOD = 6* mm (*load-*$CMOD_{num}$). On the same chart, the average of the results obtained for the MSCBT (*load-*$CMOD_{exp}$) is also plotted for comparison. The difference between the areas between the *load-*$CMOD_{num}$ and *load-*$CMOD_{exp}$ diagrams up to *CMOD = 6* mm is less than 6%. The experimental results are quite consistent when compared to the numerical results. Therefore, it is possible to emphasize that the MSCBT numerical simulations were compatible with the experimental results. As expected from a numerical model, the FEM software curve is smoother due to the numerical formulation used to obtain it.

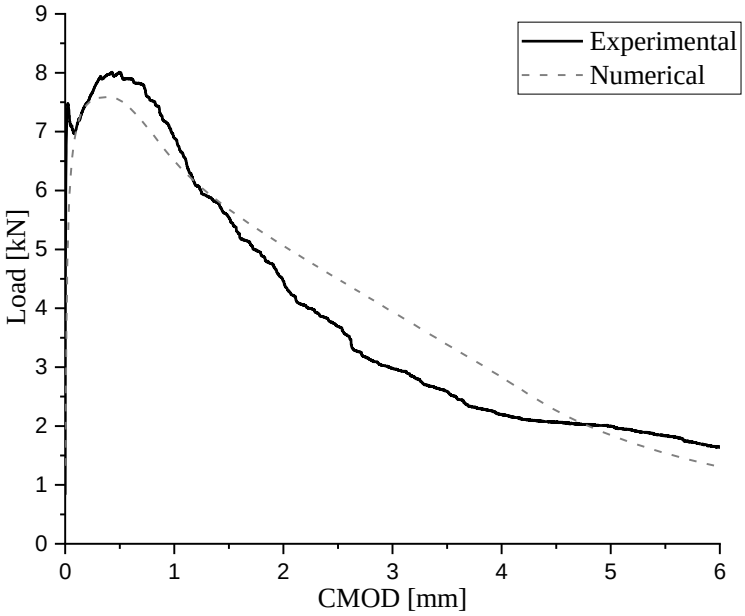


Figure 5.40 – Load–CMOD for MSCBT: comparison between average experimental result and numerical result.

5.9.3. Numerical simulation with Julia (comparing simulations with experimental results for 3PBT, UTT and MSCBT)

This section presents the results obtained from the simulations conducted according to the procedure described in Section 4.13.1 for UTT, 3PBT and MSCBT. The results for the simulations with the displacements (Ux) in the x direction for the horizontal displacement increment of 0.3 mm for UTT and 0.5 mm for the vertical displacement 3PBT and MSCBT, considering the three types of concrete: C-10, C-11, and C-12 in this analysis for UTT, 3PBT and MSCBT are presented, respectively, in Figure 5.41, Figure 5.42 and Figure 5.43. For better visualization, the displacements in these illustrations are magnified by 10 times.

This section presents the results obtained from the simulations conducted according to the procedure described in Section 4.13.7. This study employs a continuous–discontinuous approach, integrating linear bulk elements with nonlinear cohesive elements (Durand & Silva, 2019). In the simulations conducted using the Amaru library in this study, the cohesive element formulation is based on the isoparametric element (detailed in Section 4.13.1). The model for the Fracture Process Zone (FPZ) (detailed in Section 4.13.2) follows the same approach as presented in the literature (Silva, 2021; Silva, 2017). The Power Yield Crack

Model (detailed in Section 4.13.3) is a constitutive model designed to predict cracks through the opening of cohesive elements. The nonlinear behavior of concrete was represented using the Willam-Warnke model with hardening (detailed in Section 4.13.5), which is used to describe the behavior of concrete under different types of loading, such as tension, compression, and shear. The parameters and constitutive models used for this analysis are the same as those described in Section 4.13.6. The parameters are presented again in Table 5.14. Where: E is the Young's modulus, ν is Poisson's ratio, f_b is the biaxial strength wich was set to match the uniaxial compressive strength f_c, f_t is the tensile strength, ζ is the factor that controls the relative elastic displacements for cohesive elements, α is the parameter that controls the yield function shape in the fracture model, γ is the Yield criterion of the cohesive model and θ is the parameter that defines the yield function reduction in the fracture model.

Table 5.14 – Material properties of simulations according to the concrete type and constitutive model.

Constitutive model	Concrete type	E [×10³ MPa]	ν	f_c [MPa]	f_t [MPa]	f_b [MPa]	ζ	α	γ	θ
Power Yield Crack	C-10	36.3	0.2	45.6	3.4	-	5	0.51	0.05	1.2
	C-11	36.3	0.2	42.2	3.1	-	5	0.51	0.05	1.2
	C-12	36.3	0.2	35.8	2.9	-	5	0.51	0.05	1.2
William Warnke	C-10	36.3	0.2	45.6	3.4	4.08	-	-	-	-
	C-11	36.3	0.2	42.2	3.1	3.72	-	-	-	-
	C-12	36.3	0.2	35.8	2.9	3.48	-	-	-	-

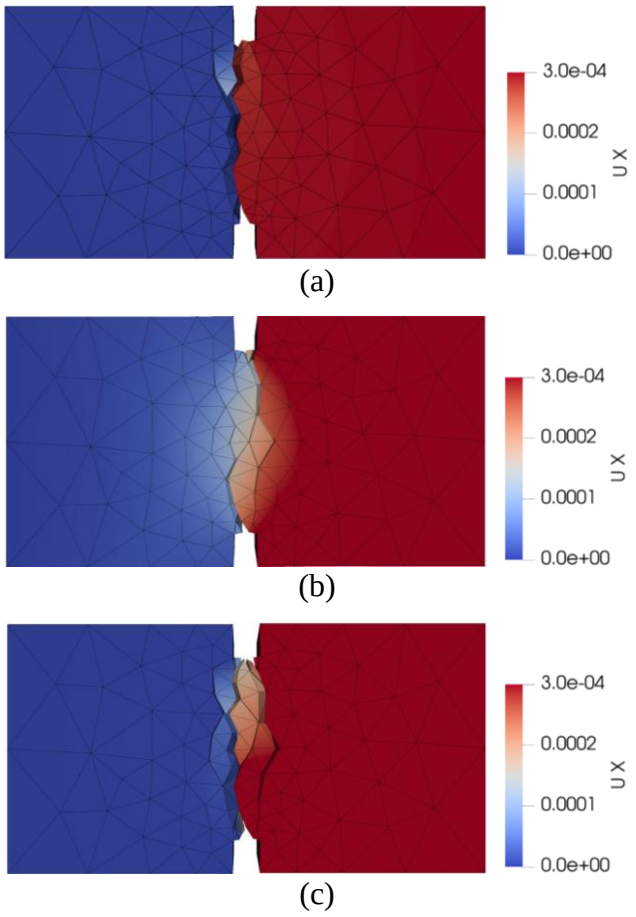


Figure 5.41 – Displacements (Ux) in the x direction for UTT for concretes: (a) C-10, (b) C-11, and (c) C-12.

For the UTT (in Figure 5.41 a, b, and c), small differences in the crack pattern can be observed, which can be attributed to variations in the types of concrete and, consequently, to the different tensile properties associated with each concrete type incorporated into the models. However, in all cases, the cracks propagated from the notch region. Situations involving single or multiple cracks were also observed in the experimental tests, as discussed in section 5.5.

Additionally, the portion with the movable support exhibits a more reddish coloration, while the fixed support area appears bluish, indicating that the bluish portion has predominantly zero displacement, whereas the reddish portion predominantly represents the extreme corresponding to the displacement increment in the simulation. This result is highly consistent with the behavior observed in the UTT experiments. Therefore, the model accurately represents the experimental test.

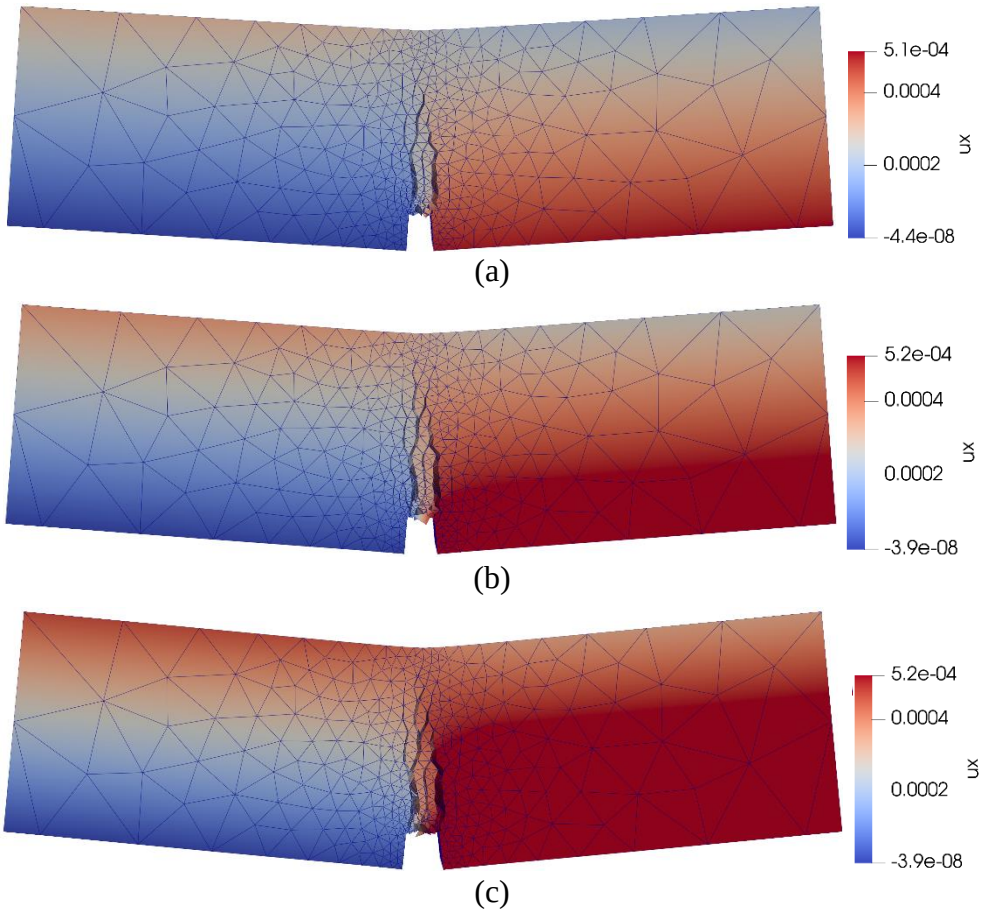
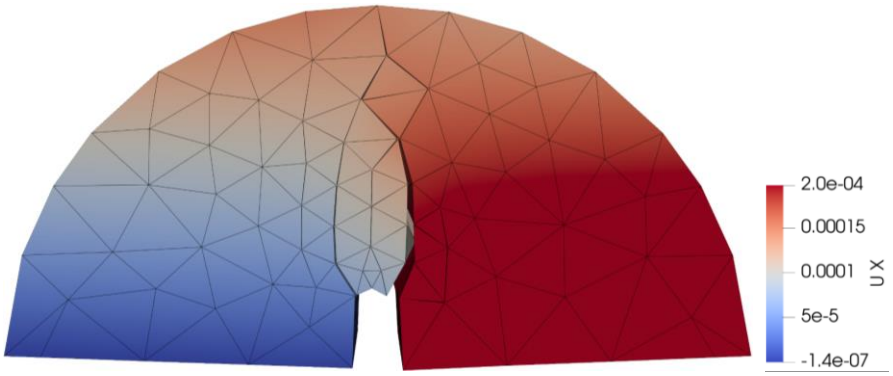
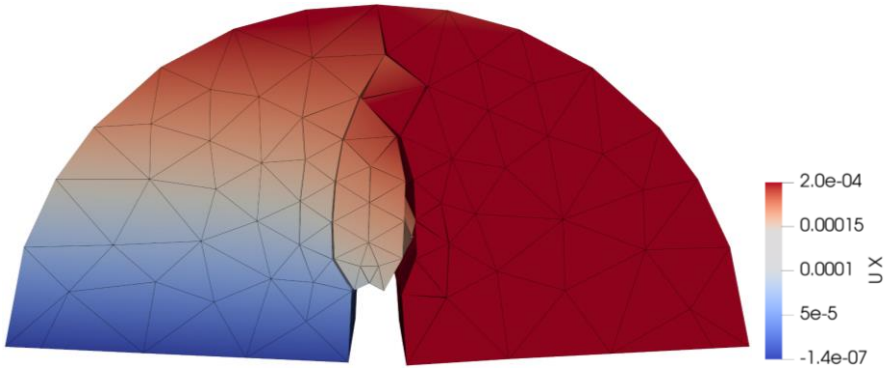


Figure 5.42 – Displacements (Ux) in the x direction for 3PBT for concretes: (a) C-10, (b) C-11, and (c) C-12.

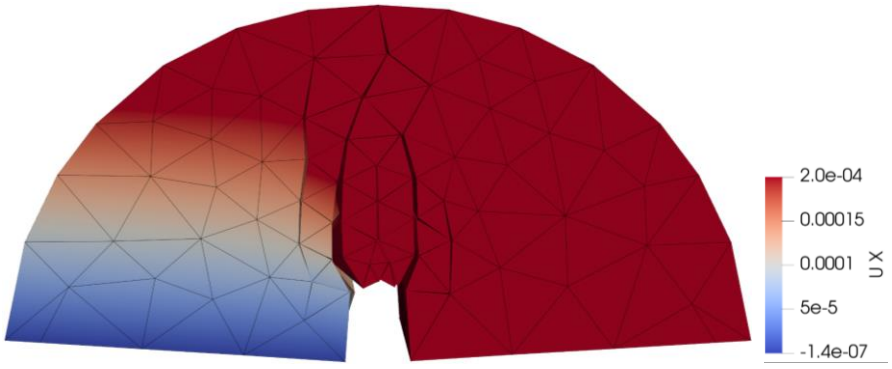
For the 3PBT (in Figure 5.42 a, b, and c), small differences in the crack pattern can be observed, which can be attributed to variations in the types of concrete and, consequently, to the different tensile properties associated with each concrete type incorporated into the models. However, in all cases, the cracks propagated from the notch region. The experimental test results for these same concretes also show cases with multiple cracks (Cardoso, et al., 2021). Thus, the simulations are consistent with the experimental results.



(a)



(b)



(c)

Figure 5.43 – Displacements (Ux) in the x direction for MSCBT for concretes: (a) C-10, (b) C-11, and (c) C-12.

For the MSCBT (in Figure 5.42a and b), the crack patterns were very similar. In all cases, the cracks propagated from the notch region. Additional cracks can be observed in the C-12 concrete (Figure 5.43c); however, they exhibit a small width. The experimental test results for these same concretes also show cases with multiple cracks for same concretes in 3PBT (Cardoso, et al., 2021). Thus, the simulations are consistent with the experimental results.

Figure 5.47 presents the Tensile vs. COD diagram for the UTT for the different simulated concrete types (C-10, C-11, and C-12). A good agreement can be observed between the simulations (dashed line) and the experimental results (solid line). The simulations also closely align with the boundaries of the envelope (upper bound and lower bound).

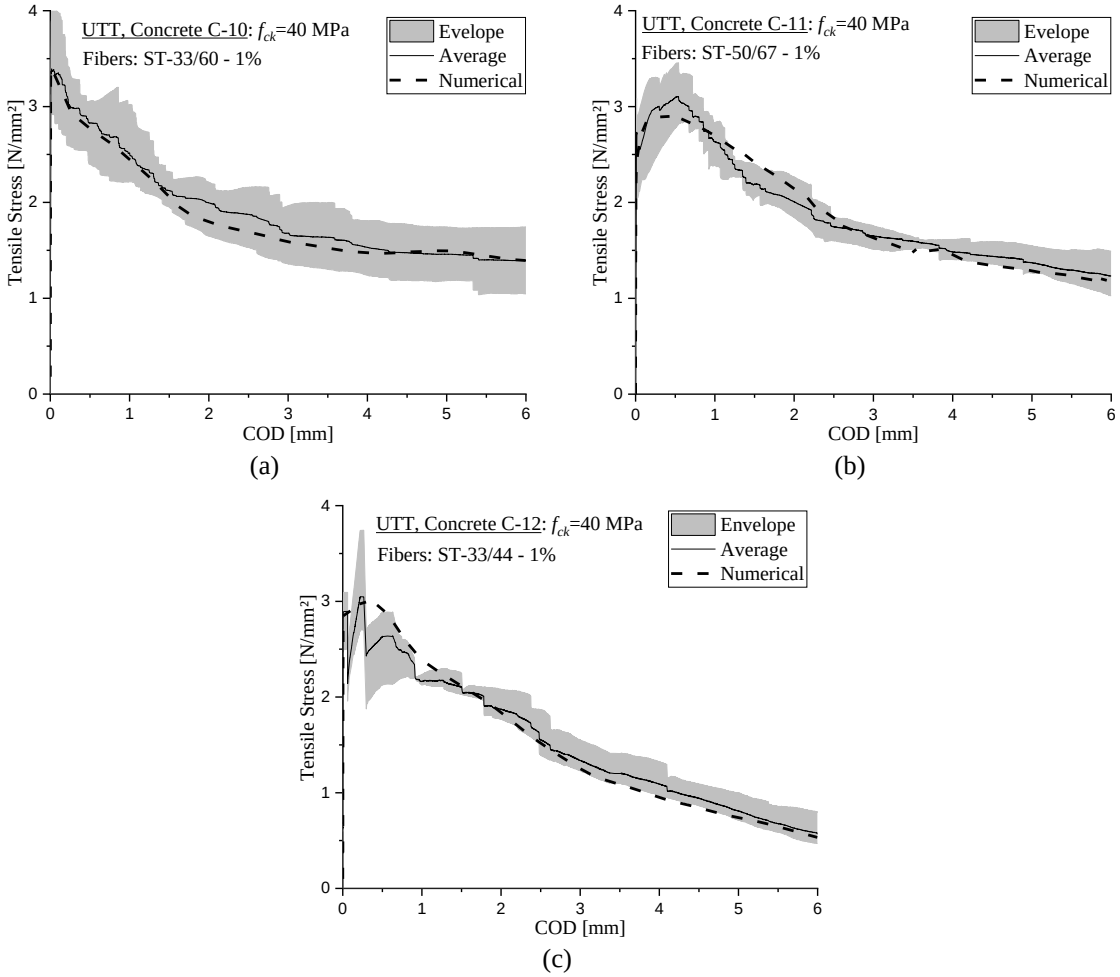


Figure 5.44 – Tensile vs. COD for the UTT numerical results, compared with the experimental average and envelope for concretes: (a) C-10, (b) C-11, and (c) C-12.

The areas under the Tensile vs. COD diagrams were calculated for average experimental diagrams and for simulations. These results are presented in the Table 5.15. Based on the results obtained, the error between the analytical and experimental response was found to be less than 4% for all the concretes studied, reinforcing the explanation provided in the previous paragraph. Similar to what was observed for the average experimental results, the numerical simulations also show a tendency for a decrease in the area under the diagram

when comparing concrete C-12 with C-11 and C-11 with C-10. The superior performance of concrete C-10 can be attributed to the higher number of fibers per gram and the high aspect ratio of the ST-33/60 fiber. The second-best performance of concrete C-11 is explained by the larger size of the ST-50/67 fiber, which guarantees effective anchoring in the matrix. The lower performance of C-12 is due to the shorter length and lower aspect ratio of the ST-33/44 fiber.

Table 5.15 – Area under the Tensile vs. COD for the UTT numerical results, compared with the experimental average for concretes: (a) C-10, (b) C-11, and (c) C-12.

Area under diagram [(N/mm²).mm]	C-10	C-11	C-12
Average experimental	11.41	11.23	9.04
Numerical	11.03	11.01	9.01
Error [%]	3.33	1.96	0.33

Figure 5.45 presents the Force vs. CMOD diagram for the 3PBT for the different simulated concrete types (C-10, C-11, and C-12). A good agreement can be observed between the simulations (dashed line) and the experimental results (solid line). The simulations also closely align with the boundaries of the envelope (upper bound and lower bound).

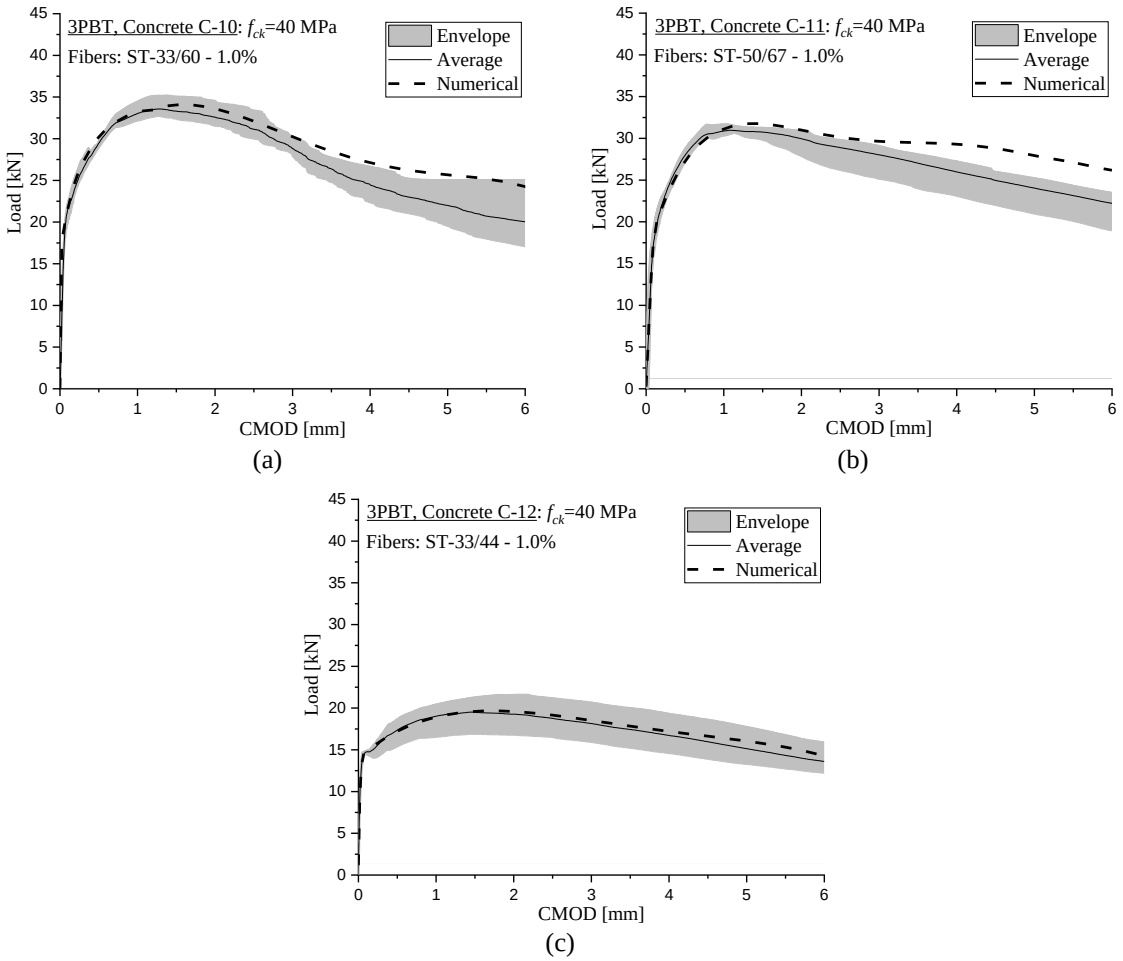


Figure 5.45 – Force vs. CMOD diagrams for the 3PBT numerical results, compared with the experimental average and envelope for concretes: (a) C-10, (b) C-11, and (c) C-12.

The areas under the Force vs. CMOD diagrams were calculated for average experimental diagrams and for simulations. These results are presented in the Table 5.16. Based on the obtained results, the error between average experimental and numerical areas was found to be less than 8% for all the concretes studied, reinforcing the explanation provided in the previous paragraph. Similar to was observed for the average experimental results, the numerical simulations also show a tendency for a decrease in the area under the diagram when comparing concrete C-12 with C-11 and C-11 with C-10. The superior performance of concrete C-10 can be attributed to the higher number of fibers per gram and the high aspect ratio of the ST-33/60 fiber. The second-best performance of concrete C-11 is explained by the larger size of the ST-50/67 fiber, which guarantees effective anchoring in the matrix. The lower performance of C-12 is due to the shorter length and lower aspect ratio of the ST-33/44 fiber.

Table 5.16 - Area under the Force vs. CMOD for the 3PBT numerical results, compared with the experimental average for concretes: (a) C-10, (b) C-11, and (c) C-12.

Area under diagram [kN.mm]	C-10	C-11	C-12
Average experimental	162.29	160.31	105.06
Numerical	174.22	172.22	102.60
Error [%]	7.35	7.43	2.34

Figure 5.46 presents the Force vs. CMOD diagram for the MSCBT for the different simulated concrete types (C-10, C-11, and C-12). A good agreement can be observed between the simulations (dashed line) and the experimental results (solid line). The simulations also closely align with the boundaries of the envelope (upper bound and lower bound).

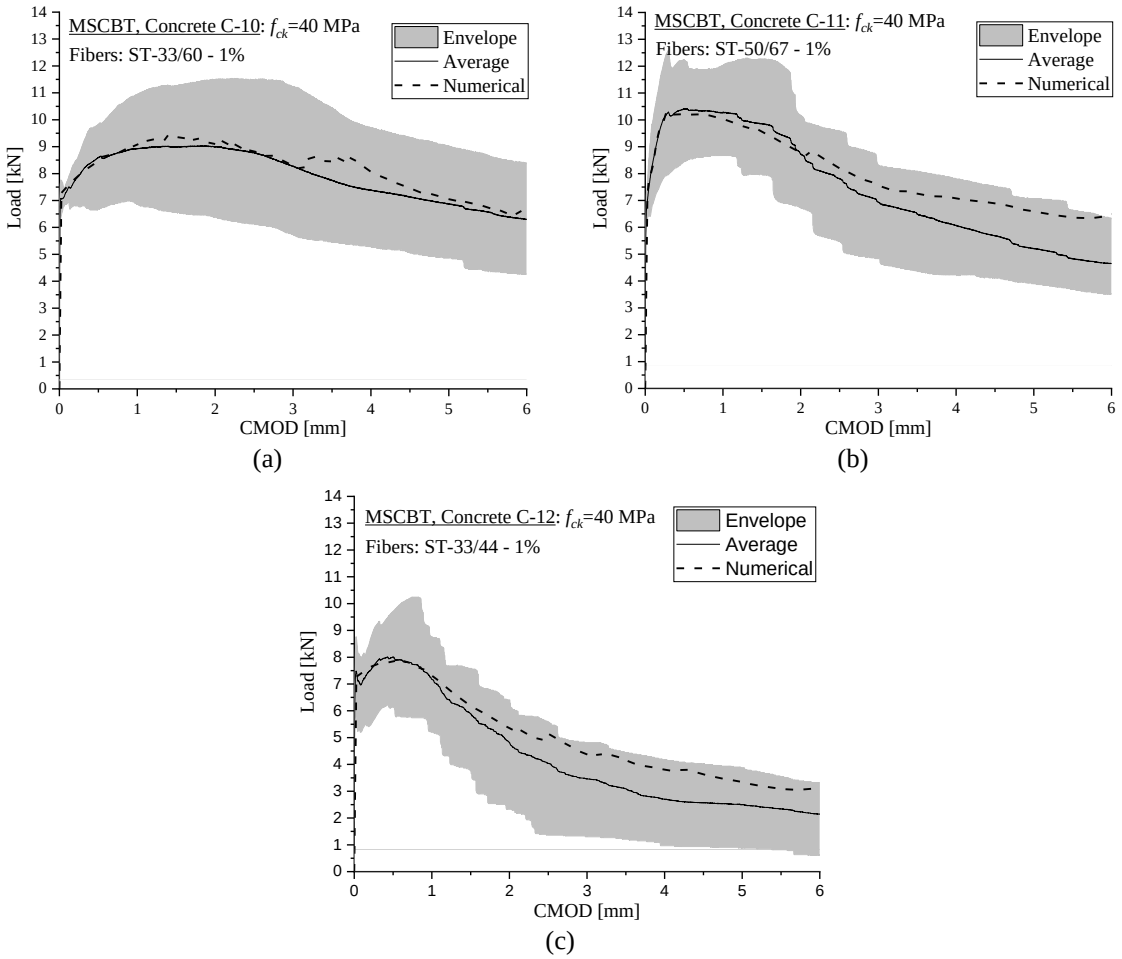


Figure 5.46 – Force vs. CMOD diagrams for the MSCBT numerical results, compared with the experimental average and envelope for concretes: (a) C-10, (b) C-11, and (c) C-12.

The areas under the Force vs. CMOD diagrams were calculated for average experimental diagrams and for simulations. These results are presented in the Table 5.17. Based on the results obtained, the error between average experimental and numerical areas was found to be less than 9% for all the concretes studied, reinforcing the explanation provided in the previous paragraph. Like was observed for the average experimental results, the numerical simulations also show a tendency for a decrease in the area under the diagram when comparing concrete C-12 with C-11 and C-11 with C-10. The superior performance of concrete C-10 can be attributed to the higher number of fibers per gram and the high aspect ratio of the ST-33/60 fiber. The second-best performance of concrete C-11 is explained by the larger size of the ST-50/67 fiber, which guarantees effective anchoring in the matrix. The lower performance of C-12 is due to the shorter length and lower aspect ratio of the ST-33/44 fiber.

Table 5.17 - Area under the Force vs. CMOD for the 3PBT numerical results, compared with the experimental average for concretes: (a) C-10, (b) C-11, and (c) C-12.

Area under diagram [kN.mm]	C-10	C-11	C-12
Average experimental	47.46	44.39	25.50
Numerical	49.00	47.97	29.63
Error [%]	3.24	8.06	16.20

5.9.4. Numerical simulation with Julia (parametric study)

This section presents the results obtained from the simulations conducted according to the procedure described in Section 4.13.7. This study employs a continuous–discontinuous approach, integrating linear bulk elements with nonlinear cohesive elements (Durand & Silva, 2019). In the simulations conducted using the Amaru library in this study, the cohesive element formulation is based on the isoparametric element (detailed in Section 4.13.1). The model for the Fracture Process Zone (FPZ) (detailed in Section 4.13.2) follows the same approach as presented in the literature (Silva, 2021; Silva, 2017). The Power Yield Crack Model (detailed in Section 4.13.3) is a constitutive model designed to predict cracks through the opening of cohesive elements. The nonlinear behavior of concrete was represented using the Willam-Warnke model with hardening (detailed in Section 4.13.5), which is used to describe the behavior of concrete under different types of loading, such as tension, compression, and shear. The parameters and constitutive models used for this analysis are

the same as those described in Section 4.13.6. The parameters are presented again in Table 5.18.

Table 5.18 – Material properties of simulations according to the concrete type.

Concrete	Young's modulus [×10³ MPa]	Poisson's ratio	Compressive strength [MPa]	Tensile strength [MPa]
C-10	36.3	0.2	45.6	3.4
C-11	36.3	0.2	42.2	3.1
C-12	36.3	0.2	35.8	2.9

Figure 5.47 displays the results for the simulations with the displacements (Ux) in the x direction for the vertical displacement increment of 0.5 mm, considering different notch sizes and varying diameters of the specimens. For better visualization, the displacements in these illustrations are magnified by 10 times.

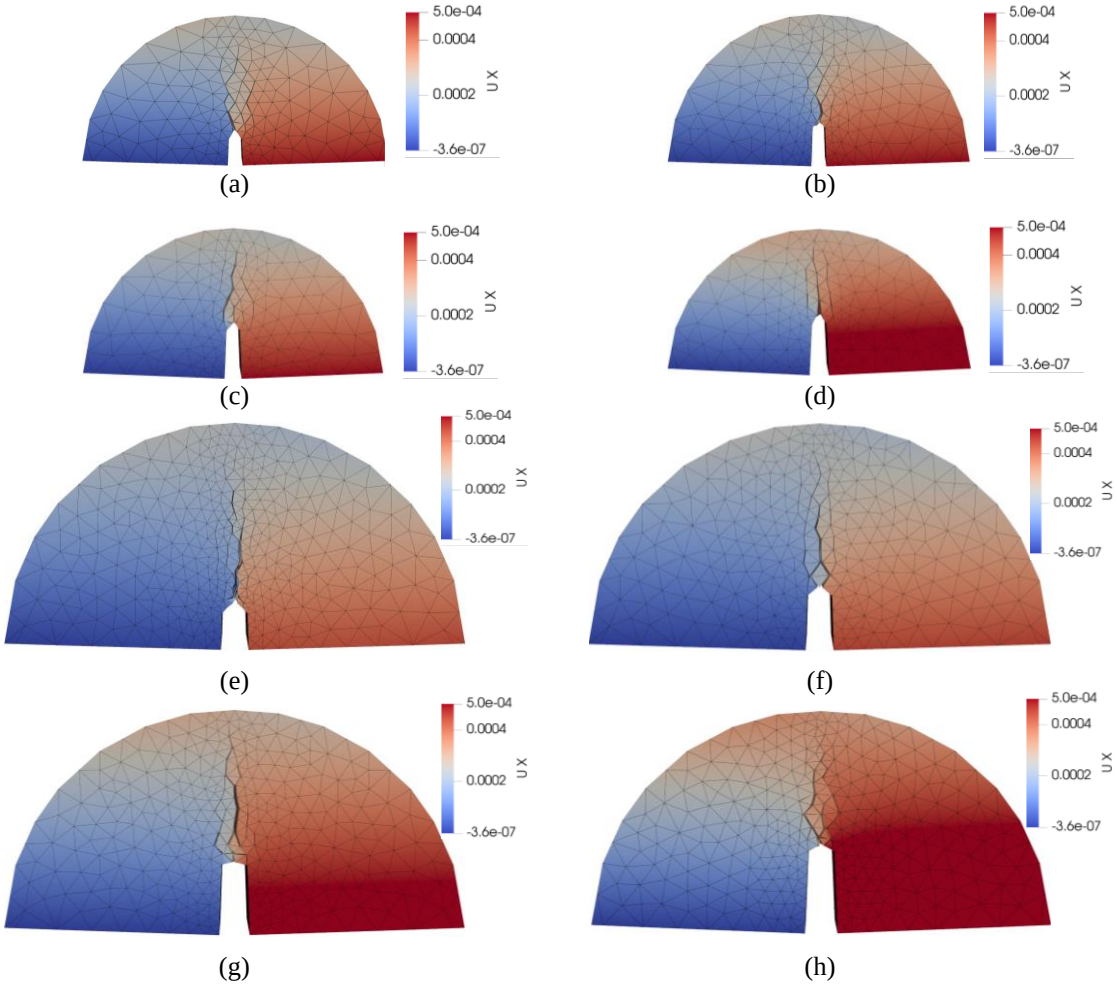


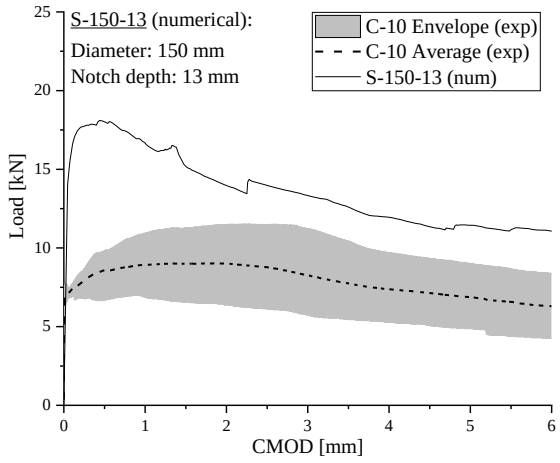
Figure 5.47 – Displacements (Ux) [m] from the MSCBT simulations conducted for: (a) S-150-13, (b) S-150-19, (c) S-150-24, (d) S-150-28, (e) S-200-16, (f) S-200-24, (g) S-200-31, (h) S-200-37.

It is observed that as the depth of the notch increases (from 13 to 28 mm), the displacements (Ux) found are predominantly greater. This can be noted by the wider range of variation in U in Figure 5.47c and Figure 5.47d compared to Figure 5.47a and Figure 5.47b. This occurs due to the loss of cross-sectional area with the increase in the depth of the notch. Regarding the cracking pattern, the formation of a single crack predominated in the central region of the notch, with small additional cracks that exhibited minimal opening for samples with notch depths of 13, 19, and 24 mm.

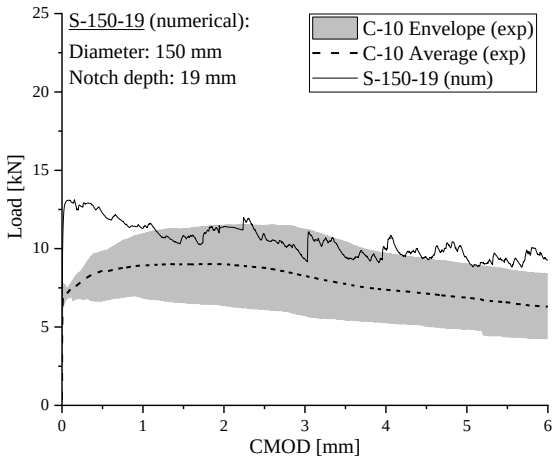
In experimental tests, it is generally observed that a single dominant macrocrack forms, propagating relatively stably from the notch or the region of highest tensile stress concentration (Karihaloo, 1995). This crack pattern typically results from stress redistribution mechanisms and fiber bridging, which tend to suppress the formation of multiple secondary cracks (Mindess, et al., 2003). In contrast, numerical simulations,

especially those employing cohesive zone models or advanced constitutive formulations for residual tensile behavior, often exhibit the formation of multiple secondary cracks throughout the tensile region (Bazant & Jaime, 1998). Models such as cohesive formulations with softening behavior may allow simultaneous development of multiple damage zones (Turon, et al., 2007).

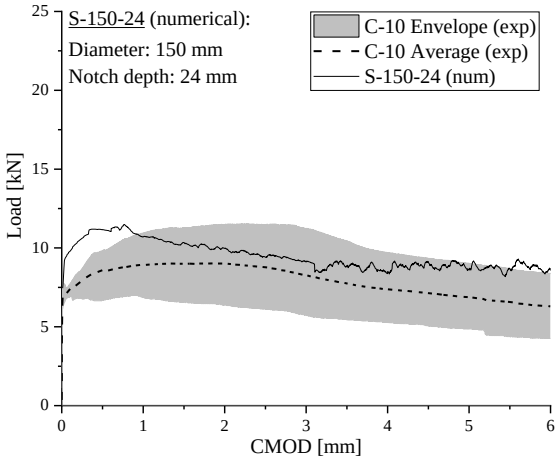
In the Figure 5.48, the force vs. CMOD results obtained from the simulations are presented. For comparative purposes, the average experimental result diagram for concrete C-10, for samples with a length of 100 mm and a notch depth of 10 mm, is also presented (dashed line), and also the envelope (hatched in gray). The portion of the diagram up to a CMOD of 6 mm has been highlighted. It is observed that all simulated samples in this section (with a minimum effective height of 47 mm) exhibit a greater effective height than the experimentally tested samples (40 mm). The latter have their results described in section 5.4.3 and correspond to samples with dimensions of 100 mm in diameter and a 10 mm notch. In contrast, the simulations in this section have diameters of 150 mm and 200 mm, with notch depths varying between 13 and 37 mm (Table 4.7).


S-150-13 (numerical):
Diameter: 150 mm
Notch depth: 13 mm
C-10 Envelope (exp)
C-10 Average (exp)
S-150-13 (num)
Load [kN]
CMOD [mm]

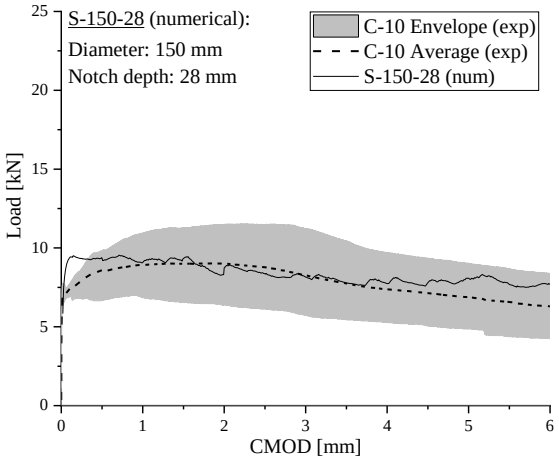
(a)


S-150-19 (numerical):
Diameter: 150 mm
Notch depth: 19 mm
C-10 Envelope (exp)
C-10 Average (exp)
S-150-19 (num)
Load [kN]
CMOD [mm]

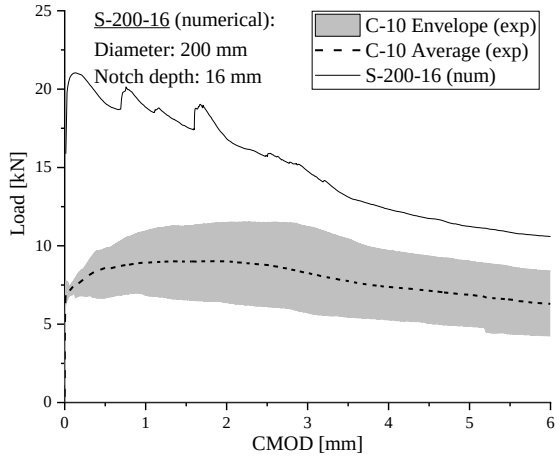
(b)


S-150-24 (numerical):
Diameter: 150 mm
Notch depth: 24 mm
C-10 Envelope (exp)
C-10 Average (exp)
S-150-24 (num)
Load [kN]
CMOD [mm]

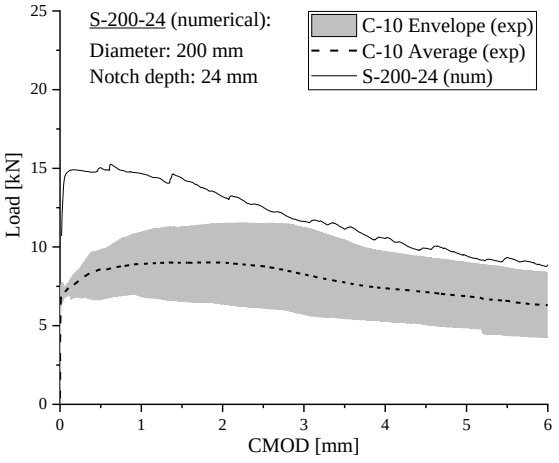
(c)


S-150-28 (numerical):
Diameter: 150 mm
Notch depth: 28 mm
C-10 Envelope (exp)
C-10 Average (exp)
S-150-28 (num)
Load [kN]
CMOD [mm]

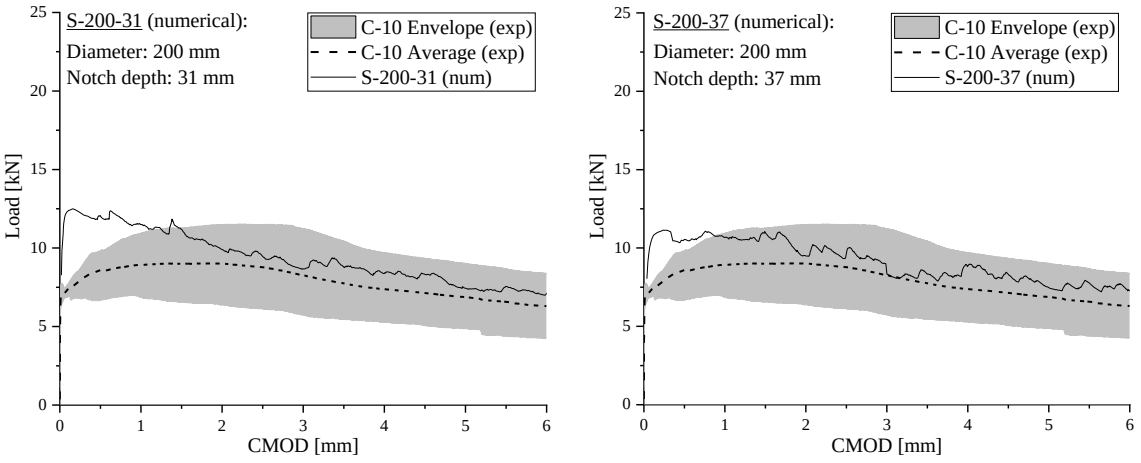
(d)


S-200-16 (numerical):
Diameter: 200 mm
Notch depth: 16 mm
C-10 Envelope (exp)
C-10 Average (exp)
S-200-16 (num)
Load [kN]
CMOD [mm]

(e)


S-200-24 (numerical):
Diameter: 200 mm
Notch depth: 24 mm
C-10 Envelope (exp)
C-10 Average (exp)
S-200-24 (num)
Load [kN]
CMOD [mm]

(f)



(g) (h)

Figure 5.48 – Force vs. CMOD response from experimental results of C-10 with samples with 100 mm of diameter and 40 mm of effective height (just for reference) and simulations of MSCBT varying the notch depth for: (a) S-150-13, (b) S-150-19, (c) S-150-24, (d) S-150-28, (e) S-200-16, (f) S-200-24, (g) S-200-31, (h) S-200-37.

Therefore, differences in the force vs. CMOD diagram are expected since, except for S-150-13 and S-200-16, there is a variation in the Effective Span / Effective Height parameter when comparing the cases in this section (Table 4.7) to the experimental tests (with a ratio of 2.25). Additionally, the effective heights differ. Given that the samples have a thickness of 75 mm, the areas of the regions where the cracks propagate are also different. The effective area at mid-span in the experiment ($75 \times 40 = 3000$ mm²) is smaller than in all simulated cases in this section (The values of these areas are presented in the Table 4.7). These larger area results in a greater number of fibers in the fractured section and a higher contribution of these fibers to the Force vs. CMOD response. Consequently, this increase in height is expected to contribute to greater stiffness. This can be observed by comparing the experimental results for concrete C-10 (Figure 5.22d) with the results in Figure 5.48.

The areas under the Force vs. CMOD diagrams are presented in the Table 5.19. The results corroborate what is stated in the previous paragraph. For samples with a length of 150 mm, the greater the effective height, the larger the area beneath the diagram.

Table 5.19 - Area under the Force vs. CMOD diagrams for simulations at each notch depth and each sample length.

Parameter	S-150-13	S-150-19	S-150-24	S-150-28	Concrete C-10 (experimental)
Area under diagram [kN.mm]	81.32	62.87	56.88	50.12	47.43

For the chosen L/H values (Table 4.7), the higher this ratio, the closer the element is to beam-like behavior. Consequently, the closer it is to this behavior, in an elastic analysis, the deformations (ε_{xx}) should exhibit a more linear variation with depth along the height (H) of the sample. Therefore, for a small vertical displacement increment (0.1 mm), the deformations were analyzed for S-150-13 and S-150-28. These two simulations were chosen because they exhibit the greatest difference in the L/H ratio (2.25 and 3.0, respectively). For this analysis, five points were selected from the finite element mesh of the vertical cross-section in the central region of the sample. Due to mesh limitations, it is not possible to collect perfectly equidistant points in the cross-section. Therefore, selected points are those illustrated in Figure 5.49.

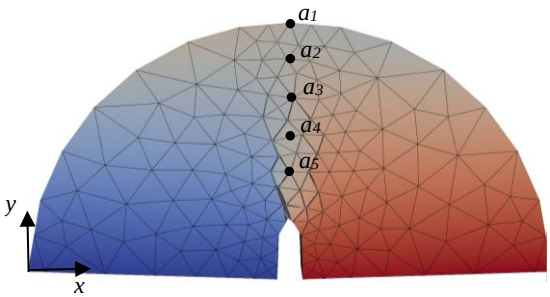


Figure 5.49 – Illustration of the selected points ε_{xx} for the analysis under a small vertical displacement increment for S-150-13.

The vertical coordinates (y) of points a_1, a_2, a_3, a_4 and a_5 and the respective ε_{xx}, relative to the coordinate axes illustrated in Figure 5.49 are presented in Table 5.20.

Table 5.20 – Vertical coordinates (y) of points a_1, a_2, a_3, a_4 and a_5 and the respective ε_{xx}, relative to the coordinate axes for simulations S-150-13 and S-150-28.

Point	S-150-13		S-150-28	
	ε_{xx}	Vertical coordinates (y) [mm]	ε_{xx}	Vertical coordinates (y) [mm]
a_1	-2.647E-4	0.0745	-4.173E-4	0.0745
a_2	-1.871E-4	0.0640	-2.061E-4	0.0636
a_3	7.267E-5	0.0525	8.300E-6	0.0522
a_4	1.432E-4	0.0417	1.528E-4	0.0452
a_5	3.175E-4	0.0311	3.072E-4	0.0305

The ε_{xx} graphs with the corresponding depths for S-150-13 and S-150-28 were plotted in Figure 5.50 and Figure 5.51, respectively. A difference of less than 2% was found in the R^2 value. The graph for S-150-28 exhibits greater linearity, which is since the geometry used in this simulation has a higher L/H ratio, resulting in a behavior closer to that of a beam, as expected for this analysis.

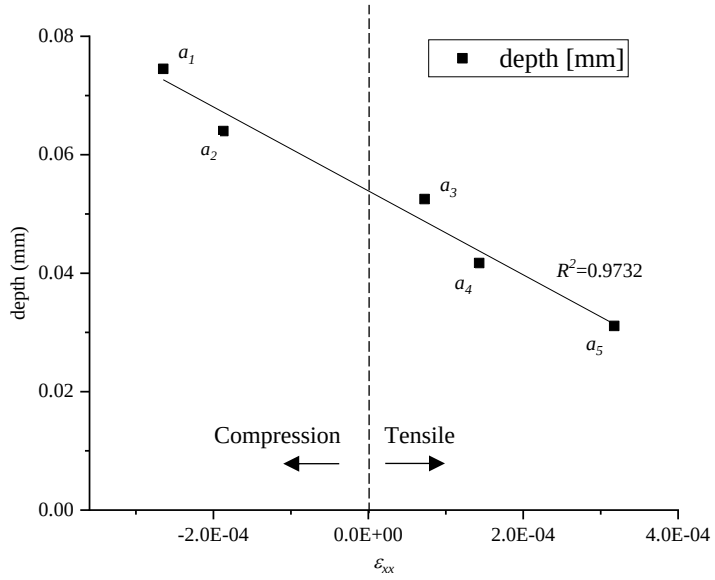


Figure 5.50 – Vertical coordinates y (depth) of points a_1, a_2, a_3, a_4 and a_5 and the respective ε_{xx}, relative to the coordinate axes for S-150-13.

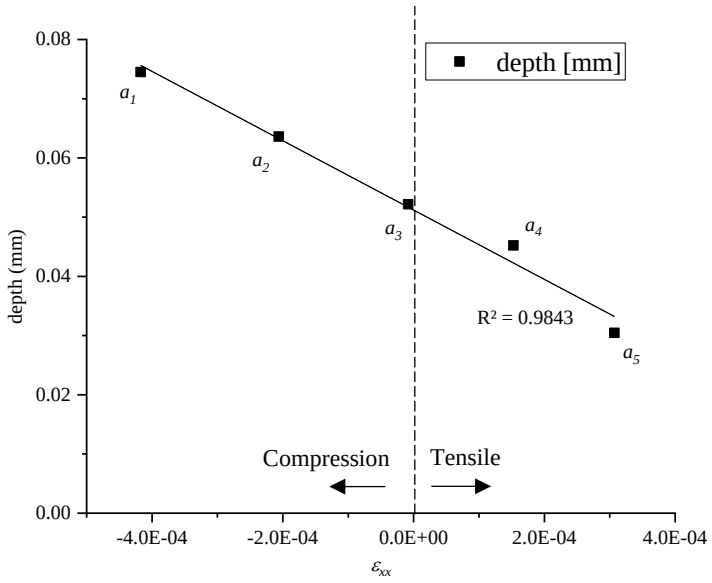


Figure 5.51 – Vertical coordinates y (depth) of points a_1, a_2, a_3, a_4 and a_5 and the respective ε_{xx}, relative to the coordinate axes for S-150-28.

5.9.5. Discussion of results

This work carried out an experimental investigation on the characterization of the post-cracking tensile behavior of FRC. The MSCBT was proposed and validated by performing an inverse analysis procedure. The results obtained by the proposed test were compared to the results obtained by UTT and 3PBT performed with the same concrete. This topic leads to the following summary:

- The proposed MSCBT is a promising procedure for the determination of the post-cracking behavior of SFRSCC.

- The MSCBT proved to be promising for obtaining samples representative of real structures and to assess the anisotropy of FRC, since the geometry of the samples in this test are compatible for extraction in a real structure using a core cutting machine.

- Most of the samples tested using the proposed methodology showed desirable failure modes, despite the need for care to perform the cutting procedure.

- The usual analytic formulation for determining the Load-CMOD curve applied to 3PBT proved to be useful for performing the inverse analysis procedure for the MSCBT applied to 3PBT proved to be useful for performing the inverse analysis procedure of the MSCBT,

since considerations of the appropriate initial parameters are carried out, considering the geometry of the sample.

- When compared to the results of the UTT and 3PBT tests, the area under the stress versus crack opening curve obtained by inverse analysis of the experimental data from the proposed test (MSCBT) showed an average error between average experimental and analytical results of 8% and 12%, respectively.

Despite the promising results obtained in the tests presented in this work, special attention should be given to the fact that these are preliminary tests. A more rigorous validation, with a larger sample size, assessing the repeatability and precision of the proposed testing method, is still necessary. Additionally, the test needs to be evaluated when applied to concretes with longer fibers. The small dimensions of the specimen used in the test proposed in this work may pose a problem for accurately characterizing concretes with longer fibers and may also negatively affect the dispersion of the results obtained.

This research presented some limitations that are proposed to be overcome in future work:

- Conducting a size-effect study on SFRCC MSCBT specimens to evaluate the influence of specimen dimensions, shear span to effective depth ratio, and the notch depth to effective depth ratio.

- Conducting a boundary conditions study to evaluate the influence of rollers for the test setup on the failure mode and results of the MSCBT.

6. CONCLUSIONS

6.1. General conclusions

This work carried out an experimental, numerical and algorithmic investigation on the characterization of the post-cracking tensile behavior of Steel Fiber Reinforced Self-Compacting Concrete (SFRSCC).

This work presented a comprehensive investigative literature review, primarily focused on the existing testing methods reported in the literature for the characterization of SFRSCC, as well as on inverse analysis procedures encompassing analytical and numerical strategies to determine the stress–crack width (σ–w) relationship and the Force versus Crack Mouth Opening Displacement (F–CMOD) diagrams for this type of concrete. The review also encompassed a detailed examination of key parameters that influence these tests, including general aspects of Fiber Reinforced Concrete (FRC), Fiber Orientation, the Wall Effect, Specimen Dimensions, and Structural Specimen configurations.

In addition, this work proposed a novel method for conducting the inverse analysis procedure specifically tailored to SFRSCC initially for 3PBT. For the proposed method, a computational algorithm is developed based on a well-validated analytical approach in which the model parameters are progressively calibrated according to experimental experiences available in literature. This procedure proved to be more time-efficient than conventional analytical methods and eliminates the need for numerical modeling due to a significant reduction in computational iterations. Its effectiveness was validated through comparison with experimental test results.

The main contribution of this work is the proposal of a novel testing method for characterizing the post-cracking behavior of SFRSCC: the Modified Semi-Circular Bending Test (MSCBT), which is based on the conventional Semi-Circular Bending (SCB) Test. In this new testing method, the CMOD is continuously monitored, enabling the construction of the Force–CMOD (F–CMOD) diagram. Moreover, the MSCBT allows for a detailed investigation of the post-cracking behavior of SFRSCC, rather than being limited to tensile strength alone. The test has proven to be both simple and rapid to perform, while also allowing core specimens to be extracted from actual structures (structural specimens). This

enhances the representativeness of the test results with respect to the real structural behavior, thereby improving the reliability and applicability of the findings.

Furthermore, a comprehensive experimental investigation is conducted for 72 samples of MSCBT are carried out. Two classes of concrete resistance (20 and 40 MPa), three types of fibers (ST-33/60, ST-50/67 and ST-33/44), as well as two fiber contents (0.5% and 1.0%) are tested. The experimental results demonstrated that MSCBT exhibited sensitivity to key parameters, including concrete strength, fiber content, and fiber type.

The proposed MSCBT was validated through the inverse analysis procedure initially developed in this work for the 3PBT, which was adapted for the MSCBT. The results obtained by the proposed test were compared to the results obtained by UTT and 3PBT performed with the same concrete.

In this study, the Splitting Test (ST) approach with V-notch specimens is conducted for 48 samples are carried out. Analogously to the procedure adopted in the MSCBT, two classes of concrete resistance (20 and 40 MPa), three types of fibers (ST-33/60, ST-50/67 and ST-33/44), as well as two fiber contents (0.5% and 1.0%) are tested. The experimental results demonstrated that ST exhibited sensitivity to key parameters, including concrete strength, fiber content, and fiber type.

An experimental study was also conducted using MSCBT specimens with two different thicknesses (150 mm and 75 mm) and two types of fibers. As expected, the results for the 75 mm thick specimens exhibited failure modes more consistent with flexural behavior. It was demonstrated that the test is more suitable for specimens with smaller thicknesses.

6.1.1. Final Considerations on the Feasibility and Robustness of the MSCBT Methodology

This work provided the following conclusions:

- The proposed MSCBT is a promising procedure for the determination of the post-cracking behavior of SFRSCC.

- It was shown that the performance of the MSCBT showed consistent results for the characterization of the post-cracking behavior of the SFRSCC.

- The MSCBT proved to be promising for obtaining samples representative of real structures and to assess the anisotropy of SFRSCC, since the geometry of the samples in this test are compatible for extraction in a real structure using a core cutting machine.

- Most of the samples tested using the proposed methodology showed desirable failure modes, despite the need for care to perform the cutting procedure.

- The usual analytic formulation for determining the Load-CMOD curve applied to 3PBT proved to be useful for performing the inverse analysis procedure for the MSCBT applied to 3PBT proved to be useful for performing the inverse analysis procedure of the MSCBT, since considerations of the appropriate initial parameters are carried out, considering the geometry of the sample.

- The MSCBT was presented as a test with sensitivity to the parameters: concrete strength, fiber type and fiber content. Samples in which these parameters were different showed variations on the residual strength parameters of the studied concretes, when they are obtained using the fib Model Code 2010 equations from 3PBT.

- Concrete with higher fiber content, or with fiber types with a higher aspect ratio (ST-33/60 and ST-50/67) or/and smaller diameter and length (ST-33/60), showed better performance. The fiber type that presented the worst performance (ST-33/44) has a larger diameter and a smaller length and, consequently, a smaller form factor. These results are already expected for bending results like 3PBT.

- The presented results show great similarity between the MSCBT and the 3PBT because bending of the sample occurs in both tests. The intensities of the loads monitored during the test, as well as the f_r parameters, presented values lower than those expected for the 3PBT. This result was already expected, since the size and amount of fibers in the MSCBT sample section are smaller.

- The MSCBT proved to be easy to perform because the final samples are small in size and light, which facilitates the transport and preparation of the samples.

- The rupture mode is as expected in most of the samples tested, corresponding adequately to the occurrence of bending in the sample.

- MSCBT samples have been shown to be easily drilled out of larger structures. This makes the test results more representative of the actual structure when compared to 3PBT.

- Despite the promising results obtained in the tests presented in this work, special attention should be given to the fact that these are preliminary tests. The small dimensions of the specimen used in the test proposed in this work may pose a problem for accurately characterizing concretes with longer fibers and may also negatively affect the dispersion of the results obtained.

- The MSCBT results showed a variation of approximately 30% between the maximum and minimum values obtained. Although this might suggest a notable level of variability, the dispersion was considered low, especially when compared to the conventional Three-Point Bending Test (3PBT), which exhibited a similar level of variation despite involving specimens with a significantly larger fracture area. This result diverges from initial expectations, as the smaller fracture surface in MSCBT specimens was anticipated to increase sensitivity to local heterogeneities, particularly fibre distribution and orientation, and thus lead to greater scatter. However, the relatively low variability observed may be attributed to the intrinsic characteristics of the MSCBT setup. The semi-circular geometry and the well-defined notch likely promote a more stable crack path and a more uniform stress distribution in the fracture process zone, contributing to more consistent responses. These findings support the reliability of the MSCBT as a viable and repeatable method for assessing the post-cracking behaviour of SFRSCC, even in specimens with limited fracture surfaces.

6.1.2. MSCBT applied to specimens of varying thicknesses

A comparative study was carried out on the experimental results of MSCBT specimens with thicknesses of 150 mm and 75 mm. A total of 26 samples were tested, all made with concrete of 40 MPa compressive strength and a fiber volume fraction of 0.5%. For the 75 mm thickness, six samples were produced using ST-33/60 type fibers and another six with ST-

33/44 type fibers. For the 150 mm thickness, seven samples were tested with ST-33/60 type fibers and another seven with ST-33/44 type fibers.

In most of the tested specimens, the failure mode observed was as expected, corresponding adequately to flexural behavior. However, a higher rate of test anomalies was identified in the 150 mm thick specimens (25%) compared to the 75 mm thick specimens (7%). These findings demonstrate that the test is more suitable for specimens with smaller thicknesses. However, a more in-depth analysis of the size effect is still required, including comparisons with specimens of smaller thicknesses.

6.1.3. Effectiveness of the used Splitting Tensile Test (ST) in Evaluating Fracture and Residual Behavior of SFRSCC

The analysis of crack propagation in the Splitting Tensile Test (ST) confirmed the expected failure mode in most specimens. A single central crack initiated at the straight notch was observed in 43 out of 48 samples, validating the test setup. Five specimens showed atypical cracking patterns—such as peripheral, transverse, or LVDT-interfering cracks—likely due to surface irregularities, misalignment, or torsional effects during molding or testing. These outliers were excluded to ensure consistent and reliable analysis.

The ST test enabled the generation of σ-COD diagrams, effectively characterizing the post-cracking behavior of SFRSCC. Results showed that increasing fiber volume from 0.5% to 1.0% led to an average 27% increase in the area under the σ-COD curve. Likewise, concretes with higher compressive strength (40 MPa) exhibited σ-COD areas approximately 28% greater than those with 20 MPa.

Fiber geometry significantly influenced performance: ST-33/60 fibers produced the highest σ-COD areas, followed by ST-50/67 and ST-33/44, with average improvements of 6% and 40%, respectively. These findings highlight the importance of aspect ratio and fiber count per gram.

Variability in results was generally below 30%, consistent with expected effects of fiber dispersion and orientation. A strong correlation (R^2=0.7616) between the number of effective fibers and σ-COD area reinforced the method's reliability.

Residual strength parameters (f_{R1} to f_{R4}) improved with increased fiber content, while tensile strength parameters (f_{ct}, $f_{fct,L}$) were more influenced by matrix strength. ST-33/60 fibers yielded the best mechanical performance across parameters, consistent with 3PBT results and theoretical models.

Overall, the ST method proved effective and sensitive to key parameters, making it suitable for assessing the mechanical behavior of fiber-reinforced self-compacting concrete.

6.1.4. Computational Simulations

Based on the computational simulations conducted in this study, the following final considerations can be drawn:

- The computational simulations supported the validation of the experimental results, as they were highly representative of the behavior observed experimentally for the MSCBT, UTT, and 3PBT tests.
- In most of the simulations performed, significant similarity was observed between the cracking patterns predicted by the simulations and those obtained experimentally.
- For the L/h ratios investigated, it was observed that increasing this ratio leads to a behavioral shift closer to that of a beam under flexural loading.

6.2. Limitations of the Study

In this work, an extensive experimental validation of the MSCBT was carried out. Different concrete strength classes, fiber types, and fiber volume fractions were tested. The experimental program was complemented by numerical validation using Finite Element Method (FEM) software and inverse analysis techniques. Therefore, the method is validated for the concrete types tested in this study. However, this study presents certain limitations.

For instance, if other types of concrete are used—such as Ultra-High Performance Concrete (UHPC) or another self-compacting concrete with significantly higher compressive strength, in the range of 70 to 80 MPa—the results may differ. This is due to the distinct mechanical behavior of these special concretes. Further studies are also needed for different fiber types and volume fractions.

However, the geometry of the tested specimens remains limited. There is a need for further testing involving specimens with varying effective heights, enabling the analysis of different fracture areas and allowing for slenderness ratios (L/h) that more closely resemble the flexural behavior observed in beams. Additionally, it is recommended that the test be conducted on specimens with a broader range of thicknesses. Furthermore, the effective height of the MSCBT specimen tested in this study was 40 mm, and the maximum aggregate size was 9.5 mm. It is recommended that tests be conducted using a greater effective height relative to the aggregate size.

Despite the significant advantages of the MSCBT presented in this document, one drawback that can be highlighted is the need for an axial cut along the cylinder. This cut must be carried out carefully and with an appropriate clamping system to ensure the safety of the cutting equipment operator and to achieve a precise cut. Consequently, the final geometry of the specimen must be adequate, with a flat and regular base suitable for proper positioning on the supports.

One of the main advantages of MSCBT is its applicability to cores extracted from real structures. Nevertheless, in the present study, the test was applied exclusively to cores obtained from prisms cast for the Three-Point Bending Test (3PBT). Therefore, it is important to perform future tests on cores extracted directly from actual structural elements, such as beams. The beams may be subjected to service loads or tested without overload to evaluate the effect of such loading conditions on the test results. Another drawback is that, as an indirect test, it still requires the application of an inverse analysis procedure to obtain the tensile behavior of the material.

Furthermore, MSCBT has potential for assessing the anisotropic behavior of Steel Fiber Reinforced Self-Compacting Concrete (SFRSCC). In this study, all specimens were extracted from the same position relative to the casting direction of the prisms. The cutting orientation was controlled so that the preferential alignment of the fibers remained consistent across all samples. Future studies could include the casting of slabs to allow core extraction in multiple directions, thus enabling a comprehensive evaluation of anisotropic behavior.

The support cylinders for the MSCBT specimens were welded to the base of the testing device. This configuration introduces friction, thereby reducing the specimen's ability to

slide freely during the test. To mitigate this issue, Teflon tapes were placed on the supports. However, the sliding capacity of the specimen may still be compromised.

In the following section, these limitations are discussed in greater detail, and proposals for future research are presented.

6.3. Recommendations for future research

Despite the contributions made through this study, several gaps in the current understanding of the MSCBT testing method for SFRSCC still remain. Therefore, proposals are presented for future works:

6.3.1. Proposed Modifications to MSCBT Specimen Geometry for Enhanced Test Reliability

The geometry of the MSCBT specimen was selected to enable the extraction of cylindrical cores from standard 3PBT (Three-Point Bending Test) prism specimens. Given that typical 3PBT specimens have a height of 150 mm, a core diameter of 100 mm was established to ensure proper extraction, maintaining a 25 mm clearance from both the top and bottom ends of the prism. However, this geometry presents certain limitations. Specifically, the resulting MSCBT specimen has an effective height (excluding the notches) of only 40 mm, whereas the specimens that yielded the most reliable test results exhibited a thickness of 75 mm. This leads to a reduced fracture area, which may result in significant variability in the outcomes depending on the quantity and orientation of fibers within the section.

Therefore, a proposed direction for future work is to extract core specimens not from 3PBT prisms, but from thin SFRSCC panels specifically cast for this purpose. This approach would allow for the extraction of larger diameter cores, resulting in MSCBT specimens with greater effective height and, consequently, a larger fracture area. As a result, a reduction in the scatter of experimental results is expected, thereby improving the reliability of the test method.

Moreover, a greater effective height would allow for an increased span-to-depth ratio of the specimen, depending on the notch depth selected. This would enable the specimen's behavior during testing to more closely resemble that of a beam rather than a deep beam or

wall-like element. As a result, the specimen would exhibit a more realistic flexural response, minimizing the likelihood that portions of the applied load might be directly transferred to the supports without adequately inducing the induced bending effects.

Furthermore, by applying this testing methodology with core extraction from cast panel, the SFRSCC could exhibit a more anisotropic mechanical behavior. This is due to the fact that when the concrete is cast from the center of the panel, the material flows predominantly in a radial direction, which influences the preferential orientation of the fibers. An additional advantage of this approach is the ability to extract specimens at a constant distance from the casting point and to perform the MSCBT in various directions. This enables an in-depth analysis of the anisotropic behavior of the material.

The effective height of the MSCBT specimen tested in this study was 40 mm, and the maximum aggregate size was 9.5 mm. It is recommended that tests be conducted using a greater effective height relative to the aggregate size.

6.3.2. Proposed Application of MSCBT to Core Samples Extracted from Real Structural Elements

As a further development of the proposed Modified Semi-Circular Bending Test (MSCBT), it is suggested that future research explore its application to core specimens extracted directly from in-service or full-scale structural elements, such as beams. While previous experimental programs relied on laboratory-cast prisms, the extraction of specimens from actual structures could significantly enhance the realism and practical relevance of the mechanical characterization of Steel Fiber Reinforced Self-Compacting Concrete (SFRSCC).

This approach would allow for a more accurate representation of the concrete's behavior under real-world casting, curing, and loading conditions, which are typically more complex and variable than those reproduced in laboratory settings. Moreover, this strategy would make it possible to investigate the impact of factors such as fiber distribution, fiber orientation, and casting-induced anisotropy as they occur naturally within structural members.

By applying the MSCBT to such specimens, it would be possible to evaluate not only post-cracking behavior under flexural loading but also the reliability and robustness of the test itself when subjected to variability inherent in real structures. Additionally, this direction of research could open the door for MSCBT to be employed as a quality control technique in the assessment of existing structures, particularly in rehabilitation and durability studies of fiber-reinforced concrete.

Such developments would represent an important step forward in bridging the gap between laboratory-based testing protocols and in-situ structural performance evaluation.

In the present study, the core diameters were selected to be compatible with the height of the standard 3PBT specimen, which is 150 mm. As a result, the MSCBT specimens were tested with an effective height of 40 mm. However, typical structural beams often exhibit greater heights than this. Therefore, it would also be feasible to test MSCBT specimens with increased heights. This would enable experimental testing of MSCBT samples with larger height dimensions and, consequently, with span-to-depth ratios more representative of the flexural behavior of structural beams.

6.3.3. Further Investigation on the Influence of Specimen Thickness in MSCBT

Although the current research evaluated the influence of specimen thickness by comparing MSCBT results for samples with 75 mm and 150 mm thicknesses, further studies are necessary to comprehensively understand the effect of specimen size on the mechanical response of SFRSCC. The observed differences in post-cracking behavior and fracture energy indicate that thickness plays a significant role in stress distribution, crack propagation, and fiber engagement across the fracture plane.

Future work should therefore explore a broader range of specimen thicknesses, enabling the establishment of trends related to the size-dependent mechanical behavior of fiber-reinforced concretes under flexural loading. This would contribute to the investigation of size effect, a well-known phenomenon in fracture mechanics, wherein the nominal strength of concrete specimens varies with specimen size due to the non-linear fracture process zone.

Such studies would not only help define the applicability limits of the MSCBT but also support the development of correction factors or scaling laws, allowing the generalization of results across different geometrical configurations. Additionally, understanding thickness

effects is crucial when interpreting results from cores extracted from real structures, where the available thickness cannot always be standardized. Therefore, advancing knowledge on the size effect in MSCBT is essential for ensuring the robustness, accuracy, and scalability of the test method for both research and practical engineering applications.

6.3.4. Mitigating Lateral Restraint Effects in MSCBT through Improved Boundary Conditions

During the MSCBT conducted in the present study, the support system consisted of steel cylinders welded to a rigid steel plate. While this configuration provided a stable base for testing, it also introduced frictional resistance, particularly when the specimen tended to slide laterally under flexural deformation. This friction may interfere with the natural development of crack openings, stress redistributions, and the mobilization of fiber bridging mechanisms. To mitigate this issue, Teflon tape was applied beneath the supports to facilitate sliding. However, it remains uncertain whether this measure is sufficient to fully eliminate the frictional restraint and its influence on the test results. Therefore, future research should aim to develop improved support systems that allow free rotational and translational movement of the specimen along the loading direction, without compromising stability or alignment. Potential solutions include low-friction rollers, or polished bearing surfaces. Investigating the influence of support conditions on test repeatability, stress distribution, and fracture behavior would provide valuable insights and could lead to standardized improvements for the MSCBT methodology.

6.3.5. Parametric Calibration of Inverse Analysis Inputs Based on Fiber Content and Hook Geometry

In the present study, the parameters associated with crack openings (w_1, w_2, w_3) were defined based on the fiber length. However, the parameter w_1 and the corresponding σ_1 depend on the fiber content and, in the case of hook-anchored fibers, also on the hook length and curvature. Therefore, a proposed direction for future work is to investigate the application of the inverse analysis procedure in both 3PBT and MSCBT using alternative initial parameter values (w_1, w_2, w_3), taking this relationship into account and deepening the study

to propose an equation that adequately estimates these parameters. In this context, a comprehensive study is proposed to derive empirical or analytical equations capable of expressing the relationship between the initial parameters of the inverse analysis and the physical and geometrical characteristics of the fibers.

6.3.6. initial estimate for w_u on inverse analysis procedure

The equation used for an initial estimate for w_u on inverse analysis procedure of this work was useful for the propose of this work. The orientation factor (η) for IURD (isotropic uniform random distribution) of 0.5 was considered because it is commonly used for 3D geometric shape elements (Krenchel, 1975; Soroushian & Lee, 1990; Cunha, 2010; Stroeven & Hu, 2006). $L_f/4$ is the average statiscal embedded length of a fiber crossing an active crack. However, for SFRSCC, it is anticipated that the value of η may be slightly different because in the self-compacting concrete cast in beams, as carried out in this research, there is a preferential orientation for the fibers. For SFRSCC 3PBT beams, a value between 0.7 and 0.9 has already been determined for η (Cunha, 2010). Therefore, as a proposal for future work, it is suggested to employ more refined initial estimates for the value of η.

6.3.7. Use of clip gauge for MSCBT

The clip gauge is a widely used device for monitoring the Crack Mouth Opening Displacement (CMOD) in both 3-Point Bending Tests (3PBT) and Uniaxial Tensile Tests (UTT). For the MSCBT configuration, its application may be suitable. However, it presents limitations in measurement range, which could result in the loss of valuable data during testing. Additionally, greater care is required during test execution to prevent detachment of the device due to the specimen size and testing conditions. These factors led to the exclusive use of conventional LVDTs in this study. Nevertheless, as a proposal for future research, it is suggested that the MSCBT be performed using clip gauges positioned beneath the specimen, closer to the crack initiation zone, in combination with LVDTs placed on the lateral faces near the notch. The use of both monitoring systems, together with inverse analysis procedures, would allow for additional validation of the test results.

6.3.8. Test Simulations

In this study, the computational simulations were performed using as input data the tensile behavior smoothed by a Bezier curve. The numerical results were compared with the experimental outcomes of the 3PBT, MSCBT, and UTT tests. As a suggestion for future work, it is proposed to reverse the procedure—that is, to use experimental results from flexural tests such as the 3PBT and MSCBT as input data, in order to simulate the tensile behavior.

REFERENCES

Abbass, W., Khan, M. I. & Mourad, S., 2018. Evaluation of mechanical properties of steel fiber reinforced concrete with different strengths of concrete. *Constr. Build. Mater.*, Volume 168, p. 556–569.

Abdalla, H. M. & Karihaloo, B. L., 2003. Determination of size-independent specific fracture energy of concrete from three-point bend and wedge splitting tests. *Magazine of Concrete Research*, 55(2), p. 133–141.

Abdallah, S. & Fan, M., 2017. Anchorage mechanisms of novel geometrical hooked-end steel fibres. *Materials and Structures*, 50(139).

Abid, S. et al., 2021. Impact resistance of steel fiber-reinforced self-compacting concrete. *Magazine of Civil Engineering*, 105(5), pp. 10504-10504.

Abrishambaf, A., Barros, J. A. O. & Cunha, V. M., 2015. Tensile stress–crack width law for steel fibre reinforced self-compacting concrete obtained from indirect (splitting) tensile tests. *Cement & Concrete Composites*, Volume 57, pp. 153-165.

Abrishambaf, A., Barros, J. A. O. & Cunha, V. M. C. F., 2013. Relation between fibre distribution and post-cracking behaviour in steel fibre reinforced self-compacting concrete panels. *Cement and Concrete Research*, Volume 51, pp. 57-66.

Accornero, F., Rubino, A. & Carpinteri, A., 2022. Post-cracking regimes in the flexural behaviour of fibre-reinforced concrete beams. *International Journal of Solids and Structures*, Volume 248.

ACI 544.1R-96, 1996. *American Concrete Institute: State-of-the-art report on fiber reinforced concrete*, Technical report,: s.n.

AFGC, 2013. *Bétons fibrés à ultra-hautes performances–Recommandations*, Fr: AFGC.

Agra, R. R., Serafini, R., Figueiredo, A. D. & Berto, A. F., 2019. *Avaliação dos Efeitos do Fogo na Resistência à Tração Residual do Concreto Reforçado com Fibras de Aço por meio do Ensaio DEWS (Double Edge Wedge Splitting).* Porto, 5º CILASCI.

Ahmad, H. & Lagoudas, D. C., 1991. Effective Elastic Properties of Fiber-Reinforced Concrete with Random Fibers. *J. Eng. Mech.*, 17(12).

Alani, A. & Beckett, D., 2012. Mechanical behaviour of a steel fibre reinforced concrete ground slab. *Mag. Concr. Res.*, p. 593–604.

Alani, A. M. & Beckett, D., 2013. Mechanical properties of a large scale synthetic fibre reinforced concrete ground slab. *Construction and Building Materials*, Volume 41, pp. 335-344.

Aliha, M. R. M. & Ayatollahi, M. R., 2011. Mixed mode I/II brittle fracture evaluation of marble using SCB specimen. *Procedia Engineering*, Volume 10, pp. 311-318.

Almeida, L. C. d., 2006. *Identificação de parâmetros estruturais com emprego de análise inversa*, Campinas: s.n.

Álvarez, A. B., 2013. *Characterization and modelling of SFRC elements*, Barcelona: Doctoral thesis. Universitat Politècnica de Catalunya. Departament d'Enginyeria de la Construcción.

Alzabeebee, S. et al., 2023. Multiscale soft computing-based model of shear strength of steel fibre-reinforced concrete beams. *Innovative Infrastructure Solutions*, 8(63).

Amin, A., Markic, T., Gilbert, R. I. & Kaufmann, W., 2018. Effect of the boundary conditions on the Australian uniaxial tension test for softening steel fibre reinforced concrete. *Construction and Building Materials*, pp. 215-228.

Amirkhanian, A., Spring, D., Roesler, J. & Paulino, G., 2012. *Disk-Shaped Compact Tension Test for Plain Concrete*, Chicago: American Society of Civil Engineers (ASCE).

Arabani, M. & Ferdowsi, B., 2008. Evaluating The Semi-Circular Bending Test for HMA Mixtures. *IJE Transactions A: Basics*, Volume 22, p. 12.

Araújo, D. L., Carmo, L. C., Nunes, F. G. T. & Toledo Filho, R. D., 2010. Computational modeling of steel fiber reinforced concrete beams subjected to shear. *IBRACON Estrut. Mater.*, 3(1), pp. 68-94.

Arcelor Mittal, 2010. *Steel fibres - Shotcrete applications*, WireSolutions: s.n.

Arcelor Mittal, 2016. *O uso de fibras de aço no concreto,* ARCELOR MITTAL: s.n.

Associação Brasileira de Normas Técnicas, 2017. *Concreto Autoadensável,* NBR 15823: s.n.

Associação Brasileira de Normas Técnicas, 2018. *Concreto – Ensaio de Compressão de Corpos de Prova Cilíndricos,* NBR 5739: s.n.

Associação Brasileira de Normas Técnicas, 2018. *NBR 5739 – Concreto – Ensaio de Compressão de Corpos de Prova Cilíndricos,* Rio de Janeiro: s.n.

ASTM C1018-89, 1991. *American Society for Testing and Materials: Standard test method for flexural toughness and first-crack strength of fiber-reinforced concrete (using beam with third-point loading),* Philadelphia: s.n.

ASTM C1550, 2010. *AMERICAN SOCIETY FOR TESTING AND MATERIALS: Standard test method for flexural toughness of fiber reinforced concrete (using centrally loaded round panel),* West Conshohocken: s.n.

ASTM C1609, 2012. *Standard Test Method for Flexural Performance of Fiber-Reinforced Concrete (Using Beam With Third-Point Loading),* West Conshohocken, USA: ASTM International.

ASTM D7313-20, 2007. *Standard Test Method for Determining Fracture Energy of Asphalt-aggregate Mixtures using the Disk-Shaped Compact Tension Geometry,* West Conshohocken: ASTM International.

ASTM E399-22, 2020. *Standard Test Method for Linear-Elastic Plane-Strain Fracture Toughness of Metallic Materials,* West Conshohocken: ASTM International.

Ayatollahi, M., Aliha, M. & Hassani, M. M., 2006. Mixed mode brittle fracture in PMMA - An experimental study using SCB specimens. *Materials Science and Engineering*, 417(1-2), p. 348–356.

Azevedo, A. F. M., Barros, J. A. O., Sena-Cruz, J. M. & Gouveia, A. V., 2003. Software in structural engineering education and design. *in: Proceedings of III Portuguese-Mozambican Conference of Engineering*, pp. 81-92.

Aziminezhad, M. et al., 2020. Loading rate effect on fracture behavior of fiber reinforced high strength concrete using a semi-circular bending test. Volume 240.

Banthia, N., Majdzadeh, F., Wu, J. & Bindiganavile, V., 2014. Fiber synergy in Hybrid Reinforced Concrete (HyFRC) in flexure and direct shear. *Cement Concr. Compos.*, Volume 48, p. 91–97.

Banthia, N. & Trottier, J.-F., 1994. Concrete Reinforced with Deformed Steel Fibers, Part I: Bond-Slip Mechanisms. *Materials Journal*, 91(5), pp. 435-446.

Barros, J. A. & Figueiras, J. A., 1999a. Flexural behavior of SFRC: Testing and modeling. *Journal of materials in civil engineering,* 11(4), pp. 331-339.

Barros, J. A. O., Taheri, M., Salehian, H. & Mendes, P. J. D., 2012. A design model for fibre reinforced concrete beams pre-stressed with steel and FRP bars. *Composite Structures*, Volume 94, pp. 2494-2512.

Bazant, Z. P., 1999. Size effect on structural strength: a review. *Archive of Applied Mechanics*, Volume 69, p. 703–725.

Bazant, Z. P. & Jaime, P., 1998. *Fracture and Size effect in Concrete and Other Quasibrittle Materials.* Boca Raton: CRC Press.

Beer, G., 1985. An isoparametric joint/interface element for finite element analysis. *Int J Numer Methods Eng*, 21(4), p. 585–600.

Bencardino, F., Rizzuti, L., Spadea, G. & Swamy, R. N., 2013. Implications of test methodology on post-cracking and fracture behaviour of Steel Fibre Reinforced Concrete. *Composites Part B: Engineering*, Volume 46, pp. 31-38.

Bentur, A. & Mindess, S., 2007. *Fibre Reinforced Cementitious Composites.* 2ª ed. Londres e Nova Yorque: Taylor & Francis Group.

Bernard, E. S., 2000. Behaviour of round steel fibre reinforced concrete panels under point loads. *Materials and Structures (RILEM)*, Volume 33, p. 181–188.

Bezanson, J., Edelman, A., Karpinski, S. & Shah, V. B., 2012. *Julia: A fast dynamic language for technical computing,* s.l.: arXiv preprint arXiv:1209.5145.

Bitencourt Jr., L. A. G., Manzoli, O. L., Bittencourt, T. N. & Vecchio, F. J., 2019. Numerical modeling of steel fiber reinforced concrete with a discrete and explicit representation of steel fibers. *International Journal of Solids and Structures*, Volume 159, pp. 171-190.

Blanco, A. et al., 2014. Constitutive model for fibre reinforced concrete based on the Barcelona test. *Cement and Concrete Composites*, Volume 53, pp. 327-340.

Blasi, G. & Leone, M., 2022. Inverse analysis-based model for the tensile behaviour of fibre-reinforced concrete with manufactured and waste tyres recovered fibres. *Case Studies in Construction Materials*, July.17(e01297).

Blazy, J., Drobiec, Ł. & Wolka, P., 2021. Flexural Tensile Strength of Concrete with Synthetic Fibers. *materials*, Volume 14, p. 4428.

Borges, L. A. C., 2017. *Ensaio de compressão de corpo de prova com duplo corte em cunha na avaliação de concretos com baixos teores de fibra de aço*, São Paulo: s.n.

Borges, L. A. C., Monte, R., Rambo, D. A. S. & Figueiredo, A. D. d., 2019. Evaluation of post-cracking behavior of fiber reinforced concrete using indirect tension test. *Construction and Building Materials*, Volume 204, pp. 510-519.

Bruhwiler, E. & Wittman, F. H., 1990. The wedge splitting test, a new method of performing stable fracture mechanics tests. *Engineering Fracture Mechanics*, Volume 35, pp. 117-125.

Buttignol, T. E. T., Santos, A. C. & Bitencourt Jr., L. A., 2024. 3D DEWS digital parametric modeling and manufacturing for obtaining the post-cracking parameters of SFRC. *Construction and Building Materials*, Volume 428, p. 136326.

Cajka, R. et al., 2020. Experiments on Fiber Concrete Foundation Slabs in Interaction with the Subsoil. *Sustainability*, pp. 1-21.

Cardoso, M. G., 2020. *Caracterização do comportamento pós-fissuração de concretos autoadensáveis com fibras para elementos de pequena espessura*, Brasília: s.n.

Cardoso, M. G., Lameiras, R. d. M. & Capuzzo, V. M. S., 2021. Influence of concrete strength, fiber content and aspect ratio in the residual flexural strength of steel fiber reinforced self-compacting concrete. *Revista IBRACON de Estruturas e Materiais*, Volume 14.

Carmona, S. & Aguado, A., 2012. New model for the indirect determination of the tensile stress–strain curve of concrete by means of the Brazilian test. *Materials and Structures*, pp. 1473-1485.

Carmona, S., Gettu, R., Hurtado, C. & Martin , M. A., 1995. *Use of the splitting-tension test to characterize the toughness of fiber-reinforced concrete.* s.l., s.n., pp. 233-238.

Carrillo, J., Ramirez, J. & Lizarazo-Marriaga, J., 2019. Modulus of elasticity and Poisson's ratio of fiber-reinforced concrete in Colombia from ultrasonic pulse velocities. *J. Build. Eng.*, pp. 18-26.

Carrilo, J., Pincheira, J. A. & Alcocer, S. M., 2017. Behavior of low-rise, steel fiber-reinforced concrete thin walls under shake table excitations. *Eng. Struct.*, Volume 138, p. 146–158.

Carvalho, P. P. M. d. & Lameiras, R. d. M., 2023b. Semi-circular Bending Test to Evaluate the Post Cracking Behaviour of Fibre Reinforced Concretes. In: *International RILEM Conference on Synergising Expertise towards Sustainability and Robustness of Cement-based Materials and Concrete Structures.* s.l.:RILEM Bookseries.

Carvalho, P. P. M. & Lameiras, R. M., 2023a. A Simplified Inverse Analysis Procedure for the Stress-Crack Opening Relationship of Fiber-Reinforced Concrete. *buildings,* 13(5).

ChatGPT, Access date: 05/12/2023. *ChatGPT was used to improve English writing,* Retrieved from https://openai.com/blog/chatgpt/: s.n.

Chen, W. F., 1970. Double punch test for tensile strength of concrete. *ACI Mater J,* 67(12), p. 993–995.

Chu, S. H., Sneed, L. H., Yoo, D.-Y. & Kwan, A., 2024. Hooking effect on flexural strength and toughness of steel fiber reinforced concrete (SFRC) beams. *ACI Materials Journal*, 121(6), pp. 15-25.

Cifuentes, H. et al., 2017. Modified Disk-Shaped Compact Tension Test for Measuring Concrete Fracture Properties. *International Journal of Concrete Structures and Materials*, Volume 11, p. 215–228.

CNR-DT 204, 2006. *Guidelines for design, construction and production control of fiber reinforced concrete structures*, National Research Council of Italy: s.n.

Committee, R. T., 2002. TC162-TDF - Test and design methods for steel fibre reinforced concrete. Design of steel fibre reinforced concrete using σ-w method: principles and aplications. June, Volume 35, pp. 262-278.

Conforti, A., Minelli, F., Plizzari, G. A. & Tiberti, G., 2017. Comparing test methods for the mechanical characterization of fiber reinforced concrete. *Structural Concrete*, 19(3), pp. 656-669.

Conforti, A., Minelli, F., Plizzari, G. & Tibert, G., 2017. Comparing test methods for the mechanical characterization of fiber reinforced concrete. *Struct. Concr.*, Volume 19, p. 656–669.

Coronel, S. d. A. et al., 2025. Effect of DEWS test simplification on the design post-crack parameters of steel fiber reinforced concrete with different fiber contents. *Construction and Building Materials*, Volume 470.

Correal, J. F. & Herrána, C. A., 2018. Performance of hybrid fiber-reinforced concrete for low-rise housing with thin walls. *Constr. Build. Mater.*, Volume 185, p. 519–529.

Cuenca, E. & Ferrara, L., 2020. Fracture toughness parameters to assess crack healing capacity of fiber reinforced concrete under repeated cracking-healing cycles. *Theoretical and Applied Fracture Mechanics*, Volume 106.

Cunha, V. M. C. F., Barros, J. A. O. & Sena-Cruz, J. M., 2009. Pullout Behavior of Steel Fibers in Self-Compacting Concrete. *Journal of Materials in Civil Engineering*, 22(1).

Cunha, V. M. C. F., Barros, J. & Sena-Cruz, J., 2008. Bond-Slip Mechanisms of Hooked-End Steel Fibers in Self-Compacting Concrete. *Material Science Forum*, Volume 587-588, pp. 877-881.

Cunha, V. M. d. C. F., 2010. *Steel Fibre Reinforced Self-Compacting Concrete (from Micro-Mechanics to Composite Behaviour)*, Guimarães: Tese (Tese de Doutorado) - University of Minho.

Dave, E. V., Oshone, M., Schokker, A. & Bennett, C. E., 2019. *Disc shaped compact tension (DCT) specifications development for asphalt pavement*, Minnesota: Final Report.

DBV – Guide to Good Practice, 2007. *Steel Fibre Concrete*, Berlin, Germany: s.n.

De Smedt, M. et al., 2021. *Uniaxial Tension Tests of Steel Fibre Reinforced Concrete with AE Monitoring.* RILEM Bookseries, Springer, p. 143–154.

Deluce, J. R. & Vecchio, F. J., 2013. Cracking Behavior of Steel Fiber-Reinforced Concrete Members Containing Conventional Reinforcement. *ACI STRUCTURAL JOURNAL*, 110(3).

Destrée, X. & Mandl, J., 2008. Steel fibre only reinforced concrete in free suspended elevated slabs: Case studies, design assisted by testing route, comparison to the latest SFRC standard documents. In: *Tailor Made Concrete Structures.* London: Tailor Made Concrete Structures, p. 437–443.

di Prisco, M., Dozio, D. & Ferrara, L., 2007. *On the connections between fresh state behavior, fiber dispersion and toughness properties of steel fiber reinforced concrete.* Bagneaux, IN HIGH PERFORMANCE FIBER REINFORCED CEMENT COMPOSITES (HPFRCC5). RILEM PUBLICATION SARL, pp. 249-258.

di Prisco, M., Felicetti, R., Lamperti, M. G. L. & Menotti, G., 2004. *On size effect in tension of SFRC thin plates.* Milano, FraMCoS-5 - Fifth International Conference on Fracture Mechanics of Concrete and Concrete Structures, pp. 1075-1082.

di Prisco, M., Ferrara, L. & Lamperti, M. G. L., 2013. Double edge wedge splitting (DEWS): an indirect tension test to identify post-cracking behaviour of fibre reinforced cementitious composites. *Materials and Structures,* Volume 46, p. 1893–1918.

di Prisco, M., Lamperti, M. & Lapolla, S., 2010. *Double-Edge Wedge Splitting test: preliminary results.* Seogwipo, Jeju, Proceedings, pp. 1579-1586.

di Prisco, M., Plizzari, G. & Vandewalle, L., 2009a. Fibre reinforced concrete: new design perspectives. *Materials and Structures,* Volume 42, p. 1261–1281.

di Prisco, M., Plizzari, G. & Vandewalle, L., 2009. Fibre reinforced concrete: new design perspectives. *Materials and Structures,* Volume 42, p. 1261–1281.

DIANA FEA, 2022. *Bending Test on a Fiber-Reinforced Concrete Notched Beam - Tutorial,* Version 10.6: s.n.

Ding, C., Gao, D. & Guo, A., 2022. Analytical methods for stress-crack width relationship and residual flexural strengths of 3D/4D/5D steel fiber reinforced concrete. *Construction and Building Materials,* Volume 346.

Ding, X. et al., 2018. Effects of different deformed steel-fibers on preparation and fundamental properties of self-compacting SFRC. *Construction and Building Materials,* Volume 168, p. 471–481.

Domski, J. & Katzer, J., 2020. Comprehensive approach to evaluation of mechanical properties of waste aggregate concrete reinforced by steel fiber. *Struct. Concr.*, 21(1), p. 428–436.

Donnini, J., Lancioni, G., Chiappini, G. & Corinaldesi, V., 2020. Uniaxial tensile behavior of ultra-high performance fiber-reinforced concrete (uhpfrc): Experiments and modeling. *Composite Structures*, Volume 258.

Doyon-Barbant, J. & Charron, J.-P., 2018. Impact of fibre orientation on tensile, bending and shear behaviors of a steel fibre reinforced concrete. *Materials and Structures,* 51(157).

Dunning, I., Huchette, J. & Lubin, M., 2017. JuMP: A modeling language for mathematical optimization. *SIAM Review,* 59(2), pp. 295-320.

Durand, R. & Silva, F., 2019. A Coulomb-based model to simulate concrete cracking using cohesive elements. *Int J Fract*, Volume 220, pp. 17-43.

Durand, R. & Silva, F. H. B. T., 2021. Three-dimensional modeling of fracture in quasi-brittle materials using plasticity and cohesive finite elements. *Int J Fract*, p. 45–70.

Durand, R., Vieira, J. F. & Farias, M. M., 2023. Numerical analysis of bonded and unbonded prestressed RC beams using cohesive and non-compatible rod elements. *Eng Struct*, 288(116157).

Edelman, A., Karpinski, S. & Shah, V. B., 2012. *Julia: A fast dynamic language for technical computing,* arXiv preprint arXiv: 1209.5145.

EFNARC, 2002. *Specification and Guidelines for Self-Compacting Concrete,* London: s.n.

EN 12697-44, 2010. *European Committee for Standardization: Bituminous Mixtures – Test Methods for Hot Mix Asphalt Part,* Brussels, Belgium: s.n.

EN 14651, 2005. *Test method for metallic fibered concrete - measuring the flexural tensile strength (limit of proportionality (LOP), residual),* Brussels: s.n.

EN 14651, 2007. *Test method for metallic fibered concrete,* Measuring the flexural tensile strength (limit of proportionality (LOP), residual): s.n.

ENCCS, 2023. *Julia for High-Performance Computing,* s.l.: European National Competence Centre in Supercomputing.

Fantilli, A. P., Chiaia, B. & Gorino, A., 2016a. Unified approach for minimum reinforcement of concrete beams. *ACI Structural Journal,* Volume 5, p. 1107–1116.

Fantilli, A. P., Chiaia, B. & Gorino, A., 2016b. Fiber volume fraction and ductility Index of concrete beams. *Cement and Concrete Composites,* Volume 65, p. 139–149.

Fares, A. M. H. & Bakir, B. B., 2025. Nonlinear finite element analysis of layered steel fiber reinforced concrete beams. *Computers & Structures*, Volume 307, p. 107637.

Ferrara, L., Faifer, M., Muhaxheri, M. & Toscani, S., 2012. A magnetic method for non destructive monitoring of fiber dispersion and orientation in steel fiber reinforced cementitious composites. Part 2: Correlation to tensile fracture toughness. *Materials and Structures*, 45(4), p. 591–598.

Ferrara, L. & Meda, A., 2006. Relationships between fibre distribution, workability and the mechanical properties of SFRC applied to precast roof elements. *Materials and Structures,* Volume 39, pp. 410-20.

Ferrara, L., Park, Y. D. & Shah, S. P., 2008. Correlation among Fresh State Behavior, Fiber Dispersion, and Toughness Properties of SFRCs. *Journal of Materials in Civil Engineering*, 20(7), p. 493-501.

fib, 2012. *Model code 2010,* Lausanne: s.n.

Figueiredo, A. D. d., 2011. *Concreto Reforçado com Fibras,* São Paulo: s.n.

Frazão, C., Barros, J. & Bogas, J. A., 2021. Influence of the Chloride Attack on the Post-Cracking Behavior of Recycled Steel Fiber Reinforced Concrete. *Materials*, 14(5).

Frazão, C. et al., 2022. Technical and environmental potentialities of recycled steel fiber reinforced concrete for structural applications. *Journal of Building Engineering*, Volume 45.

Frazão, C. M. V., 2019. *Recycled Steel Fiber Reinforced Concrete for Structural elements subjected to chloride attack: Mechanical and Durability performance*, Braga: s.n.

Frazão, C. M. V., Barros, J. A. O. & Bogas, J. A., 2019. Durability of Recycled Steel Fiber Reinforced Concrete in Chloride Environment. *Fibers*, 7(12).

Galeote, E., Blanco, A., Cavalaro, S. H. P. & de la Fuente, A., 2017. Correlation between the Barcelona test and the bending test in fibre reinforced concrete. *Construction and Building Materials*, Volume 152, pp. 529-538.

Gao, D., Ding, C., Yuyang, P. & Chen, G., 2021. An inverse analysis method for multi-linear tensile stress-crack opening relationship of 3D/4D/5D steel fiber reinforced concrete. *Construction and Building Materials*, 309(125074).

García, N. A., 2019. *Quantificação da incerteza em modelos de fratura e fadiga utilizando polinômios de expansão de caos*, Distrito Federal: Tese de Doutorado.

Germano, F., Tiberti, G. & Plizzari, G., 2016. Post-peak fatigue performance of steel fiber reinforced concrete under flexure. *Materials and Structures*, Volume 49, pp. 4229-4245.

GitHub, 2024. *Amaru.jl: A finite element library in Julia.* [Online] Available at: https://github.com/NumSoftware/Amaru.jl [Accessed 24 April 2025].

Gödde, L. & Mark, P., 2015. Numerical simulation of the structural behaviour of SFRC slabs with or without rebar and prestressing. *Materials and Structures*, Volume 48, p. 1689–1701.

Gorino, A. & Fantilli, A. P., 2020. Scaled Approach to Designing the Minimum Hybrid Reinforcement of Concrete Beams. *Materials*, 13(22).

Gough, J., 2013. Open-source software for computational science and engineering: A new paradigm for scientific collaboration. *Journal of Computational Physics*, Volume 259, pp. 21-29.

Govindjee, S., Kay, G. J. & Simo, J. C., 1995. Anisotropic Modelling and Numerical Simulation of Brittle Damage in Concrete. *INTERNATIONAL JOURNAL FOR NUMERICAL METHODS IN ENGINEERING*, Volume 38, pp. 3611-3633.

Grünewald, S., 2004. *Performance-based design of self-compacting fibre reinforced concrete,* Delft: s.n.

Gudzulic, V., Dang, T. S. & Meschke, G., 2019. Computational modeling of fiber flow during casting of fresh concrete. *Computational Mechanics*, Volume 63, pp. 1111-1129.

Hamad, A. J. & Sldozian, R. J. A., 2019. Flexural and Flexural Toughness of Fiber Reinforced Concrete- American Standard Specifications Review. *GRD Journal for Engineering*, 4(3).

Hillerborg, A., 1980. Analysis of fracture by means of the fictitious crack model, particularly for fiber-reinforced concrete. *International Journal Composites Cements,* 2(4), pp. 177-184.

Hillerborg, A., Modéer, M. & Petersson, P. E., 1976. Analysis of crack formation and crack growth in concrete by means of fracture mechanics and finite elements. *Cement and Concrete Research*, pp. 773-781.

Hird, C. C. & Kwok, C. M., 1989. Finite element studies of interface behaviour in reinforced embankments of soft ground. *Comput Geotech*, 8(2), p. 111–131.

Hordijk, D., 1991. *Local approach to fadigue of concrete,* s.l.: s.n.

Hordijk, D., 1991. *Local approach to fadigue of concrete,* Delft: s.n.

Hosseini, A. S. et al., 2023. Semi-circular bending setup for predicting fracture characteristics of high-strength fiber-reinforced concrete. *Theoretical and Applied Fracture Mechanics*, Volume 123.

Huo, L., Bi, J., Zhao, Y. & Wang, Z., 2021. Constitutive model of steel fiber reinforced concrete by coupling the fiber inclining and spacing effect. *Construction and Building Materials*, 280(122423).

Islam, M. M. et al., 2014. Finite element analysis of steel fiber-reinforced concrete (SFRC): validation of experimental tensile capacity of dog-bone specimens. *International Journal of Advanced Structural Engineering*, 6(63).

Iyengar, K. T. S. R., Raviraj, S. & Ravikumar, P. N., 1998. *Analysis study of fictitious crack propagation in concrete beams using a bi-linear σ–w relation.* Japan, s.n., p. 315–324.

JCI-S-003-2007, 2007. *Method of test for bending moment-curvature of FRCC,* s.l.: s.n.

Jin, Z.-H., Paulino, G. & Dodds, R., 2003. Cohesive fracture modeling of elastic–plastic crack growth in functionally graded materials. *Eng Fract Mech*, 70(14), p. 1885–912.

Jones, P. A., Austin, S. A. & Robins, P. J., 2008. Predicting the flexural load-deflection response of steel fibre reinforced concrete from strain, crack-width, fibre pull-out and distribution data. *Materials and Structures,* Volume 41, pp. 449-463.

JSCE-SF4, 1984. *THE JAPAN SOCIETY OF CIVIL ENGINEERS - Part III - 2 method of tests for steel fiber reinforced concrete,* Concrete Library of JSCE: s.n.

Karihaloo, B. L., 1995. *Fracture Mechanics and Structural Concrete,* Harlow: Longman Pub Group.

Karihaloo, B. L., Abdalla, H. M. & Imjai, T., 2003. A simple method for determining the true specific fracture energy of concrete. *Magazine of Concrete Research*, 55(5), p. 471–481.

Karrer, S. et al., 2022. Direction-dependent behaviour and size effect of steel fibre reinforced concrete based on the double punch test. *Materials and Structures*, 55(176).

Katzer, J. & Domski, J., 2012. Quality and mechanical properties of engineered steel fibres used as reinforcement for concrete. *Constr. Build. Mater.*, p. 243–248.

Kooiman, A. G., 2000. *Modelling Steel fibre reinforced concrete for structural design,* s.l.: s.n.

Krenchel, H., 1975. *Fibre spacing and specific fibre surface.* Horneby, RILEM Symposium, pp. 69-79.

Kumar, S. & Barai, S. V., 2011. *Concrete Fracture Models and Applications,* Berlin: Springer, p. 262.

Kuruppu, M. D. et al., 2014. ISRM-suggested method for determining the mode i static fracture toughness using semi-circular bend specimen. *Rock Mechanics and Rock Engineering*, Volume 47, pp. 267-274.

Kwan, A. K. H. & Chu, S. H., 2018. Direct tension behaviour of steel fibre reinforced concrete measured by a new test method. *Eng. Struct.*, Volume 176, p. 324–336.

Kwon, S., Nishiwaki, T., Kikuta, T. & Mihashi, H., 2014. Development of Ultra-High-Performance Hybrid Fiber-Reinforced Cement-Based Composites. *Aci Materials Journal*, 111(3).

Lameiras, M., Magalhães, C. A. & Soares, R. P., 2021. Amaru.jl: A flexible and extensible finite element library in Julia for solid mechanics analysis. *Journal of Computational Mechanics*.

Lameiras, R., Barros, J. A. O. & Azenha, M., 2015. Influence of casting condition on the anisotropy of the fracture properties of Steel Fibre Reinforced Self-Compacting Concrete (SFRSCC). *Cement and Concrete Composites*, pp. 60-76.

Lameiras, R. d. M., 2016. *Sandwich structural panels comprising thin-walled SFRSCC and GFRP connectors: from material features to structural behaviour,* Guimarães: Tese (Tese de Doutorado) - University of Minho.

Laranjeira, F. d. O., 2010. *Design-oriented constitutive model for steel fiber reinforced concrete,* Barcelona: s.n.

Ledesma Villalba, A., 1987. *Identificación de Parámetros en Geotecnia: Aplicación a la Excavación de Túneles*, Barcelona: Escuela Técnica Superior de Ingenieros de Caminos, Canales.

Lim, I. L., Johnston, I. W., Boland, J. N. & Choi, S. K., 1994a. Fracture Testing of a Soft Rock with Semi-circular Specimens Under Three-point Bending. Part 1 - Mode I.

International Journal of Rock Mechanics and Mining Sciences & Geomechanics Abstracts, 31(3), pp. 185-197.

Lim, I. L., Johnston, I. W., Choi, S. K. & Boland, J. N., 1994b. Fracture testing of a soft rock with semi-circular specimens under three-point bending. Part 2 - Mixed-mode. *International Journal of Rock Mechanics and Mining Sciences & Geomechanics Abstracts*, Volume 31, pp. 199-212.

Löfgren, I., Stang, H. & Olesen, J. F., 2004. *Wedge Splitting Test - A test to determine fracture proprieties of FRC.* Varenna, FRC BEIFIB, pp. 379 - 388.

Löfgren, I., Stang, H. & Olesen, J. F., 2005. Fracture Properties of FRC Determined through Inverse Analysis of Wedge Splitting and Three-Point Bending Tests. *Journal of Advanced Concrete Technology*, 3(3), pp. 423-434.

Luo, X., Sun, W. & Chan, S. Y. N., 2001. Steel fiber reinforced high-performance concrete: a study on the mechanical properties and resistance against impact. Volume 34, p. 144–149.

Malatesta, S. C., de Cea, A. A. & Borrell, C. M., 2012. Generalization of the Barcelona test for the toughness control of FRC. *Materials and Structures*, Volume 45, p. 1053–1069.

Mandal, T., Hanz, A. J. & Bahia, H. U., 2019. Challenges in using the Disc-Shaped Compact Tension (DCT) test to determine role of asphalt mix design variables in cracking resistance at low temperatures. *International Journal of Pavement Engineering*, 20(11), p. 1275–1284.

Marcalikova, Z. et al., 2020. Determination of Mechanical Characteristics for Fiber-Reinforced Concrete with Straight and Hooked Fibers. *Crystals*, Volume 10, pp. 1-21.

Markovic, I., 2006. *High-Performance Hybrid-Fiber Reinforced Concrete: Development and Utilisation*, Delft: Doctoral Thesis, Delft University of Technology.

Martinie, L., Rossi, P. & Roussel, N., 2010. Rheology of fiber reinforced cementitious materials: classification and prediction. *Cement and Concrete Research*, 40(2), p. 226-234.

Massicotte, B., 2004. *Implementing SFRC design into North American codes: application to a building floor.* Bergamo, s.n., p. 73–80.

Matos, L. M. P., Barros, J. A. O., Ventura-Gouveia, A. & Calçada, R. A. B., 2021. A new inverse analysis approach for predicting the fracture mode I parameters of fibre reinforced concrete. *Engineering Fracture Mechanics,* Volume 246.

Medina, N. A., 2019. *Caracterização do Comportamento do Concreto Pós-fissuração do Concreto Autoadensável Reforçado com Fibras de Aço de Elementos de Pequena Espessura,* Foz do Iguaçu: s.n.

Mehta, P. K. & Monteiro, P. J. M., 2006. *Concrete: Microstructure, Properties, and Materials.* 3ª ed. Berkeley: McGraw-Hill.

Mena-Alonso, A., González, D., Mínguez, J. & Vicente, M., 2024. Mechanical behavior of high-strength steel fiber-reinforced concrete. *IntechOpen*.

Meng, G., Wu, B., Xu, S. & Huang, J., 2021. Modelling and experimental validation of flexural tensile properties of steel fiber reinforced concrete. *Construction and Building Materials,* Volume 273.

Mindess, S., Young, J. F. & Darwin, D., 2003. *Concrete.* 2ª ed. Upper Saddle River: Prentice Hall.

Minelli, F. & Plizzari, G., 2009. Round panel vs beam tests toward a comprehensive and harmonic characterization of FRC materials. In: *Proceedings of the Brittle Matrix Composites 9 Conference.* Warsaw: IFTR and Woodhead Publishing, p. 23–32.

Minelli, F. & Plizzari, G., 2011. A New Round Panel Test for the Characterization of Fiber Reinforced Concrete: A Broad Experimental Study. *Journal of Testing and Evaluation*, Volume 39, pp. 889-897.

Minelli, F. & Plizzari, G., 2015. Derivation of a simplified stress–crack width law for Fiber Reinforced Concrete through a revised round panel test. *Cement & Concrete Composites*, Volume 58, pp. 95-104.

Minelli, F. & Plizzari, G. A., 2010a. *Fiber reinforced concrete characterization through round panel test - part I: experimental study,* Korea: In:.

Minelli, F. & Plizzari, G. A., 2010b. *Fiber reinforced concrete characterization through round panel test - part II: analytical and numerical study,* Korea: s.n.

Mirsayar, M. M., Shi, S. & Zollinger, D. G., 2017. Evaluation of interfacial bond strength between Portland cement concrete and asphalt concrete layers using bi-material SCB test specimen. *Engineering Solid Mechanics*, 5(4), pp. 293-306.

Mobasher, B., Bakhshi, M. & Barsby, C., 2014. Backcalculation of residual tensile strength of regular and high performance fiber reinforced concrete from flexural tests. *Construction and Building Materials,* Volume 70, p. 243–253.

Mobasher, B. & Destreé, X., 2010. Design and construction aspects of steel fiber-reinforced concrete elevated slabs. In: *Fiber Reinforced Self-Consolidating Concrete: research and applications - Technical Sessions at the ACI Fall 2009.* New Orleans, LA: ACI, pp. 95-107.

Molins, C., Aguado, A. & Saludes, S., 2009. Double punch test to control the tensile properties of FRC (Barcelona Test). pp. 415-25.

Montaignac, R., Massicotte, B. & Charron, J.-P., 2012. Design of SFRC structural elements: Flexural behavior prediction.. *Material and Structures*, p. 13.

Monte, R. et al., 2023. Simplified DEWS test for steel fibre-reinforced concrete characterisation. *Rev. IBRACON Estrut. Mater.*, 16(6).

Mudadu, A. et al., 2018. The effect of fiber orientation on the post-cracking behavior of steel fiber reinforced concrete under bending and uniaxial tensile tests. *Cement and Concrete Composites*, Volume 93, pp. 274-288.

Mudadu, A., Tiberti, G., Germano, F. & Plizzari, G. A., 2018. The effect of fiber orientation on the post-cracking behavior of steel fiber reinforced concrete under bending and uniaxial tensile tests. *Cement and Concrete Composites*, Volume 93, pp. 274-288.

Nanni, A., 1988. Splitting-Tension Test for Fiber Reinforced Concrete. *Materials Journal*, 85(4), pp. 229-233.

Nanni, A., 1991. Pseudoductility of fiber reinforced concrete. *Journal of materials in civil engeneering*, fevereiro, Volume 3, pp. 78-90.

Neuner, M., Smaniotto, S. & Hofstetter, G., 2022. A modified wedge splitting test for susceptible quasi-brittle materials. *Construction and Building Materials*, Volume 326.

Nogueira, A. B. et al., 2021. Evaluation of the repeatability and reproducibility of the double punch test. *Construction and Building Materials*, 268(121145).

Nour, A., Massicotte, B., de Montaignac, R. & Jean-Philippe, C., 2015. Development of an inverse analysis procedure for the characterisation of softening diagrams for FRC beams and panels. *Construction and Building Materials*, Volume 94, pp. 35-44.

Nour, A., Massicotte, B., Montaignac, R. & Charron, J.-P., 2011. Derivation of a crack opening deflection relationship for fibre reinforced concrete panels using a stochastic model: Application for predicting the flexural behaviour of round panels using stress crack opening diagrams. *Cement and Concrete Research*, Volume 41, p. 964–974.

Olesen, J. F., 2001. FICTITIOUS CRACK PROPAGATION IN FIBER-REINFORCED CONCRETE BEAMS. *JOURNAL OF ENGINEERING MECHANICS*, Volume 127, pp. 272-280.

Oliver, J., 1989. A consistent characteristic length for smeared cracking models. *International Journal for Numerical Methods in engineering*, 28(2), pp. 461-474.

Olivito, R. S. a. Z. F. A., 2010. An experimental study on the tensile strength of steel fiber reinforced concrete. *Composites Part B: Engeneering.*

Ortega-López, V. et al., 2022. Validation of slag-binder fiber-reinforced self-compacting concrete with slag aggregate under field conditions: Durability and real strength development. *Construction and Building Materials*, 21 February, Volume 320.

Ozyurt, N., Mason, T. O. & Shah, S. P., 2007. Correlation of fiber dispersion, rheology and mechanical performance of FRCs. *Cement and Concrete Composites*, pp. 70-79.

Paegle, I. & Fischer, G., 2013. *Evaluation of test methods used to characterize fiber reinforced cementitious composites,* Riga, Latvia: s.n.

Parvez, A. & Foster, S. J., 2015. Fatigue behavior of steel-fiber-reinforced concrete beams. *Journal of Structural Engineering*, 141(4), p. 04014117.

Pasa Dutra, V. F., 2012. *Um modelo constitutivo para o concreto reforçado com fibras de aço via Teoria da Homogeneização,* Porto Alegre: Doctoral Thesis. Universidade Federal

do Rio Grande do Sul. Escola de Engenharia. Programa de Pós-Graduação em Engenharia Civil.

Pedersen, C., 1996. *New production processes, materials and calculation techniques for fiber reinforced concrete pipes,* s.l.: s.n.

Pereira, L. S., Monte, R., Bitencourt Júnior, L. A. & Figueiredo, A. D., 2019. *Caracterização e controle do concreto com fibras para obras de infraestrutura com ensaio de tração indireta.* Fortaleza, 61° Congresso Brasileiro do Concreto - IBRACON.

Perkel, J. M., 2019. Julia: Come for the syntax, stay for the speed. *Nature*, 572(7771), p. 141–142.

Piembsystech, 2023. *Exploring the scientific computing ecosystem in Julia.* [Online] Available at: https://piembsystech.com/exploring-the-scientific-computing-ecosystem-in-julia/
[Accessed 24 april 2025].

Planas, J., 2007. Re-port rep039: Experimental Determination of the Stress-Crack Opening Curve for Concrete in Tension. In: *Minimum demands for de-formation controlled uniaxial tensile tests.* Madrid, Spain: Final report of RILEM Technichal Committe TC 187-SOC.

Planas, J. et al., 2007. *Experimental determination of stress-crack opening curve of concrete in tension,* s.l.: RILEM TC 187-SOC.

Plesha, M. E., Ballarini, R. & Parulekar, A., 1989. Constitutive model and finite element procedure for dilatant contact problems. *J Eng Mech*, 115(12), p. 2649–2668.

Pujadas, P. et al., 2013. New analytical model to generalize the barcelona test using axial displacement. *Journal of Civil Engineering and Management*, 19(2), pp. 259-271.

Pujadas, P. et al., 2014. Multidirectional double punch test to assess the post-cracking behaviour and fibre orientation of FRC. *Construction and Building Materials*, Volume 58, pp. 214-224.

Qing, L., Yu, K. & Forth, J. P., 2019. Uniaxial tensile behavior of aligned steel fibre reinforced cementitious composites. *Materials and Structures*, 52(70).

Rambo, D. A. S., 2012. *Concreto Autoadensáveis Reforçados com Fibras de Aço Híbridas: Aspectos Materiais e Estruturais*, Rio de Jaineiro: s.n.

Ranocha, H., Winters, A. R. & Ketcheson, D. I., 2021. Trixi.jl: A tree-based numerical simulation framework for hyperbolic PDEs in Julia. *arXiv preprint arXiv:2108.06476*.

Rauecker, J. C. N., Junior, W., Pituba, J. & Lima Araújo, D., 2019. Uma abordagem experimental e numérica para determinação de curvas de compressão para concreto simples e reforçados com fibras de aço. *Matéria*, Volume 24.

RILEM TC 162-TDF, 2000. Bending Test. *Materials and Structures*, 33(1), pp. 3-5.

RILEM TC 162-TDF, 2002. Test and design methods for steel fibre reinforced concrete - Design of steel fibre reinforced concrete using the σ-w method: Principles and application. *J. Mater. Struct.*, Volume 35, p. 262–276.

RILEM TC 162-TDF, 2002. Test and design methods for steel fibre reinforced concretes: Uni-axial tension test for steel fibre reinforced concrete. *Journal of Materials and Structures*, 34(1), pp. 3-6.

Robins, P. J., Austin, S. A. & Jones, P. A., 2003. Spatial distribution of steel fibres in sprayed and cast. *Magazine of Concrete Research*, pp. 225-235.

Roelfstra, P. E. & Wittmann, F. H., 1986. Numerical method to link strain softening with failure of concrete. In: London: Wittmann FH, editor.

Roy, Y. A. & Dodds, R. H., 2001. Simulation of ductile crack growth in thin aluminum panels using 3-D surface cohesive elements. *Int J Fract*, 110(1), p. 21–45.

Salehian, H., 2015. *Evaluation of the Performance of Steel Fibre Reinforced Self-Compacting Concrete in Elevated Slab Systems; from the Material to the Structure*, Guimarães: Tese (Tese de Doutorado) - University of Minho.

Salehian, H. & Barros, J. A., 2015. Assessment of the performance of steel fibre reinforced self-compacting concrete in elevated slabs. *Cement and Concrete Composites*, Volume 55, pp. 268-280.

Saludes, A. R., Aguado, A. & Molins, C., 2007. *Ensayo de doble punzonamiento aplicado al hormigón reforzado con fibras,* Barcelona: s.n.

Santos, F. L. G. d. & Forti, T. L. D., 2022. Concrete cohesive curves for specimens with different sizes: A study of inverse analysis and size effect. *Engineering Fracture Mechanics,* Volume 261.

Santos, F. P., 2022. *Avaliação do ensaio de duplo puncionamento aplicado para o controle do concreto projetado reforçado com fibras de aço,* São Paulo: Dissertação (Mestrado em Engenharia Civil) - Universidade de São Paulo para a obtenção do título de mestre em Ciências.

Santos, F. P. et al., 2023. Investigation of specimen size effect on the use of double punch test as quality control method of the steel fiber reinforced shotcrete. *Matéria*, 28(3).

Santos, N. O., 2015. *Modelos de dano para concreto,* Rio de Jaineiro: s.n.

Sarmiento, E. V., Zirgulis, G., Sandbakk, S. & Geiker, M. R., 2012. *Influence of concrete flow on fibre distribution, orientation and mechanical properties of fibre reinforced concrete.* Guimarães, BEFIB2012–Fibre reinforced concrete.

Sarzalejo, A. G., 2010. *Fibras como elemento estrutural para reforço de concreto - manual técnico.* São Paulo: Maccaferri do Brasil Ltda..

Segura-Castillo, L., Monte, R. & Figueiredo, A. D. d., 2018. Characterisation of the tensile constitutive behaviour of fibre-reinforced concrete: A new configuration for the Wedge Splitting Test. *Construction and Building Materials*, Volume 192, pp. 731-741.

Selby, R. G. & Vecchio, F. J., 1995. *Three-dimensional Constitutive Relations for Reinforced Concrete,* Toronto, Canada: Univ. Toronto, dept. Civil Eng..

Serafini, R. et al., 2021. Double Edge Wedge Splitting Test to Characterize the Design Postcracking Parameters of Fiber-Reinforced Concrete Subjected to High Temperatures. *J Mater Civ Eng*, 33(5).

Shah, S. P. & Ferrara, L., 2008. *Self consolidating fiber reinforced concrete.* Chennai, RILEM Publications, p. 641–659.

Sharifi, Y. & Moghbeli, A., 2020. New predictive models via gene expression programming and multiple nonlinear regression for SFRC beams. *Journal of Materials Research and Technology*, 9(6), pp. 14294-14306.

Shi, X. et al., 2020. Constitutive behaviors of steel fiber reinforced concrete under uniaxial compression and tension. *Construction and Building Materials*, Volume 233.

Shoaib, A., Lubell, A. S. & Bindiganavile, V. S., 2014. Size Effect in Shear for Steel Fiber-Reinforced Concrete Members without Stirrups. *ACI Structural Journal*, Volume 111, p. 1081.

Silva, F. H. B. T., 2017. *Análise Numérica da Fratura no Concreto em Modo I e Modo Misto Utilizando Elemento de Junta*, Brasília: Dissertação de Mestrado em Estruturas e Construção Civil.

Silva, F. H. B. T., 2021. *Modelagem Tridimensional De Fratura Em Materiais Quase Frágeis Com Aplicações Em Fraturamento Hidráulico Usando Elementos Finitos*, s.l.: Doutorado Em Estruturas E Construção Civil - Departamento De Engenharia Civil E Ambiental - Universidade de Brasília.

Simão, L. d. C. R., 2019. *Estudo de Sistemas de Controle para o Ensaio de Duplo Puncionamento*, São Paulo: s.n.

Simão, L. d. C. R. et al., 2019. Influence of the instability of the double punch test on the post-crack response of fiber-reinforced concrete. *Construction and Building Materials*, Volume 217, pp. 185-192.

Singh, H., 2016. *Steel Fiber Reinforced Concrete: Behavior, Modelling and Design*. s.l.:Springer.

Singh, S. P., Mohammadi, Y. & Madan, S. K., 2006. Flexural fatigue strength of steel fibrous concrete containing mixed steel fibres. *Journal of Zhejiang University-Science A*, 7(8), pp. 1329-1335.

Skoček, J. & Stang, H., 2008. Inverse analysis of the wedge-splitting test. *Engineering Fracture Mechanics*, 75(10), pp. 3173-3188.

Soltanzadeh, F., Cunha, V. M. d. C. F. d. & Barros, J. A. O., 2019. Assessment of different methods for characterization and simulation of post-cracking behavior of self-compacting steel fiber reinforced concrete. *Construction and Building Materials,* Volume 227.

Soranakom, C. & Mobasher, B., 2008. Correlation of tensile and flexural responses of strain softening and strain hardening cement composites. *Cement & Concrete,* Volume 30, pp. 465-477.

Sorelli, L. G., Meda, A. & Plizzari, G. A., 2005. Bending and Uniaxial Tensile Tests on Concrete Reinforced with Hybrid Steel Fibers. *Journal of Materials in Civil Engineering,* 17(5), p. 519–527.

Soroushian, P. & Lee, C.-D., 1990. Distribution and orientation of fibers in steel fiber reinforced concrete. *ACI Materials journal,* 87(5), pp. 433-439.

Stahli, P., Custer, R. & Van Mier, J. G., 2008. On flow properties, fibre distribution, fibre orientation and flexural behaviour of FRC. *Materials and structures,* Volume 41, pp. 189-196.

Stephen, S. J., Raphael, B., Gettu, R. & Jose, S., 2019. Determination of the tensile constitutive relations of fiber reinforced concrete using inverse analysis. *Construction and Building Materials,* Volume 195, p. 405–414.

Strack, M., 2008. *Modelling of crack opening of SFRC under tension and bending.* s.l., s.n., p. 323–332.

Stroeven, P. & Hu, J., 2006. Effectivness near boundaries of fibre reinforcement in concrete. *Materials and Structures,* Volume 39, pp. 1001-1013.

Sucharda, O. et al., 2017. Comparative Evaluation of Mechanical Properties of Fibre Reinforced Concrete and Approach to Modelling of Bearing Capacity Ground Slab. *Period. Polytech. Civ. Eng.*, 61(4), p. 972–986.

Su, C., Wu, Q., Weng, L. & Chang, X., 2019. Experimental investigation of mode I fracture features of steel fiber-reinforced reactive powder concrete using semi-circular bend test. *Engineering Fracture Mechanics,* Volume 209, p. 187–199.

Taheri, M. & Barros, J. A. O., 2011. *A design model of strain-softening and strain-hardening fiber reinforced elements reinforced longitudinally with steel and FRP bars,* s.l.: Composites Part B: Engeneering.

Taheri, M., Barros, J. & Salehian, H., 2012. Parametric study of the use of strain softening/hardening FRC for rc elements failing in bending. *Journal of Materials in,* Volume 24, pp. 259-274.

Toledo Filho, R. D., 2001. *Materiais compósitos reforçados com fibras naturais: caracterização experimental,* Rio de Janeiro: s.n.

Trindade, Y. T. et al., 2020. Design of SFRC members aided by a multiscale model: Part I – Predicting the post-cracking parameters. *Composite Structures,* Volume 241.

Tschegg, E., 1986. *Equipment and appropriate specimen shapes for tests to measure fracture values.* s.l. Patent No. 390328.

Tschegg, E. K., 1991. New Equipments for Fracture Tests on Concrete. *Materials Testing,* Volume 33, pp. 338-342.

Turon, A., Camanho, P. P., Costa, J. & Dávila, C. G., 2007. A damage model for the simulation of delamination in advanced composites under variable-mode loading. *Mechanics of Materials,* 38(11), p. 1072–1089.

Ulfkjaer, J., Krenk, S. & Brincker, R., 1995. Analytical model for fictitious crack propagation in concrete beams. *Journal of Engeneering Mechanics,* p. 7–15.

UNI 11039-2:2003, 2003. *Steel Fiber Reinforced Concrete – Test Method for Determination of First Crack Strength and Ductility Indexes,* Milan, Italy: s.n.

UNI 11188, 2004. *Design, production and control of Steel Fibre Reinforced structural elements,* Italy: s.n.

van Mier, J. G. M. & van Vliet, M. R. A., 2002. Uniaxial tension test for the determination of fracture parameters of concrete: state of the art. *Engineering Fracture Mechanics,* 69(2), pp. 235-247.

Van Vliet, M. R. A., 2000. *Size effect in Tensile Fracture of Concrete and Rock*, The Netherlands: s.n.

Vasconcelos, R. E., 2012. *Fratura do concreto reforçado com fibras de aço e de polipropileno em meios normal e agressivo*, Campinas: s.n.

Vecchio, F. J. & Collins, M. P., 1993. Compression response of cracked reinforced concrete. *Journal of Structural Engineering*, 119(12).

Venkateshwaran, A., Tan, K. H. & Li, Y., 2018. *Residual Flexural Strengths of Steel Fiber Reinforced Concrete with Multiple Hooked-End Fibers*, Lausanne: International Federation for Structural Concrete.

Vipulanandan, C. & Paul, E., 1990. Performance of epoxy and polyester polymer concrete. *ACI Materials Journal*, 87(3), pp. 241-251.

Vrijdaghs, R., di Prisco , M. & Vandewalle, L., 2020. Creep of polymeric fiber reinforced concrete: A numerical model with discrete fiber treatment. *Computers & Structures*, 233(106233).

Wagnoner, M. P., Buttlar, W. G. & Paulino, G. H., 2005. Disk-shaped compact tension test for asphalt concrete fracture. *Experimental Mechanics*, Volume 45, p. 270–277.

Wagoner, M. P., Buttlar, W. G., Paulino, G. H. & Blankenship, P., 2005. Investigation of the Fracture Resistance of Hot-Mix Asphalt Concrete Using a Disk-Shaped Compact Tension Test. *Transportation Research Record: Journal of the Transportation Research Board*, 1929(1), pp. 183-192.

Willian, K. J. & Warnke, E. P., 1974. *Constitutive Model for The Triaxial Behaviour of Concrete*. Italy, Proceedings of IABSE Seminar on Concrete Structures Subjected to Triaxial Stresses.

Wilson, G. et al., 2014. Best practices for scientific computing. *PLOS Biology*, 12(1), p. e1001745.

Yin, Y., Qiao, Y. & Hu, S., 2019. Four-point bending tests for the fracture properties of concrete. *Engineering Fracture Mechanics*, Volume 211, pp. 371-381.

Yoo, D. Y. & Banthia, N., 2019. Impact resistance of fiber-reinforced concrete – A review. *Cement and Concrete Composites*, Volume 104, p. 103389.

Zhang, J. & Ju, X., 2011. Investigation on stress-crack opening relationship of engineered cementitious composites using inverse approach. *Cement and Concrete Research*, 41(8), pp. 903-912.

Zhang, J. & Li, V. C., 2004. Simulation of crack propagation in fiber-reinforced concrete by fracture mechanics. *Cement and Concrete Research*, 34(2), pp. 333-339.

Zhang, J. & Stang, H., 1998. APPLICATIONS OF STRESS CRACK WIDTH RELATIONSHIP. *Cement and Concrete Research*, Volume 28, pp. 439-452.

Zhao, K. et al., 2019. Application of Natural Plant Fibers in Cement-Based Composites and the Influence on Mechanical Properties and Mass Transport. *materials*, Volume 12, p. 3498.

Zhou, F. P., 1988. *Some aspects of tensile fracture behaviour and structural response of cementitious materials*, Lund, Swenden: s.n.

Zhu, B. et al., 2019. Development of 3D printable engineered cementitious composites with ultra-high tensile ductility for digital construction. *Materials and Design*, Volume 181, p. 108088.